ISAS - INTERNATIONAL SCHOOL
FOR ADVANCED STUDIES

N-BODY COMPUTATIONS OF THE ACTION OF DYNAMICAL FRICTION ON GLOBULAR CLUSTERS

A Thesis submitted for the degree of
Doctor Philosophiae

Candidate
S.MANORAMA

Supervisor
D. W. SCIAMA

December 1986

TRIESTE

SISSA - SCUOLA
INTERNAZIONALE
SUPERIORE
STUDI AVANZATI
TRIESTE
Strada Costiera 11

Abstract

Numerical computations have been performed to study the action of dynamical friction on globular clusters in galaxies. Over a Hubble time, the distribution of globular clusters can be altered significantly by the action of dynamical friction which leads to the destruction of massive globular clusters in galaxies. We investigated the orbital decay rates for globular clusters in elliptical and spiral galaxies separately and compared the two decay rates to check whether dynamical friction is responsible for the difference observed in the luminosity functions for globular clusters in these types of galaxies, in the sense that more massive globular clusters are observed in ellipticals than in spirals.

Chapter one of the thesis discusses the determination of extra-galactic distances by using globular clusters, based on the assumption that the luminosity function of these systems is invariant throughout the universe. We also show the evaluation of the Hubble constant H_o, from the distance determined to the Virgo cluster in this way. There are no compelling reasons to expect the luminosity function of the globular clusters to be the same in galaxies of all types and we report recent observations of the differences seen in the luminosity functions in elliptical and spiral globular cluster systems. The mechanisms which might lead to this difference are discussed and it is concluded here that dynamical friction might be the possible mechanism for the depletion of massive globular clusters in spiral galaxies.

Chapter two reviews and discusses the theory and formulation of dynamical friction in detail.

The third chapter is concerned with the finding of a suitable numerical integrator to solve the equations of motion in our N-body calculations. Various algorithms were checked and tested for efficiency, stability and accuracy, in particular, Aarseth's N-body code. We finally chose a second-order predictor corrector (Hybrid method) for our restricted N-body code.

Chapter four deals with the galaxy models, initial conditions for the particles that trace the density distributions in our galaxies and the globular cluster models that go into the N-body calculations.

In chapter five, we discuss the numerical work for globular clusters orbiting in spiral galaxies. Preliminary results show that resonances play an important role in the orbital evolution of the globular cluster. The slow orbital decay rates we have obtained indicated that dynamical friction is not enough to account for the observed depletion of massive globular clusters in spirals.

Chapter six deals with the numerical work on globular clusters in ellipticals. We did not observe much decay in the orbits for these globular clusters, compared to the decay rates of clusters in spirals.

In chapter seven, conclusions about this work and outlines for future work are sketched.

Acknowledgements

It is a pleasure to thank Dennis Sciama for suggesting this problem and for his constant encouragement during the course of this study.

I am also very grateful to Patrick Mann for introducing me to numerical work and for his guidance in the initial development of the code. Chapter three of this thesis is based on the work done in collaboration with him.

My special thanks go to Antonio Lanza for helping me with the Multi-grid code.

Thanks are also due to John Miller, Philip Palmer, Maria Petrou, Riccardo Valdarnini and Vincenzo Antonuccio for their valuable suggestions.

I wish to thank the staff of the SISSA computing centre for their technical assistance.

I acknowledge SISSA for providing financial support and travel grants to Oxford and Padova during the course of this work.

I finally wish to thank my family, friends and colleagues who helped in finishing this work.

Contents

CHAPTER ONE

GLOBULAR CLUSTERS AND THE HUBBLE CONSTANT

Globular clusters are among the oldest and most versatile astronomical objects in the Universe. They are spherical and very luminous objects containing up to more than a million stars. Our Galaxy has a halo of more than a hundred globular clusters and in more massive galaxies thousands of them have been observed. The most noticeable feature of globular clusters is the similarity displayed by them in a vast diversity of galaxies. All their masses and radii lie within a narrow range, their density profiles are homologous following the same law that applies to simplest elliptical galaxies and they apparently seem to share an unique luminosity function. Though each individual globular cluster does show some peculiarities, notably in metallicity etc., but once again some universal trends with the parent galaxy mass or type can be found. The overall picture of the observed universality and their great ages have linked the study of globular clusters, especially their origin to Cosmology.

The formation of globular clusters with masses typically around $10^6 M_\odot$ inside galaxies is still an unsolved problem. It was generally believed that globular clusters formed through contraction after the galaxy had come into existence but because the Jeans mass just after recombination is so near the observed masses of globular clusters, it was suggested [Peebles and Dicke 1968] that the growing condensations at the epoch of recombination should be associated with the formation of globular

clusters. In this scenario the formation of the larger systems in the Universe, like galaxies, clusters of galaxies and superclusters takes place by the merging of these proto-globular clusters. van den Bergh (1975) had pointed out however that globular clusters do differ systematically from one another in certain traits which argues for a post-galaxy formation. By studying the various properties exhibited by these mysterious systems, one might have some clues about the formation of structure in the Universe.

Within our own Galaxy, globular clusters have played key roles in galactic structure, early chemical and dynamical history, evolution of low mass and metal-poor stars, dynamics of stellar systems and recently on the nature of certain X-Ray sources. An excellent review on globular clusters as probes of galactic structure and evolutionary history, their uniform behavior in disparate systems and their kinematical and dynamical properties was given by Harris and Racine [Harris & Racine 1979].

The study of globular clusters in external galaxies is equally enriching and a vast field now. It is beginning to shed light upon the earliest formation and chemical enrichment episodes during proto-galaxy collapse, elucidating the importance of subsequent mergers and interactions between galaxies.

For the present studies, our interest in globular clusters lies in the role they play as extragalactic distance indicators. Based on the assumption that the luminosity function of globular clusters is invariant throughout the Universe, extragalactic distances are determined by comparing the magnitude of the peak in the luminosity function of the globular clusters in the galaxy

whose distance has to be determined with the luminosity function of nearby globular clusters, say those seen in the Local Group galaxies. Using the luminosity distribution of the globular clusters observed in five Virgo cluster galaxies and comparing the luminosity function with the luminosity function of the Local Group globular clusters, Hanes (1977a) determined the distance modulus of the Virgo cluster. Using this distance to the Virgo cluster, Hanes (1979) evaluated the value of the Hubble constant, H_0. H_0 so determined relies heavily on the assumption that the luminosity function of the globular clusters in the Virgo galaxies is similar to the luminosity function of the globular clusters in the Local Group galaxies.

There are various reasons for expecting the luminosity functions to be different. The galaxies used by Hanes to study the globular clusters in Virgo cluster were all giant ellipticals, while the galaxies used to study the globular clusters in the Local Group were mainly spirals. The question that can arise is whether the luminosity function of the globular clusters in these different types of galaxies assumed to be the same is justified or not. Globular clusters in spiral galaxies are subjective to disruptive events like disk passages [Fall and Rees 1977] and these experiences are not shared by their counterparts in elliptical galaxies. The action of dynamical friction which preferentially destroys bright, massive objects could also be more enhanced in spiral galaxies because of the presence of disks [Tremaine, Ostriker and Spitzer 1975] thus leading to a carving away of the primordial luminosity function

into one rather dissimilar to the luminosity function observed from globular clusters in elliptical galaxies - assuming that these two luminosity functions were the same primordially, which is a different, unanswered question yet again.

However, believing that the differences are small, globular clusters were used to determine extragalactic distances and hence the Hubble constant H_0. [Hanes 1979, de vaucouleurs 1979, van den Bergh, Pritchet and Grillmair 1985]. In this chapter, a review of these distance determinations is presented. In section I.1, the advantages and disadvantages of using globular clusters as extragalactic distance indicators are discussed. Section I.2 gives details regarding the distance determination to the Virgo cluster and the evaluation of H_0. I.3 raises the question about having a Universal luminosity function and in I.4, the mechanisms that could lead to different luminosity functions are discussed.

I.1 Globular Clusters as Extra galactic Distance Indicators

Many attempts were made to extend the galactic distance scale to greater and greater depths in the Universe. The establishment of the far-field extra galactic distance scale necessitates the measurements of the distances of galaxies whose peculiar velocities are small compared to the rate of cosmic expansion at that distance. This means studying galaxies at least as remote as those in the Virgo cluster, where an estimate of the mean recession velocity can be obtained by averaging over a large number of the cluster members. The procedure simply is to compare luminous Local Group objects with their apparently

fainter counterparts, say in Virgo cluster galaxies and thereby obtaining the luminosity distance directly. Most distance determinations so far however have relied on distance indicators that were not sufficiently luminous to make this single-step determination. Or the bright indicators that were used, such as ScI galaxies are not found in the Local Group and therefore their absolute calibration follows in steps from a series of distance determinations for nearby groups, using others known indicators like Cepheids, HII regions, brightest stars within galaxies etc. Good reviews on extragalactic distance determinations can be found in Hodge (1981) and Sandage & Tammann (1976).

When the extragalactic realm was discovered, Hubble's approach (Hubble 1926, Hubble 1936) was generally a three-step processes, which were:

(1) find distances to local galaxies from cepheids;

(2) use the brightest star criterion, which he calibrated in the local galaxies, to extend the scale to more distant field galaxies and the Virgo cluster;

(3) use the total magnitude of the galaxy, together with luminosity calibrated in step (2), to arrive statistically at distances for galaxies with measured redshifts.

The conclusions from Hubble's papers which stood for many years were the following:

The distance modulus of Virgo cluster was

$$\mu_o = (m - M) = 26.8$$

corresponding to a distance of $2.3 * 10^6$ parsecs and the constant of proportionality in the velocity-distance relation,

known as the Hubble constant H_0 now, was

$$H_0 = 526 \text{ Kms}^{-1} \quad \text{MPC}^{-1}$$

A major revision of distances occured in 1956, with the publication of an extensive, detailed new survey of radial velocities and magnitudes by Humason, Mayall and Sandage (1956). The result of these new distance determinations was that the value of H0 was reduced to

$$H_0 = 180 \text{ Kms}^{-1} \text{ MPC}^{-1} .$$

Sandage (1958) reviewed once again the whole Hubble distance scheme, discovered many errors made along the way, most notably in the identification of the brightest star in galaxies, as many of Hubble's identifications were HII regions or star associations and came to the conclusion that the value of H0 should be

$$H_0 = 75 \text{ Kms}^{-1} \text{ MPC}^{-1} .$$

It seems that without any effort on the part of the Universe, it had expanded by a factor of roughly seven in twenty years. Though the allowed range for H_0 is considerably narrowed and almost fixed now, it is still a hot and debatable point whether $H_0 = 50 \text{ Kms}^{-1}$ MPC as given by Sandage & Tammann (1976) or $H_0 = 100 \text{ Kms}^{-1} \text{ MPC}^{-1}$, as obtained by de vaucouleurs (1978, 1979), each of these values obtained by the authors in their own unique ways. To play it safe, physicists use a non-controversial value of $H_0 = 75 \text{ Kms}^{-1} \text{ MPC}^{-1}$ but it would be an important step to fix the value of the Hubble "constant".

Globular clusters as extragalactic distance indicators have great advantages over other indicators. The brightest globular

clusters are far more luminous than any other stellar "standard candles" except supernovae and there is no problem in the identification of these systems up to great distances. The advantages of using globular clusters as extragalactic distance indicators can be summarized as follows:

(i) They will provide a single-step determination of distances, free of the uncertainties of the methods used to date. All that is necessary to do here is to compare the luminosity function of the globular clusters in the galaxy whose distance has to be evaluated to that of the luminosity function of the globular clusters in the known nearby galaxies.

(ii) The globular cluster distance modulus will rely only upon pure Population II indicators. The globular clusters themselves and RR Lyrae stars can be used to set calibrations in the sample of globular clusters in our Galaxy. The distance scale thus found eventually will be free of the usual methods which are based on Population I indicators like cepheids, HII regions, brightest supergiants and the ScI galaxies. Also, the use of globular clusters can give an independent check on other distance determination techniques.

(iii) The globular cluster distance scale is independent of the effects of interstellar obscuration. This is because the difference between the apparent magnitude, V_{HB} , of a horizontal branch star and the integrated magnitude, V_{cl} , of the globular cluster to which it belongs is independent of any intervening absorption. Thus from two measurable quantities V_{HB} and V_{cl} and the known absolute magnitude $M_{v,HB}$ of RR Lyrae stars calibrated

locally, the absolute magnitude of globular clusters can be derived regardless of the amount of obscuration present.

In principle, globular clusters should therefore provide a one-step distance evaluation of far-away galaxies with all the advantages listed above. But many attempts that were made earlier [Racine 1968, Sandage 1968] failed when it was established that the dependence of globular properties were unclear. However, de vaucouleurs [1977, 1978b] demonstrated about how a population - corrected brightest globular cluster could still be used as a distance indicator. Also the photometric data presented by Hanes (1976b) for the globular clusters associated with twenty bright galaxies in the Virgo cluster established the population dependence of globular cluster luminosity and permitted a reappraisal of their use in distance determinations.

The fundamental assumption made in determining distances using globular clusters is that the shape of their luminosity function is same in galaxies of all types. Evidences for this uniformity have been presented by Hanes (1977d) and Harris and Racine (1979). The validity of a universal luminosity function for globular clusters was questioned by van den Bergh [1967, 1968]. The objection raised by him was that the distribution in color is not the same for all globular clusters in our Galaxy and M31 which can be interpreted as an evidence that the globular cluster sample in M31 has relatively more metal-rich clusters, suggesting that the globular clusters in M31 are different from our Galaxy. The metallicity parameter on which van den Bergh based his objections was not reddenning-free (Racine 1973) and

therefore making van den Bergh's arguments not very rigorous. Hanes (1977d) re-examined the distribution of the colors for globular clusters in our Galaxy, M31 and M87, the giant elliptical in the Virgo cluster and came to the conclusion that the colors exhibited by these globular clusters is entirely consistent with a unique distribution. The extension of the cluster color to a bright and massive galaxy like M87 implies that the globular cluster colors differ very little over a factor 10^6 in galaxy mass. The same conclusion was also obtained by Ables, Newell and O'Neil (1974).

However useful globular clusters are in determining extragalactic distances, there are various disadvantages associated with globular clusters in distance determinations. These can be listed as follows:

(i) The most obvious difficulty is that the globular clusters span a wide range of absolute magnitudes, from $M_v \sim -10$ to $M_v \sim -3$ for example in our Galaxy, and this does not permit straightforward comparisons without a clearer understanding of what can constitute a reliable benchmark - the mean magnitude or the absolute magnitude of the brightest globular cluster in a galaxy [Sandage 1968] or the full luminosity function [Hanes 1979] or some other factors.

(ii) The second difficulty lies in the identification of globular clusters in very distant galaxies. At the distance of the Virgo cluster for example, they are unresolved. A discrimination between the field stars and the globular clusters can become a problem. This difficulty can however be overuled by restricting

the study of globular clusters to a relevant color range and enhancing the constrast between globular clusters and the field stars and thus making identifications easy. Modern techniques in multi-color photometry are very useful in making these identifications.

(iii) The Virgo cluster spiral galaxies are just beyond the feasible establishment of a reliable luminosity function for their globular clusters. Therefore the distance determination to the Virgo cluster has to rely on the luminosity function of the globular clusters belonging to its brightest and massive elliptical galaxies like M87 etc. This can make the distance obtained questionable as there is no strong proof that the luminosity function of globular clusters in elliptical galaxies is the same as that for spiral galaxies' globular clusters. We feel that this assumption is the strongest disadvantage in using globular clusters as distance indicators till the exact dependence of the luminosity function of globular clusters on galactic environment is known.

(iv) At distances well beyond the Virgo cluster, globular clusters have been detected around NGC 3311 in Hydra I cluster, with the brightest globular cluster appearing just at the limit of telescope detection at a blue magnitude of 23.5. Globular clusters though seen to distances up to 100 MPC, reliable distance measurements can be obtained only if a large number of globular clusters associated with a galaxy are observed. This restricts distance determinations using globular clusters between 10 - 20 MPC.

I.2 DISTANCE TO THE VIRGO CLUSTER AND THE HUBBLE CONSTANT

Extragalactic distances are determined simply by comparing the magnitude of the peak in the observed luminosity function of extragalactic globular clusters with that of Local Group globular clusters by making the untested assumption that the luminosity function of globular clusters is invariant throughout the Universe. It would be ideal to compare the entire observed luminosity function of the globular clusters in the distant galaxy with the luminosity function of the globular clusters in the Local Group to get reliable distance measurements. But such detailed comparisons are not yet possible. Except for our Galaxy, previously studied galaxies either had too poor statistics or the available data on the globular clusters failed to reach the peak of the distributions.

Figure 1 shows the luminosity distributions of the globular clusters in our Galaxy. The data is from Webbink (1985) and the luminosity function for 148 globular clusters is shown in the figure.

A least-squares fit to the data points for $\langle M_V \rangle < -6.0$ gives a Gaussian curve characterized by (van den Bergh 1985)

$$\langle M_V \rangle = -7.11 + 0.11$$

and a standard dispersion of

$$\sigma = 1.35 \text{ magnitude}$$

Harris and Racine (1979) obtained a Gaussian curve by fitting through a sample of 93 globular clusters characterized by

$$\langle M_V \rangle = -7.34 \quad \text{and} \quad \sigma = 1.17 \text{ magnitude}$$

The dispersion σ, obtained by van den Bergh is larger than what Harris and Racine found from their sample. This might be

FIGURE 1

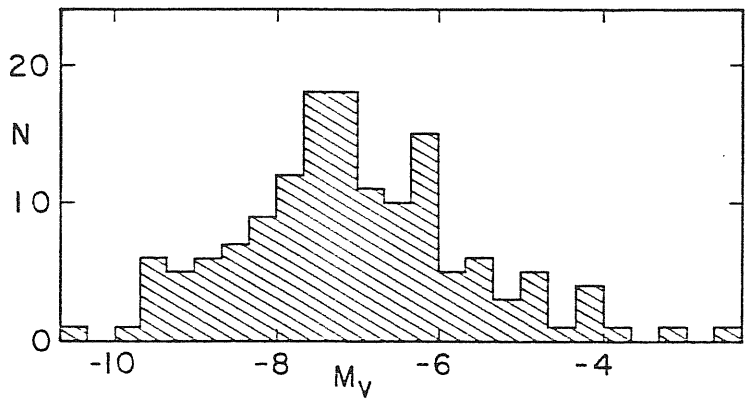

Luminosity function of Galactic globular clusters (one object at $M_V = -1.7$ is not plotted). Note that the luminosity function is assymetrical with a long tail extending to faint magnitudes.

due to incompleteness of their sample. A striking feature in figure 1 is that the luminosity distribution is non-symmetrical with a long tail extending to faint magnitudes. This deviation from a Gaussian is statistically significant. It seems probable that some of the globular clusters in the faint tail of the Galactic luminosity function are objects that have suffered major mass loss resulting from tidal interactions with the Galaxy. To minimize the bias introduced by this tail in the luminosity function, van den Bergh neglected the faintest globular clusters from his sample and found that the distribution was not significantly different from a Gaussian.

Figure 2 shows the distribution of the globular clusters in M31. The data for the globular clusters in M31 can be found in Crampton et al (1985), Racine and Shara (1979) and van den Bergh (1985). The data given by Racine and Shara is only for globular clusters in the halo of M31. Their data could be adequately fitted by a Gaussian with

$\langle M_V \rangle = -7.48$ and $\sigma = 1.13$ magnitude

Crampton et al. published studies of 505 non-stellar objects in and near M31. van den Bergh (1985) divided this data into three samples based on their color as following:

(a) clusters with $B - V < 0.70$

(b) clusters in the rage $0.70 < B - V < 1.00$

(c) Non-stellar objects with $B - V > 1.00$

Out of these three categories, the first sample (a) was mostly galactic open clusters. Sample (b) was globular clusters with a mixture of old or reddened open clusters and sample (c) a

FIGURE 2

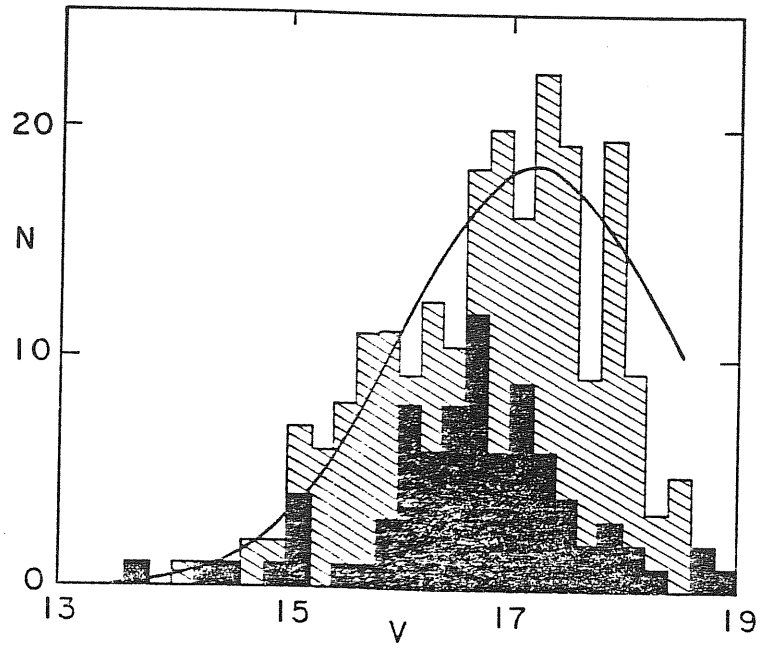

Luminosity function of clusters with $0.70 \leq B-V < 1.00$ in M31. The smooth curve is a Gaussian with V(max) = 17.2 and σ = 1.2 mag. The lower histogram shows the luminosity function of the halo of M31 derived by Racine and Shara (1979).

mixture again of reddened globular clusters and background ellipticals. Sample (b) which is the most relevant is incomplete due to observational effects and also not all clusters in this sample have (B - V) color measurements.

Considering only sample (b) van den Bergh (1985) gave a relation to obtain the number of globular clusters in M31 by assuming that the fraction of clusters with measured color is only a function of V but not of B-V as;

$$N = \frac{N_{obs}}{[1 - F(v)]}$$

where F(v) is the fraction of the globular clusters of magnitude V for which the B-V colors are available.

Figure 2 shows the plotted luminosity function for this sample. The data is well-represented by a Gaussian with

$$V_{max} = 17.2 \qquad \text{and} \qquad \sigma = 1.2 \text{ magnitude}$$

The luminosity function derived by Racine & Shara (1979) peaked at

$$V_{max} = 16.8$$

This value is 0.4 magnitudes brighter than the value obtained by van den Bergh. This difference might be due to the incompleteness in the halo cluster sample of Racine & Shara. Assuming a distance modulus of $(m - M)_V = 24.37 + 0.11$ to M31 the peak of the M31 globular cluster luminosity function is at

$$M_V = -7.1$$

Assuming a symmetry about $V_{max} = 17.2$, van den Bergh found that the total cluster population in M31 was 276.

These recent compilations of data by van den Bergh (1985) on the globular clusters in the Galaxy and M31 shows that the cluster luminosity functions in these two galaxies do not differ significantly. In both of these Local Group galaxies the globular cluster luminosity is a Gaussian curve that peaks at

$M_V = -7.1$ and has a disperson $\sigma = 1.2$ magnitudes.

Figure 3 shows the distribution function for globular clusters in LMC+SMC and dwarf-ellipticals. Adding the dwarf ellipticals and Magellanic clouds samples to the samples in M31 and our Galaxy, we find that the luminosity function of globular clusters in all these galaxies can be represented quite well by a Gaussian that peaks at

$\langle M_V \rangle = -7.28$ and has a dispersion $\sigma = 1.2$

Table I shows the mean and the standard deviations for Gaussian fits to the globular cluster luminosity functions in Local Group galaxies.

FIGURE 3

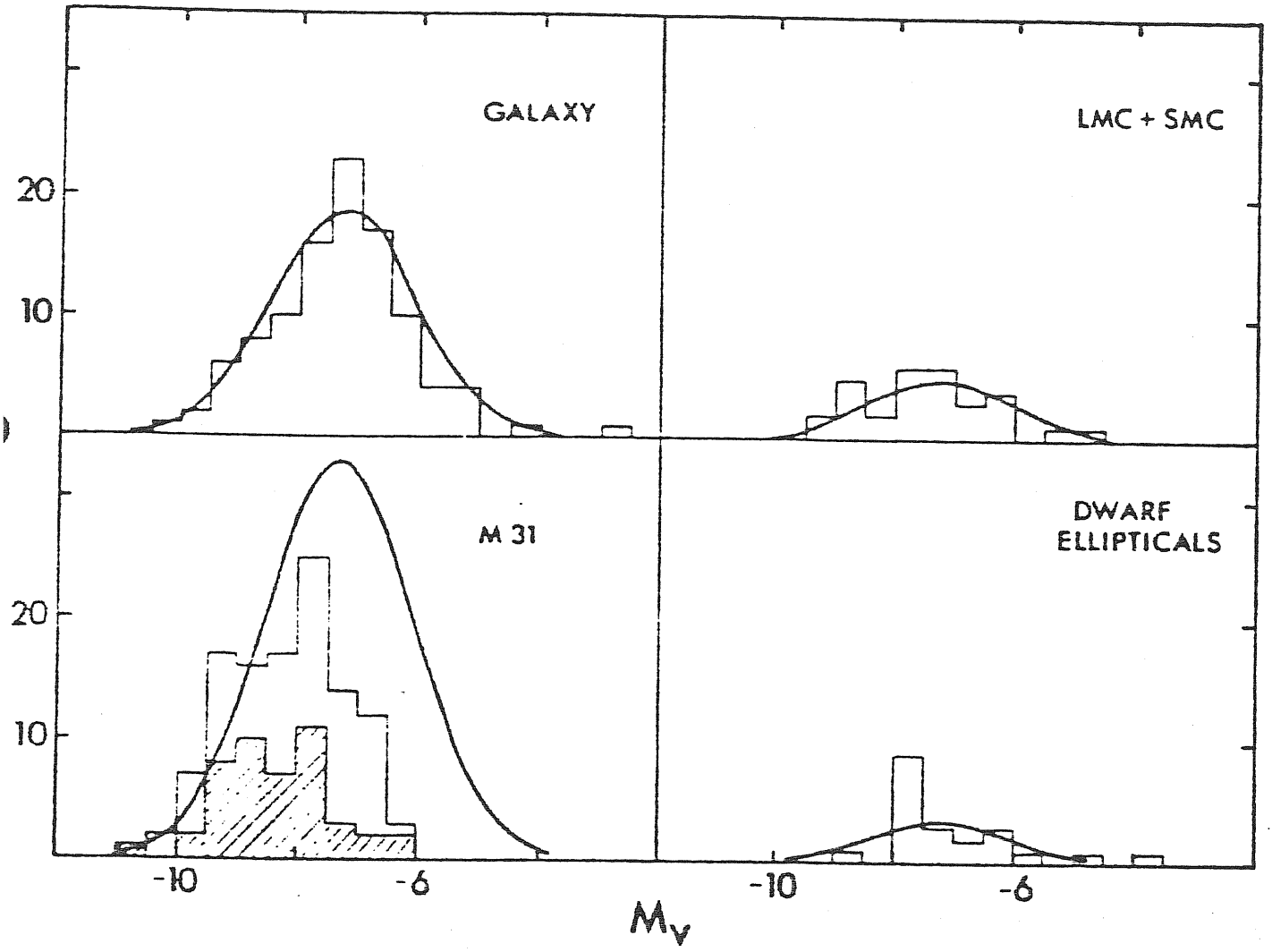

TABLE I

Mean absolute visual magnitude of globular clusters in Local Group Galaxies

GALAXY	M_V (GALAXY)*	$\overline{M}_V$ (globular cluster)@	Number of globular clusters observed	Distance modulus of the galaxy assumed
The galaxy	(- 20)	-7.34 ± 0.18	103	-
M31	- 21.1	-7.59 ± 0.25	86	24.38
M33	- 18.9	-7.87 ± 0.40	6	24.38
LMC	- 18.5	-7.43 ± 0.34	17	18.64
SMC	- 16.9	-7.03 ± 0.37	13	18.95
N 147, 185,205	- 15.5	-6.87 ± 0.34	15	24.38
Fornax	- 13.6	-7.26 ± 0.53	5	20.90

Average $\overline{M}v$ = - 7.26 + 0.12

* Absolute visual magnitudes of galaxy

@ Average absolute visual magnitude of globular clusters in galaxy

We see from this table that despite the range of a factor of 1000 in galaxy luminosities, the globular cluster luminosity distributions are consistent with being of the same form in all the galaxies. This seems to suggest that the globular cluster population in galaxies was formed with the same distribution of cluster masses, hence luminosities, in all galaxies and that this distribution has not been modified by subsequent evolutionary effects.

Hanes (1977a) used the Gaussian luminosity distribution to

determine the distance modulus of the Virgo cluster by comparing the mean magnitude distribution for globular clusters in five Virgo elliptical galaxies with the luminosity function for globular clusters in the Galaxy and M31. The five galaxies chosen by Hanes in the Virgo cluster together contained 75% of thetotal globular cluster population in the Virgo. M87, one of the elliptical galaxies chosen by Hanes, alone accounted for half of the total globular cluster population in the Virgo cluster.

Hanes used a fitting scheme to the globular cluster data of these five galaxies in the Virgo cluster. In order to obtain a statistically secure determination of the cluster mean apparent magnitude, Hanes applied this fitting scheme to the sum of all the five cluster populations. The fitting scheme of Hanes was as follows:

A normally distributed population is represented by

$$y = \frac{N}{\left[(2\pi)^{1/2}\,\sigma\right]} \exp\left[-(m-\bar{m})^2/2\sigma^2\right] \qquad (1.1)$$

The logarithmic form of this is

$$\ln y = \left[\ln \frac{N}{(2\pi)^{1/2}\,\sigma} - \frac{\bar{m}^2}{2\sigma^2}\right] + \frac{\bar{m}}{\sigma^2}\,m - \frac{m^2}{2\sigma^2} \qquad (1.2)$$

Hanes introduced a quantity S defined as

$$S = \ln y + \frac{m^2}{2\sigma^2} = \text{const} + \left(\frac{\bar{m}^2}{\sigma^2}\right) m \qquad (1.3)$$

Figure 4 shows the best fit that was determined by weighted linear least-squares for the data comprising the sum of the

FIGURE 4

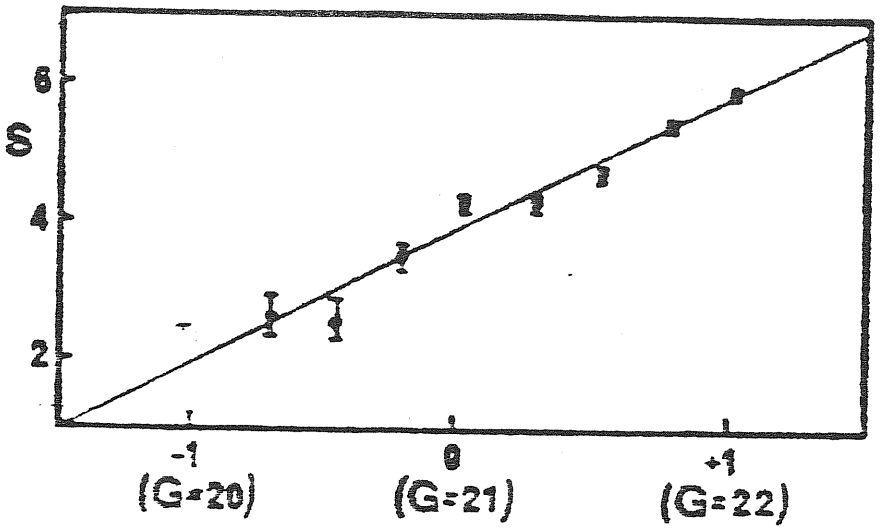

FIGURE 5

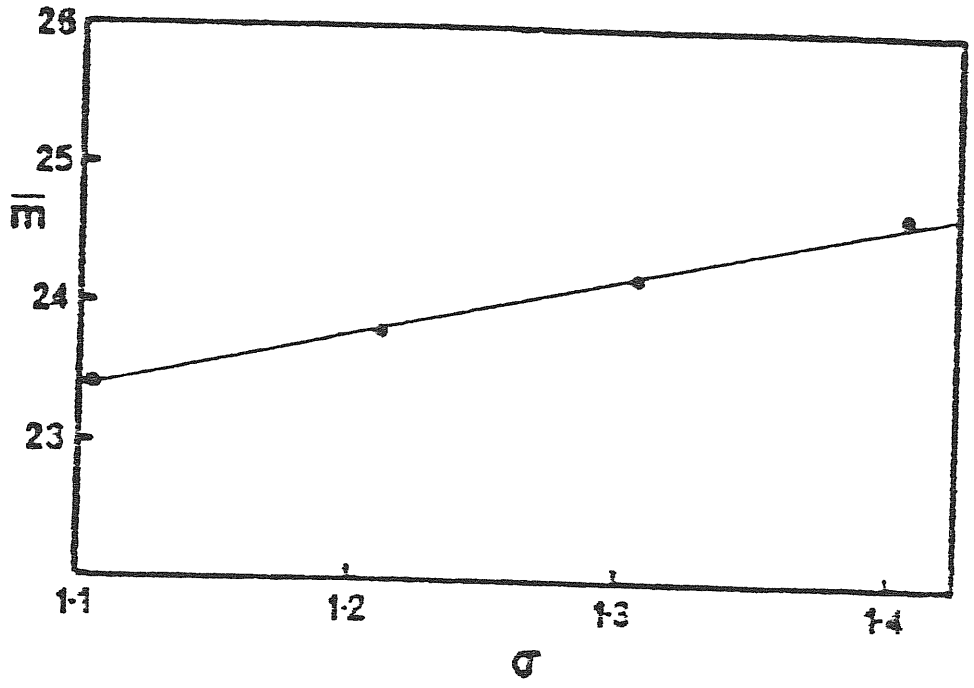

globular cluster populations for the given elliptical galaxies in the Virgo cluster. The magnitude G in the figure is obtained from the color equation

$$G = B - (0.23 \pm 0.03)(B - V)$$

Hanes used data down to G = 22.0 only to ensure for completeness in the sample. The dispersion adopted by Hanes was σ =1.10 magnitudes.

Treating m in equation (1.3) as a variable free of random error, the linear regression of S upon m gives the determination of the mean apparent magnitude $\bar{m}$ of the globular cluster in the Virgo cluster galaxies. This determination of $\bar{m}$ depends only on σ, the standard dispersion. This is shown in figure 5. The straight line in the figure shows the correlation between $\bar{m}$ and σ.

Table II gives the various estimates of the cluster mean apparent magnitude $\bar{m}$ implied by the fits.

TABLE II

Data set	$\bar{m}$
Sum of five Virgo cluster galaxies globular clusters	23.38 ± 0.05
Same data as above to G = 22.25	23.48 ± 0.05
NGC 4374	23.15 ± 0.53
NGC 4406	23.23 ± 0.08
NGC 4472	23.61 ± 0.04
NGC 4486 (M87)	23.26 ± 0.05
NGC 4526	23.05 ± 0.15
NGC 4596	23.12 ± 0.18
NGC 4647	23.35 ± 0.10

The value of $\bar{m}$, the mean apparent magnitude of Virgo cluster, as seen in the above table seems to be in close accord for all the galaxies.

Taking the calibration established for the Galactic and M31 globular clusters to be M = 6.91 $\pm$ 0.10 , σ = 1.10, Hanes obtained a distance modulus to the Virgo cluster as

$$\mu_0 = (m - M)_{app} = 30.27^{+0.49}_{-0.45}$$

With data reaching one magnitude deeper than in this study, he (Hanes 1979) derived the distance modulus to the Virgo cluster as μ_0 = 30.7 $\pm$ 0.3.

Harris and Racine (1979) using a similar method found the distance modulus to the Virgo cluster to be μ_0 = 30.9 $\pm$ 0.3 which is in accord with the value obtained by Hanes. This is not surprising since Harris and Racine actually used the same globular cluster data as Hanes.

By this method, the distance modulus to Virgo cluster can be taken as μ_0 = 30.8.

The Virgo cluster distance modulus can be obtained in another way by directly comparing the luminosity function of the globular clusters in Virgo cluster with the luminosity function of the Local Group globular clusters by making adjustments in the magnitude scale to account for the different distances and in the observed numbers to allow for different total populations.

Hanes (1979) used this method to obtain the distance to the

Virgo cluster. He used an integrated luminosity function for the globular clusters associated with the five Virgo elliptical galaxies to compare with the integrated luminosity function of the Local Group globular cluster populations. The data used by Hanes for the Virgo cluster globulars extended down to a magnitude G = 23.8 + 0.3.

Figures 5(a) - 5(d) show the luminosity functions for the globular clusters in Virgo cluster galaxies and the Local Group galaxies. The solid points in the figures refer to the globular clusters sample in the Local Group and the open boxes to the Virgo sample. The four figures show the luminosity function of the globular clusters associated with the Local Group galaxies as it would appear if removed to an apparent distance modulii of 30.0, 30.5, 31.0 and 31.5 magnitude respectively.

Hanes scaled the two curves so that they crossed at G = 22.0. This point of scaling is completely arbitrary. From the figures it could be seen that the Virgo cluster distance modulus in the range 30.5 - 31.0 magnitude is preferred over other values. Hanes found that the residuals for a distance modulus of 30.5 magnitude appeared to be scattered randomly around zero, while the residuals for the distance modulus 31.0 magnitude showed persistent systematic runs. From this, Hanes suggested that a distance modulus of 30.5 should be preferred to 31.0 magnitude. On average, he concluded that the apparent distance modulus of Virgo cluster galaxies should be taken as

$\mu_o = 30.7 \pm 0.3$ magnitude

The Virgo cluster provides an useful link to determine the

FIGURE 5(a)

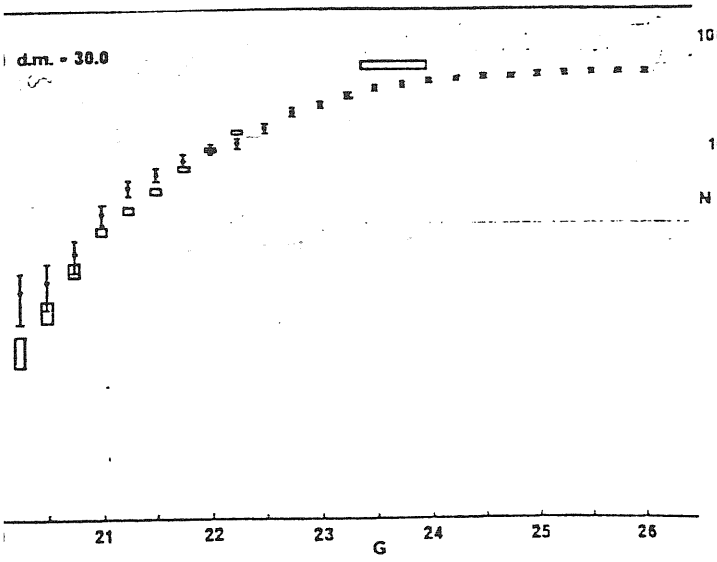

FIGURE 5(b)

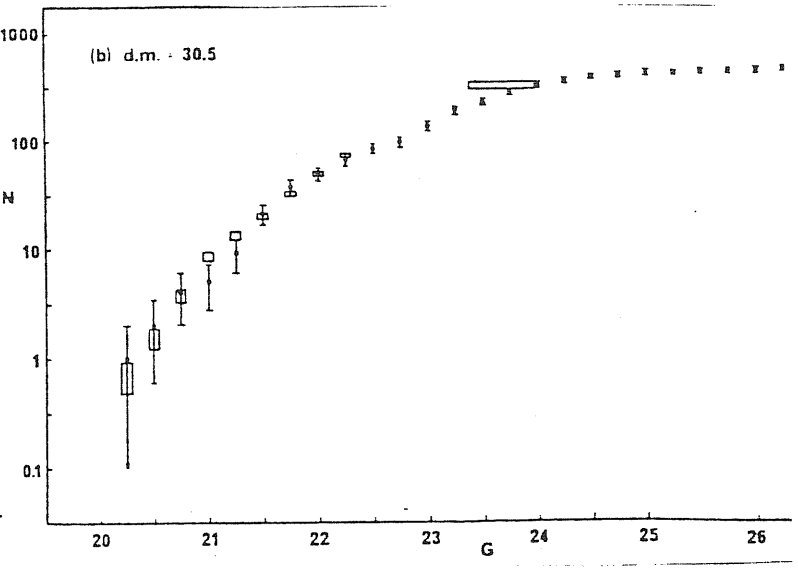

FIGURE 5(c)

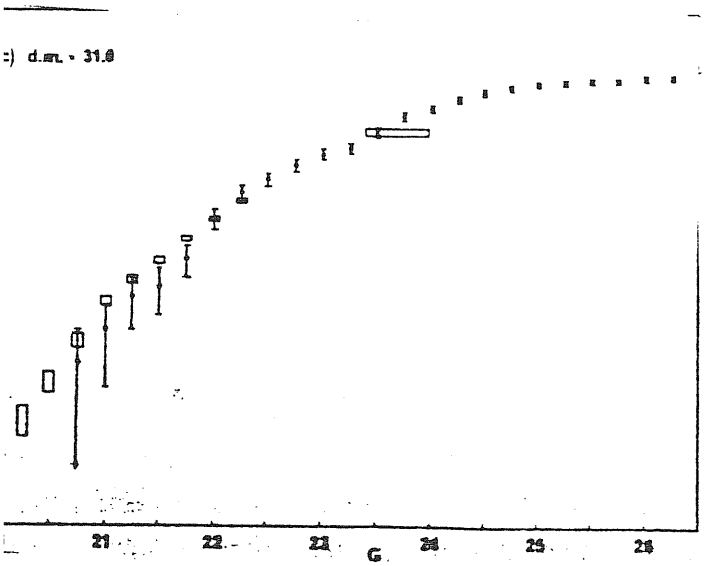

FIGURE 5(d)

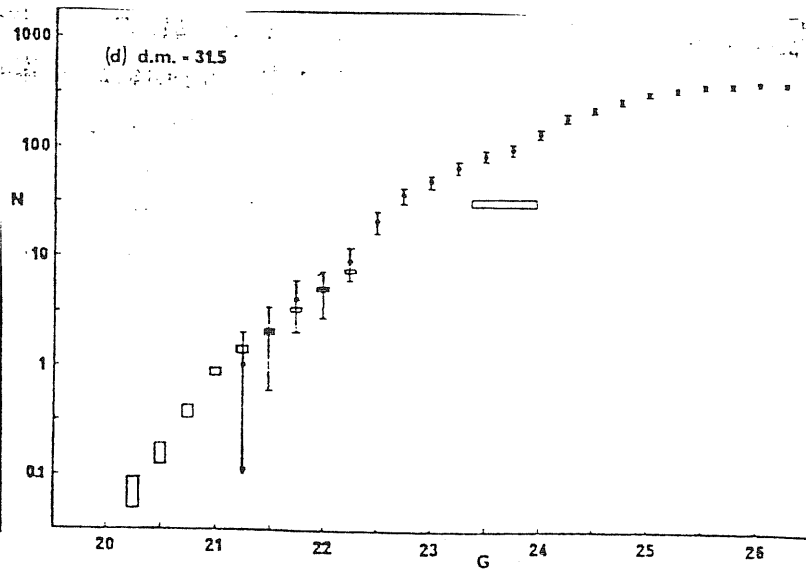

Hubble constant. Its mass lies within an order of magnitude of the great clusters and scaling outward from it may not require large corrections. Assuming that the recession velocity of the Virgo cluster of galaxies is CZ = 1100 $\pm$ 68 Kms/sec and that this velocity represents the full Hubble flow, Hanes (1979) determined the value of the Hubble constant to be

$$H_0 = 80 \pm 11 \text{ Kms}^{-1} \text{ MPC}^{-1}$$

Figure 5(d) of Hanes shows that the globular cluster counts around Virgo cluster galaxies have a shortfall of over a factor 3 around G = 23.7 magnitude compared to the population predicted by scaling of the luminosity function of globular clusters in the Local Group at a presumed distance modulus of 31.5 magnitude. This difference is beyond the explanation range of uncertainties both in counts and in photometric limits.

A possible explanation might be that the luminosity function of globular clusters in the elliptical galaxies of the Virgo cluster is different from the luminosity function of the globular clusters associated with the Local Group. The Local Group globular cluster sample is mainly from the spiral galaxies, our Galaxy and M31. Though it has often been stressed and demonstrated (Harris & Racine 1979, Hanes 1977a) that the luminosity function of globular clusters is the same in all kinds of galaxies, there is no compelling reason to believe so. It would be ideal to compare however the luminosity function of the globular clusters in Virgo cluster spiral galaxies with the Local Group globular cluster function. But observations of the globular clusters in Virgo spirals are too few to give any secure

answers.

We have two objections to the way Hanes determined the distance modulus to the Virgo cluster using this method:

(i) Hanes luminosity function for the globular clusters in the Virgo cluster galaxies is incomplete. He determined the distance modulus by comparing just the available bright tail of the luminosity function. The weakness in such a determination is that the fit can be shifted up or down by >0.5 magnitude.

(ii) The scaling used to match the two curves is completely arbitrary. Hanes used G = 22.0 as the matching point for the two functions. The two functions can be made to match at other values of G and the distance modulus can be different.

The first objection cannot be checked till the complete luminosity function of the globular clusters in Virgo cluster galaxies is known, and this means going to magnitudes fainter than G = 22.25. The second objection can however be verified which we did by using the same data of Hanes but making the two luminosity curves to match at different values of G. Figures 6(a - d) - 10 (a - d) show such fits for curves scaled vertically to cross at G = 21.25, 21.50, 21.75, 22.00 (Hanes value) and 22.25 respectively. The conclusion from these figures can be summarized as follows:

For the various matching points that we used, the curves seemed to be better matched at a distance modulus of 31.0 magnitude, which is higher than what Hanes suggested. This value is however not rigorous. The weakness in these determinations is that the fit can be shifted up or down by more than 0.5 magnitude. More secure determinations can be obtained if the

FIGURE 6

(a)

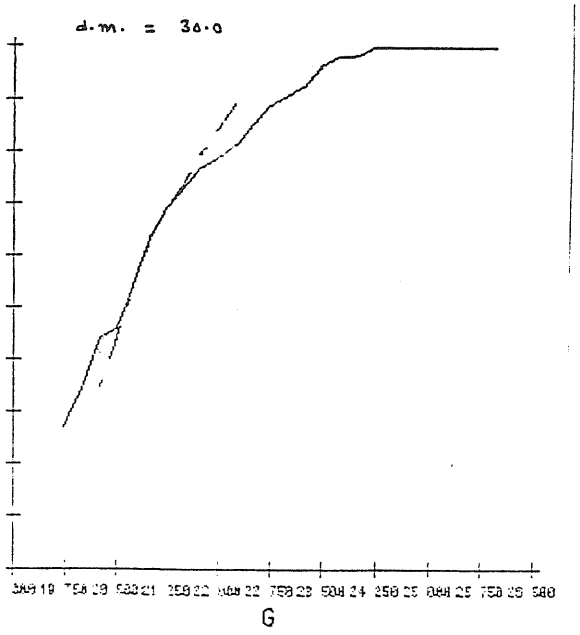

(b)

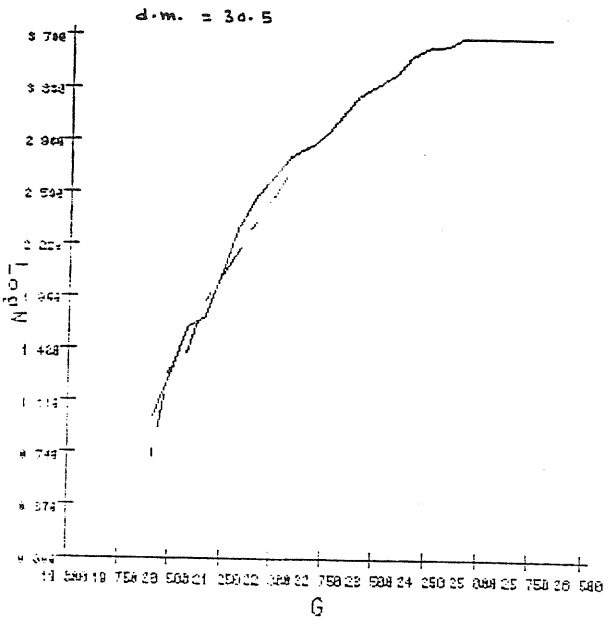

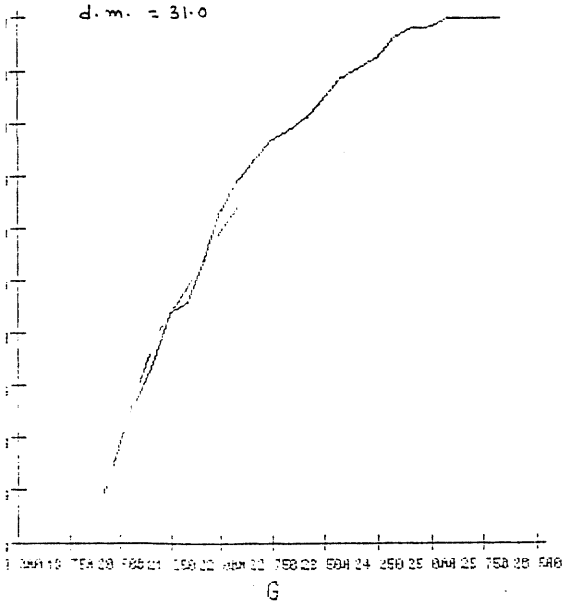

(c)

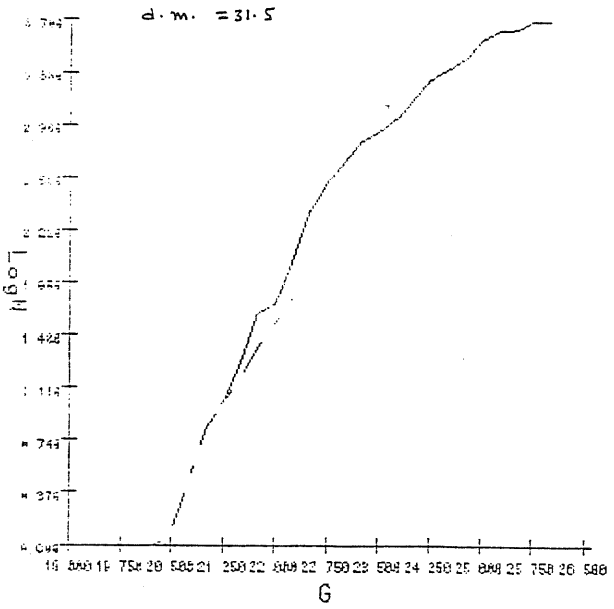

(d)

---- Virgo data

———— Local Group data

Figure 7

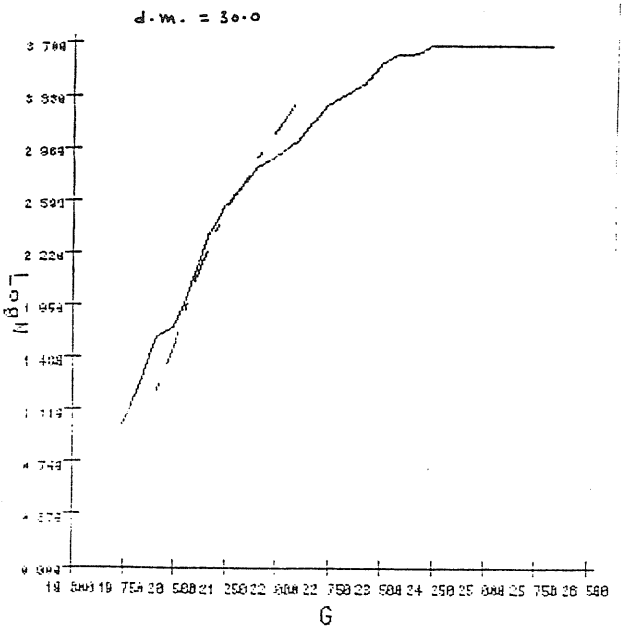

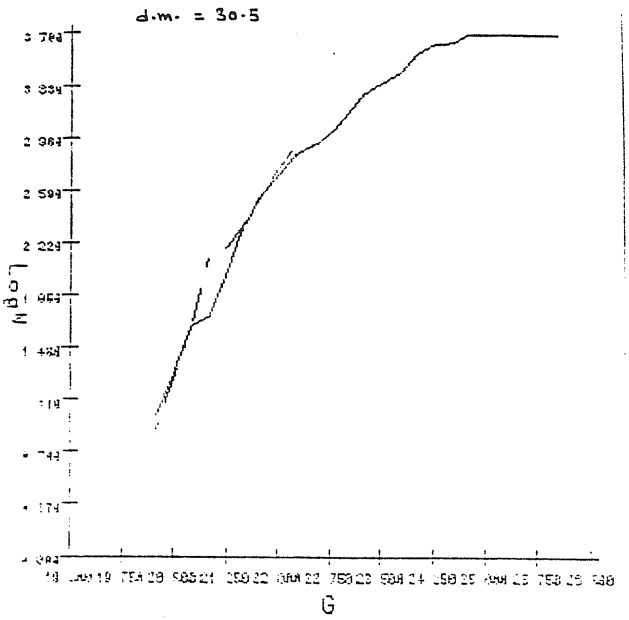

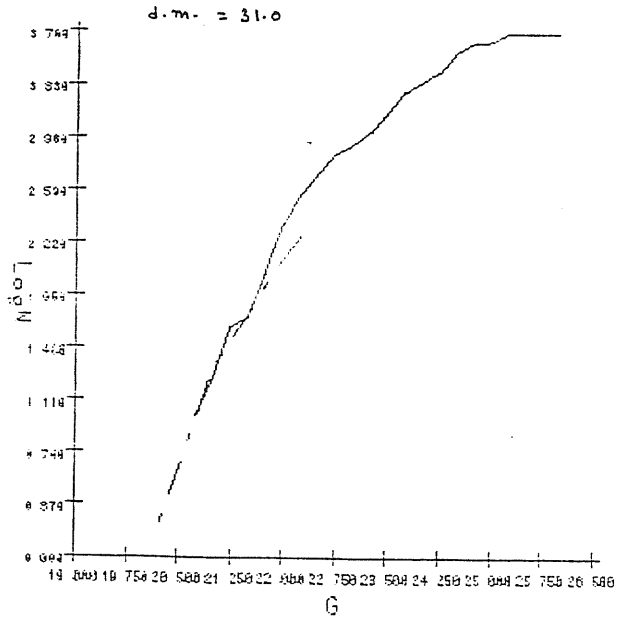

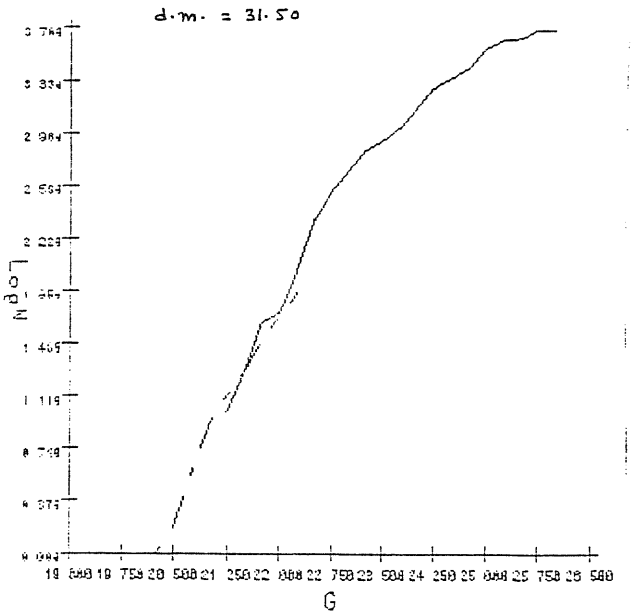

FIGURE 8

d.m. = 30.0

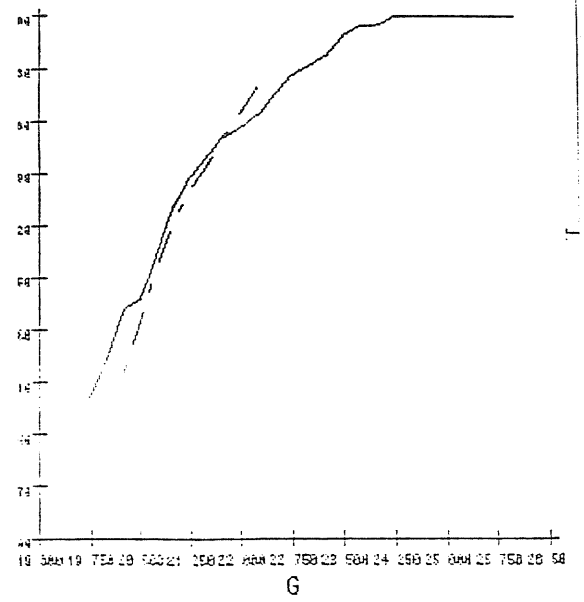

d.m. = 30.5

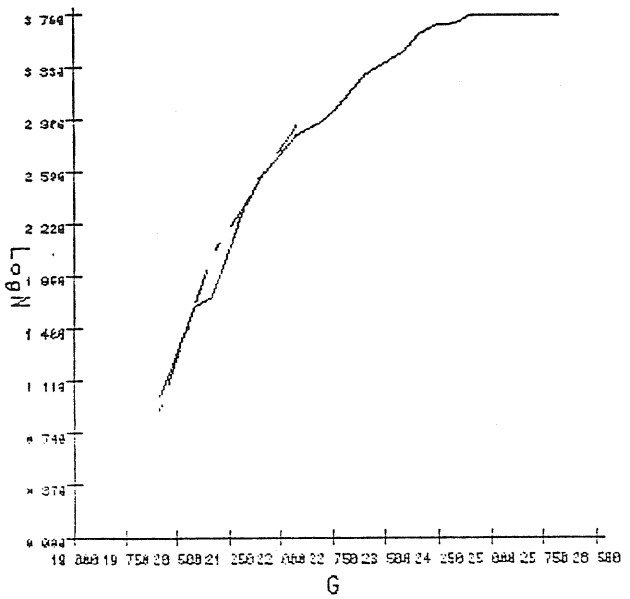

d.m. = 31.0

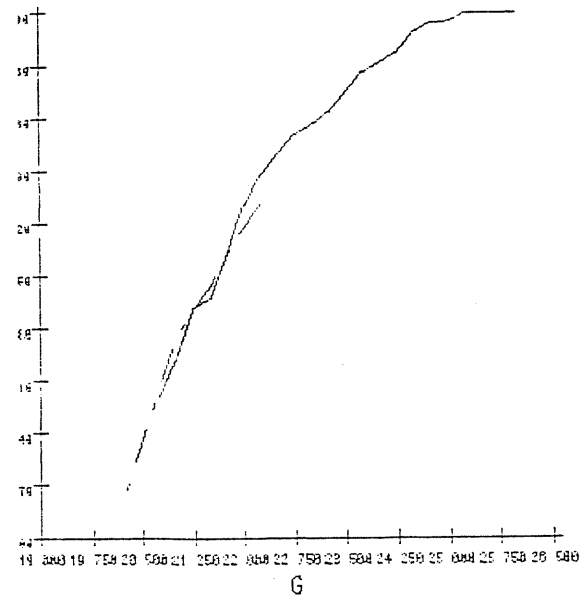

d.m. = 31.5

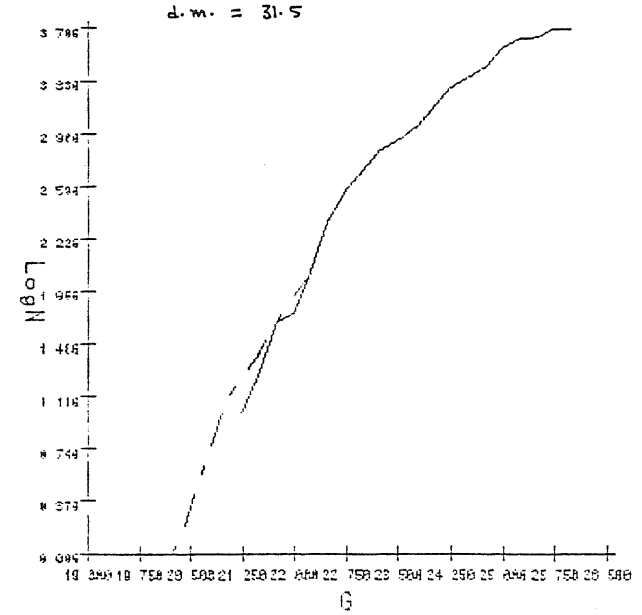

FIGURE 9

d.m. = 30.0

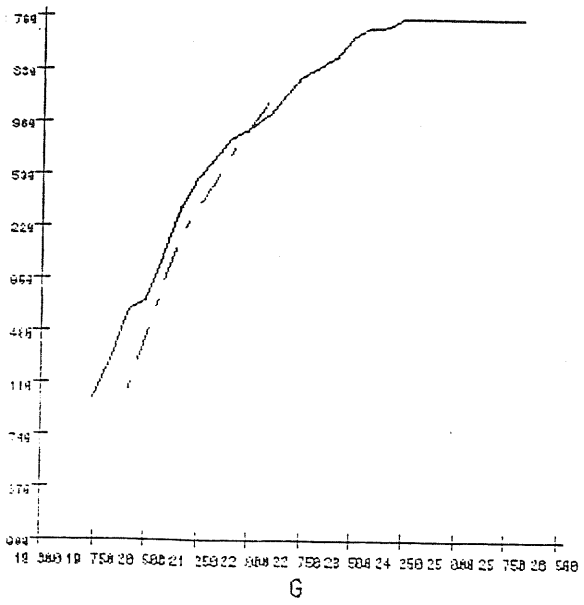

d.m. = 30.5

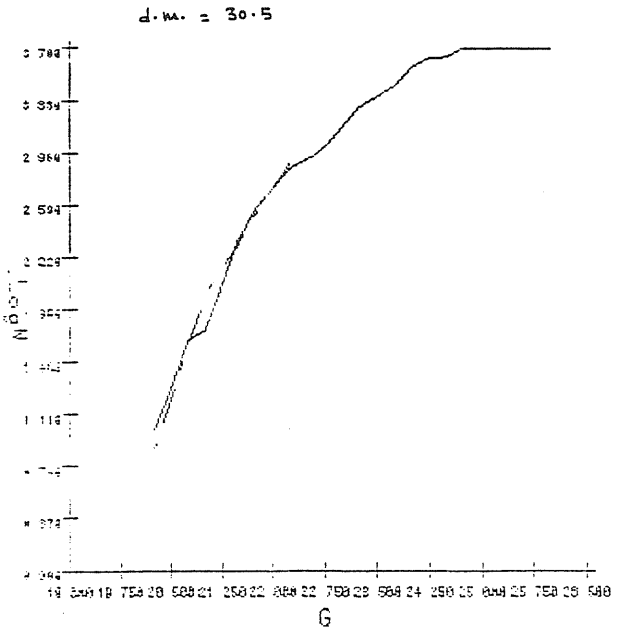

d.m. = 31.0

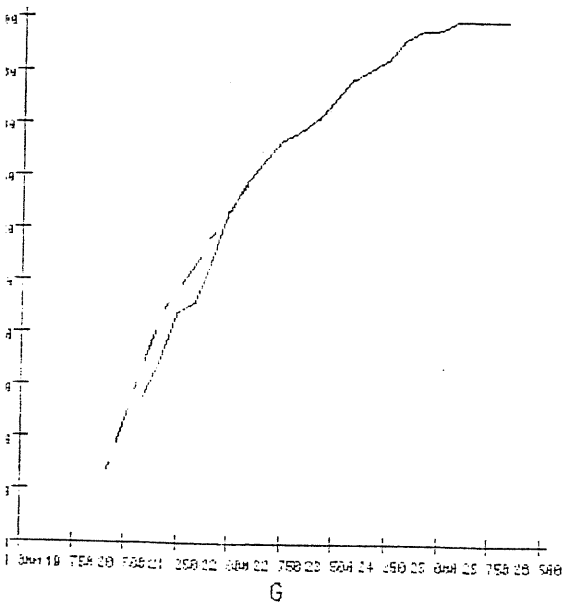

d.m. = 31.5

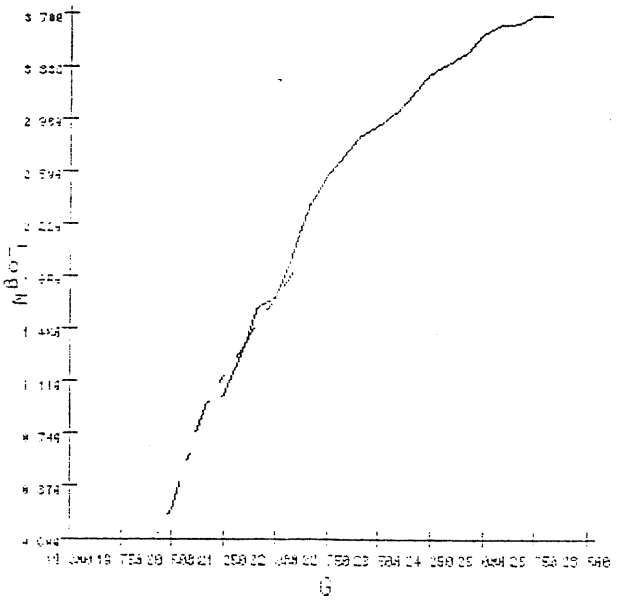

FIGURE 10

(a)

d.m. = 30.0

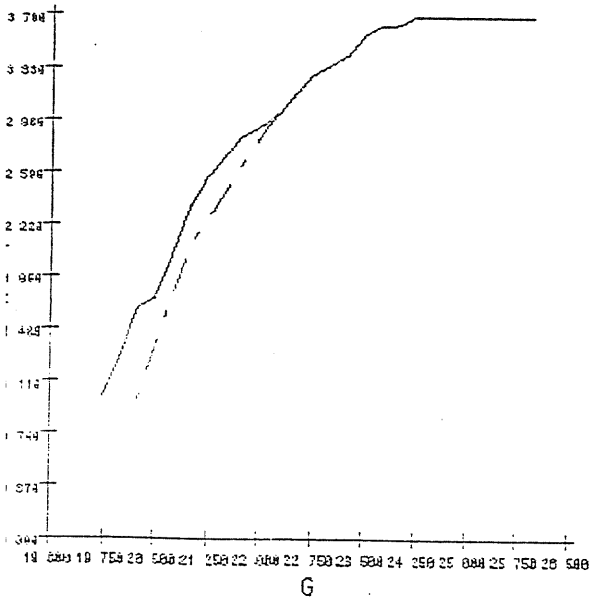

(b)

d.m. = 30.5

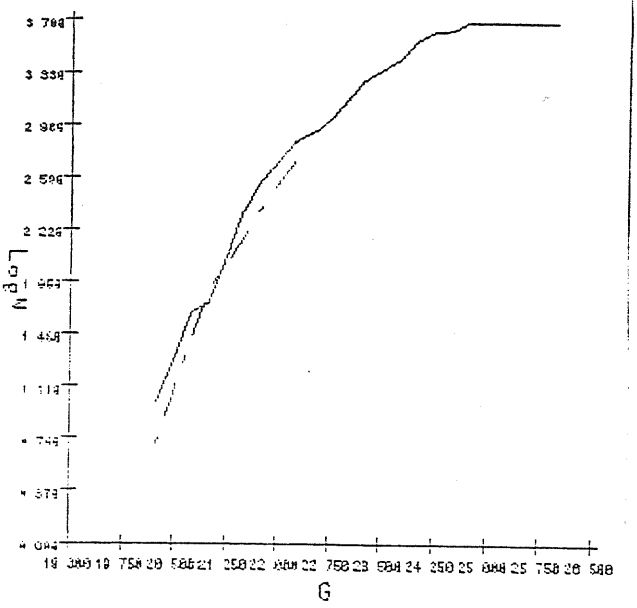

d.m. = 31.0

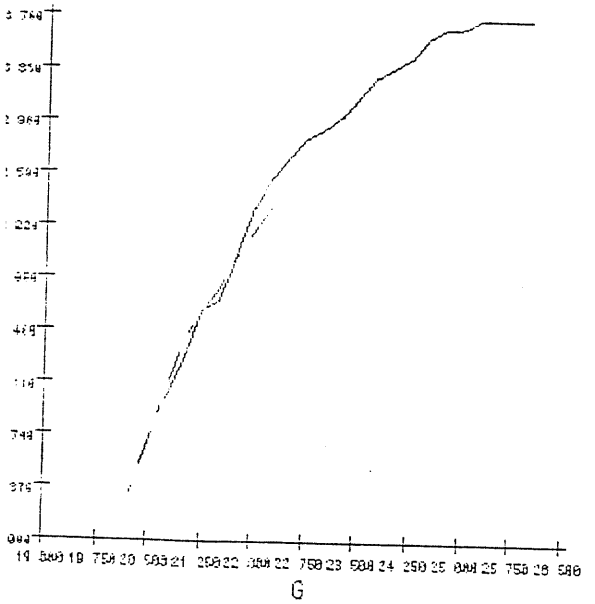

(c)

d.m. = 31.5

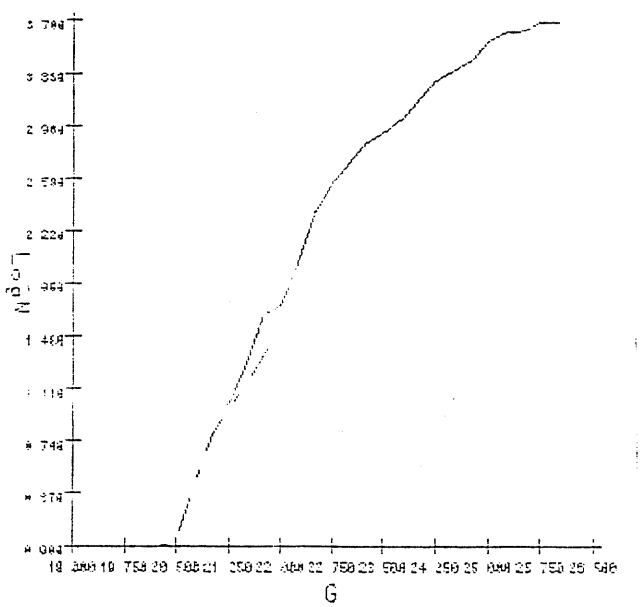

(d)

peak of the luminosity function of the globular clusters in Virgo cluster galaxies is compared to the peak of the Local Group globular clusters luminosity function. This means extending the luminosity function of the globular clusters in Virgo cluster galaxies down to much fainter magnitudes than G = 22.25 (or B=22.2) as used by Hanes (1979). It was thought that to see the peak in the luminosity function for the globular clusters in Virgo cluster galaxies, one had to wait for the space telescope. But van den Bergh, Pritchet & Grillmair (1985), taking the advantage of the good seeing on Mauna Kea and the high quantum efficiency of the CCD detector at the prime focus of the Canada-France-Hawaii telescope, managed to get the luminosity function of the globular clusters in M87 down to a magnitude of B = 25.4.

M87, the giant elliptical galaxy at the centre of the Virgo cluster is an ideal candidate for making distance determinations using globular clusters. It possesses a large number of globular clusters around $2 * 10^4$ and the luminosity function in principle, could be obtained with high precision. The most exciting result of van den Bergh, Pritchet & Grillmair was that the luminosity function they determined for the globular clusters in M87 possessed a turnover at B = 25.0 + 0.3, which was 0.4 magnitude above the limiting magnitude of their plate.

Figure 11 shows the luminosity function for the globular clusters in M87. From this figure it can be seen that the globular clusters counts in M87 rises steeply from B=21, flattens at B = 24 and turnsover at B = 25. This means that the peak of the luminosity function of the M87 globular cluster system has

FIGURE 11

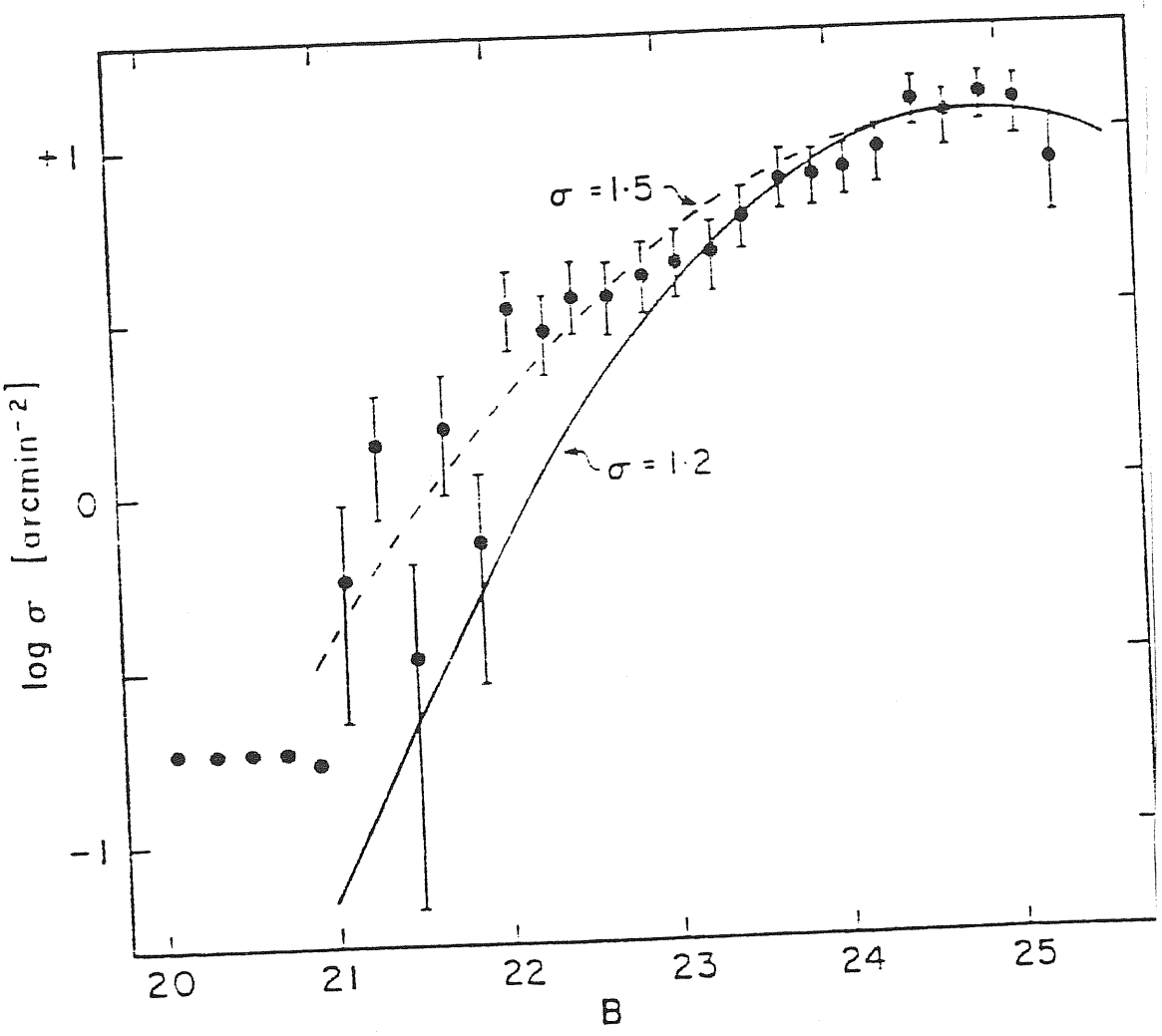

been reached. Now we have the possibility to compare the two peaks of the luminosity functions of globular clusters in M87 and Local Group galaxies and remove the uncertainties seen before in obtaining the distance modulus to the Virgo cluster. van den Bergh and others determined the distance modulus to the Virgo clusters using this latest observational data on M87 globular clusters by making the assumption that the peak in the luminosity function they observed for M87 globular clusters is at the same magnitude as the peak of the luminosity function for Local Group globular clusters.

The peak of the Local Group globular clusters Gaussian curve is at

$$\langle M_V \rangle = -7.3 \pm 0.1$$

and has a dispersion

$$\sigma = 1.20 \pm 0.05$$

Using the least-squares fit of a Gaussian with $\sigma = 1.2$ to M87 data in the range $23 < B < 25.5$, the peak obtained by van den Bergh and others, to M87 globular cluster system was

$$B(\max) = 25.0 \pm 0.3$$

Taking a value of $\langle B - V \rangle = 0.80$ for the M87 globular clusters,

$$V(\max) = 24.2 + 0.3$$

which gives

$$M_V (\max) = -7.3$$

This yields an apparent distance modulus of M87 to be

$$(m - M)_V = 31.5 \pm 0.3$$

Taking into account interstellar reddening to be

$$E_{B-V} = 0.01 \pm 0.02$$

in the direction of Virgo cluster and the total absorption to be $A_b = 0.09$ (or Av = 0.07), the true distance modulus to M87 becomes

$$(m - M)_o = 31.43 \pm 0.3$$

implying a distance of D = 19.3 $\pm$ 2.7 MPC for the Virgo cluster.

Taking the mean velocity of the Local Group towards the Virgo cluster (Tammann & Sandage 1984, van den Bergh 1981) to be

$$\Delta v = 252 \text{ Kms}^{-1}$$

and the mean velocity of the Virgo cluster relative to the Local Group (Huchra, Davis & Latham 1984) to be

$$\langle v \rangle = 1055 \pm 40 \text{ Kms}^{-1} ,$$

the cosmological Hubble flow velocity of Virgo cluster is found to be

$$\langle v \rangle + \Delta v = 1304 \pm 64 \text{ Kms}^{-1}$$

Using the relation V = HD and taking the distance D of Virgo cluster to be 19.3 $\pm$ 2.7 MPC, van den Bergh, Pritchet & Grillmair (1985) obtained the value of the Hubble constant to be

$$H_0 = 68 \pm 10 \text{ Kms}^{-1} \text{ MPC}^{-1}$$

Note that this value is much lower than the one determined by Hanes (1979) and is closer to the value of H_0 claimed by Sandage & Tammann (1976).

The errors in the results derived so far by Hanes (1979), van den Bergh, Pritchet & Grillmair (1985) does not take into account the uncertainty resulting from the assumptionthat the luminosity functions for the globular clusters in the Virgo cluster galaxies has the same form as the luminosity function for

Local Group globular clusters. Moreover, not too much weight should be placed on the Gaussian form of the luminosity function, since the bright end of the combined luminosity function for the Galaxy and M31 can also be fitted by a power law

$$\Phi(M) \propto 10^{\alpha M} \qquad (1.4)$$

where $\Phi(M)dM$ is the number of globular clusters with absolute magnitude in the range M to M + dM and the value of α = 1.2 $\pm$ 0.2. For M87 and the other giant ellipticals in the Virgo cluster, the bright end of the luminosity function can be fitted by α = 0.8 $\pm$ 0.2. A luminosity function of the form (1.4) would not allow distances to be determined using globular clusters since a slight shift in distance could be exactly compensated by a change on the total number of globular clusters. An important test of the distance to the Virgo cluster might be derived from observations of clusters surrounding spiral galaxies in the Virgo, whose luminosity function might be expected to match the luminosity function of Local Group globular clusters. Spirals, however possess cluster surface densities that are more than an order of magnitude lower than observed in M87 field. As a consequence, statistical and non-statistical fluctuations in the background counts will have a huge effect on the luminosity function. A superior spatial resolution and limiting magnitude would therefore be required and maybe the Space Telescope will help in a fresh attack of this problem.

Another way to determine extragalactic distances and the value of H_0 is by using the brightest globular cluster in the galaxy as a distance indicator. de vaucouleurs (1977) derived distances of three nearby clusters of galaxies using the brightest globular clusters in the brightest galaxies of these clusters. The clusters were the Virgo, Fornax and Hydra. Using this assumption that there exists an Universal Gaussian luminosity function for globular clusters with mean absolute magnitude $\langle M_v \rangle = -7.3$ and standard deviation $\sigma = 1.1$ and also assuming that the total number of globular clusters in a galaxy N_t is related to the absolute blue magnitude of the galaxy $M_B^o(G)$ by

$$\log N_t = -0.3 \left[M_B^o(G) + 11.0 \right] \qquad (1.5)$$

de vaucouleurs calculated the distance modulii of the three clusters. His results are presented in Table III.

TABLE III

CLUSTER	VELOCITY V_o (Kms^{-1})	DISTANCE D(MPC)	HUBBLE 'CONSTANT' Kms^{-1} MPC^{-1}
Vir I (E)	1,000 (1+0.07)	12.3 (1+0.07)	81 (1+0.10)
Vir I (E+5)	1,100 (1+0.06)	12.3 (1+0.07)	89 (1+0.10)
For I (E)	1,450 (1+0.09)	17.0 (1+0.10)	85 (1+0.12)
For I (E+5)	1,450 (1+0.06)	17.0 (1+0.10)	85 (1+0.12)
Hya I (E)	3,650 (1+0.06)	40.5 (1+0.10)	91 (1+0.12)
Hya I (E+5)	3,500 (1+0.03)	40.5 (1+0.10)	87 (1+0.10)

The distances derived to the three clusters using the brightest globular clusters all gave a value of the Hubble constant to be around

$$H_0 = 86 + 9 \text{ Kms}^{-1} \text{ MPC}^{-1}$$

Sandage & Tammann, on the other hand, using a similar method derived $M_o = 31.45 \pm 0.5$ for the Virgo cluster galaxies. The discrepancy in the results merely reflects the unrealiability in using the brightest globular cluster in a galaxy as a distance indicator.

We also know that in Magellanic clouds and other late type galaxies, globular clusters are found which are much bluer and younger than those found in our Galaxy and in the giant ellipticals. Thus the concept of an universal cluster luminosity function has to be used with care. In the next section the validity of an universal luminosity function is considered. The results discussed in this section for the distance modulus of the Virgo cluster and the value of the Hubble constant determined using these distances are summarized in table IV.

TABLE IV

Source	distance mod.	Hubble constant H_0
Hanes (1979)	30.7 + 0.3 mag.	80+11 Kms^{-1} MPC^{-1}
de vaucouleurs (1979)	30.4 + 0.3 mag.	86+9 Kms^{-1} MPC^{-1}
Sandage & Tammann (1979)	31.45+0.5 mag.	50.3+4.2 Kms^{-1} MPC^{-1}
van den Bergh, Pritchet & Grillmair (1985)	31.43+0.3	68 + 10 Kms^{-1} MPC^{-1}

From the Table IV, we see that using globular clusters as

distance indicators the value of H_0 can be anywhere between 50 - 100 Kms^{-1} MPC^{-1} .

I.3 An Universal luminosity function ?

In the last section we have seen that using globular clusters as distance indicators depends strongly on the assumption that the luminosity function of the globular clusters in all types of galaxies has the same Gaussian form that peaks at the same value $\langle M_V \rangle = -7.3$ and has the same standard dispersion $\sigma = 1.2$. The photometric and spectroscopic data on the globular clusters seems to demonstrate that this assumption is not far from wrong (Hanes 1977a, Harris & Racine 1979). Hanes (1977a) moreover argues that since the distance modulus obtained to Virgo cluster is not significantly different from the values obtained by other independent techniques, (de vaucouleurs 1979) the assumption of an universal luminosity function is quite valid as it is improbable that the intercomparison of two different luminosity functions can give rise to a distance modulus that is within the usual realm of discourse. The validity of an universal luminosity function for globular clusters in galaxies of all kinds cannot be thoroughly checked however, as the data on globular clusters in far away galaxies is still too small to be reliable. Till the van den Bergh, Pritchet & Grillmair's results were presented, the shape of the luminosity function for globular clusters in M87 was not known completely either.

Consider figure II again. It shows the luminosity function of M87 globular cluster system. The curves show that the luminosity function is better fitted by a Gaussian having a

dispersion σ = 1.5 rather than σ = 1.2, which is the value that fits the luminosity function for the Local Group globular clusters quite well. van den Bergh et al. rejected the σ = 1.2 magnitude fit at 99% confidence level.

The deviations between the two luminosity functions are in the sense that M87 contains a longer fraction of luminous globular clusters than the Local Group galaxies. van den Bergh et al. tested statistically the M87 and Local Group cluster samples using the Kolmogoroff-Smirnoff test and concluded that there is only a 5% probability that the two samples, M87 and Local Group, were drawn from the same parent population. We can summarize these results of van den Bergh et al. as:

(i) The luminosity function of the M87 globular cluster system differs from that of the Local Group globulars.

(ii) van den Bergh, Pritchet & Grillmair adopted too faint a value for B(max) $\sim$ 2.50 $\pm$ 0.3 for M87 cluster system. That is, they have overestimated the distance modulus.

(iii) The adopted distance to M31 in the Local Group is slightly in error. Increasing M31's distance modulus by 0.2 magnitude would increase the probability that M87 and Local Group clusters have been drawn from the same parent population to 11%.

The first of these two hypothesis seems to be the most plausible. A definite decision must wait however till the study of M87 globular clusters is extended to magnitude levels fainter than B = 25.4.

The discrepancy between the two luminosity functions is that there are more bright globular clusters in M87 than in the Local

Group galaxies. The Local Group globular cluster sample is drawn mainly from the Galaxy and M31, both spirals and M87 is a giant elliptical. The disk components in spiral galaxies may play a major role in destroying bright, massive globular clusters [Fall and Rees 1977, Tremaine, Ostriker and Spitzer 1976, Caputo and Castellani, 1984], leading to a luminosity function that is different from the luminosity function for elliptical globular cluster systems.

We can see from figure 11 that the number of bright globular clusters missing from the Local Group galaxies to make both the curves to be similar is not much (< 100). There must be some mechanism to destroy these globular clusters in spiral galaxies. In the next section, a few of the mechanisms will be considered.

I.4 Destruction of Globular Clusters

Recent observations of van den Bergh, Pritchet and Grillmair (1985) have shown that the luminosity function for M87 globular clusters is different from the function for Local Group globular clusters in the sense that M87 has more bright, massive globular clusters than the Local Group galaxies. The use of globular clusters as distance indicators relies heavily on the assumption that the luminosity function for these systems is invariant throughout the Universe. There are a number of effects that cause the luminosity function to depend on galactic environments.

By astronomical standards, globular clusters are remarkably similar to one another. In particular, most of them have masses and radii that fall within very narrow limits. Fall and Rees (1977) considered tidal and evaporative disruption of an initial

spectrum of galactic substructure that was assumed to span a wide range of masses and sizes and suggested that what we see today as globular clusters are the surrived substructures. Figure 12 shows the survival triangle for the galactic substructure. The sides of the triangle are set by three stellar-dynamical processes that might limit the present gross structural properties of substructure. A power-law spectrum of initial substructure is indicated by stippling but any spectrum that passes through the observed globular clusters and avoids the large mass side of the triangle will do. In the figure 12, we see that all the globular clusters represented by open circles lie together in a rather narrow space.

In our Galaxy, globular clusters have a mass interval from 10^4 M⊙ to 2 * 10^6 M⊙ [Harris and Racine 1979]. The reasons why there are no globular clusters found outside this range could be:
(1) Globular clusters had an initial mass function such that the expected number of more massive (Mass > 2 * 10^6 $M_\odot$) and less massive (Mass < 10^4 $M_\odot$) is very small, suggesting that such globular clusters never existed.
(2) Maybe the low mass globular clusters (< 10^4 $M_\odot$) are not seen due to their low luminosity.
(3) Globular clusters outside the mass range 10^4 - 2 * 10^6 $M_\odot$ might have existed but have had sufficient time to disintegrate during the evolution of the Galaxy.

There are three main stellar-dynamical mechanisms that can limit the positions of galactic substructures in the mass (m) vs. radius (r) plane (figure 12). These are:

FIGURE 12

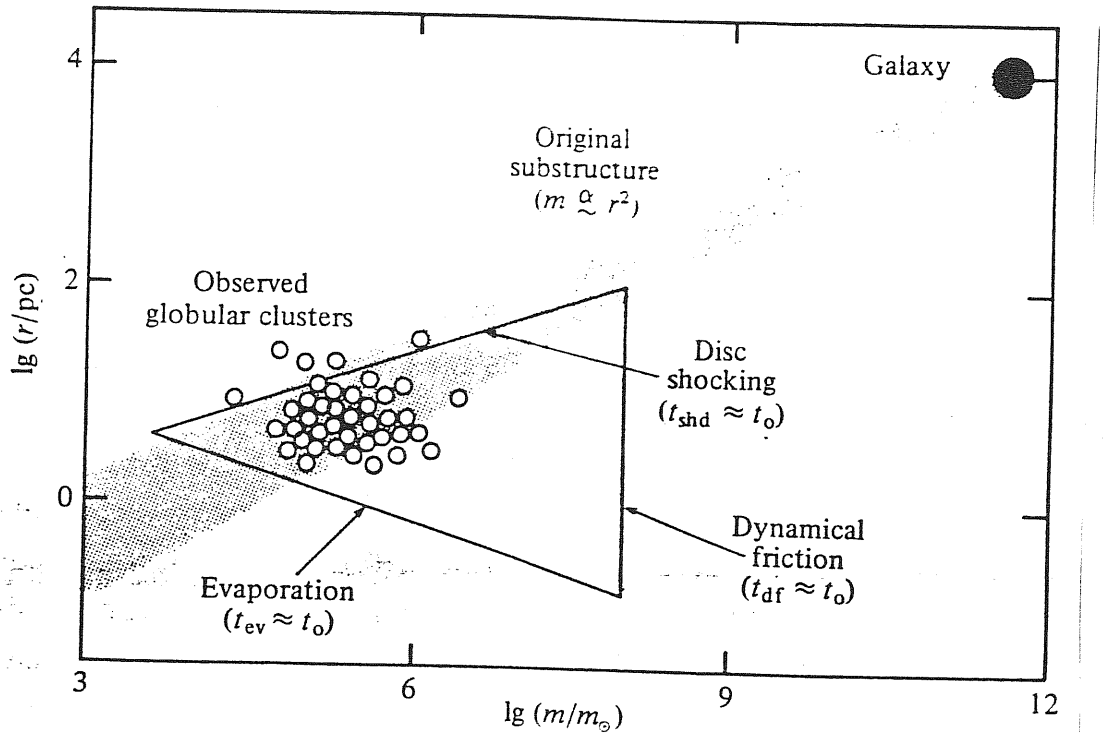
Galaxy
Original substructure
($m \propto r^2$)
Observed globular clusters
Disc shocking
($t_{shd} \approx t_o$)
Dynamical friction
($t_{df} \approx t_o$)
Evaporation
($t_{ev} \approx t_o$)
lg (r/pc)
lg ($m/m_\odot$)
4
2
0
3
6
9
12

(i) Evaporation of stars from the globular clusters (Spitzer 1975).

(ii) Shocking of clusters during passages through the galactic disk (Ostriker, Spitzer and Chevalier 1972).

(iii) Dragging of clusters into the galactic centre by dynamical friction (Tremaine, Ostriker and Spitzer 1975; Keenan 1979).

The time scales for these processes are given approximately by the following formulae:

Stellar evaporation (mean stellar mass = 0.3 M⊙)

$$t_{ev} \approx 2 \times 10^{7} \left(m/m_{\odot} \right)^{1/2} \left(r/pc \right)^{3/2} \text{ years}$$

Disk shocking

$$t_{dsh} \approx 1 \times 10^{8} \left(m/m_{\odot} \right) \left(r/pc \right)^{-3} \text{ year}$$

Dynamical friction (distances ~ 7 KPC)

$$t_{df} \approx 1 \times 10^{18} \left(m/m_{\odot} \right)^{-1} \text{ years}$$

When these time scales are set equal to the Hubble time scale, $t \approx 10^{10}$ yr, they define a 'survival triangle' in the $\ln M - \ln r$ plane, as seen in figure 12. Substructures outside the triangle could have been destroyed by any one of these mechanisms. The triangle in the figure is shrinking and will continue to shrink until no clusters remain. From the figure it

is seen that the triangle is not completely filled by the observed globular clusters, especially at the large mass side. Dynamical friction must have destroyed the massive clusters and also it might have destroyed a few smaller ones near the galactic centre. Fall & Rees (1977) feel that dynamical friction might not have been the important mechanism in setting the maximum masses of the surviving substructure, suggesting that the original mass-radius relation of substructure somehow avoided the high-mass side of the triangle.

The difference between the luminosity functions of M87 and Local Group globular clusters is in the sense that bright, massive clusters are missing in the Local Group galaxies, while they exist in M87. The main galaxies in the Local Group are the Galaxy and M31, both Sb type. Dynamical friction is a process that preferentially destroys larger systems. The disks in the spiral galaxies might have played an important role in contributing to total dynamical friction, while dynamical friction is not so enhanced in elliptical galaxies.

Grillmair et al. (1986) recently published data on the observations of globular clusters in the core region of M87, using CCD techniques. They examined the distribution of globular clusters in M87 down to B = 24.4 as a function of both magnitude and projected radius and looked for any radial changes in the luminosity function that might be indicative of mass-dependent evolutionary processes such as dynamical friction and tidal disruption. If these processes exist, they produce a distribution in globular clusters that is somewhat depleted near

the core.

Their results are:

(i) Up to a magnitude of B = 24.4, there seems to be no significant radial trend in the globular cluster luminosity function in the region

$20 < r < 160$ arc.sec. of M87

(ii) The data suggests that the radial surface-density profile for the globular clusters is flatter than the galaxy luminosity profile.

(iii) Simple model calculations carried out by Grillmair et al. have indicated that globular clusters near the core are not there because of dynamical friction, suggesting that dynamical friction is not very effective in M87.

In spiral galaxies dynamical friction might be more important and can be the mechanism to destroy bright, massive globular clusters. Caputo and Castellani (1984) found that in our Galaxy, there are no massive globular clusters ($> 10^6 M_\odot$) present at radii greater than 13 KPC, suggesting that all these massive globular clusters were dragged to smaller radii by dynamical friction.

Determination of distances to faraway galaxies using globular clusters is based on the assumption that the luminosity function of globular clusters has the same form in galaxies of all types. There are effects like dynamical friction which destroys massive, bright globular clusters thus leading to a luminosity function that could be different in different types of galaxies. Recent observations on the globular cluster systems in M87 has indeed shown that the luminosity function for M87

globular clusters is different in shape from the function for Local Group globular clusters in the sense that there are more bright globular clusters present in M87. The disks of spiral galaxies might be responsible for enhancing mechanisms that act preferentially on massive systems. Dynamical friction is one such mechanism and might be responsible for the absence of massive globular clusters in spiral galaxies. In the next chapter, the theory of dynamical friction will be discussed in detail.

CHAPTER TWO

Dynamical Friction

Dynamical friction possibly plays an important role in the evolution of galaxies and of their satellite systems. Tremaine, Ostriker & Spitzer (1975) and Tremaine (1976a) have considered the possible formation of nucleii of galaxies by the spiralling of globular clusters from spherical stellar bulges, due to dynamical friction. Ostriker and Tremaine (1975) and White (1976a) investigated the possible luminosity and dynamical evolution of large galaxies due to the spiralling in of smaller companion systems and their eventual disolution in the larger systems. Keenan (1979) discussed the possibility of globular clusters around masses $\sim 10^6$ $M_\odot$ being removed from the disk of our Galaxy by the action of dynamical friction.

In the last chapter, it was suggested that dynamical friction might be an effective mechanism in removing bright, massive globular clusters in spiral galaxies, causing the luminosity function of the globular clusters in these galaxies to be different from the one observed for the globular clusters in elliptical galaxies. A detailed, comparative study of the effect of dynamical friction on globular clusters in spirals and ellipticals might be the answer to really understand the difference in luminosity functions observed for spirals and elliptical globular clusters. Since this difference is not very large, we expect the action of dynamical friction to be small but sufficient enough in removing the massive globular clusters in spirals. Analytical treatment of dynamical friction between spiral galaxies and satellites have been carried out by Goldreich

& Tremaine (1979), Palmer & Papaloizon (1982) and Palmer (1983). But these works have generally been restricted to sufficiently weak interactions so that the linear perturbation theory could be used. Moreover, it was shown numerically [Quinn & Goodman (1986), Byrd, Sarinen & Valtonen (1986)] that when the interactions were strong, linear theory could not be used even for rough estimates as it predicted wrong signs for certain effects. For example, Byrd et al. got results opposite to Palmer & Papaloizou's analytical treatment of cold disks.

In this chapter, the general principles of dynamical friction are reviewed. Section II.1 gives the Chandrasekhar's formula for dynamical friction. Section II.2 discusses the applications of this formula and in II.3, the validity of Chandrasekhar's formula is discussed. In section II.4, dynamical friction in spherical systems is reviewed. In section II.5, the numerical work on dynamical friction is reviewed.

II.1 The theory of dynamical friction

A massive object passing through a collisionless medium induces a wake of accreted matter. The gravitational field of this wake produces an effective deceleration on the object known as dynamical friction.

Chandrasekhar (1943) derived the force of dynamical friction for a point mass moving through a homogeneous background of particles with an isotropic Maxwellian velocity distribution, by simply adding the exchange of momentum for the various encounters. He showed that the dynamical friction or the drag

force on a test object of mass m_s moving at speed v_s through an infinite homogeneous medium of stars with a Gaussian velocity distribution with one-dimensional dispersion σ is

$$\frac{dv_s}{dt} = - \frac{4\pi G^2 m_s \rho(<v_s)}{v_s^2} \left[\phi(x) - x\phi'(x)\right] \ln\Lambda \qquad (2.1)$$

where $\rho(<v_s)$ is the total density of the background stars with speeds less than v_s,

$$x = \frac{1}{\sqrt{2}} \frac{v_s}{\sigma}$$

ϕ = error function

and $\Lambda = p_{max}/p_{min}$ where p_{max} and p_{min} are the maximum and minimum impact parameters respectively.

Dynamical friction is a second order effect in m_s, since the force on m_s is $\propto m_s^2$. Chandrasekhar's formula (eqn. 2.1) neglects the self-gravity of the background medium i.e., it considers only the interaction of the stars with the test object and not with one another.

The maximum impact parameter, p_{max}, is usually taken to be the scale size of the background field of stars and the minimum impact parameter to be $p_{min} = \max\left(r_s, \frac{G m_s}{v_s^2}\right)$ where r_s is the size of the test object.

The exact value of $\Lambda = \frac{p_{max}}{p_{min}}$ is however not well-defined. Chandrasekhar (1943) had showed that if all the background particles could be treated as point masses, then p_{min} should be taken as $\frac{G m_s}{\langle v^2 \rangle}$, where $\langle v^2 \rangle$ is the rms velocity of the background. White (1976 b) derived the minimum impact parameter for extended objects that could be applied to globular clusters.

Consider an encounter between a cluster and a field star with impact parameter p and relative velocity at infinity v. The deflecting force on the star perpendicular to its initial direction of motion to first order is given by

$$F_{\perp} = \frac{G m M(r) p}{r^3} \qquad (2.2)$$

where G is the Gravitational constant

r is the distance of the star from the cluster centre

m is the mass of the star

M(r) is the cluster mass contained within radius r.

Integrating the force (2.2) along a straight undeflected path, the total change in velocity of the star perpendicular to its initial direction of motion is obtained as

$$\Delta V_{\perp} = \frac{2GP}{V} \int_{P}^{\infty} \frac{M(r)\, dr}{r^2 (r^2 - p^2)^{1/2}} \qquad (2.3)$$

As a result of the encounter the star is deflected through an angle,

$$\cos \psi = \frac{GP}{v^2} \int_{P}^{\infty} \frac{M(r)\, dr}{r^2 (r^2 - p^2)^{1/2}} \qquad (2.4)$$

where ψ is the measure of deflection (Chandrasekhar 1943 a).

Following Chandrasekhar's treatment exactly, we obtain

$$\log_e \left(\frac{p_{max}}{p_{min}} \right) = \frac{1}{M_t^2} \int_{0}^{p_{max}} p^3 \left[\int_{P}^{\infty} \frac{M(r)\, dr}{r^2 (r^2 - p^2)^{1/2}} \right]^2 dp \qquad (2.5)$$

Here M_t is the total mass of the globular cluster.

If M_t is assumed to be the mass contained within some tidal

radius r_t, then the integral in eqn.(2.5) can be evaluated over the range $r_t \leq P \leq p_{max}$ and equation (2·5) reduces to

$$\log_e\left(\frac{r_t}{p_{min}}\right) = \frac{1}{M_t^2}\int_0^{r_t} P^3 \left[\int_P^{\infty} \frac{M(r)\,dr}{r^2(r^2-P^2)^{1/2}}\right]^2 dP \qquad (2.6)$$

This treatment requires that cos ψ should be small for all encounters at typical field star velocities and this means, $G\,M(P)/P\langle v^2\rangle$ must be small for all P. Therfore this does not hold good for an object with high central condensation or small extent. For compact objects, Chandrasekhar's $p_{min} = \frac{G\,m_s}{\langle v^2\rangle}$ is sufficient. White (1976 a) evaluated p_{min} for a series of King's models and found that the values of p_{min} were always close to 1/5 of the tidal radius. White's results are shown in Table V.

TABLE V

$c = r_t/r_t$	P_{min}/r_t
6.05	0.27
9.08	0.24
14.80	0.20
27.40	0.17
55.80	0.16
107.00	0.17
181.00	0.19
432.00	0.21
1740.00	0.21

Here $c = r_t/r_c$ measures the central condensation of the cluster model and P_{min}/r_t was calculated from equation (2·6).

Tremaine, Ostriker and Spitzer (1975) in their calculations to determine dynamical friction on a globular cluster spiralling into the centre of the galaxy (they chose M31) chose the minimum impact parameter to be $p_{min} = r_{core}$ (core radius of the cluster). This means that their evolution of the orbital rates are large by

a factor of nearly 2.

As $\Lambda = p_{max}/p_{min}$ enters logarithmically in the formula for dynamical friction (equation 2.1), it is often not treated rigorously [Tremaine 1976, Keenan 1979], so the orbital rates determined are always wrong by a fator of two or more.

II.2 Applications of the Chandrasekhar's formula

Equation (2.1) was applied to study the evolution of cD galaxies in rich clusters [Ostriker & Tremaine (1975), White (1976b)], the formation of galactic nuclei (Tremaine, Ostriker & Spitzer (1975)) and to study the orbital decay and eventual merger of satellite galaxies with parent galaxies [Tremaine (1976a), White (1978) & Lin & Tremaine (1983)]. It seems that the dynamical friction formula of Chandrasekhar gives a reliable rough estimate of the rate of orbital decay, though doubts were raised by White (1983), in his numerical calculations. The frequency of mergers of satellite galaxies is relatively small unless the central galaxies have extended massive halos. If the halo mass distribution is an isothermal sphere with one-dimensional velocity dispersion σ, the density at radius r is given by

$$\rho(r) = \frac{\sigma^2}{2\pi G r^2} \qquad (2.7)$$

A satellite in a circular orbit then has a speed given by

$$V_s = \sqrt{2}\,\sigma \qquad (2.8)$$

From equation (2.1), the evolution of the satellite's orbital

radius r_s can be calculated by

$$r_s^2(t) = r_s^2(0) - 0.605 \frac{G m_s t}{\sigma} \ln \Lambda \qquad (2.9)$$

or

$$r_s(t) = \left[r_s^2(0) - (52\ \mathrm{kpc})^2 \left(t/10^{10}\ \mathrm{yr} \right) \left(\frac{m_s}{10^{10} M_\odot} \right) \left(\frac{100\ \mathrm{km\,s^{-1}}}{\sigma} \right) \ln \Lambda \right]^{\frac{1}{2}} \qquad (2.10)$$

where m_s is the mass of the satellite.

Let us suppose that the number of density of satellites initially is n(r). Then the flux through a given radius is proportional to $r^2 n(r)\, dr/dt$ which is proportional to r*n(r).

If the number density $n(r) \propto r^{-\nu}$, a depletion of massive satellite galaxies at small radii for $\nu > 1$ and an over abundance of bright close satellites for $\nu < 1$ is expected. Peebles (1980) gives $\nu \simeq 1.8$. From the above hypothesis, therefore, a depletion is expected. The amount of depletion can however be uncertain because tidal stripping may reduce the mass of the satellite m_s and thus $\left| \frac{dr}{dt} \right|$, as the satellite spirals in. Ostriker and Turner (1979) point out that depletion may also be masked by brightening of spiralling galaxies due to tidal shocks which induce star formation. Observations of depletion [Ostriker & Turner (1979) & White & Valdes (1980)] are not very clear and do not give an evidence for or against the rapid decay rate and short lifetimes of nearby satellites predicted by the dynamical friction formula [equation (2.1)] if massive halos are present.

Tremaine (1980) gave a rough estimate of how much mass a typical galaxy can accrete in the form of small satellites. The number density of galaxies of mass m_s at separation r from a given galaxy is (Peebles 1980)

$$\eta(r, m_s)\,dm_s = n_0(m_s)\,dm_s \left(\frac{r}{r_0}\right)^{-\nu} \qquad (2.11)$$

Where $n_0(m_s)\,dm_s$ is the field density

$\nu \simeq 1.8$ $\quad r_0 \simeq 3h^{-1}$ MPc

Equation (2.11) is valid for $r \ll r_0$. The field density, $m_s)dm_s$ can be obtained from Schechter's (1976) luminosity function assuming that M/L is a constant, as

$$n_0(m_s)\,dm_s = n^*\left(\frac{m_s}{m^*}\right)^{-\alpha} \exp\left(-\frac{m_s}{m^*}\right)\frac{dm_s}{m^*} \qquad (2.12)$$

where

$$n^* = 0.04\,h^3\ \text{MPc}^{-3}$$

$$m^* = 6.8 \times 10^9\, h^{-2}\,(M/L)\,M_\odot$$

$$\alpha = 1.25$$

Using equation (2.9) to determine r(o) for r(t) = 0, a typical galaxy accretes

$$\frac{m_{acc}}{m^*} = \int_0^\infty n_0(m_s)\left(\frac{m_s}{m^*}\right)dm_s \int_0^{r(o)} 4\pi\,(r/r_0)^{-\nu} r^2\,dr$$

or

$$m_{acc} = 4.1 \times 10^8 \left[(H_0 t)\ln\Lambda\left(\frac{100\ \text{kms}^{-1}}{\sigma}\right)\right]^{0.6} (M/L)^{1.6} M_\odot\, h^{-2.6} \qquad (2.13)$$

where

$$h = H_0 \,/\, 100\ \text{kms}^{-1}\ \text{MPc}^{-1}$$

Taking

$$\sigma \simeq 140\ \text{kms}^{-1},\ \frac{M}{L} \approx 6,\ H_0 t \approx 1,\ h \approx 1,\ \ln\Lambda \approx 3$$

which are reasonable values, the mass accreted by a galaxy is then

$$m_{acc} \approx 6 \times 10^{9} M_{\odot} \qquad (2.14)$$

which is comparable to the mass of the Large Magellanic cloud.

The mass accreted by a galaxy (equation 2.14) is almost 10% the total mass of the disk in our Galaxy. If these estimates are correct then most spiral galaxies must have absorbed several satellites in 10^{10} years.

Tremaine (1976a) estimated the decay rate of the orbit of Large Magellanic cloud due to the halo of our Galaxy by applying Chandrasekhar's formula (equation 2.1). He assumed the mass distribution of the Galaxy to be spherical leading to a density distribution,

$$\rho(r) = V_c^2 / 4\pi G r^2 \qquad r < r_{max}$$

$$= 0 \qquad r > r_{max}$$

where V_c is a constant circular velocity in the outer parts of the Galaxy and ,

$r_{max} \rightarrow$ an adjustable outer radius of the Galaxy, beyond which the Galactic mass density is assumed to vanish.

The present mass and distance to LMC are $M_{LMC} = 1.5 \times 10^{10} M_{\odot}$, $D = 52$ pc The parameters for the orbits of the LMC used by Tremaine are given in the Table VI below.

TABLE VI

Parameters of model orbits of LMC

	model 1	model 2	model 3	model 4
R^{max} (KPC)	200	200	30	30
V^c (Kms^{-1}) (local rotational velocity)	250 Kms	200	250	200
Time at which LMC is disrupted (yr)	$2 * 10^9$	$2.1 * 10^9$	$2.6 * 10^9$	$3.6 * 10^7$

Figure 13 shows the plot for the radial component. The LMC orbit evolves considerably over 10^{10} years in all models.

According to the results of Tremaine, the orbit of the LMC decayed considerably in 10^{10} years and finally will be tidally disrupted by the Galaxy.

The accretion of LMC and such similar satellites would suggest that the luminosity of the Galaxy will change significantly in time. For example, the luminosity of LMC is $M_B = -18.2$ [de vaucouleurs & Freeman (1972)]; $M_B(\text{GALAXY}) \approx -19.7$.

The accretion of LMC causes a change in the luminosity of the galaxy $\Delta M_B = -0.24$ within approximately 3×10^9 years. If this value was typical in the past, then

$$\frac{dM_B}{dt} \approx -0.08 \text{ mag} / 10^9 \text{ years}$$

These rough estimates predict that galaxies may increase in luminosity by accretion of satellites due to dynamical friction at a rate exceeding -0.05 magnitude/10^9 years. The frequency of such mergers however is quite small, unless galaxies have

FIGURE 13

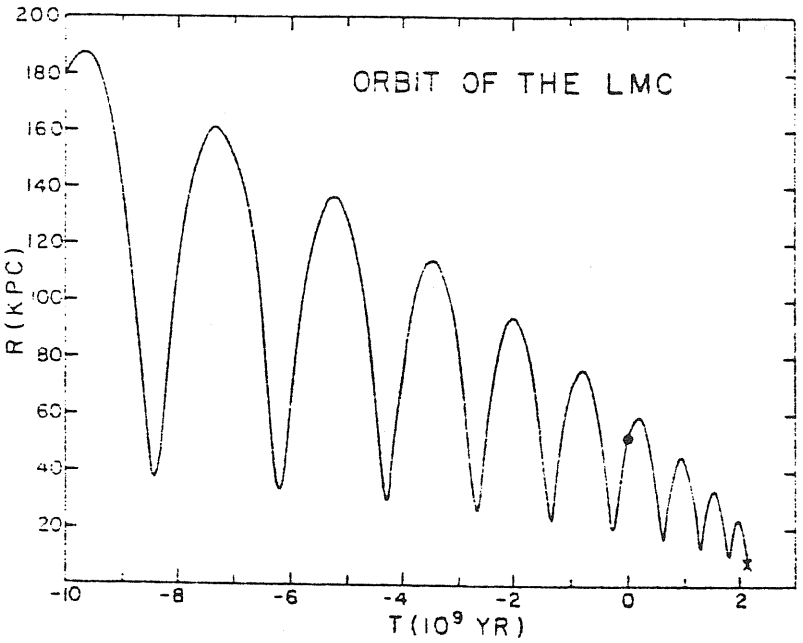

The radial component of the orbit of the Large Cloud in the model with $V_c = 200$ km s^{-1} and $R_{max} = 200$ kpc. The present position is marked by a dot, and the point of tidal disruption is marked by a cross.

extended halos, which they do [Faber and Gallagher (1979)]. This eating of small satellites by larger systems does has cosmological implications, which will not be considered here.

The sinking rate of a globular cluster due to the halo alone of a galaxy can be calculated as following. Suppose a globular cluster at radius r_s, is moving in a circular orbit with velocity V_c in an isothermal halo distribution with one-dimensional velocity dispersion σ and density at r given by

$$\rho(r) = \frac{\sigma^2}{2\pi G r^2} \qquad (2.15)$$

The deceleration rate of the globular cluster using Chandrasekhar's formula [equation 2.1] is

$$\frac{dv_s}{dt} \sim - \frac{4\pi G^2 m_s}{V_s^2} \frac{\sigma^2}{2\pi G r^2} \ln \Lambda \qquad (2.16)$$

$$\frac{dv_s}{dt} \sim - \frac{G m_s \ln \Lambda}{r^2} \qquad (2.17)$$

Then the rate of evolution of the orbital radius r_s of the globular cluster due to the dynamical friction of the halo is

$$\left(\frac{dr_s}{dt}\right)_{halo} \sim - \frac{V_s G m_s \ln \Lambda}{2\sigma^2 r} \qquad (2.18)$$

$$\left(\frac{dr_s}{dt}\right)_{halo} \sim - 0.3 \frac{G m_s}{V_c r} \ln \Lambda \qquad (2.19)$$

Taking typical halo parameters, mass of the halo $M_H = 10^{11} M_\odot$, extent of the halo R_H = 20 KPC, the sinking rate of a globular cluster of mass of $m_s = 10^6 M_\odot$ in a circular orbit at radius 20 KPC is

$$\left(\frac{dr_s}{dt}\right)_{halo} \sim - 1.5 \times 10^{-4} \text{ kpc/year} \qquad (2.20)$$

Here $\Lambda = \frac{R_H}{0.5 * r_t}$ where r_t =100 pc, is the tital radius of the

globular cluster given by King (1962).

In 10^{10} years, the globular cluster sinks from an initial radius of 20 KPC to 19.4 KPC only, which is negligible. However, to check for the total dynamical friction on a cluster moving in a galaxy it is necessary to combine the friction due to all components of a galaxy, for example, the disk, spheroid and halo components in a spiral galaxy. The results of the sinking rate depend on the galaxy model used because dynamical friction is directly proportional to the density of background stars. Realistic models of the galaxy are absolutely necessary to get correct values of dynamical friction.

The dynamical friction on a globular cluster due to the disk of our Galaxy has been computed by Keenan (1979). Using Chandrasekhar's formula for dynamical friction, Keenan found that globular clusters in the mass range 10^5 - 10^6 $M_\odot$ are removed by the disk provided that the globular clusters are close to the disk ($R \lesssim 4$ KPC) and their z peculiar motion is not too large. He found that dynamical friction due to the disk acts first to reduce the pecular motion of the object to zero (relative to circular motion) and then to cause it to spiral in towards the centre along with galactic plane.

The Galaxy model chosen by him was that of Innanen's (Innanen 1973). This model consists of nine spheroids developed to fit the observed kinematical and stellar distribution of the Galaxy. Four of these spheroids represent the disk, four the halo and one, the nuclear bulge. The halo component is not modelled quite well and this makes this model uncertain. However, Keenan

was interested studying only the effect of dynamical friction due to the disk, as he found that the dynamical friction due to the halo is negligible unless the cluster has a mass $\gtrsim 10^7 M_\odot$.

Figures 14 show the decay times to circularity for non-planar orbits. The total decay time for a cluster is the decay time to circularity plus the time for the cluster to spiral towards the nucleus to $\gamma < 2$ kpc. From the figures, it can be inferred that a globular cluster of mass $\sim 7 \times 10^5 M_\odot$ will have its orbit circularized in $\lesssim 6 * 10^9$ years if its maximum z amplitude is $\lesssim 1$ KPC. In 10^{10} years, objects ofmass $> 3.5 * 10^5$ $M_\odot$ and initial z amplitude $\lesssim 1$ KPC have their orbits circularized. The dotted contours in the figures represent those initial orbital parameters such that the globular cluster decays to $r \lesssim 2$ KPC in a time 10^{10} years. All orbits with initial parameters to the left of this line decay to $r < 2$ KPC in less than 10^{10} years. This means that massive clusters can be removed within the life time of the Galaxy.

For a cluster inside the disk, its velocity v with respect to the disk material is very small, though it is not absolutely zero because of asymmetric drift $V_{a.d}$ of the spheroid. Figure 15 indicates the sensitivity of dynamical friction to the velocity dispersion σ and the asymmetrical drift $V_{a.d}$.

When the cluster is in a near circular orbit, its velocity V is close $\sim V_{a.d}$ for that particular spheroid. This corresponds to $X < 1$ [$x = \frac{1}{\sqrt{2}} \frac{V}{\sigma}$]. In the figure 15 it can be seen how sensitive dynamical friction is to the exact values of V and σ. Because the dynamical properties of the Galaxy are not known

FIGURE 14

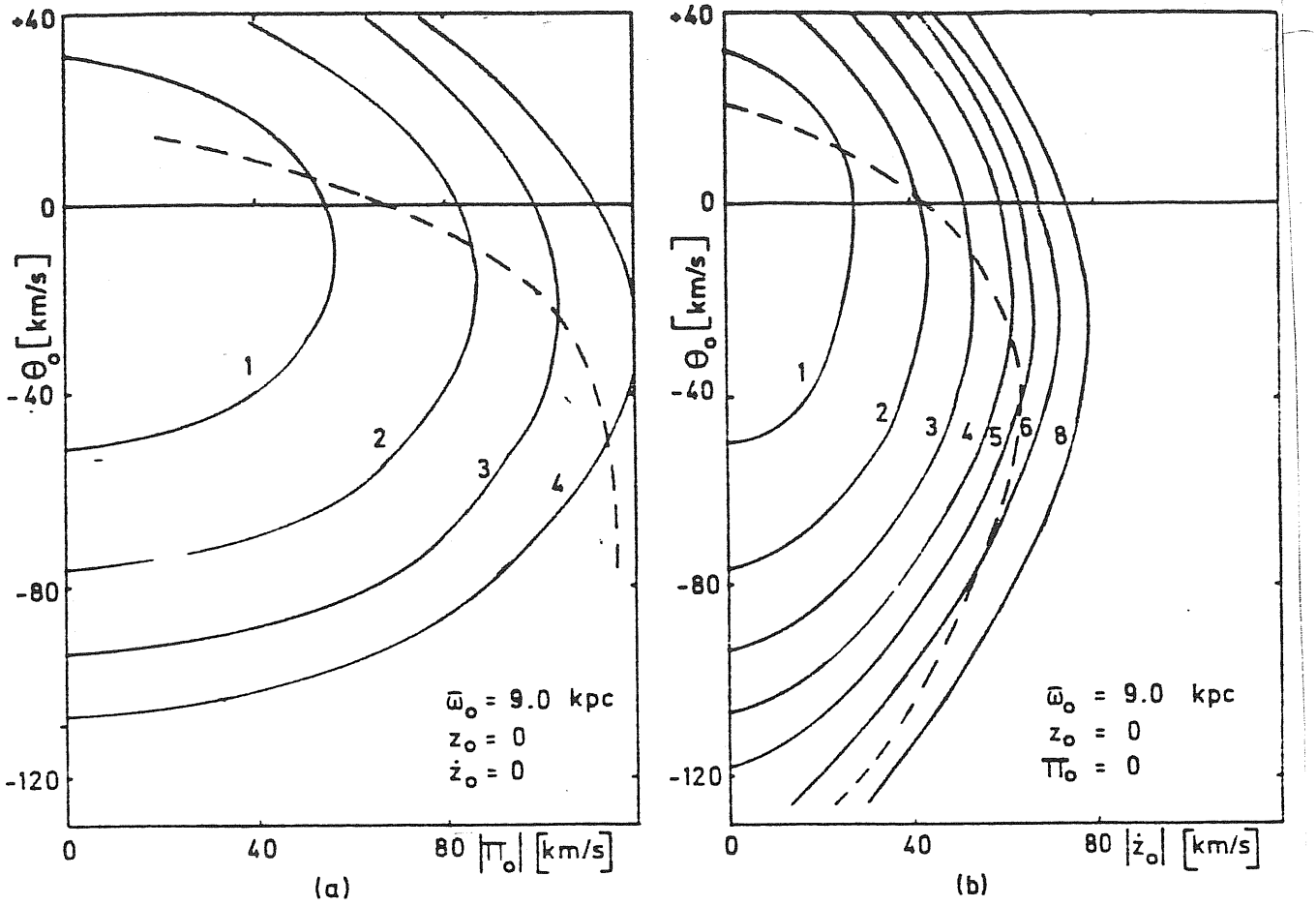
+40
0
-40
-80
-120
Θ_o [km/s]
1
2
3
4
5
6
8
$\bar{\omega}_o$ = 9.0 kpc
z_o = 0
$\dot{z}_o$ = 0
Π_o = 0
0
40
80 $|\Pi_o|$ [km/s]
80 $|\dot{z}_o|$ [km/s]
(a)
(b)

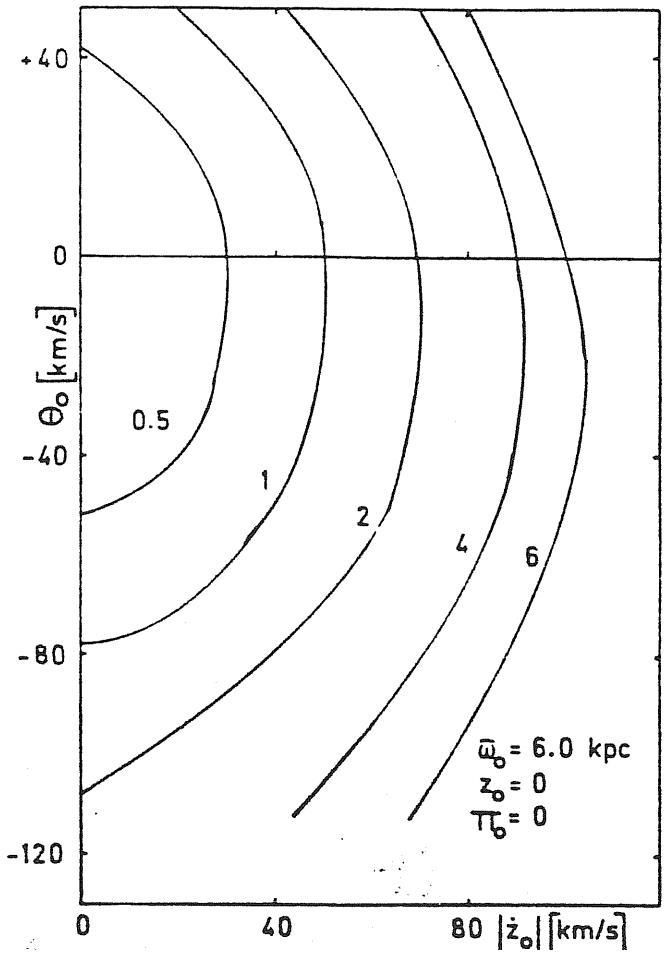
+40
0
-40
-80
-120
Θ_o [km/s]
0.5
1
2
4
6
$\bar{\omega}_o$ = 6.0 kpc
z_o = 0
Π_o = 0
0
40
80 $|\dot{z}_o|$ [km/s]

FIGURE 15

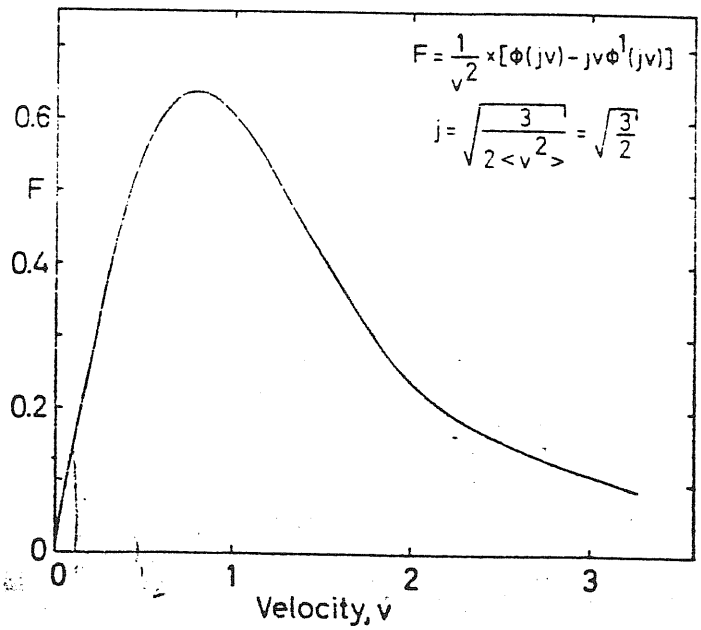
$F = \frac{1}{v^2} \times [\Phi(jv) - jv\Phi^1(jv)]$
$j = \sqrt{\frac{3}{2<v^2>}} = \sqrt{\frac{3}{2}}$
0.6
F
0.4
0.2
0
0
1
2
3
Velocity, v

exactly, except perhaps the rotation curve, the estimates of the decay times for circular orbits are quite uncertain.

The results from Keenan's work can be summarized as follows:

(1) Globular clusters of masses $\gtrsim 4 * 10^5 M_\odot$ whose orbits are confined to the disk will be absorbed in $\lesssim 10^{10}$ years.

(2) Dynamical friction acts first to reduce the peculiar motion of the cluster to zero and then cause it to spiral in towards the centre of the galaxy.

Chandrasekhar's formula [equation 2.1] has been widely applied to get sinking rates of satellites in galaxies. The results obtained however are not exact because of the various approximations used in the computations. In the next section, the validity of Chandrasekhar's formula will be discussed.

II.3 The validity of the Chandrasekhar's formula

Chandrasekhar's dynamical friction formula (equation 2.1) is simple and appealing and as was seen to give reasonable estimates of the decay rates in various cases. However, the formula is not rigorous and it becomes too difficult to generalize it from an infinite homogeneous background system to a finite inhomogeneous system, which galaxies generally are, or simply to a spherical system. The main problems associated with the Chandrasekhar's formula for dynamical friction can be listed as follows:

(1) The exact value of $\Lambda = p_{max}/p_{min}$ is not well-defined. The value of p_{min} can be given quite accurately as was seen before, but the choice of p_{max} = size of the background system is only a device to remove a divergence in the formula (equation 2.1) for an infinite homogeneous system. The logarithmic dependence

on p^{max}, the maximum impact parameter suggests that most of the contribution to the deceleration comes from encounters with large impact parameters, for which an infinite homogeneous model of the galaxy is a poor approximation.

(2) Equation (2.1) shows that the deceleration is proportional to the local density ρ. If the satellite orbits just outside the galaxy then equation (2.1) predicts that there should be no drag since $\rho = 0$. But numerical N-body experiments (Lin & Tremaine 1983) have shown otherwise.

(3) It is not possible to generalize equation (2.1) to a spherical system. Dynamical friction apparently violates Poisson's theorem in celestial mechanics, which states that in an N-body system there will be no secular energy changes in first or second order perturbation theory. Close encounters with $b = \frac{G m_s}{v_s^2}$ cannot be treated by perturbation theory but these contribute only a fraction $\sim (\ln \Lambda)^{-1}$ of the total drag force. Equation (2.1) shows that the force on the satellite is $m_s \frac{dv}{dt} \propto m_s^2$, so dynamical friction is a second-order perturbation. Therefore, the drag given by equation (2.1) cannot be reconciled with the Poisson's theorem.

(4) Equation (2.1) neglects the self-gravity of the background medium. It considers only the interaction of the stars with the satellite, and not with one another. Kalnajs (1972) computed dynamical friction in a galaxy model consisting of a uniformly rotating sheet of stars. This is the only analytical model in which the collective effects due to the self-gravity of the stars are included. Kalnajs found that the collective modify the stars response in such a way that there is no dynamical friction, at

least in linear theory.

The difficulties associated with Chandrasekhar's formula can be seen from the following simplified example.

Consider a star in a galaxy which is initially on a circular orbit in the plane of the satellite orbit. Suppose that the satellite is on a circular orbit with radius r_s. The angular speed of the star Ω is given by

$$\Omega = \left[\frac{1}{r}\frac{dU}{dr}\right]^{1/2} \qquad (2.21)$$

where u(r) is the potential of the central galaxy and r is the radius of the star.

The potential from the satellite is written as a series of terms of the form (Tremaine 1980)

$$\Phi_s = \phi_m(r)\cos m(\theta - \Omega_s t) \qquad (2.22)$$

where $\Omega_s = \Omega(r_s)$ is the angular velocity of the satellite

m is an integer

θ azimuthal angle in the orbital plane.

The equations of motion of the star due to a single term in the perturbing potential then are

$$d^2r/dt^2 - J^2/r^3 = -\frac{dU}{dr} - \frac{d\phi_m}{dr}\cos m(\theta - \Omega_s t) \qquad (2.23)$$

$$dJ/dt = m\phi_m \sin m(\theta - \Omega_s t) \qquad (2.24)$$

where $J = r^2 d\phi/dt$ is the angular momentum.

Suppose the perturber is turned on at time t = 0 then the solutions of equations (2.23) and (2.24) to first order in ϕ_m are

$$r_1 = \left[d\phi_m/dr + 2\Omega\phi_m/r(\Omega - \Omega_s)\right] r_0 / \left(\kappa_0^2 - m^2(\Omega_0 - \Omega_s)\right) *$$

$$\left\{\cos\left[m(\Omega_0 - \Omega_s)t + m\theta_0\right] - \cos\kappa_0 t \cos m\theta + \frac{m(\Omega_0 - \Omega_s)}{\kappa_0}\sin\kappa_0 t \sin m\theta\right.$$

$$+ \frac{2\Omega_0\phi_m(r_0)}{r_0\kappa_0^2(\Omega_0 - \Omega_s)}\cos m\theta_0(1 - \cos\kappa_0 t) \qquad (2.25)$$

where (r_0, θ_0) are the initial co-ordinates of the star at t=0

$\Omega_0 = \Omega(r_0)$, angular speed at t=0

κ_0 = epicyclic frequency given by $\kappa_0^2 = \left[\frac{d^2U}{dr^2} + 3\frac{1}{r}\frac{dU}{dr}\right]_{r_0}$

and

$$J_1 = -\left(\frac{\phi_m}{\Omega - \Omega_s}\right)\left\{\cos\left[m(\Omega_0 - \Omega_s)t + m\theta_0\right] - \cos m\theta_0\right\} \quad (2.26$$

From the solution it is seen that there is no secular torque on the star to first order. Calculations carried to second order show the same result. Furthermore, there is no increase in the star's energy since

$$\frac{dE}{dt} = \Omega_s \frac{dJ}{dt}$$

by Jacobi's integral. Consequently, there is no drag on the satellite analogous to dynamical friction which is also a second order effect in the perturbing potential. This was also the conclusion reached by Kalnajs (1972).

The resolutions to the problems (1) - (4) are all related. First, consider only close encounters. That is, in the Chandrasekhar's formula [equation (2.1)] , $p_{max} = 2p_{min}$

For these encounters the approximation of an infinite homogeneous background is valid since the impact parameter is less than the scale size of the system and the given star is unlikely to have more than one close encounter. This restriction decreases the drag force in equation (2.1) by only $\ln\Lambda$. A lower limit, therefore can be obtained to the drag force using Chandrasekhar's formula by putting $\ln\Lambda \sim 1$.

Second, from equations (2.25) and (2.26) it can be seen that

the first order perturbations r_1 and J_1 diverge at

$$K_0^2 = m^2 (\Omega_0 - \Omega_s)^2 \qquad \text{[Lindblad resonance]}$$

and $$\Omega = \Omega_s \qquad \text{[co-rotation resonance]}$$

Therefore, the perturbances near these resonances are large. Moreover, it is seen that the second order torque $\frac{dJ_2}{dt}$ has periodic terms of long period near these resonances.

Consider the Lindblad resonance at $K = m(\Omega_0 - \Omega_s)$. The second-order torque near due to divergent long-period terms is

$$\frac{dJ_2}{dt} = -\frac{m}{4K_L r_L^2}\left(r\frac{d\phi_m}{dr} + \frac{2m\Omega}{K}\phi_m\right)_{r_L}^2 \frac{\sin[K - m(\Omega_0 - \Omega_s)]t}{K - m(\Omega_0 - \Omega_s)} \qquad (2.27)$$

where r_L is the resonance radius defined by

$$K = m(\Omega_0 - \Omega_s)$$

The torque on a given star grows $\propto t$ until it drops out of resonance at $\sim \pi$. As time goes on the number of stars in resonance decreases as 1/t but each star feels a torque $\propto t$. Thus the total torque is independent of time. The more general form of equation (2.27) can be found in Lynden-Bell & Kalnajs (1972), who also recognized the existence of secular torques at resonances. Equation (2.27) eventually fails because the perturbations on the stars which are still in resonance become non-linear. However the evolution of the satellite orbit will bring fresh stars into resonance so that a secular torque continues to be present always. In a real galaxy, with eccentric and complicated orbits for the satellite and stars, the resonance structure is more complicated than a single Lindblad resonance. However, it can be seen that near-resonant stars in a galaxy can

exert secular torques on a satellite.

These torques are analogous for spherical or axisymmetric systems of the drag force given by Chandrasekhar's dynamical friction formula for infinite homogeneous systems. To see this, consider a resonance with azimuthal wave no. $m \sim 1$. Then $\phi_m \sim \frac{Gm_s}{r}$ where m_s = mass of the satellite

r = orbital radius of the satellite

The epicyclic frequency K is set to Ω . The number of field stars in an interval $d\Delta$ is given by $n \sim \rho r^2 d\Delta / \Omega$ where ρ is the mean density of the galaxy.

Considering equation (2.27) and integrating it over Δ,

$$dJ_2/dt \sim G^2 m_s^2 \rho / \Omega^2 r \qquad (2.28)$$

is obtained. Chandrasekhar's formula equation (2.1) gives the same result:

$$dJ_2/dt \sim m_s r \frac{dV}{dt}$$

$$\sim \frac{G^2 m_s^2 \rho r}{V^2} \sim \frac{G^2 m_s^2 \rho}{\Omega^2 r} \qquad (2.29)$$

In principle, the exact frictional force on a satellite in a given orbit in an axisymmetric galaxy can be computed. The resolutions of the problem (1) - (4) can be summarized as follows:

(1) The divergence in the drag formula from an infinite homogeneous background arises because the discrete resonances in a finite system have been replaced by a continuum. Putting p_{max} = size of the system gives approximate results but for a rigorous result, one has to sum the secular perturbations from all near-resonant stars.

(2) Drag force s can occur even if the satellite orbits outside the galaxy, so long as it has resonances which lie within the

the galaxy, so long as it has resonances which lie within the galaxy.

(3) In a galaxy with 10^{11} - 10^{12} stars, there are always stars which are close to resonance that their perturbations have periods which exceed the evolution time of the system. These secular terms can produce decelerations despite the Poisson theorem.

(4) Kalnajs' model has artificial properties that make it unreliable to guide to the behavior of more realistic systems. Foremost among these is the fact that since the unperturbed stellar orbits all have the same epicyclic frequency there are no orbits resonant with the perturber except for very special values of the perturber's own orbital frequency, whereas at least when self-gravity is neglected, dynamical friction is due entirely to resonant stars [Tremaine & Weinberg 1984].

White (1983) showed in his N-body calculations that the rate of orbital decay is suppressed if the self-gravity of the system is neglected. This will be discussed in the final section of this chapter, where the numerical works done so far to study dynamical friction in systems are reviewed.

II.4 Dynamical Friction Formula in Spherical Systems

Chandrasekhar's formula for dynamical friction is only approximate and it was shown how the formula becomes difficult when trying to generalize it to realistic systems. In this section, a convenient expression for the torque on a satellite is given which is applicable to spherical systems. For many problems in galactic dynamics, the underlying stellar

distribution is better described being spherical rather than homogeneous. Therefore, it is worth understanding the mechanics of spherical dynamical friction, how much it differs from Chandrasekhar's theory of dynamical friction and the limit in which they agree in the context of orbital decay of satellites. he detailed arguments for computing dynamical friction in sphericals can be found in Tremaine & Weinberg (1984), Weinberg (1985) and Weinberg (1986). An alternate formula for the orbital decay of a satellite in a spherical system has also been calculated by Palmer & Papaloizon (1985). The main difference between the two formulae is that Tremaine & Weinberg neglect self-gravity while Palmer & Papaloizon include self-gravity in their theory. Both the formalisms and results will be discussed in this section. It should be added however that these analytical results were restricted to weak interactions where linear perturbation theory could be used.

(i) **Tremaine & Weinberg formula for drag force in spherical systems**

Consider orbits in a spherical system. For a given orbit, the angular momentum J and energy E are constants of motion given by

$$J = \left(r^4\dot{\theta}^2 + r^4\sin^2\theta\,\dot{\phi}^2\right)^{1/2} \qquad (2.30)$$

$$E = \frac{1}{2}\dot{r}^2 + \frac{J^2}{2r^2} + U(r) \qquad (2.31)$$

where u(r) is the unperturbed gravitational potential a spherical galaxy modeled here as an isothermal sphere and (r,θ,ϕ) are the usual spherical co-ordinates. The energy equation (2.31) has real solutions for r only when $r_p < r < r_a$ where r_p and r_a the periapse and apoapse satisfy

$$E = \frac{J^2}{2r^2} + U(r) \qquad (2.32)$$

For an orbit confined to the plane, there are two characteristic frequencies: a radial frequency and an azimuthal frequency. The radial frequency Ω_1 and radial period t_r (time from periapse to periapse) are given by

$$t_r = \frac{2\pi}{\Omega_1} = 2\int_{r_p}^{r_a} \frac{dr}{[2(E-U) - J^2/r^2]^{1/2}} \qquad (2.33)$$

In one radial period the star advances by an angle in the plane of its orbit $\Delta\psi$ where $\Delta\psi = \Omega_2 t_r$ and $\frac{\Omega_2}{\Omega_1} = \frac{J}{\pi}\int_{r_p}^{r_a} \frac{dr}{r^2\left[2(E-U) - \frac{J^2}{r^2}\right]^{1/2}}$

the radial action is

$$I_r = \frac{1}{2\pi}\oint dr p_r = \frac{1}{\pi}\int_{r_p}^{r_a} dr \left[2(E-U) - \frac{J^2}{r^2}\right]^{1/2} \qquad (2.34)$$

A set of canonical variables $[I_1, I_2, I_3] = [I_r, J, J_z]$ are hereafter used to describe the spherical system by Tremaine & Weinberg. The conjugate co-ordinates are the angles (W_1, W_2, W_3). The quantities I_j are constants of motion and W_j are periodic functions of time. The angle W_1 described the phase of a star's orbit in its radial oscillation and is given by $\Omega_1 \int_{c_1} \frac{|dr|}{[2(E-U) - J^2/r^2]^{1/2}}$ The integration contour c_1 goes from periapse to the current position. The integrals are line integrals which increase monotonically along the orbit. It follows from equation (2.33) that w_1 is zero at periapse and increases by 2π in one radial period.

The second angle w_2 describes the mean angular phase of the orbit in the orbital plane. It is given by

$$W_2 = \psi + \int_{c_1} |dr| \left[2(E-U) - J^2/r^2\right]^{-1/2} (\Omega_2 - J/r^2) \qquad (2.35)$$

where

$$\psi = J\int_{c_2} |d\theta| \left[J^2 - J_z^2/\sin^2\theta\right]^{-1/2} \qquad (2.36)$$

The integration contour c_2 starts at an ascending node, that is $\theta = \frac{\pi}{2}$, $\theta < 0$.

To interpret the angle ψ , an inclination β is defined, by

$$J_z = J \cos\beta \qquad (2.37)$$

Integrating (2.36), $\sin\psi \sin\beta = \cos\theta$ (2.38)

The quantity ψ is the angle from the ascending node to (r, θ, ϕ) measured in the orbit plane along the direction of orbital motion. It follows from equation (2.34) and (2.35) that in one orbital period $\Delta w_2 = \Delta\psi$.

The third angle w_3 , the azimuth of the ascending mode is a constant since E is independent of J_z .

The Hamiltonian equation for a particle of unit mass in the unperturbed galaxy potential u(r), $H_0 = \frac{1}{2}\left[\dot{r}^2 + r^2\dot{\theta}^2 + r^2\sin^2\theta\dot{\phi}^2\right] + U(r)$ (2.39)

From equations (2.33) - (2.34) it is seen that

$$\left(\frac{\partial I_r}{\partial E}\right)_J = \frac{1}{\Omega_1} \;,\; \left(\frac{\partial I_r}{\partial J}\right)_E = -\frac{\Omega_2}{\Omega_1} \qquad (2.40)$$

so that

$$\left(\frac{\partial E}{\partial I_r}\right)_J = \Omega_1 \;,\; \left(\frac{\partial E}{\partial J}\right)_{I_r} = \Omega_2 \;,\; \left(\frac{\partial E}{\partial J_z}\right)_{I_r, J} = 0$$

defining

$$\Omega_3 = 0 \;;\quad \frac{\partial E}{\partial I_j} = \Omega_j \qquad (2.41)$$

The Hamiltonian H_0 equation for a particle of unit mass in the unperturbed galaxy potential u(r) is eqn.(2.39).

In terms of the new variables (I_j, w_j), the Hamiltonian H_0 can be written by solving equation (2.34) for $E=H_0$. Since H_0 depends only on I_1, I_2 the equations of motion in the new canonical variables read

$$\frac{dI_j}{dt} = -\frac{\partial H_0}{\partial w_j} = 0$$

$$\frac{dw_j}{dt} = \frac{\partial H_0}{\partial I_j} = \Omega_j (I_1, I_2) \qquad (2.42)$$

To obtain the perturbing potential, the satellite is assumed to move on a circular orbit which has the azimuthal frequency given by

$$\Omega_s^2 = \frac{1}{r}\frac{\partial u}{\partial r} \qquad (2.43)$$

The perturbing potential is expanded in spherical harmonics (McMillan 1958) as

$$U_s(\underline{r}, t) = \sum_{l=1}^{\infty} \sum_{m=-l}^{l} U_{lm}(r)\, Y_{lm}(\theta, \phi_{rot}) \qquad (2.44)$$

where $\phi_{rot} = \phi - \Omega_s t$. The l=0 term in equation (2.44) can be omitted since it does not contribute to the torque and can be absorbed in the galaxy potential u(r). U_{lm} are independent of time if it is assumed that the intrinsic structure of the satellite does not evolve with time..

Since the motion of an unperturbed star is periodic in the canonical co-ordinates w_j , the satellite potential may be expanded in a Fourier series as

$$U_s = \sum_{l_3=0}^{\infty} \sum_{l_1, l_2=-\infty}^{\infty} \Psi_{l_1 l_2 l_3}(I_1, I_2, I_3) \cos(l_1 w_1 + l_2 w_2 + l_3 w_3 - l_3 \Omega_s t)$$

where $\Psi_{l_1 l_2 l_3}(I_1, I_2, I_3) = \sum_{l=2}^{\infty} \left(\frac{2}{1+\delta_{l_3 0}}\right) \gamma^{l}_{l_2 l_3}(\beta)\, Y_{l l_2}\left(\frac{\pi}{2}, 0\right) i^{l_3 - l_2} *$

$$\frac{1}{\pi}\int_0^{\pi} dw_1 \cos\left[l_1 w_1 - l_2(\psi - w_2)\right] U_{l l_3}(r)$$

l_3 = equivalent to index m in equation (2.44)

β = is the inclination defined in equation (2.37)

Since $U_s(\underline{r}, t)$ is even in ϕ_{rot} , the terms with a given l_3 may be combined with those for $-l_3$. Then l_3 goes from 0 to ∞ instead

of $-\infty$. ∞ . V_{lnm} is defined as $V_{lnm}=0$ for $|n|>l$ or $|m|>l$ and $r^{4}_{mn}(\beta)$ are rotation matrices, which satisfy the orthogonolity condition .

The total Hamiltonian H can be written as

$$H = H_0 + U_s(\underline{r},t) \qquad (2.45)$$

where $U_s(\underline{r},t)$ is the perturbing potential (equation 2.44)

The equations of motion become $\frac{dI_j}{dt} = \frac{-\partial H}{\partial w_j} = \frac{-\partial U_s}{\partial w_j}$ (2.46)

$$\frac{dw_j}{dt} = \frac{\partial H}{\partial I_j} = \Omega_j + \frac{\partial U_s}{\partial I_j}$$

To compute the torque on a single star, it is assumed that

$$0\left(\frac{U_s}{U}\right) << 1 .$$

Then the Hamilton's equations (2.46) can be solved by successive iterations. To first iteration, the torque is computed by iterating around the unperturbed trajectory:

$$\Delta_1 I_j = \frac{\partial \chi}{\partial w_j} , \quad \Delta_1 w_j = \frac{-\partial \chi}{\partial I_j} \qquad (2.47)$$

where

$$\chi = -U_s = -\sum_{l_3=0}^{\infty} \sum_{l_1,l_2=-\infty}^{\infty} \psi_{l_1 l_2 l_3}(I_1,I_2,I_3)\cos(l_1 w_1 + l_2 w_2 + l_3 w_3 - l_3 \Omega_s t)$$

from equation (2.44)

On the unperturbed orbit $\Delta_1 I_j$ and $\Delta_1 w_j$ are periodic in the initial phases. Since the initial phases are uniformly distributed, and vanish after averaging over the initial phases: $\langle \Delta_1 I_j \rangle = \langle \Delta_1 w_j \rangle = 0$.

On the second iteration, the torque is computed by integrating around the first order perturbed trajectory. In order to avoid transient effects caused by suddenly turning on the satellite, $l_3\Omega_s + i\eta$ is assumed, where the small positive parameter $\eta \Rightarrow U_s \propto e^{\eta t}$ i.e., it is assumed that the perturbation is turned on adiabatically in the distant past. The second order contribution is

$$\langle \Delta_2 \dot{I}_j \rangle = \frac{1}{2}\eta e^{2\eta t} \sum J_j J_k \frac{\partial}{\partial I_k} \frac{|\Phi|^2}{|J_p\Omega_p - J_3\Omega_s - i\eta|^2} \qquad (2.48)$$

In equation (2.48) the torque diverges as $J_p\Omega_p - J_3\Omega_s \to 0$. At this point, the orbital frequencies and the angular frequency of the satellite are in resonance. If the resonance passes through the orbit rapidly due to a varying Ω_s then $\eta \to 0$ and the divergent fator is written as a delta function $\delta(x) = \frac{1}{\pi}\lim_{\eta\to 0} \eta |x - i\eta|^{-2}$. It is seen that the angular momentum is exchanged only with stars whose orbits are in resonance with the satellite's orbit. Integration of equation (2.48) over all stars gives the total angular momemtum transfer or the total torque:

$$\langle\langle \Delta_2 \dot{I}_j \rangle\rangle = 4\pi^4 \int dI_j \sum J_j J_k f(I_j) \frac{\partial}{\partial I_k} |\Psi_{J_1 J_2 J_3}|^2 \delta(J_1\Omega_1 + J_2\Omega_2 - J_3\Omega$$

where $f(I_j) = f(I_1, I_2)$ is the phase space distribution function for a spherical galaxy.

The expression for the total torque on the satellite can be written as:

$$\tau_2 = 4\pi^4 \int_0^\infty dI_1 \int_0^\infty dI_2 \int_{-I_2}^{I_2} dI_3 \sum_{J_3=0}^{\infty} \sum_{J_1, J_2 = -\infty}^{\infty} J_3 J_k \frac{\partial f}{\partial I_k} |\Psi_{J_1 J_2 J_3}|^2 \delta(J_1\Omega_1 + J_2\Omega_2 - J_3\Omega_3 \qquad (2.49)$$

Equation (2.49) is the dynamical friction formula in a spherical system.

(ii) **Palmer & Papaloizou formula for dynamical friction in a spherical system**

Tremaine & Weinberg (1984) calculated the dynamical friction formula (equation 2.49) by neglecting self-gravity in their spherical system i.e., the stars in their spherical galaxy do not interact with one another. Palmer & Papoloizou (1985) gave an analytical expression for the orbital decay of a satellite in a spherical system in which self-gravity was not neglected. They

considered the satellite to be in a circular orbit and assumed that the tidal response could be calculated from linear theory. A brief discussion of this analytical formula for the decay rate obtained by Palmer & Papaloizou will be given here.

The basic equation that described the interaction is the Vlasov equation. Choosing the origin of the co-ordinates $\underline{r}$ to be the centre of the stellar system of total mass M, we write

$$\frac{df}{dt} = \frac{\partial f}{\partial t} + \underline{v} \cdot \frac{\partial f}{\partial \underline{r}} - \frac{\partial \psi}{\partial \underline{r}} \cdot \frac{\partial f}{\partial \underline{v}} = 0 \qquad (2.50)$$

where $\underline{v}$ is the stellar velocity

ψ is the gravitational potential

The gravitational potential ψ can be written as

$$\psi = \Phi + \psi_p \qquad (2.51)$$

where Φ is the potential from the stellar distribution and ψ_p, the perturbing potential due to a satellite, considered to be a point mass in circular orbit is

$$\psi_p = - \frac{GM_p}{\left[r^2 + R^2 - 2rR \sin\theta \cos(\phi - \omega t)\right]^{1/2}} \qquad (2.52)$$

where M_p = satellite's mass

and R = is its ortibal radius

(r, θ, ϕ) are the spherical polar co-ordinates so chosen that the orbital plane is given by $\theta = \pi/2$ and the orbital period by $2\pi/\omega$.

Expnding equation (2.52) in spherical harmonics, we get

$$\psi_p = - \frac{GM_p}{R} \sum_{n=0}^{\infty} \sum_{m=-n}^{n} \frac{(n-|m|)!}{(n+|m|)!} \left(\frac{r}{R}\right)^n P_n^{|m|}(\cos\theta) P_n^{|m|}(0) \exp\left[im(\phi - \omega t)\right] \qquad (2.53)$$

where $P_n^{|m|}$ are the Legendre polynomial functions.

considering only linear perturbations to the stellar system, we can write the distribution function f, and the potential Φ as

$$f = f_0 + f_1$$
$$\underline{\Phi} = \underline{\Phi}_0 + \underline{\Phi}_1 \qquad (2.54)$$

where f_0, $\underline{\Phi}_0$ denote unperturbed values and

f_1, $\underline{\Phi}_1$ denote perturbed values.

The linearized form of the Vlasov's equation (2.50) which governs the perturbations is then

$$\frac{\partial f_1}{\partial t} + \underset{\sim}{v} \cdot \frac{\partial f_0}{\partial \underline{r}} - \frac{\partial \underline{\Phi}_0}{\partial \underline{r}} \cdot \frac{\partial f_1}{\partial \underline{v}} - \frac{\partial \underline{\Phi}_1}{\partial \underline{r}} \cdot \frac{\partial f_0}{\partial \underline{v}} = \frac{\partial \psi_p}{\partial r} \cdot \frac{\partial f_0}{\partial \underline{v}} \qquad (2.55$$

writing

$$\psi_p = \hat{\psi} \exp(i\omega_p t) \qquad (2.56)$$

$$f_1 = \hat{f}_1 \exp(i\omega_p t) \qquad (2.57)$$

$$\underline{\Phi}_1 = \underline{\hat{\Phi}}_1 \exp(i\omega_p t) \qquad (2.58)$$

$$i\omega_p \hat{f}_1 + \underline{v} \cdot \frac{\partial \hat{f}_1}{\partial \underline{r}} - \frac{\partial \underline{\Phi}_0}{\partial \underline{r}} \cdot \frac{\partial \hat{f}_1}{\partial \underline{v}} - \frac{\partial \underline{\hat{\Phi}}_1}{\partial \underline{r}} \cdot \underline{v} \frac{\partial f_0}{\partial \epsilon} = \frac{\partial \hat{\psi}}{\partial \underline{r}} \cdot \underline{v} \cdot \frac{df_0}{d\epsilon} \qquad (2.59$$

where $\hat{f}_1 = f_s + f_A$ is even in f_s and f_A is odd in $\underline{v}$, the expression for f_A from equation (2.59) after taking even and odd parts is

$$-\omega_p^2 f_A + B^2(f_A) = i\omega_p \frac{df_0}{d\epsilon} \left(\underline{v} \cdot \frac{\partial \underline{\hat{\Phi}}_1}{\partial \underline{r}} + \underline{v} \cdot \frac{\partial \hat{\psi}}{\partial \underline{r}} \right) \qquad (2.60)$$

where the operator B is given by

$$B \equiv i \left(\underline{v} \cdot \frac{\partial}{\partial \underline{r}} \cdot \frac{\partial \underline{\Phi}}{\partial r} \cdot \frac{\partial}{\partial \underline{v}} \right)$$

The potential perturbation $\underline{\hat{\Phi}}_1$, can be expressed as

$$\underline{\hat{\Phi}}_1 = -G \int \frac{f_s(\underline{r}', \underline{v}')}{|\underline{r} - \underline{r}'|} d^6 z' = \frac{iG}{\omega_p} \int \frac{f_A(\underline{r}', \underline{v}') \underline{v}' \cdot (\underline{r} - \underline{r}')}{|\underline{r} - \underline{r}'|^3} d^6 z' \qquad (2.61)$$

Combining equations (2.60) and (2.61), we get an equation for f_A :

$$-\omega_p^2 \left(\frac{df_0}{d\epsilon} \right)^{-1} f_A = L(f_A) + S \qquad (2.62)$$

where

$$L(f_A) = i\omega_p \underline{v} \cdot \frac{\partial \Phi_1}{\partial r} - \left(\frac{df_0}{d\epsilon}\right)^{-1} B^2(f_A)$$

and

$$S = i\omega_p \underline{v} \cdot \frac{\partial}{\partial r} \hat{\Psi}$$

The properties of f_A depends on the spectrum of L, which can be taken to consist of discrete real eigen values ω_j^2 with associated eigenfunctions ψ_j ,(j=1,2,3,.....). Assuming that $\omega_j > 0$, any function $F(\underline{r},\underline{v})$ odd in $\underline{v}$ has the eigenfunction expansion

$$F(\underline{r},\underline{v}) = \sum_{j=1}^{\infty} a_j v_j \quad \text{where} \quad a_j = -\int \left(\frac{df_0}{dE}\right)^{-1} \psi_j^* F(\underline{r},\underline{v}) d^6z \qquad (2.63)$$

The solution for f_A is

$$f_A = \sum_{j=1}^{\infty} b_j v_j \qquad (2.64)$$

where

$$b_j = \frac{-i\omega_p}{(\omega_j^2 - \omega_p^2)} \int \psi_j^* \underset{\sim}{v} \cdot \frac{\partial \hat{\Psi}}{\partial r} d^6z \qquad (2.65)$$

The rate of change of orbital energy E_0 can be found now from

$$\frac{d\epsilon_0}{dt} = \int Re\left[f_A \exp(i\omega_p t) \right] Re\left[\underline{v} \cdot \frac{\partial \psi_p}{\partial r} \right] d^6z \qquad (2.66)$$

The resonant singularities are handled by using

$$\frac{1}{(\omega_p \pm \omega_j)} \equiv P_r\left[\frac{1}{(\omega_p \pm \omega_j)} \right] + \pi i \delta(\omega_p \pm \omega_j) \qquad (2.67)$$

where P_r denotes Principal value

δ is Dirac's function.

Equation (2.66) becomes $\frac{d\epsilon_0}{dt} = -\pi \left(\frac{R_s}{R}\right)^{2n+2} \sum_j (I_j)^2 \left[\delta(\omega_j + \omega_p) + \delta(\omega_j - \omega_p) \right]$ (2.68)

where $I_j = \int \psi_j^* \underline{v} \cdot \frac{\partial W}{\partial r} d^6z$.

From equation (2.68) we see that $\frac{d\epsilon_0}{dt}$ is negative definite and so orbital energy is always lost.

II.5 Numerical Works

Both the analytical treatments discussed so far have been restricted to weak interactions where linear perturbation theory could be used. Numerical approach is necessary when the interactions are strong, like in the case of a satellite of mass at least ten percent that of the disk in a prograde, inclined orbit close to the disk. Also numerical works carried out so far to determine the orbital decay rates of satellites in galaxies have given some interesting results. The numerical works that are of most interest to us are those of Lin and Tremaine (1983), White (1983), Quinn and Goodman (1986), Byrd, Sarrinen and Valtonen (1986). The main results of these works will be presented below.

Lin and Tremaine studied the orbital evolution of satellite galaxies using a N-body code where the two-body forces between stars in the halo of the parent galaxy were neglected.

They investigated a system containing three types of objects:

(1) a central galaxy described by a potential

(2) N stars of mass m which orbit the central galaxy

(3) a satellite galaxy of mass m_s, also orbitting the central galaxy.

The stars interact gravitationally with the central galaxy and the satellite; the difference from a standard N-body program is that the stars do not interact with each other. Turning off the star-star attraction in this way eliminated two-body relaxtion effects, increased numerical accuracy and computational

speed. The only sacrifice made in this type of a code is that the self-gravity of the outer parts of the central galaxy has been neglected.

Lin and Tremaine constructed a galaxy with central mass M=1, (in units with G=1) surrounded by a halo of N=450 stars with total mass Nm = 1. The stars were initially distributed with a phase space density f depending only on energy $E = \frac{1}{r} - \frac{1}{2}v^2$, $f(E) \propto E^{2.5}$ The mass of the satellite taken was $m_s = 0.1$ and it was placed in a circular orbit of radius $r_s = 2.3$, over a factor of two larger than the halo edge. The evolution of the angular momentum J_s of the satellite is shown in figure 16. The angular momentum changes slowly at first but with increasing speed as the orbit decays. The arrow in the figure marks the point corresponding to a circular orbit at the edge of the halo, $R = 1$. The orbital decay is very fast beyond this point as the satellite is within the halo itself. These results show that strong frictional effects are present even in a satellite orbiting well outside the radius of most of the stars. In the second run, Lin and Tremaine began with some initial conditions but froze the satellite into its initial circular orbit at $r = 2.3$ for 120 time units, which correspond to $\sim$ 8 orbital periods of the satellite, before it was permitted to decay. In this case the decay time for the satellite to reach the edge, was 138 time units after release, whereas in the first case, the decay time was only 51 time units. Later stages of the decay are very similar in both cases, suggesting that the system loses all memory of the freezing, once the decay has begun. In figure 16, both the cases

are drawn.

The main result of Lin and Tremaine's numerical experiment was that they found the numerical results agreed accurately with Chandrasekhar's dynamical friction formula (equation 2.1) for a satellite orbiting within the halo of its parent galaxy. In particular, the formula correctly predicted the variation of the orbital decay rate with satellite size, with satellite mass and with the number density and mass of the stars in the halo.

Satellites orbiting outside the central galaxy are subjected to frictional forces which are not described by the dynamical friction formula. These depend strongly on the distribution of mass in the outer parts of the galaxy and fall off rapidly as the orbital radius increases.

Lin and Tremaine's calculations were based on simple idealized models rather than representations of real galaxies. These lead to several shortcomings:

(1) The central point mass M was kept fixed in order to eliminate two-body relaxation effects. This procedure strongly affects the tidal force from the satellite near M. In particular for $r \ll r_s$ the satellite force in a frame attached to M is $\frac{Gm_s \underline{r}}{r_s}$ when M is fixed and has a smaller value $Gm_s \left[-\underline{r} + 3(\underline{r}\cdot\underline{r}_s)/r_s^2 \right] / r_s^3$ when M is free. This effect leads to an overestimation of the frictional force [White 1983].

(2) Because each star is attracted by only point mass M and not other stars, its velocity is lower than it would be in a more realistic model. Hence $f(<v)$ in equation (2.1) is too high and the resulting frictional force is artificially large.

(3) In a real galaxy, the self-gravity of the halo stars enhances the wake formed behind an orbitting point mass and thus increases frictional force. This cannot be modeled in codes where the self-gravity is neglected.

White (1983) found in his simulations that the decay rate of a satellite depends on the global response of the parent galaxy. He also came to the same conclusions as Lin and Tremaine that the decay rate becomes artificially enhanced when the centre of the parent galaxy is fixed and is suppressed by neglecting the self-gravity of the response. Chandrasekhar's local dynamical friction formula cannot, therefore, be a complete description of the underlying physics, although it does predict decay rates that are approximately correct. Lin and Tremaine's decision to nail down the center of their galaxy entirely altered the global pattern of the response and in White's calculation this alteration greately changed the orbital decay rate. White's calculations also showed the response should be calculated in a self-consistent manner if its effect on the satellite is to be modelled correctly; neglecting self-gravity of the response lead to an incorrect phase lap and to a much reduced torque on the orbit. Quinn and Goodman (1986) studied the interaction of a spiral galaxy with its system of satellites, that lead to the orbital decay of the satellites on time scales comparable to their orbital periods. They found that over a Hubble time, the disk of the spiral galaxy and the distribution of the satellites could be altered significantly by the action of dynamical friction.

CHAPTER THREE

N-Body Codes

To study the effect of dynamical friction on globular clusters orbiting in galaxies, a numerical approach becomes necessary. Analytical treatments as seen in the previous chapter, are restricted to weak interactions so that the linear perturbation theory could be used. Morever, numerical works have shown that linear theory cannot be used [Quinn & Goodman 1986; Byrd, Saarinen and Valtonen 1986] to predict even rough estimates for decay rates as it predicts wrong signs in certain effects. Chandrasekhar's dynamical friction formula, which gives approximately correct decay rates is not enough to understand the complete underlying physics [White 1983]. Direct numerical simulations offer the best methods to handle dynamical issues. The basic necessitates to start off a numerical project are a good computer, a big computing budget, an efficient integrator scheme for solving the equations of motion for the N-bodies in the system and a set of initial conditions.

In this chapter, the formulations and numerical integration of large system of differential equation occuring in the gravitational problem of N-bodies is discussed. Several integration schemes are compared to check stability, accuracy and practicability of these methods and what seemed the most efficient one is chosen for our numerical work. In section III.1 the formulation of the gravitational N-body problem is presented. III.2 discusses the difficulties encountered in such problems. In section III.3, the 'semi-restricted N-body codes' are introduced. In III.4 various numerical schemes to solve the

differential equations of motion are compared and tested. III.5 discusses the algorithm finally chosen by us.

III.1 The formulation of the N-body problem

The gravitational N-body problem has a long and distinguished history. The case N=2 is the well-known Kepler's problem while N=3 is the famous three-body problem. The basic approach in a classical N-body problem is that starting with masses, positions and velocities of N-bodies of a system at a given time, it is possible to calculate the state of the system at any later time, by numerically solving the equations of motion for the N-bodies. These equations of motion are

$$m_i \ddot{\underline{r}}_i = -G m_i \sum_{\substack{j=1 \\ i \neq j}}^{N} m_j \frac{(\underline{r}_i - \underline{r}_j)}{|\underline{r}_i - \underline{r}_j|^3}, \quad i = 1, 2 \cdots N \qquad (3.1)$$

where $\underline{r}_i$ and m_i are the position vector and mass of the i^{th} body respectively and G is the gravitational constant. The dots represent the time derivatives.

The problem therefore is to solve the N second-order differential equations from a given set of initial conditions. The system of equations (3.1) are nonlinear and strongly coupled in the sense that successive encounters lead to nonlinear error propogation. It is nevertheless possible to perform accurate integrations of small systems by means of regularization methods [Bettis & Szebenely 1972].

Full N-body calculations that directly integrate the equations (3.1) have been carried out by Aarseth (1972), Ahmad & Cohen (1973), White (1978, 1979), Roos and Norman (1979) and

Dekel, Lecar and Shaham (1980).

III.2 Difficulties associated with N-body programs

The full N-body approach is entirely self-consistent and problems in celestial mechanics, orbits of artificial satellites, applications to stellar dynamical problems like simulations of star clusters, galaxies etc., have given satisfactory results. However, there are some basic factors which lead to difficulty in integrating the equations (3.1) of the system. These are:

(i) The force on each body depends on the position of all other bodies and the time needed to calculate the force increases as the square of the number of particles being integrated. That is, the total computational time to compute the forces goes as N(N-1)/2 and this becomes a basic limitation in dealing with systems having large N. A typical galaxy has $\sim 10^{11}$ stars. To study the evolution of such a system completely, 10^{11} number of particles would be required. There is no computer up to now that can handle such a program, not forgetting that the time of computation $\propto N^2$. At present, the direct integration of equations (3.1) are limited to systems containing $N \sim 10^4$. This is seven orders of magnitude less than what would be required to model a real galaxy. This leads to the assumption that in N-body simulations of galaxies, the dynamics of a system of $10^{11} - 10^{12}$ particles are represented by a model containing only 10^4 particles. Caution must be executed when undertaking simulations with small number of particles because problems with small number statistics may arise while attempting to derive a realistic and smooth gravitational potential field from equation (3.1).

(ii) A second difficulty concerning N-body calculations is the problem caused by relaxation effects. In the equation (3.1) when $|\underline{r}_i - \underline{r}_j| \to 0$, i.e., during a close encounter of the ith and jth bodies, the differential equation (3.1) become singular. These two-body encounters cause appreciable orbital deflections and the two-body relaxation effects become large. This results in the reduction of the relaxation time of the system. Two-body relaxation effects are important in N-body simulations but not in a real galaxy. These two-body encounters therefore lead to an artificial evolution of the system even when it is isolated. Therefore, the system cannot be expected to mimic real galaxy for the timescales that are needed.

Chandrasekhar (1942) gave the two-body relaxation time T_{relax} for a homogeneous system as $T_{relax} = \dfrac{V^3}{8\pi N_D G^2 m^2 \ln\Lambda}$ (3.2)

where v = characteristic encounter velocity

N_D = Number of density of particles

m = mass of a particle

and $\Lambda = \dfrac{R_{max} V^2}{Gm}$ where R_{max} is the radius of the system.

It is common nowadays to use the Spitzer and Hart (1971) version of the formula evaluated half-way in mass out from the centre of the system, which is

$$T_{relax} = \frac{V_m^3}{15.4\, G^2 m^2 n_d \ln(0.4N)} \qquad (3.3)$$

$$= \frac{0.06\, M^{1/2} R_h^{3/2}}{m\, G^{1/2} \log(0.4N)} \qquad (3.4)$$

where N = total number of stars

m = mass of a star

R_h = Half-mass radius

n_d = mean stellar density interior to R_n

$V_m = 0.6\left(\frac{GM}{R_h}\right)^{1/2}$ is the root mean square stellar velocity

From equations (3.2) or (3.3); we see that the relaxation time $T_{relax} \propto N$ to first order, where N is the total number of particles (or stars) in the system,

The crossing time, T_{cross} of the system is defined as

$$T_{Cross} = \frac{R_h}{V_m} \qquad (3.5)$$

$$= \frac{1.58\, R_h^{3/2}}{(GM)^{1/2}} \qquad (3.6)$$

From equations (3.4) and (3.6),

$$T_{relax} \simeq \frac{T_{Cross} \cdot N}{26 \log (0.4N)} \qquad (3.7)$$

or

$$\frac{T_{cross}}{T_{relax}} \sim \frac{26 \log (0.4N)}{N} \qquad (3.8)$$

For a simulated system of say, $N \sim 10^3$ particles,

$$T_{relax} \sim T_{cross} \sim 10^8 \text{ years} \ll T_{Hubble} \qquad (3.9)$$

where T_{Hubble} is the Hubble-time. Therefore a limited N cannot represent a galaxy for times longer than $T_{relax} \sim T_{cross} \sim 10^8$ years, compared with $\sim 10^{18}$ years in real elliptical galaxies.

These short relaxation times have two effects: First, the

structure of the system changes causing an evolution to the model galaxies and second, relaxation imparts a (spurious) effective viscosity (Chandrasekhar 1942) to the galaxy. This viscosity causes evolution of the satellite orbit, which may mask the effects of the dynamical friction that we want to investigate.

From equation (3.7), we see that the relaxation time can be lengthened by increasing the number of particles N. This will lead us back to the difficulty (i), for which there is no practical solution.

The standard remedy to avoid two-body relaxation effects is to introduce a parameter ε, called the softening length into the equations (3.1). That is, the equations of motion are now written as

$$m_i \ddot{\underline{r}}_i = - G m_i \sum_{\substack{j=1 \\ i \neq j}}^{N} m_j \frac{(\underline{r}_i - \underline{r}_j)}{(|\underline{r}_i - \underline{r}_j|^2 + \varepsilon^2)^{3/2}} \qquad (3.10)$$

With the introduction of ε, we are no longer solving a N-body problem. Instead of having the particles or stars in systems to interact via a $1/r^2$ force, we have changed it to $\frac{1}{(r^2+\varepsilon^2)}$ force. We see that by introducing ε, we also avoid the singularity when $\underline{r}_i \to \underline{r}_j$. White (1978) has showed that by introducing ε, the relaxation time T_{relax} can be increased by a factor 2. This can be seen as follows:

In the equation (3.8) replace (log 0.4N) by log (R_{max}/R_{min}). Here, R_{max} is the upper limit imposed on the integration over impact parameters generally taken to be = R_h and $R_{min} \sim 1.65\varepsilon$ (White 1978). Then for a reasonable choice of ε, T_{relax} can be

increased by a factor 2.

Instead of carrying out full N-body techniques, alternative approaches were used, where the potential calculations were carried out in a different way. Miller (1978) Fourier grid technique and Van Albada & Van Gorkom (1977) Legendre Polynomial techniques are some of them. But the problem with the Fourier grid technique is that there is a practical limit to the extent of the three-d grid, which results in a coarse resolution. The Legendre Polynomial method is 2-D, so its applicability to realistic situations is restricted. But both the methods have the advantage that the time to compute the gravitational force is directly proportional to the number of particles N.

III.3 The Restricted N-body code (RNB)

To model a galaxy, we need as many particles as we can and as seen in the last section, this means that the number of force calculations $\sim N^2$. The total number of particles that can be used is also limited by the available storage on the computer and a compromise has to be made between realisitic galaxy models, computer storage and computer budget. Lin & Tremaine (1983) presented a novel numerical technique to study orbital decay of satellites in galaxies which is free from most of the problems associated with N-body programs. [Toomre and Toomre (1972) were however the first to use this method to study small changes in the orbit of a passing galaxy and this method was also used by Borne (1982) with some variations for his study of interacting binary galaxies.] The essential change in the code from the

conventional N-body codes is that the N bodies do not attract one another. This means two important benefits:

(1) A great saving in computational time since the task of computing N(N-1)/2 two-body forces is avoided. As a result, more simulations can be run with more number of particles than allowed before for a full N-body code.

(2) Since there are no two-body interactions between the bodies, there is no relaxation and the previously mentioned spurious viscosity is zero. However, to avoid the singularity in equation (3.1), a softening parameter is still required.

Lin & Tremaine called codes of this type semi-restricted N-body (RNB) programs and the idea was later on used by White (1983) and Quinn & Goodman (1986).

For the purpose of studying dynamical friction on globular clusters orbiting in galaxies we have also constructed a semi-restricted N-body code (henceforth RNB). Because of the need to explore a range of orbital parameters like initial radius, inclination, masses, eccentricity etc., a code of this type is preferable over a full N-body code since the 'semirestricted code' is fast and many simulations could be run. The serious drawback of such a code is that the self-gravity of the system is neglected. To study the effect of self-gravity in our cases, a full N-body, self-consistent simulations were also ran.

The equations of motion, for a galaxy of mass M made of N number of particles and a satellite of mass m_s in the RNB code are:

$$\ddot{\underline{r}}_i = - G m_s \frac{(\underline{r}_i - \underline{r}_s)}{\left[|\underline{r}_i - \underline{r}_s|^2 + \varepsilon^2 \right]^{3/2}} \qquad i = 1, \cdots N \qquad (3.11)$$

$$\ddot{\underline{r}}_s = - G \sum_{i=1}^{N} m_i \frac{(\underline{r}_s - \underline{r}_i)}{\left[|\underline{r}_s - \underline{r}_i|^2 + \varepsilon^2 \right]^{3/2}}$$

where $\underline{r}_i$ and $\underline{r}_s$ represent the positions of the particles and satellite respectively, ε is the softening parameter and G the gravitation constant. The total mass of the galaxy is

$$M = N m_i \qquad (3.12)$$

From our experiments, we have found that the RNB is 100 times faster than the full N-body code.

More details on the RNB code, the initial conditions, galaxy models etc., will be given in the following chapters. The next section is devoted to finding an ideal integration routine to solve the equations of motion, both for the full N-body code (equation 3.10) and for the RNB code (equation 3.11).

III.4 Integrator schemes

Once the equations of motion are written down, to solve them numerically, both in a full N-body program or RNB, means looking for an integrator routine that solves these second-order differential equations efficiently, accurately and satisfactorily with enough speed. The most popular and widely used integrator routine in astrophysical N-body problems is that of Aarseths', which is made easily available by him to all. A copy of his code (N BODY 1) was sent to us on asking and we set it up quickly to run a few test cases and to see if it was suitable for our

problem.

Aarseth's code uses a fourth-order polynomial method for the integration of the equations of motion in a full N-body problem. The basic scheme, the computational algorithm and the results of our test runs will be discussed below.

The Basic difference scheme

The equation of motion for a particle is given by

$$\underline{F}_0 = \ddot{\underline{r}}_i = -G \sum_j m_j \frac{(\underline{r}_i - \underline{r}_j)}{|\underline{r}_i - \underline{r}_j|^3} \quad (j \neq i) \qquad (3.13)$$

where m, $\underline{r}_i$, denote mass and position for the i^{th} particle

G -> Gravitational constant

and the summation in equation (3·13) extends over the other N-1 members.

Knowing $\underline{F}$, the force per unit mass (we have omitted the particle subscripts here) at four previous times, t_0, t_1, t_2, t_3 with t_0 being the most recent, a fourth-order fitting polynomial at time t can be written as

$$\begin{aligned}\underline{F}(t) = \; & \underline{F}(t_0) + \underline{D}^1(t-t_0) + \underline{D}^2(t-t_0)(t-t_1) \\ & + \underline{D}^3(t-t_0)(t-t_1)(t-t_2)(t-t_3) + \\ & \underline{D}^4(t-t_0)(t-t_1)(t-t_2)(t-t_3)(t-t_4)\end{aligned} \qquad (3.14)$$

where $\underline{D}^1$, $\underline{D}^2$, $\underline{D}^3$ denote the divided differences defined by

$$\underline{D}^k[t_0, t_k] = \frac{\underline{D}^{k-1}[t_0, t_{k-1}] - \underline{D}^{k-1}[t_1, t_k]}{t_0 - t_k}; \quad k = 1, 2, 3 \qquad (3.15)$$

In equation (3·15), $\underline{D}^0$ represents $\underline{F}$ itself.

The fourth divided difference $\underline{D}^4$ is defined as

$$\underline{D}^4[t_1, t_4] = \frac{\underline{D}^3[t, t_2] - \underline{D}^3[t_0, t_3]}{t - t_3} \qquad (3.16)$$

and is evaluated at time t.

It is convenient to represent the force fitting polynomial [equation 3.14] by a Taylor series which may then be integrated twice to give the new solutions for $\underline{r}$ and $\dot{\underline{r}}$, as a set of six first-order equations.

Equating terms in equations (3.14) and its successive derivations with an equivalent Taylor series yields the coefficients

$$\begin{aligned}
\underline{F}_0 &= \underline{D}^1 + \underline{D}^2 t_1' + \underline{D}^3 t_1' t_2' + \underline{D}^4 t_1' t_2' t_3' \\
\ddot{\underline{F}}_0 &= 2!\left[\underline{D}^2 + \underline{D}^3 (t_1' + t_2') + \underline{D}^4 (t_1' t_2' + t_2' t_3' + t_1' t_3')\right] \qquad (3.17) \\
\dddot{\underline{F}}_0 &= 3!\left[\underline{D}^3 + \underline{D}^4 (t_1' + t_2' + t_3')\right] \\
\ddddot{\underline{F}}_0 &= 4!\,\underline{D}^4
\end{aligned}$$

The contribution from $\underline{D}^4$ is only added at the end of the step. This gives increased accuracy at little cost and no extra memory.

Computational algorithm

Given the initial conditions for m_i, $\underline{r}_i$, $\dot{\underline{r}}_i$ for $i = 1, \cdots N$, the required Taylor series coefficients are generated cumbersomly by the explicit differentiation of equation (3.13); putting

$G_1 = 1$, we have

$$\underline{F}_0 = - \sum_{\substack{j=1 \\ i \neq j}}^{N} m_j \frac{[\underline{r}_i - \underline{r}_j]}{[|\underline{r}_i - \underline{r}_j|]^3}$$

writing $\underline{r}_i - \underline{r}_j = \underline{r}_{ij}$ and $r_{ij} = |\underline{r}_{ij}|$ and denoting Taylor series derivatives by dots, we have

$$\dot{\underline{F}}_0 = \sum_j m_j \left\{ \frac{\dot{\underline{r}}_{ij}}{r_{ij}^3} - \frac{3\underline{r}_{ij}(\underline{r}_{ij} \cdot \dot{\underline{r}}_{ij})}{r_{ij}^5} \right\}$$

$$\ddot{\underline{F}}_0 = \sum_j m_j \left\{ \frac{\ddot{\underline{r}}_{ij}}{r_{ij}^3} - 6\dot{\underline{r}}_{ij} \frac{(\underline{r}_{ij} \cdot \dot{\underline{r}}_{ij})}{r_{ij}^5} + \right.$$

$$\left. \frac{3\underline{r}_{ij}}{r_{ij}^5} \left[\frac{5(\underline{r}_{ij} \cdot \dot{\underline{r}}_{ij})^2}{r_{ij}^2} - \dot{\underline{r}}_{ij} \cdot \dot{\underline{r}}_{ij} - \underline{r}_{ij} \cdot \ddot{\underline{r}}_{ij} \right] \right\}$$

(18)

$$\dddot{\underline{F}}_0 = - \sum_j m_j \left\{ \frac{\dddot{\underline{r}}_{ij}}{r_{ij}^3} - 9\ddot{\underline{r}}_{ij} \frac{(\underline{r}_{ij} - \dot{\underline{r}}_{ij})}{r_{ij}^5} - \right.$$

$$\frac{\dot{\underline{r}}_{ij}}{r_{ij}^5} \left[9\dot{\underline{r}}_{ij} \cdot \ddot{\underline{r}}_{ij} + 9\underline{r}_{ij} \cdot \dddot{\underline{r}}_{ij} - 45\frac{(\underline{r}_{ij} \cdot \dot{\underline{r}}_{ij})^2}{r_{ij}^2} \right] -$$

$$\frac{\underline{r}_{ij}}{r_{ij}^5} \left[3\underline{r}_{ij} \cdot \ddddot{\underline{r}}_{ij} + 9\ddot{\underline{r}}_{ij} \cdot \dddot{\underline{r}}_{ij} - 45\frac{(\underline{r}_{ij} \cdot \dot{\underline{r}}_{ij})(\underline{r}_{ij} \cdot \ddot{\underline{r}}_{ij})}{r_{ij}^2} \right.$$

$$\left. \left. - 45\frac{(\underline{r}_{ij} \cdot \ddot{\underline{r}}_{ij})(\dot{\underline{r}}_{ij} \cdot \ddot{\underline{r}}_{ij})}{r_{ij}^2} + 105\frac{(\underline{r}_{ij} \cdot \ddot{\underline{r}}_{ij})^3}{r_{ij}^4} \right] \right\}$$

The second and third derivatives in equation (3.18) are readily determined once all the current forces and the corresponding first derivatives have been found. A softened potential, of the form $\left[r_{ij}^2 + \varepsilon^2\right]^{1/2}$ can be introduced into the terms in the denominator of equation (3.18).

Initial time-steps δt_i have to be allocated to each particle. Aarseths' uses (Aarseth 1972)

$$\delta t_4^3 = \eta \frac{\underline{F}_0}{1/6\,\dddot{\underline{F}}_0} \qquad (3.19)$$

where η specifies a permissible relative change of force during new step. Equation (3.19) is independent of mass and has the property of preserving relative accuracy of each orbit during close encounters by reducing the integration interval. The integration, though begins at t=0, backward times have to be initialized for general formulation. This initialization is done by

$$\delta t_k = -k\,\delta t_4 \quad (k = 1, 2, 3) \qquad (3.20)$$

Then the conversion to polynomial derivatives is obtained by inverting equation (3.17) to order $\dddot{\underline{F}}_0$ giving

$$\underline{D}^{(1)} = \dot{\underline{F}}_0 - \frac{1}{2}\ddot{\underline{F}}_0\delta t_3 + \frac{1}{6}\dddot{\underline{F}}_0\delta t_3^2 \qquad (3.21)$$

$$\underline{D}^{(2)} = \frac{1}{2}\ddot{\underline{F}}_0\frac{(\delta t_2 + \delta t_3)}{\delta t_3} - \frac{1}{6}\dddot{\underline{F}}_0\frac{(\delta t_2 + 2\delta t_3)(\delta t_2 + \delta t_3)}{\delta t_3}$$

$$\underline{D}^{(3)} = \frac{\underline{D}^2\,\delta t_2^2 - \delta t_1\delta t_3}{(\delta t_2 + \delta t_3)\delta t_2\delta t_3} + \frac{1}{6}\dddot{\underline{F}}_0\frac{(\delta t_1 + \delta t_2 + \delta t_3)(\delta t_1 + \delta t_2)}{\delta t_2\delta t_3}$$

The choice of a fourth-order polynomial representation is a

compromise between efficieny and programming effort, however involving complexities of combining two force polynomials. Aarseth uses an individual time step method to integrate the equations of motion. The individual time-step method requires a total of 30 variables per particle as follows: m, $\underline{r}(t_0)$, $\underline{\dot{r}}(t)$ $\underline{V}$, $\underline{F}$, $\underline{\dot{F}}_0$, $\underline{D}^1$, $\underline{D}^2$, $\underline{D}^3$, δt, t_0, t_1, t_2, t_3.

We ran Aarseth's code with N=100 particles. The main results of these test runs can be summarized as follows:

(1) The accuracy of the Aarseth's code is very good. The fractional change in energy E of the system, $\frac{\Delta E}{E}$ was less than 10^{-5} per time step. This kind of accuracy was not achieved in any of the algorithms we tested later. Our own code gave $\frac{\Delta E}{E} \sim 1-2\%$.

(2) Though Aarseth's code is noted for its accuracy, there were a lot of problems connected with it. The main problem being, the code forces binary formations. We discovered that the code actually encourages close encounters, which one wants to avoid in an N-body calculation and the results of these close encounters is reduction of the relaxation time of the system of the system and ~~also~~ forces the binary formation. Aarseth's code is suitable to study stellar systems like globular clusters, where close encounters play a dominant role in their evolution. In a galaxy, such close encounters are not present and should be avoided. We also found out that when the code is made to run for a sufficient number of crossing times, a spiral kind of structure begins to

appear in the system, which started off a spherically symmetric model initially. This spiral structure is due to numerics and nothing to do with the real dynamics of the system. In the kind of problem we are interested in, we want the galaxy to be stable and not evolve, in the time scales of interest to us.

Another problem with the code was, the force calculations, carried out as shown in the last section are too complicated - that is, the integration routine, though extremely accurate, cannot be easily modified. Moreover, the algorithm is too difficult to vectorize, which is necessary if one wants to run the simulations on super computers like the Cray.

For a model galaxy having 500 particles, our test runs showed that to cover two crossing times, this code needed 2 hours 32 minutes of CPU time on the Gould 32/97. This showed that if the particle number if increased, CPU times required were beyond our budget. Also, it was not very easy to change this full N-body code to RNB code, because of the complicated force calculations.

So instead of using Aarseth's code which was ready and available, we decided to write our own N-body code. To find an efficient numerical integrator method, we tested various finite difference schemes such as the Runge-kutta and predictor-corrector methods, various hybrid methods which combined both the schemes and finally selected a method which was appropriate for us.

The various algorithms used for our tests are discussed

below. These can be found in any numerical analysis book [Ralston & Rabinowitz] and we found that most of these methods were simple and relatively easy to handle than the Aarseth's fourth-order polynomial scheme.

The finite-difference schemes for solving ordinary differential equations

The motions of the N-bodies are described by the differential equations

$$\frac{d\underline{v}}{dt} = \underline{F} \qquad (3.22)$$

and

$$\frac{d\underline{x}}{dt} = \underline{v} \qquad (3.23)$$

where

$\underline{F}$, $\underline{v}$, $\underline{x}$ stand for acceleration, velocity, position

In total, we have to solve 6N such diffeential equations. The various finite-difference methods that could be used for integrating numerically the above equations for step-size h are:

(1) The Runge-Kutta methods

$$y_{k+1} = y_k + \frac{1}{2}\left[s_1 + s_2\right]$$

$$s_1 = h f(x_k, y_k)$$

$$s_2 = h f\left(x_k + \frac{1}{2}h, y + \frac{1}{2}s_1\right)$$

Second-order Runge-Kutta

$$y_{k+1} = y_k + \frac{1}{6}\left[S_1 + 4S_2 + S_3\right]$$

$$S_1 = h f(x_k, y_k)$$

$$S_2 = h f\left(x_k + \tfrac{1}{2}h,\ y_k + \tfrac{1}{2}S_1\right)$$

$$S_3 = h f(x_k + h,\ y_k - S_1 + 2S_2)$$

Third-order Runge-Kutta

$$y_{k+1} = y_k + \frac{1}{6}\left(S_1 + 2S_2 + 2S_3 + S_4\right)$$

$$S_1 = h f(x_k, y_k)$$

$$S_2 = h f\left(x_k + \tfrac{1}{2}h,\ y_k + \tfrac{1}{2}S_1\right)$$

$$S_3 = h f\left(x_k + \tfrac{1}{2}h,\ y_k + \tfrac{1}{2}S_2\right)$$

$$S_4 = h f(x_k + h,\ y_k + S_3)$$

Fourth-order Runge-Kutta

The differential equation solved in the above methods is $\frac{dy}{dx} = f(x,y)$.

These methods have to be applied to $\underline{v}$ and $\underline{r}$ separately.

[Equations 3.22 and 3.23].

(2) Predictor-Corrector methods

The predictor-corrector methods we tested to solve equations (3.22) and (3.23) were:

Predictor:

$$r_{k+1} = r_k + h V_k$$

$$V_{k+1} = V_k + h F_k$$

Second-order mid-point Predictor-Corrector

Corrector:

$$r_{k+1} = r_k + \frac{h}{2}\left[V_k + V_{k+1}\right]$$

$$V_{k+1} = V_k + \frac{h}{2}\left[F_k + F_{k+1}\right]$$

$$v_{k+1} = v_k + h F_k$$

$$r_{k+1} = r_k + \frac{h}{2}\left[v_k + v_{k+1}\right]$$

Hybrid I

$$v_{k+1} = v_k + \frac{h}{2}\left[F_k + F_{k+1}\right]$$

$$r_{k+1/2} = r_k + \frac{h}{2} v_k$$

$$v_{k+1} = v_k + h F_{k+1/2}$$

Hybrid II

$$r_{k+1} = r_k + \frac{h}{2}\left[v_k + v_{k+1}\right]$$

Table V gives the comparision of methods of the various difference schemes used by us to solve the equations of motion.

TABLE V

METHOD	LOCAL ERROR	GLOBAL ERROR	FUNCTION eval/step	STABILITY	ACCURACY
2nd order Runge-Kutta	$0(h^3)$	$0(h^2)$	2	poor	10^{-2}
3rd order Runge-Kutta	$0(h^4)$	$0(h^3)$	3	poor	10^{-2}
4th order Runge-Kutta	$0(h^5)$	$0(h^4)$	4	good	10^{-4}
2nd order predictor-corrector	$0(h^3)$	$0(h^2)$	2	good	10^{-1}
Hybrid I	$0(h^3)$	$0(h^2)$	2	good	10^{-2}
Hybrid II	$0(h^3)$	$0(h^2)$	2	good	10^{-3}

To check the efficiency and accuracy of each difference scheme, we evolved just one test particle of mass m in a central force field. Conservation of energy and angular momentum were taken as the tests for accuracy. For simplicity we have restricted the motion to (X - Y) plane and in all the runs we have taken the central galaxy mass M=1 and the gravitational constant G=1. The equation of motion for the particle to be integrated is just

$$\ddot{\underline{r}} = -\frac{\underline{r}}{|r|^3} \qquad (3.24)$$

As a standard test, we chose an elliptical orbit which is close to the gravitational radius ($r = 2m = 2$) so that the run-times are short, but far enough away so that $1/r^2$ effects are not present. The time steps were identical in all cases and derived from $\Delta t < \varepsilon \frac{m}{V^3}$ for velocity V.

A series of graphs (figures 16 – 21) using different differencing schemes to solve the problem [equation 3.24] are presented. The method used in each is shown in the figures. Graphs showing the energy and angular momemtum conservation in each method are also shown. The results from these test runs can be summarized as:

(1) A 2nd order Runge-Kutta method is unstable. Conservation of energy and angular momemtum using this method is poor as can be seen from the figure 16.

(2) A 2nd order midpoint predictor-corrector method is unstable also [figure 17]. In this case, the conservation of energy and angular momentum is of the order of 10^{-1}, which indicates the poor accuracy of this method.

(3) A 3rd order Runge-Kutta method seems better than the earlier two schemes. The orbit [figure 18] of the particle looks quite

SECOND- ORDER RUNGE KUTTA

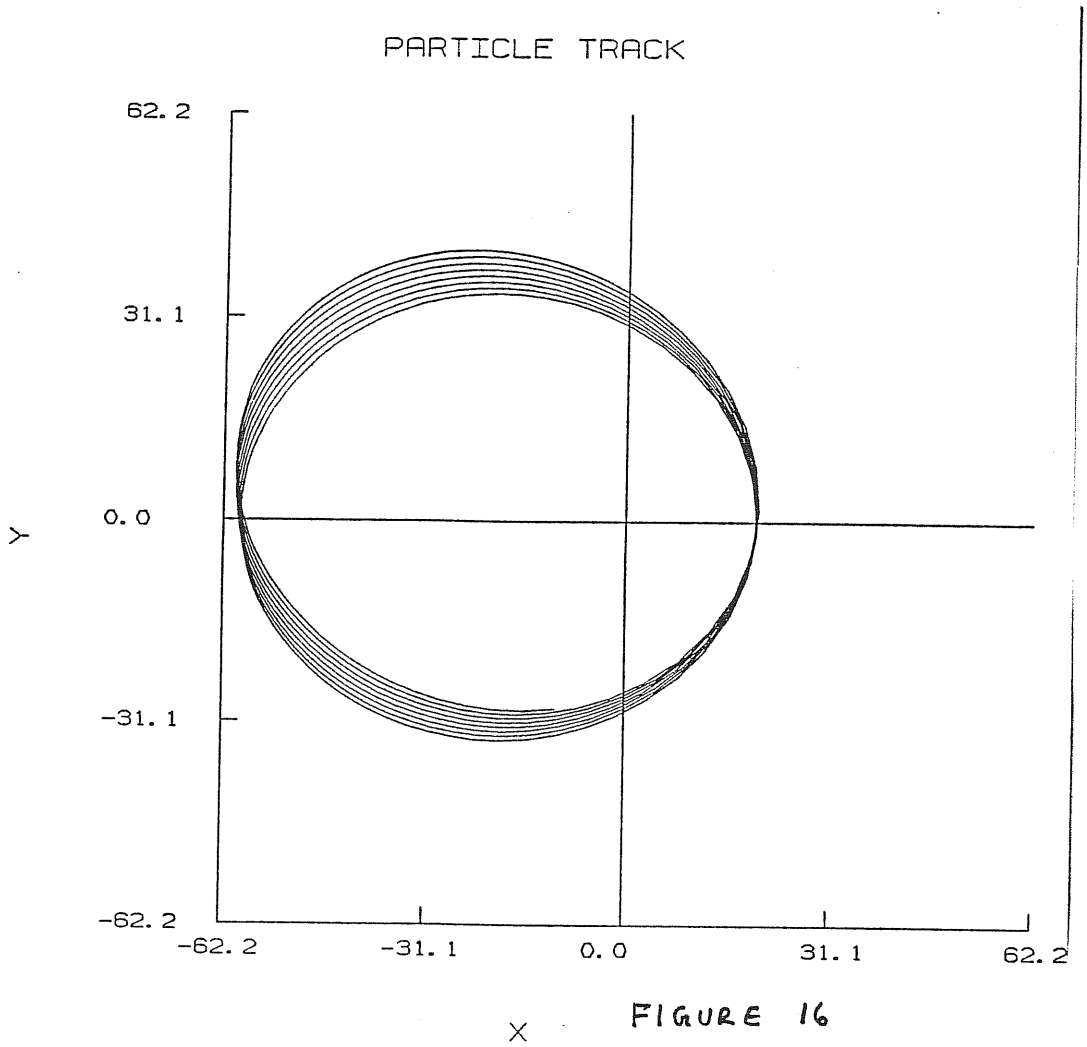

FIGURE 16

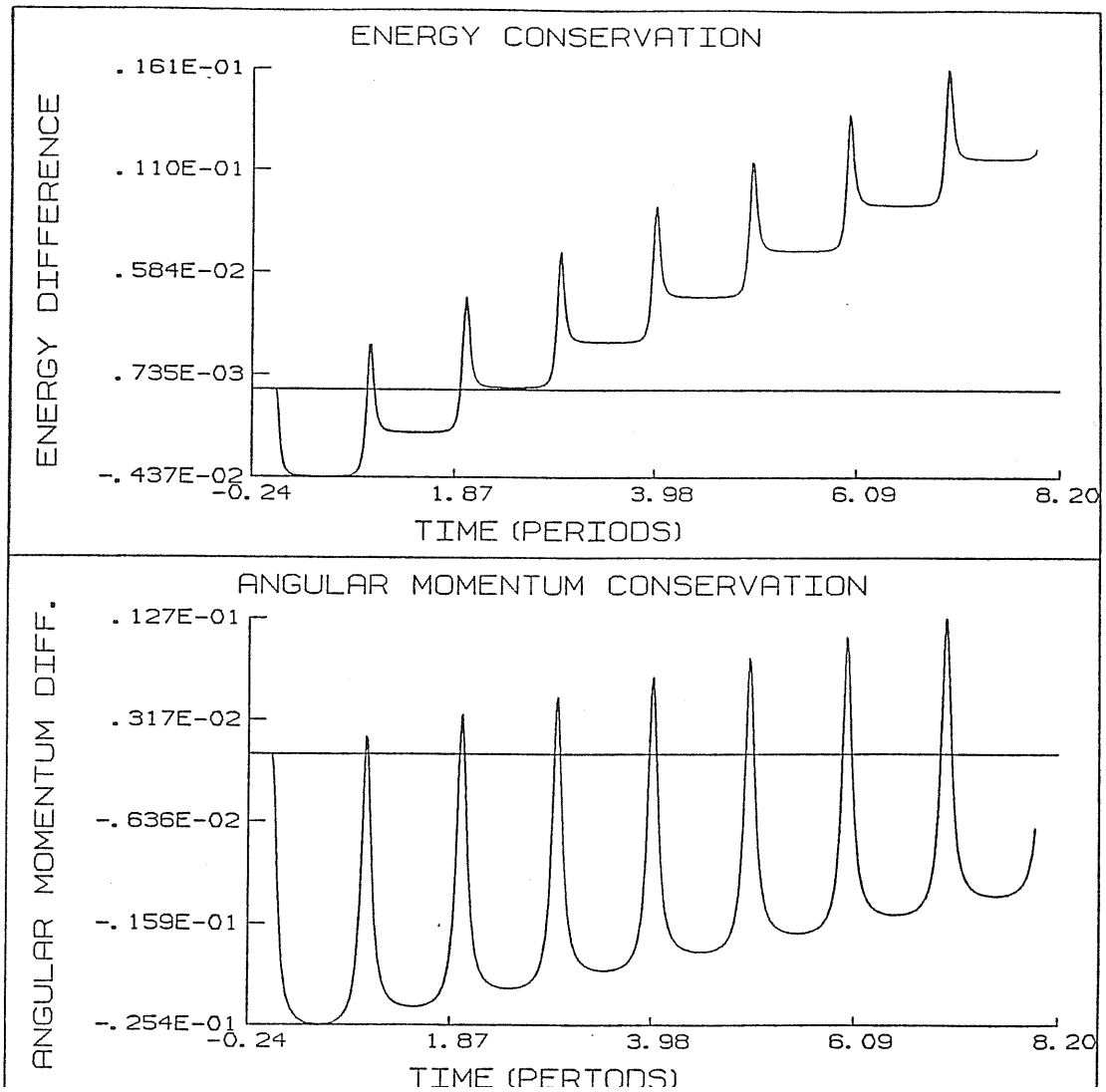

SECOND-ORDER [illegible] PREDICTOR-CORRECTOR

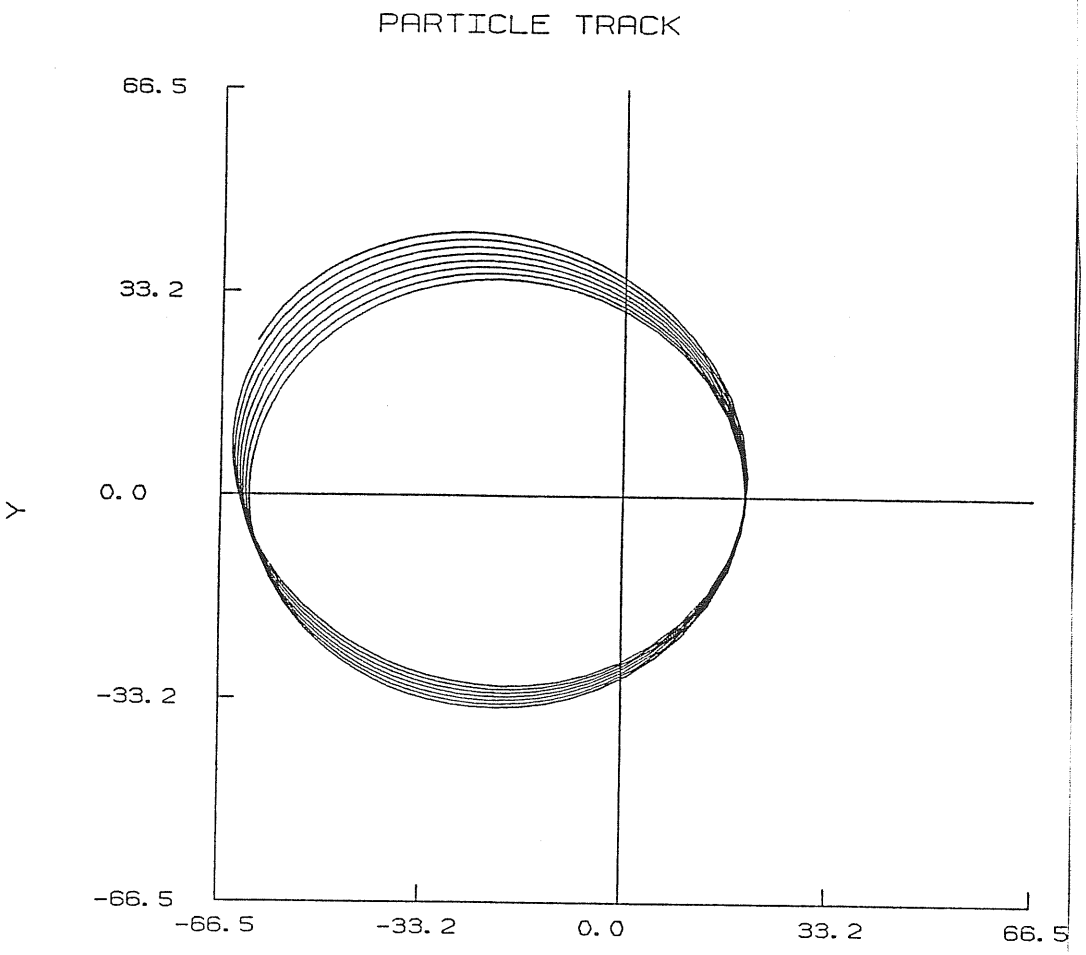

FIGURE 17

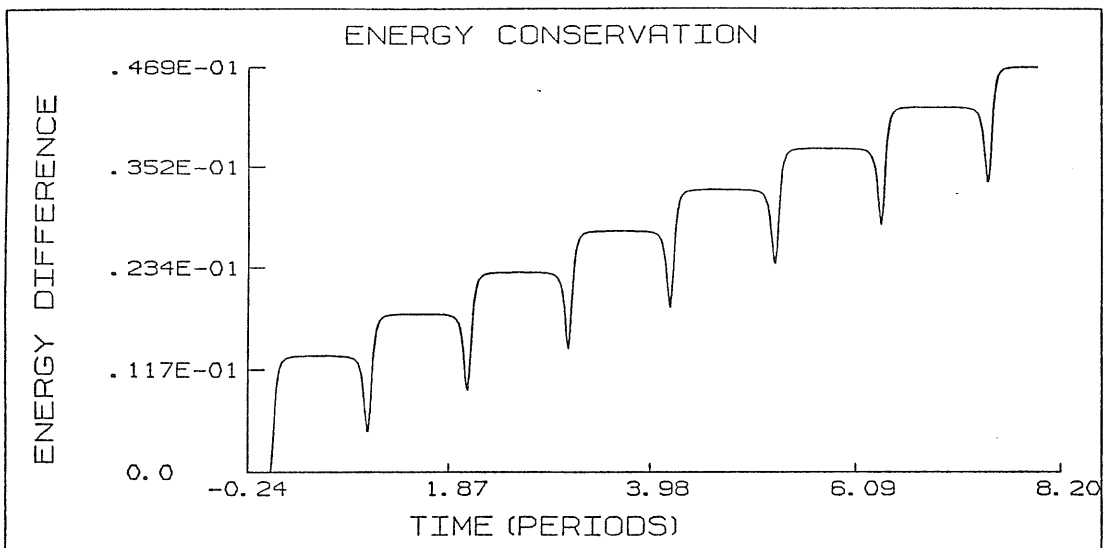

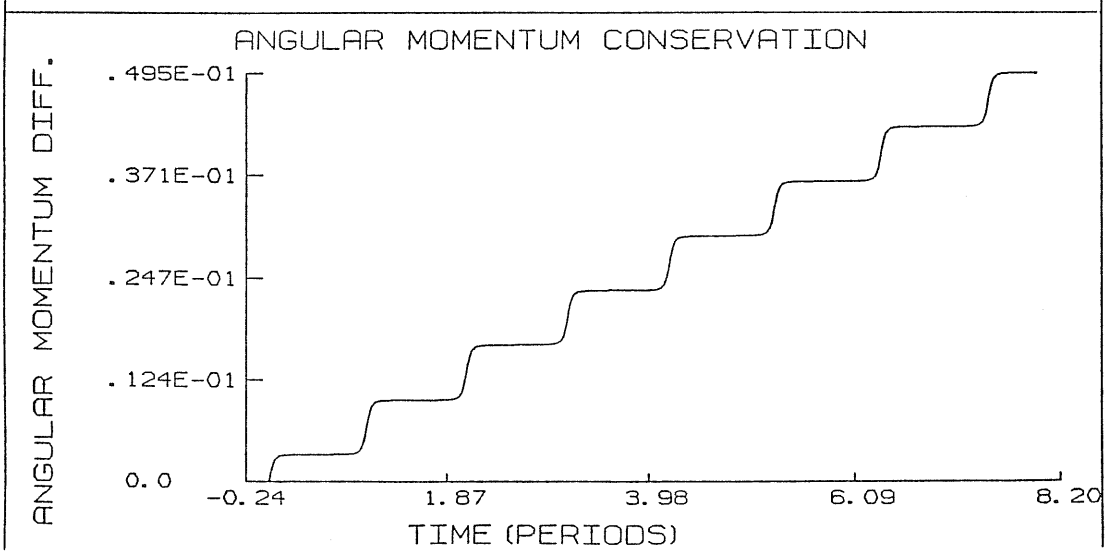

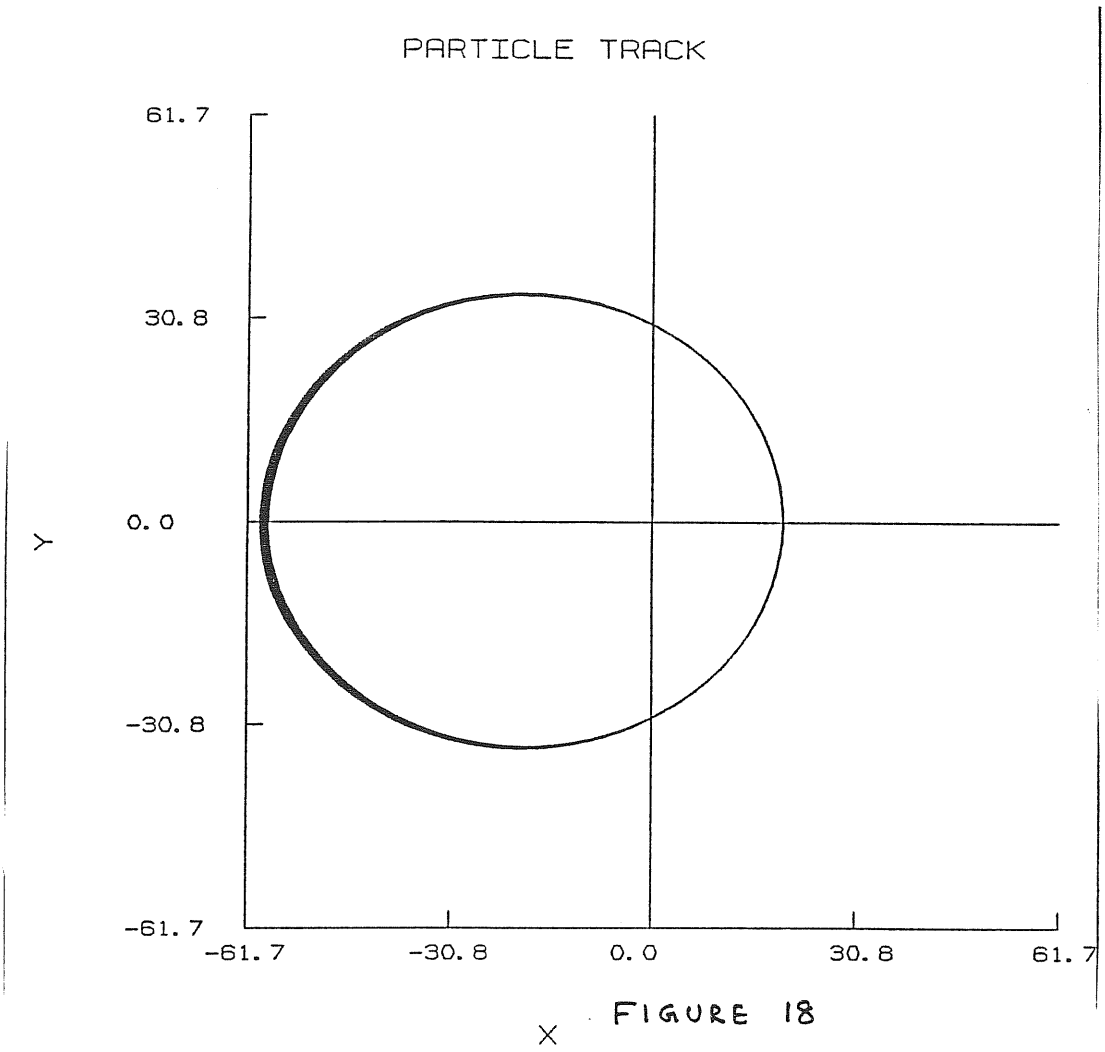
PARTICLE TRACK
61.7
30.8
0.0
-30.8
-61.7
Y
-61.7
-30.8
0.0
30.8
61.7
X

FIGURE 18

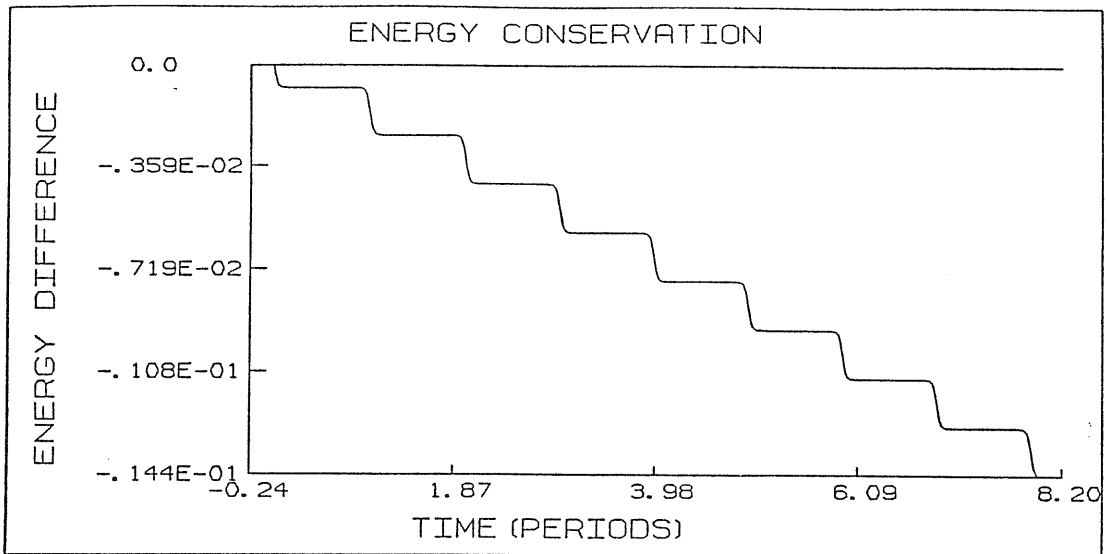
ENERGY CONSERVATION
ENERGY DIFFERENCE
0.0
-.359E-02
-.719E-02
-.108E-01
-.144E-01
-0.24
1.87
3.98
6.09
8.20
TIME (PERIODS)

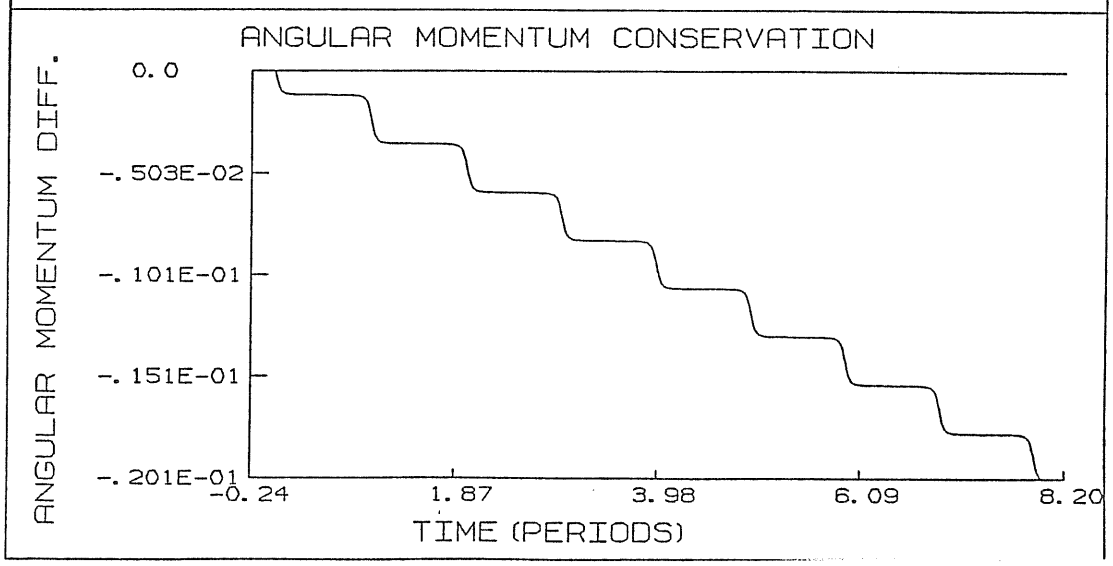
ANGULAR MOMENTUM CONSERVATION
ANGULAR MOMENTUM DIFF.
0.0
-.503E-02
-.101E-01
-.151E-01
-.201E-01
-0.24
1.87
3.98
6.09
8.20
TIME (PERIODS)

stable and the energy and angular momentum conservation in this case is of the order 10^{-2}.

(4) A 4^{th} order Runge-Kutta method worked extremely well. The orbit was extremely stable [figure 19] and the energy and angular momentum conservation were of the order of 10^{-5} In this method however, we used a scheme that predicts ahead and finally averages in the last step, making it a partly predictor-corrector like scheme. In our test runs, we decided that this was the most stable and accurate out of all the other methods but this has one serious drawback. It takes a longer time to run than other schemes and since speed in computation was one of the main criteria for the choice of an integrator, we decided not to use this method. The wiggle in the graphs for energy and angular momentum curves is because machine precision is being reached and showing up as noise in the last digit.

(5) The hybrid methods, schemes Hybrid I and Hybrid II both seemed stable and the accuracy was around 10^{-3} in each case. These methods are fast and in the case of Hybrid II, the force calculations, the right hand side of the equation of motion is called only once at each time step. Since the force calculations are the longest in the code, calling it only once means a great saving in computational time. We felt that though the 4^{th} order Runge-Kutta method is better in accuracy and stability by an order of magnitude, the Hybrid methods were better suitable to the kind of problems where a large number of particles and hence a number of differential equations have to be solved. In both the Hybrid methods, angular momentum is conserved to machine precision.

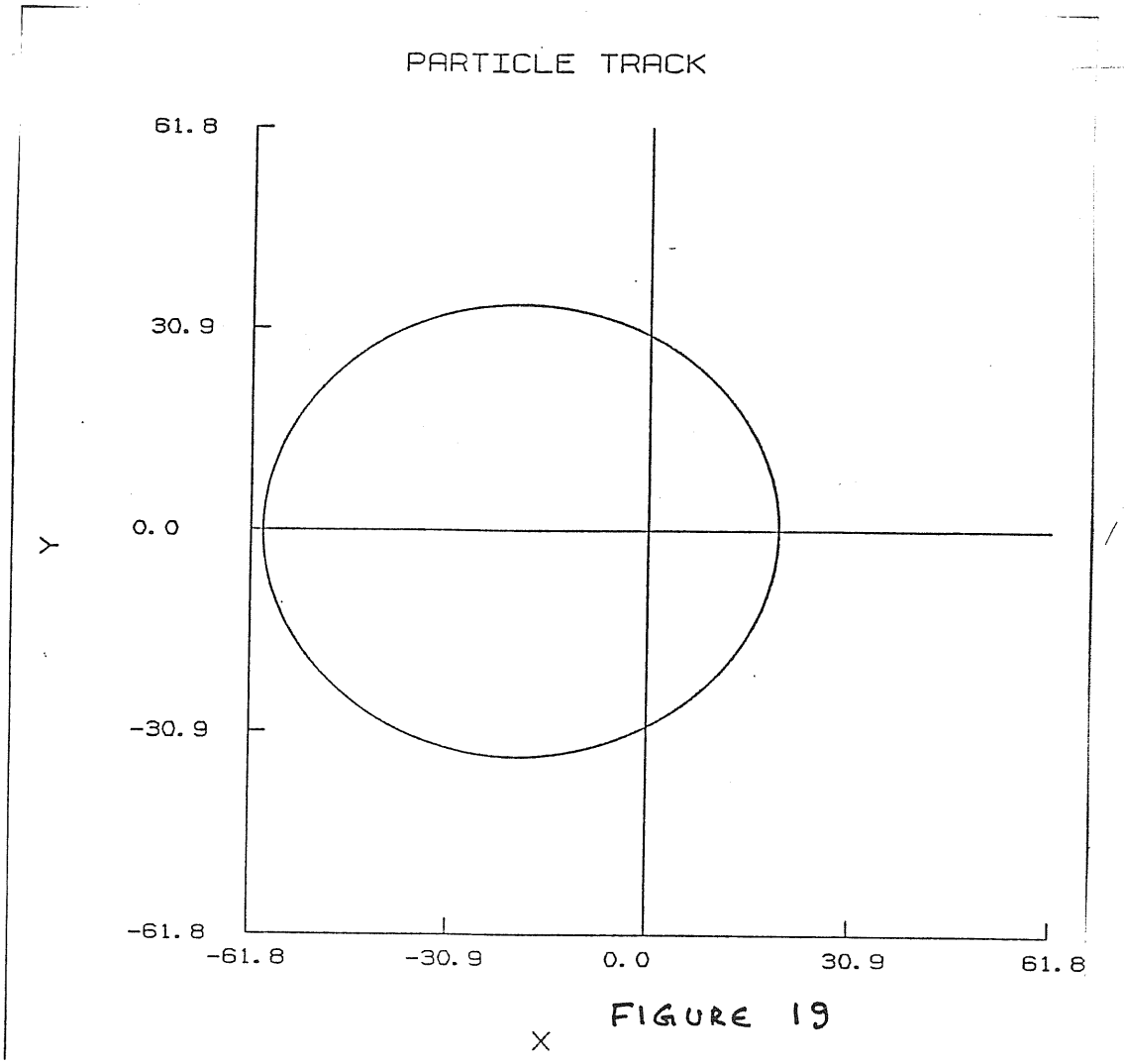
PARTICLE TRACK
61.8
30.9
0.0
-30.9
-61.8
Y
-61.8
-30.9
0.0
30.9
61.8
X

FIGURE 19

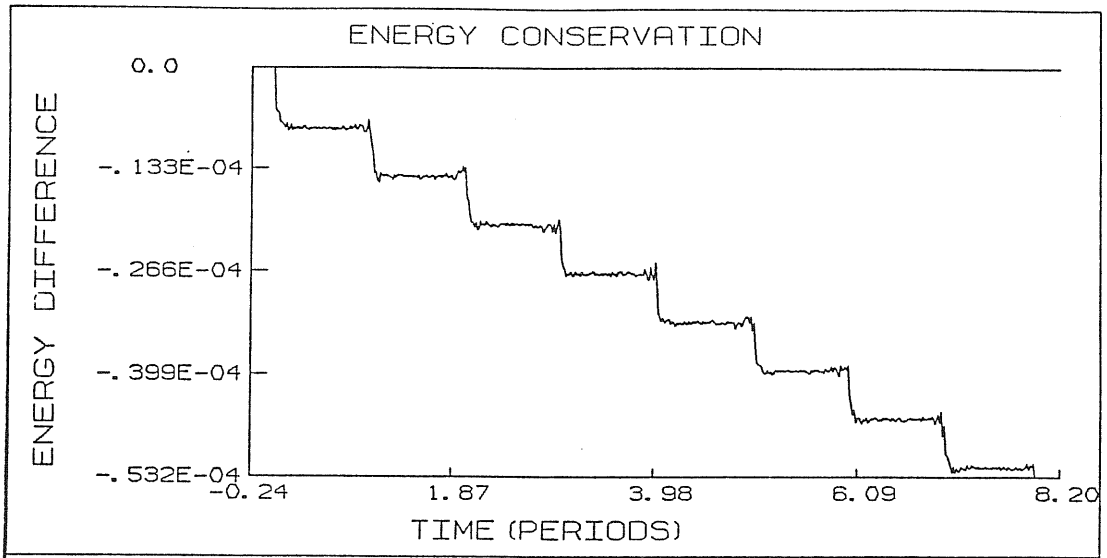
ENERGY CONSERVATION
ENERGY DIFFERENCE
0.0
-.133E-04
-.266E-04
-.399E-04
-.532E-04
-0.24
1.87
3.98
6.09
8.20
TIME (PERIODS)

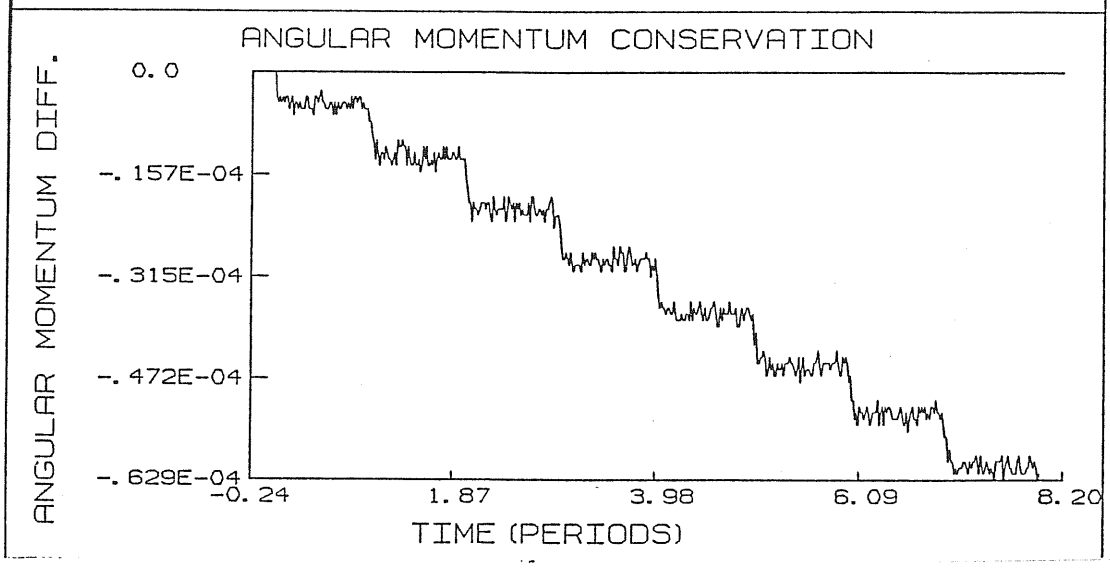
ANGULAR MOMENTUM CONSERVATION
ANGULAR MOMENTUM DIFF.
0.0
-.157E-04
-.315E-04
-.472E-04
-.629E-04
-0.24
1.87
3.98
6.09
8.20
TIME (PERIODS)

HYBRID I

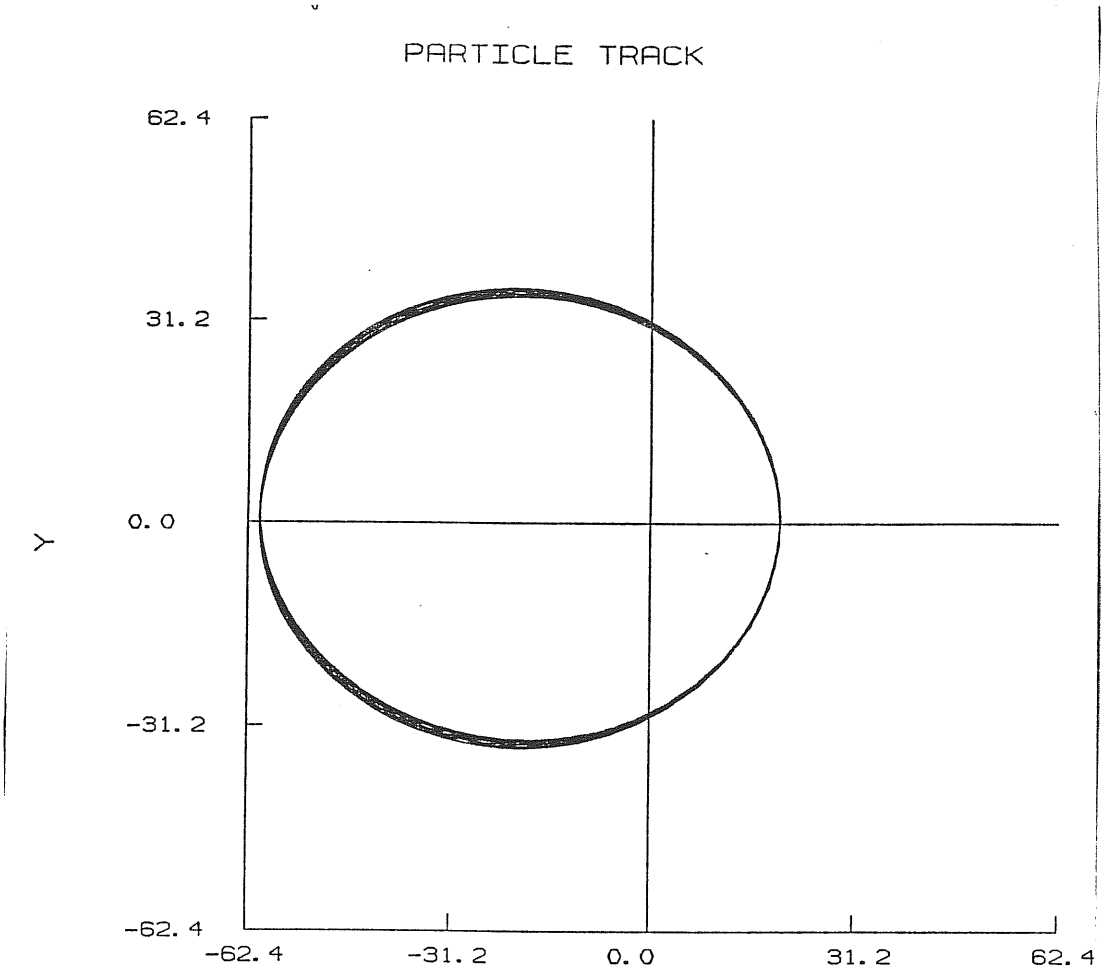

FIGURE 20

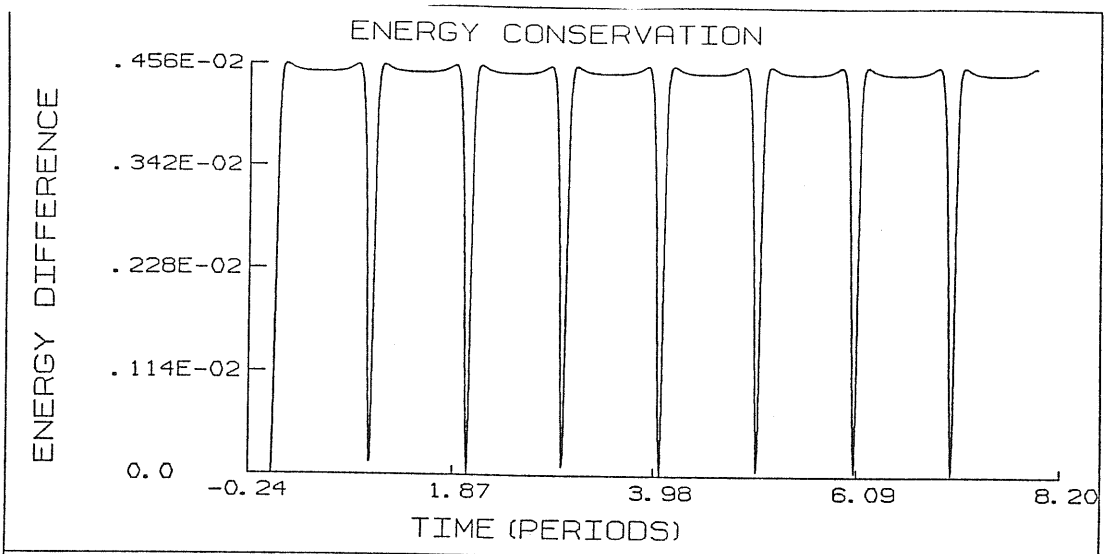

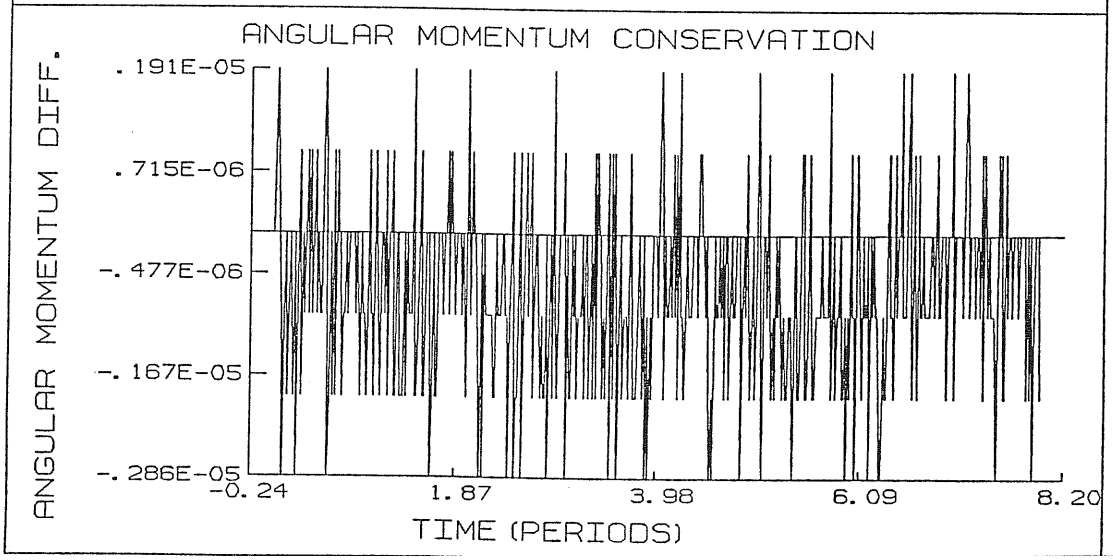

HYBRID II

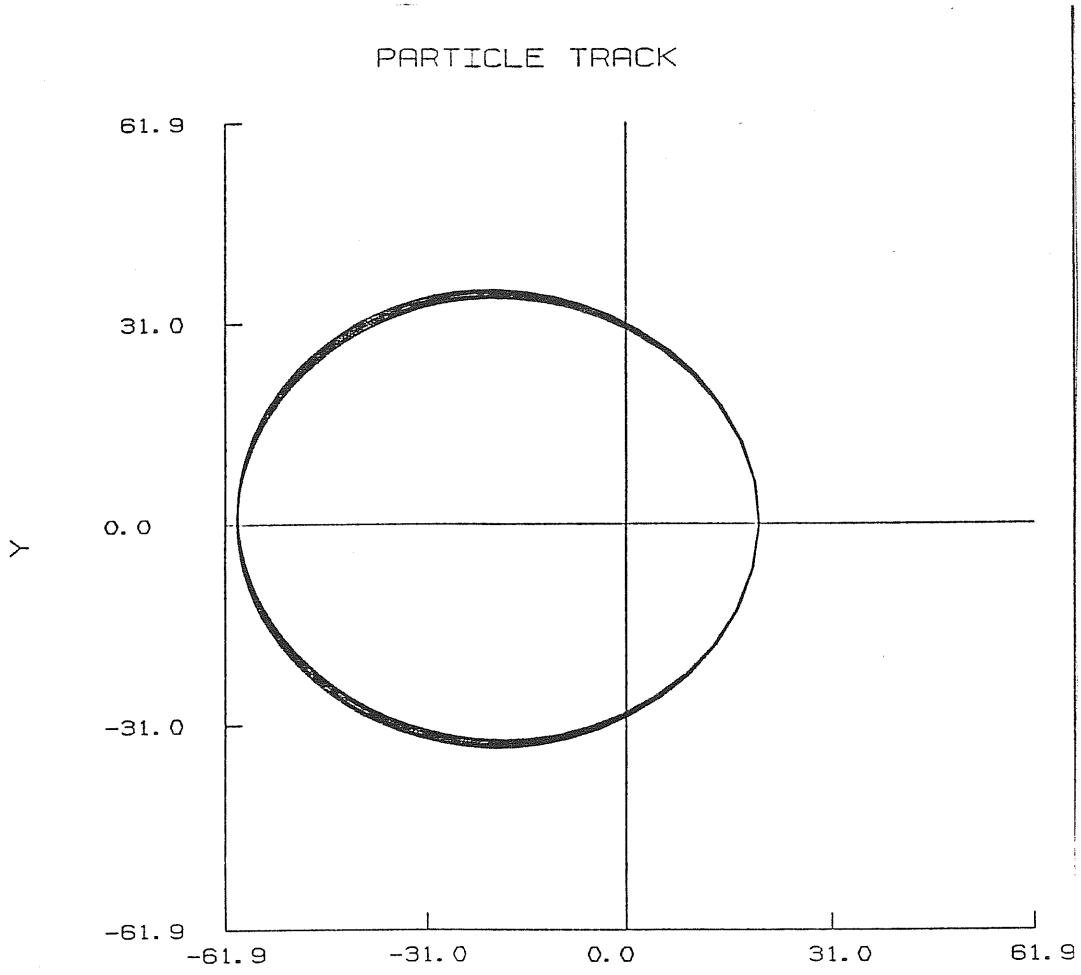

FIGURE 21

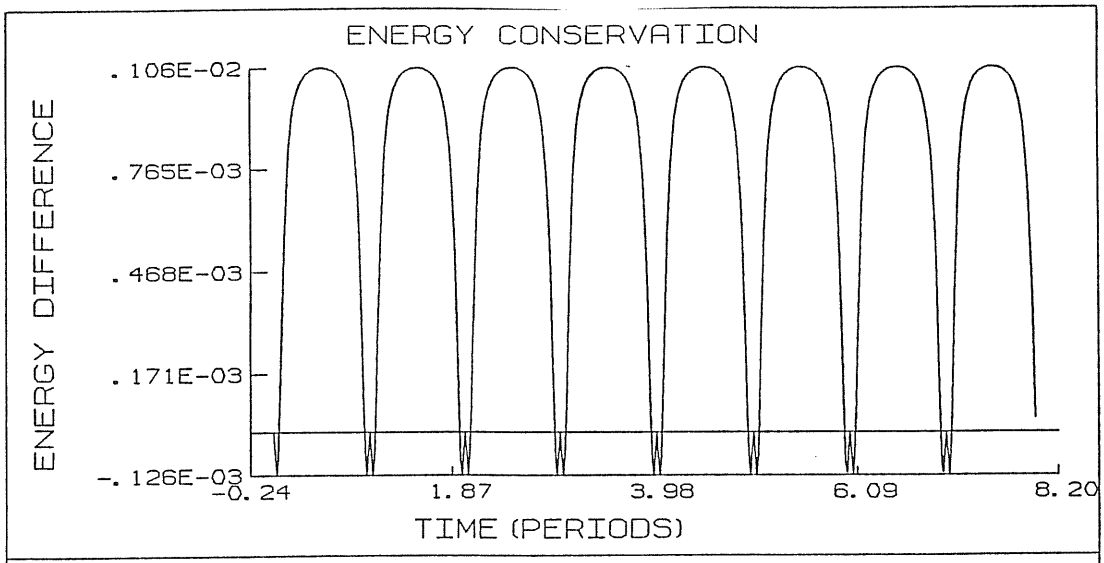

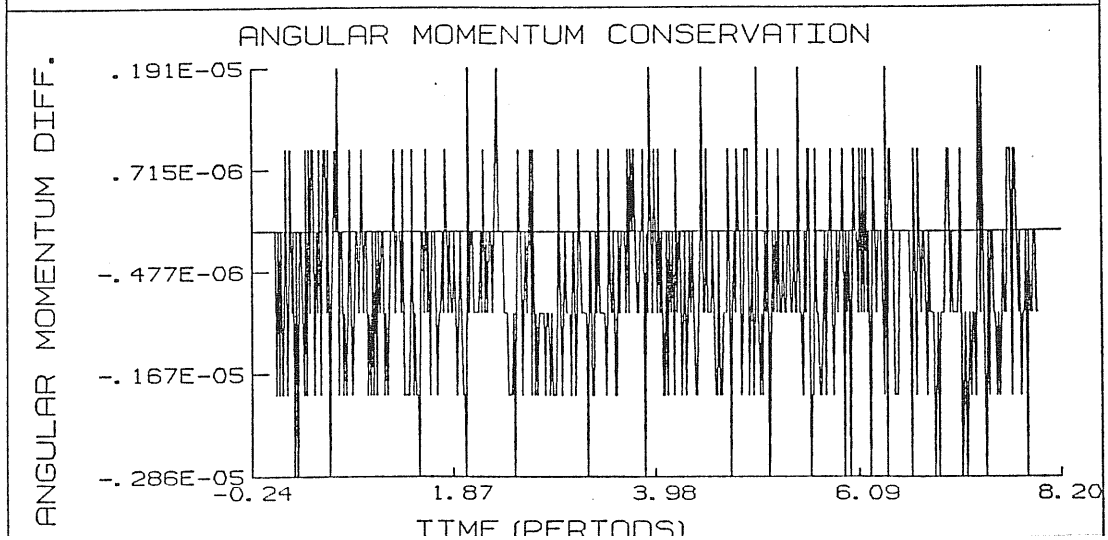

III.5 The Algorithm

The method finally chosen by us to be used in our N-body codes, both RNB and full N-body programs was Hybrid II, but used as follows:

$$V_{k+\frac{1}{2}} = V_k + \frac{h}{2} F_k$$

$$r_{k+1} = r_k + h * V_{k+1/2} \qquad (3.25)$$

$$V_{k+1} = V_k + \frac{h}{2} * [F_k + F_{k+1}]$$

The energy and angular momemtum conservation was of the order 10^{-3} in this case and the choice of step-size was taken variable and was determined by the maximum velocity or acceleration. All the simulations were performed on the Gould 32/97 and each simulation lasted around 3 hours for 5000 particles in the case of RNB code.

CHAPTER FOUR

GALAXY MODELS AND INITIAL CONDITIONS

We developed the 'semi-restricted N-body code' (RNB) to study the action of dynamical friction on globular clusters orbiting in galaxies. As discussed before such codes result in great saving of computational time. We propose to study the evolution of the orbits of the globular clusters in spiral and elliptical galaxies and compare the decay of the orbits due dynamical friction in both types of galaxies. Observations of globular clusters in galaxies have shown that the luminosity function of these systems in elliptical galaxies is not of the same form as that for the globular clusters in spiral galaxies (van den Bergh, Pritchet and Grillmair 1985), assuming that the two functions were of the same form primordially. The two luminosity functions are different in the sense that more bright, hence massive globular clusters are seen in elliptical galaxies than in spirals. Dynamical friction is a mechanism that acts preferentially on massive objects leading to their destruction. The absence of massive globular clusters in spiral galaxies seem to suggest that dynamical friction is more enhanced here and therefore we should see larger decay rates for the clusters in these galaxies than for the globular clusters in elliptical galaxies. A numerical work where a wide range of orbital parameters (initial orbital radius, eccentricity and cluster mass) could be explored, helps in studying and comparing these decay rates.

The most striking difference between elliptical and spiral

galaxies is the presence of a disk component in the latter. This extra component in spirals might be responsible for the enhanced decay rate in the orbits of the globular clusters in these galaxies. Over a Hubble time therefore, the disks of spirals and the distribution of globular clusters might have altered significantly by the action of dynamical friction, leading to a luminosity function that is different than what is observed for globular clusters in elliptical galaxies.

To compare the decay rates of globular clusters and to understand the mechanism of dynamical friction in spirals and ellipticals it is necessary to model these galaxies as realistically as possible. Dynamical friction is the drag force exerted by the wake induced by the globular cluster as it moves in the field of stars in the galaxy. Since the interaction between the field stars and the cluster is gravitational, the force on the globular cluster can be inferred from the spatial distribution of the field stars. If the expectation value of this force is calculated by averaging over an ensemble, then it can be concluded that the density of the field stars cannot be uniform if there is to be dynamical friction. In the code, we have to compute the drag force on the globular cluster from the perturbations it causes in the density distribution of the galaxy in which it is orbiting. This requires the knowledge of the complete density distribution in the galaxy and a way to trace it as accurately as possible. We have chosen a large number of particles to trace the density in a given galaxy model and called these particles the " tracers ". These tracers interact gravitationally with the globular cluster and the back response of the perturbations caused by the cluster

as it moves among them determines the drag force on the globular cluster..

The RNB code chosen to study decay rates was broken up into three sub-systems. The first sub-system was the galaxy potential and the form of this potential was kept fixed in space and time. The second sub-system was the globular cluster, which was considered to be a point mass in most of our runs except in few cases where it is modelled as a spherical Plummer sphere. The final sub-system were the tracers, an N number of particles responsive to the forces imposed by the earlier two sub-systems. The assumption made here is that these tracer particles do not interact with one another. In doing so, we avoid the task of computing the N(N-1)/2 two-body forces and save computational time.

In this chapter, the discussion these three sub-systems will be given. Galaxy models and the calculation of the potentials for spiral and elliptical galaxy models will be presented in sections 1V.1 and 1V.2 respectively. In section 1V.3 the initial conditions for the tracer particles in spiral galaxies will be discussed. Section 1V.4 deals with the initial conditions for the tracers in elliptical galaxies. In section 1V.5 we discuss the Plummer models used for the globular clusters.

1V.1 The Spiral Galaxy Model and the Potential Calculations

We have desired to model the galaxy and obtain the potential as realistically as possible. The spiral galaxy models developed by us were based on the model given by Caldwell and Ostriker (1981)

for our Galaxy. The Caldwell and Ostriker model (henceforth C-O model) for the Galaxy consists of three components: the disk, the spheroid and the halo. We have computed the potentials for each of these components separately using the density distributions chosen for them. These potential calculations will be discussed separately for each component below.

(i) The Disk

The disks in late type spirals have exponential distribution of surface density given as (Freeman 1970)

$$\Sigma_D(r) = \Sigma_D(0)\, e^{-\alpha r} \qquad (4.1)$$

where r is the radial co-ordinate and
α is the exponential scale-length.

For a zero-thickness exponential disk in centrifugal equilibrium, Toomre (1963) wrote down the surface density $\Sigma(r)$ as the Bessel integral

$$\Sigma_D(r) = \int_0^\infty J_0(kr)\, k\, S(k)\, dk \qquad (4.2)$$

where

$$S(k) = \int_0^\infty J_0(kr)\, u\, \Sigma(u)\, du \qquad (4.3)$$

Using the Poisson's equation, the potential of such a disk can be found to be

$$\Phi_D(r, z) = -2\pi G \int_0^\infty J_0(kr)\, S(k) \exp(-k|z|)\, dk \qquad (4.4)$$

where (r,z) are the standard cylindrical co-ordinates.

The stars that take part in the spiral structure of a galaxy lie within a thin ellipsoid whose axis ratio is 20:1. Such a system can be treated quite accurately with the approximation of a thin disk, made of stars whose motion is confined to the plane. The action of dynamical friction due to the disk alone leads to an exchange of mass and energy between the disk and globular cluster. To compute dynamical friction due to the disk, to understand the processes that take place when the globular cluster is in the disk and also knowing that the disks in spirals are not really thin, we decided to use thick disks models in our calculations. The thickness of the disk, Z_D used in the code is the parameter that appears in the $Sech^2$ law

$$\rho_D(z) = \rho_0 \, Sech^2\left(\frac{z_D}{\beta}\right) \qquad (4.5)$$

The $Sech^2$ law is probably not a good model for the vertical density distribution at the outside radius of the disk (Bahcall and Casertano 1984), but we felt that Z_D is an adequate measure of the disk's thickness. Acted upon by the differential tidal force of the galaxy, globular clusters posses a physical limiting radius r_t, called the tidal radius beyond which the member stars of the globular cluster are no longer bound to the parent cluster. The typical values for $r_t \sim 150$ pc , which is lesser than the thickness observed for the disks in spirals. We have chosen the total thickness of the disk Z_D to be 1 Kpc. The disk scale-height β chosen by us was 0.7 Kpc (Caldwell and Ostriker 1981).

The disks used by us had a volume density given by

$$\rho_D(r,z) = \rho_0 e^{-\alpha r} e^{-\beta|z|} \qquad (4.6)$$

where (r,z) are the standard cylindrical co-ordinates

α and β are the disk's scale-length and height respectively.

Since the mass and light distribution in many spirals appears not to be truncated at the limits of the observations and the HII gas layers extend to large radii (Bosma 1983), we considered our disks to be extensive in the radial direction. We chose a cut-off radius R_D = 28 Kpc in the radial direction of the disk, which is the same distance at which we chose the galaxy's density to fall off to zero. The mass distribution in such a disk is given by

$$M_D(r) = 2\pi * 2 \int_0^{R_D} \rho_D(r,z)\, r\, dr\, dz \qquad (4.7)$$

Using equation (4.6) we get

$$M_D(r) = \frac{4\pi\rho_0}{\alpha^2\beta}\left[1 - e^{-\alpha R_D}(1+\alpha R_D)\right]\left[1 - e^{-\beta|z|}_{D}\right]$$

The potential of the disk can be obtained from the Poisson equation

$$\nabla^2 \Phi_D = -4\pi G \rho_D(r,z) \qquad (4.8)$$

To solve this equation, we have used numerical techniques, one of which was the Multi-grid methods developed by Achi Brandt (1977) for elliptic equations. The basic ideas and the techniques of the Multi-grid method are discussed in Appendix A.

We also used a direct numerical integrator to solve the Poisson's equation. Following a method similar to Toomre (1963), the potential of the disk using Fourier transforms can be written

down as

$$\Phi_D(r,z) = -\int_0^\infty dk \; \frac{K J_0(kr)}{[k^2+1]^{3/2}} \frac{\beta^2}{[\beta^2-k^2]} \left[\frac{e^{-k|z|}}{k} - \frac{e^{-\beta|z|}}{\beta}\right] \quad (4.9)$$

This expression for the potential (equation 4.9) is derived in Appendix B. The form of this potential is similar to the one used by Quinn and Goodman (1986) for the disks in their spiral galaxy models.

Equation (4.9) can now be integrated numerically to obtain the potential of the disk. To do so, we used the Gauss-Quadrature routine of the CERN library. The potentials obtained using both the methods, the multi-grid and the Gauss-Quadrature, were in close accord and gave a check on the numerical techniques employed by us. In our runs we had found that the multi-grid method took only 43 second to compute the potentials, while the Gauss-Quadrature integrator routine took 3 minutes and 41 seconds.. The multi-grid method is definitely advantageous as it is very fast.

The potentials computed numerically were stored on a grid (132*132) and were read into the RNB code directly.The resultant forces were computed in the RNB code itself. These force calculations will be discussed in detail in the next chapter.

The parameters used by us for the disk of our spiral galaxy are given in Table VI . The values chosen are the standard values for a typical Sb galaxy. (C-O model).

TABLE VI

Dimensional quantity	Symbol in the text	Standard value
Disk mass	M_D	$0.78 * 10^{11} M_\odot$
Disk scale-length	α	3.5 Kpc
Disk scale-height	β	0.7 Kpc
Radial extent	R_D	28 Kpc
Thickness	Z_D	1 Kpc

(ii) The Spheroid

The light profile in elliptical galaxies is fit fairly well by the Hubble law (Oemler 1976, Kormendy 1977)

$$\rho_{Sp}(r) = \frac{\rho_s}{\left[1+(r/r_s)^2\right]^{3/2}} \qquad (4.10)$$

where p_s and r_s are the spheroid density and radius respectively.

Since in the solar vicinity the Population II tracers follow a similar distribution (Oort 1965), we have chosen a similar density distribution for the spheroidal component of our spiral galaxy. The surface density of this component is given as

$$\Sigma_{Sp}(r) = \frac{\Sigma_s(0)}{\left[1+(r/r_s)\right]^2} \qquad (4.11)$$

There is evidence (Spinrad et.al. 1978) that at large radii, the surface brightness of galaxies falls off somewhat faster than given by the Hubble law but we felt that a cut-off to

the Hubble law is unnecessary since at these large radii the mass density in our spiral galaxy models is determined by the halo component and not by the spheroid. The dynamical fitting procedure thus would be quite insensitive to any outer cut-off of the spheroid component.

The mass distribution in the spheroid is given by

$$M_{sp}(r) = 4\pi \int_0^{R_{sp}} \rho(r)\, r^2\, dr \qquad (4.12)$$

Using equation (4.10) into this, we get

$$M_{sp}(r) = 4\pi \rho_s r_s^3 \left[\frac{-(r/r_s)}{\sqrt{1+(r/r_s)^2}} + \log\left(\frac{r}{r_s} + \sqrt{1+(r/r_s)^2} \right) \right] \qquad (4.13)$$

The potential for this component is

$$\Phi_{sp}(r) = -\frac{4\pi \rho_s r_s^3}{r} \left[\log\left(r/r_s + \sqrt{1+(r/r_s)^2} \right) \right] \qquad (4.14)$$

The force is then given by

$$\frac{\partial \Phi_{sp}}{\partial r} = \frac{4\pi \rho_s r_s^3}{r} \left[\frac{(r/r_s)}{\sqrt{1+(r/r_s)^2}} - \log\left(r/r_s + \sqrt{1+(r/r_s)^2} \right) \right] \qquad (4.15)$$

Equations (4.14) and (4.15) are derived in Appendix C.

The spheroidal component parameters used in the code are given in Table VII .

TABLE VII

Dimensional quantity	Symbol in the text	Standard values
Spheroid mass	M_S	$0.81 * 10^{11} M_O$
Extent	R_{Sp}	10 Kpc
Scale-length	r_s	0. 10311 Kpc

(iii) The Halo

Accurate rotation curves are now available for a number of galaxies, often extending well beyond the optical image of the galaxy. The rotation velocities are found not to decline in the outer edges of galaxies where no appreciable light is visible. (Faber and Gallagher 1979, V.C Rubin et. al. 1982).

The techniques by which the mass of a distance object is measured relies upon the Kepler's third law

$$GM = \gamma \times v^2 \qquad (4.16)$$

where r and v are the orbital radius and velocity of a test object respectively, which orbits a galaxy of mass M. This mass M can be determined by studying the orbits of globular clusters, stars or gas clouds at a distance from the center of the galaxy known as the Holmberg radius R_{Hol}. This radius is defined as the distance at which the surface brightness of an object reaches an apparent magnitude of 26.7 mag/sq.arc sec. It is a convenient measure of the optical extent of a galaxy. For a typical spiral galaxy, R_{Hol} 10-30 Kpc. If the luminous mass was the only constituent of a

galaxy, then we would expect the observed velocities to drop off as $r^{-1/2}$, as implied by equation (4.16). But the lack of decrease in rotational velocities out to large radii in galaxies suggests that the total mass interior to r, increases linearly with r and therefore the density goes as $\rho(r) \propto \frac{1}{r^2}$. This constancy of the rotational velocity curves is taken as an example for the " missing mass " problem in galaxies. This missing mass inferred from the rotational curves is found to be 3-10 times more than the luminous component. Kinematical studies on globular clusters in our Galaxy have shown that the halo of our Galaxy extends to at least 44 Kpc (Innanen, Harris and Webbink 1983). From the orbital dynamics of the Magellanic clouds, it was suggested that the halo of our Galaxy should extend to atleast 70 Kpc (Lin and Lynden-Bell 1982). Theoretically, Ostriker and Peebles (1973) had suggested that a massive halo is necessary to avoid bar-like instabilities in the disks of spiral galaxies and that the disks must be embedded in a stabilizing massive halo. Other evidences supporting massive halos though not as compelling as the galaxy rotation curves, comes from the studies of binary galaxies (Turner 1976; Peterson 1979). In our model of the spiral galaxy, we chose the halo to have a mass M_H

$$\frac{M_H}{M_D} \sim 3.0 \qquad (4.17)$$

and a cut-off at R_H = 28 Kpc. which is the same as the disk's radial extent. This cut-off is fixed in advance for each model rather than be treated as an adjustable parameter that is to be determined from observations.

A simple form for the density distribution in the halo

was chosen following based on the C-O model. This is

$$\rho_H(r) = \frac{\rho_h}{1+(r/r_h)^2} \qquad (4.18)$$

This density at large radii $r>>R_H$ approaches the density distribution of an isothermal sphere. The mass distribution in the halo is given by

$$M_H(r) = 4\pi\rho_h r_h^3 \left[\left(\frac{r}{r_h}\right) - \tan^{-1}(r/r_h)\right] \qquad (4.19)$$

The potential is obtained as

$$\Phi_H(r) = -4\pi\rho_h r_h^2 \left[1 - \frac{\tan^{-1}(r/r_h)}{(r/r_h)} - \frac{1}{2}\log\left[1+(r/r_h)^2\right]\right] \qquad (4.20)$$

and the force as

$$\frac{\partial\Phi_H(r)}{\partial r} = -\frac{4\pi\rho_h r_h^2}{r^2}\left[\frac{(r/r_h)^2}{1+(r/r_h)^2} + \frac{1}{1+(r/r_h)^2} - \frac{\tan^{-1}(r/r_h)}{(r/r_h)}\right] \qquad (4.21)$$

These expressions are derived in Appendix C.

The halo parameters used in the code are summarized in Table VIII.

TABLE VIII

Dimensional quantity	Symbol used in the text.	Standard values
Halo mass	M_H	$2.34 * 10^{11} M_o$
Extent	R_H	28 Kpc
Scale-length	r_h	7.812 Kpc

IV.2 The Elliptical Galaxy Model and the Potential Calculations

Elliptical galaxies are the simplest type of galaxies. All that was known until recently about these galaxies was that their isophotes were elliptical and that their smooth luminosity can be represented by a suitable function with just one or two parameters (Oemler 1976). There was also a small sample of measured velocity dispersions but these have shown to be systematically high (Richstone and Sargent 1972, Faber and Jackson 1976). These measurements in principle allow oblate, prolate or triaxial models for these galaxies.

The classification schemes for galaxies are based on smooth variation of properties between elliptical galaxies and the spheroidal component of spiral galaxies. Photographs of spirals show that both nearly oblate and prolate bulges exist. Nevertheless, all modelling of ellipticals has been done on the basis of assumed oblate spheroids with nearly isotropic velocity dispersions. Observations and theory both indicate however the need to explore alternative models.

Grillmair, Pritchet and van den Bergh (1986) have shown that dynamical friction on globular clusters in M87, a giant elliptical in the Virgo cluster is not important, based on the fact that they could not find any strong radial trend in the luminosity function of these clusters in M87. Evolutionary processes such as dynamical friction and tidal disruption of globular clusters produce a distribution of the globular clusters that is somewhat depleted near the core regions of galaxies. Grillmair, Pritchet and van den Bergh also found that large

orbital eccentricities (e >0.9) were needed in order for these processes to be effective in the inner regions of M87. This again supports the idea that dynamical friction is not large in M87.

There is however one complication that might affect this result regarding dynamical friction, which is that the shape of M87 might be triaxial. This was not considered by the above authors. In this case, a significant number of globular clusters would be on non-elliptical orbits that can make close approaches to the center of M87 and therefore enhance both dynamical friction and tidal disruptions. A detailed triaxial modelling of elliptical galaxies might therefore be necessary, which we intent to do at a later stage. For the present work, we used only the simplest models for our elliptical galaxies.

The surface brightness of ellipticals as a function of radial distance was first given by Hubble as

$$\Sigma(r) = \frac{\Sigma_e}{(1 + r/r_c)^2} \qquad (4.22)$$

where r_c is the core-radius.

The Hubble law is quite good for the inner portions of these galaxies but overestimates the surface brightness in the outer regions. The most widely used improvements on the Hubble's law are

(a) de vaucouleurs (1948) law:

$$\log(\Sigma) = \log(\Sigma_e) - 3.25\left[\left(\frac{r}{r_c}\right)^{1/4} - 1\right] \qquad (4.23)$$

(b) Hubble law modified by an exponential cut-off (Omeler 1976) ;

$$\Sigma(r) = \Sigma_e \frac{\exp\left[-(r/r_c)^2\right]}{(1 + r/r_c)^2} \qquad (4.24)$$

The constraint of isotropic velocity dispersions in elliptical galaxies has been a common feature of most models (Wilson 1975). The argument made was that elliptical galaxies are oblate spheroids whose collapse proceeded more rapidly along the axis of rotation than in the two co-ordinates supported by rotation. Detailed observational and theoretical studies have not been able to support this idea. Wilson found that he could not make galaxies flatter than E4 with radial intensity profiles which matched those of real galaxies. In addition, any model with isotropic dispersion flatter than E4 violates the Ostriker-Peebles stability criterion (Ostriker and Peebles 1973) and thus is probably unstable to the formation of a bar-like mode. Finally it seems difficult in the context of standard theories of galaxy formation to acquire more than about 1/3 of the angular momentum these models have. (Thuan and Gott 1977; Binney and Silk 1978 and Efsthathiou and Jones 1979). Recent observations (Bertola and Capaccioli 1975; Illingworth 1977; Schechter and Gunn 1979) have indicated that the flattening observed has to be due to global velocity anisotropy. We have not considered these details in the present work.

To model our elliptical galaxies, we have chosen the simplest case of a spheroid to represent the complete galaxy. This spheroid has a volume density distribution given by

$$\rho(r) = \frac{\rho_e}{\left[1 + (r/r_c)^2\right]^{3/2}} \qquad (4.25)$$

The core radius r_c was chosen to be 1/60 th of the total radial distance R_a(Aarseth and Binney 1978). The mass distribution is given by

$$M_{Gal}(r) = 4\pi \rho_e r_c^3 \left[- \frac{(r/r_c)}{\sqrt{1+(r/r_c)^2}} + \log\left(r/r_c + \sqrt{1+(r/r_c)^2} \right) \right] \quad (4.26)$$

The potential is given by

$$\Phi_{Gal}(r) = \frac{4\pi \rho_e r_c^3}{r} \left\{ \log\left(r/r_c + \sqrt{1+(r/r_c)^2} \right) \right\} \quad (4.27)$$

and the force by

$$\frac{\partial \Phi_{Gal}(r)}{\partial r} = \frac{4\pi \rho_c r_c^3}{r^2} \left[\frac{r/r_c}{\sqrt{1+(r/r_c)^2}} - \log\left(\frac{r}{r_c} + \sqrt{1+(r/r_c)^2} \right) \right] \quad (4.2$$

The elliptical galaxy and the spheroidal component of the spiral galaxy were modelled the same way in our calculations, as it was argued by de Vaucouleurs (1959) and Ostriker (1977) that at the heart of every spiral galaxy sits a small elliptical galaxy, around which the disk that dominates the light distribution is assembled. Another unknown factor of elliptical galaxies is whether they posses a halo component like the spiral galaxies. One might anticipate an increase in M/L towards outer regions also in elliptical galaxies but unfortunately observations are not definite to demonstrate that elliptical galaxies have halos. In our models, we chose not to introduce an halo component for the ellipticals.

The parameters used for our elliptical galaxy models are given in Table 1x

TABLE IX

Dimensional quantity	Symbol used in the text	Standard values
Mass of the galaxy	M_{Gal}	$4 * 10^{11} M_{\odot}$
Radius	R_{Gal}	28 Kpc
Core radius	r_c	0.5 Kpc

IV.3 Initial Conditions: Spiral Galaxies

The next sub-system to be considered in the RNB code is to obtain the positions and velocities for each of the N tracers of density in the galaxy. For most of our runs we had chosen N = 5000 particles. This number, though very small to represent the entire density of the galaxy with great resolution, we feel it is sufficient without running into memory shortage problems and other difficulties on the computer. As mentioned earlier, these tracers feel the forces imposed by the galaxy and the globular cluster but do not interact with one another. That is, we are neglecting the self-gravity of the multi-particle sub-system.

These tracer particles should follow the density distributions we had chosen for our spiral galaxy model. They move in the galaxy potential, which we have assumed to be fixed in space and time, and interact with the globular cluster orbiting in the galaxy. The back response of these tracers onto the globular cluster is the drag force which is responsible for the decay in the orbit of the globular cluster.

As discussed earlier, our spiral galaxy model has three

components.- the disk, spheroid and the halo. The N tracers are required to trace the density distributions considered for these three components.

Out of the total N = 5000 tracer particles, we had chosen the number of particles to represent the disk density, N_D to be 3000, the number of spheroid tracers, N_{SP} = 1000 and the tracers in the halo N_H = 1000. We will discuss the initial conditions, that is the positions and velocities for each of these particles which trace the density distribution for each component separately below.

(a) The Disk Density Tracers

The disk has the density distribution given by equation (4.6). The tracer particles in the disk should be given masses, positions and velocities such that they represent the disk upto large radii, in our case upto R_D = 28 Kpc. The mass distribution in the disk is given by equation (4.7). The tracer particles are either chosen to have equal masses or exponential masses that varies with the radius. In our runs, in order to represent the disk well at large radii with a limited number of particles (= 3000), we decided that our disk tracer particles should have masses that vary exponentially with radius. The positions of the tracer particles were computed in the following way.

Let

$$K = \frac{4\pi}{\alpha^2\beta}\left[1 - e^{-\alpha R_D}(1+\alpha R_D)\right]\left[1 - e^{-\beta|z_D|}\right] \qquad (4.29)$$

in the equation (4.7).

Then, we have

$$M_D(r) = \rho_0 K \qquad (4.30)$$

Let the mass of the disk be

$$(\text{total})\quad M_D = \Sigma m_d \qquad i = 1, \cdots N_D \qquad (4.31)$$

The next step is to distribute the particles in shells of thickness (Δr, Δz), where

$$\Delta r = \frac{R_D}{N_r} \quad \text{and} \quad \Delta z = \frac{z_D}{N_z} \qquad (4.32)$$

Here N_r and N_z are the number of shells chosen in the r and z directions respectively. In our runs, we had chosen N_r = 100 and N_z = 5.

The fraction of the disk's mass ΔM, in each shell is given by

$$\Delta M_D(r, r+\Delta r, z, z+\Delta z) = 2\pi \rho_0 e^{-\alpha r} e^{-\beta|z|} r\,\Delta r\,\Delta z \qquad (4.33)$$

$$\Delta M_D = n_0 m_d 2\pi r\,\Delta r\,\Delta z \qquad (4.34)$$

where n_0 is the number density of the particles.

From equation (4.34) it follows that

$$n_0 m_d = \rho_0 e^{-\alpha r} e^{-\beta|z|} \qquad (4.35)$$

where equation (4.35) follows from equation (4.33).

The mass of each tracer particle is then given by

$$m_d = \frac{\rho_0}{n_0} e^{-\alpha r} e^{-\beta|z|} \qquad (4.36)$$

$$\rho_0 = \frac{M_D(r)}{k} \qquad (4.37)$$

from equation (4.30).

We can write the total number of particles in the disk N_D, to be

$$N_D = \int_0^{R_D} n_0 \, 4\pi r \, dr \, dz \qquad (4.38)$$

which is

$$N_D = 2\pi n_0 R_D^2 z_D \qquad (4.39)$$

From this equation (4.39), we can get the number density n_0, as

$$n_0 = \frac{N_D}{2\pi R_D^2 z_D} \qquad (4.40)$$

Substituting equations (4.37) and (4.40) into equation (4.36) we get the mass of tracer particle to be

$$m_d = \frac{M}{K N_D} 2\pi R_D^2 z_D e^{-\alpha r} e^{-\beta|z|} \qquad (4.41)$$

where K is given by the equation (4.29). Then, number of tracer particles in each shell is given by

$$\Delta N_D = \frac{2 N_D r \, \Delta r \, \Delta z}{R_D^2 z_D} \qquad (4.42)$$

Knowing the number of particles to be present in each shell and also their masses, we then choose their positions randomly in each shell by using a random number generator provided on the Gould 32/97. Using this, first the particles in the vertical

direction z, of the disk were filled r fixed and then the radial direction of the disk was filled.

The next step is to determine the velocities for these tracer particles in the disk. This was done as follows. Initially, all the disk tracers were given a circular velocity such that they were in a centrifugal equilibrium with respect to the radial force in the disk. That is, the disk is initially considered to be cold, a zero velocity dispersion. Toomre's (1964) local criterion for suppression of all axisymmetric instabilities requires a minimum radial velocity dispersion, (a Gaussian distribution) given by

$$\sigma_{min} = \frac{3.36\, G\, \rho_0(r)}{K(r)} \qquad (4.43)$$

where G is the Gravitational constant

and K(r), is the epicyclic frequency defined by

$$K(r) = \frac{1}{m}\frac{\partial}{\partial r} F(r) + \frac{3v^2(r)}{r} \qquad (4.44)$$

Here, F(r) is the radial force in the plane at radius r.

The epicyclic frequency, K(r) was evaluated by computing the local radial derivative force using shells and then from equation (4.44).

Numerically, the procedure to find the velocity of each particle in the disk is done as follows:

(i) The circular velocities of each particle is determined such that they are in centrifugal equilibrium with respect to the radial component of the force in the plane of the disk.

(ii) Superimposed on this circular velocity, each particle is

given a velocity dispersion chosen from a Gaussian velocity distribution, since Toomre's criterion is strictly valid only for these type of distributions.

The next step we did was to compute the energy of each particle. This is obtained from

$$E = \frac{1}{2} m_i v_i^2 - G \frac{m_i m_j}{r_{ij}} \qquad (4.45)$$

where v_i is the velocity of the i^{th} particle and $r_{ij} = \underline{r}_i - \underline{r}_j$, with $\underline{r}_i$ and $\underline{r}_j$ are the positions of the i^{th} and j^{th} particles respectively.

If $E \leq 0$, then the co-ordinates (positions and velocities) are assigned to the particle; otherwise they are rejected and new co-ordinates are selected, subjective to the same negative energy condition.

(b) The Spheroid Density Tracers

The initial positions and velocities for $N_{Sp} = 1000$ tracer particles in the spheroidal component of the spiral galaxy were computed as follows:

The density and the mass distributions in the spheroid are

$$\rho_{Sp}(r) = \frac{\rho_s}{\left[1 + (r/r_s)^2\right]^{3/2}} \qquad (4.46)$$

$$M_{Sp}(r) = 4\pi \rho_s r_s^3 \left[\log\left(\frac{r}{r_s} + \sqrt{1+(r/r_s)^2} \right) - \frac{(r/r_s)}{\sqrt{1+(r/r_s)^2}} \right] \qquad (4.47)$$

We assume that the total mass of the spheroid M_{SP} is given by

$$M_{SP} = N_s m_i \qquad i = 1, \cdots N_s \qquad (4.48)$$

where m_i is the mass of each spheroid tracer particle, assumed to be the same for all the particles.

Now suppose

$$k = 4\pi r_s^3 \left\{ \log\left(r/r_s + \sqrt{1+(r/r_s)^2} \right) - \frac{r/r_s}{\sqrt{1+(r/r_s)^2}} \right\} \qquad (4.49)$$

in equation (4.47).

Then

$$M(r) = \rho_s \cdot k = N_s m_i \qquad (4.50)$$

from equation (4.48). We therefore get

$$\rho_s = \frac{N_s m_i}{k} \qquad (4.51)$$

As done before for the disk tracer particles, we distribute the spheroid tracers in shells of thickness Δr given by

$$\Delta r = \frac{R_{sp}}{n_s} \qquad (4.52)$$

where n_s is the number of shells chosen (= 100). and R_{sp} is the total radius of the spheroid (See Table VII).The mass fraction in each shell is

$$\Delta M_{SP}(r, r+\Delta r) = 4\pi \rho(r) r^2 \Delta r \qquad (4.53)$$

$$\Delta M_{SP} = \frac{4\pi \rho_s r^2}{\left[1 + (r/r_s)^2\right]^{3/2}} \Delta r \qquad (4.54)$$

The number of particles in each shell having a mass ΔM is then given by

$$\Delta N_{SP} = \frac{\Delta M}{m_i} \qquad (4.55)$$

From equations (4.51) and (4.54) we find

$$\Delta N_{SP} = \frac{4\pi N_s}{K} \frac{r^2}{\left[1 + (r/r_s)^2\right]^{3/2}} \qquad (4.56)$$

The value of K in equation (4.56) is obtained from equation (4.49).

The positions of the tracer particles in each shell are chosen randomly as before. The velocities for these tracers in the spheroid are computed in a similar way as for the disk's tracers. Each particle was first given a circular velocity, superimposed on which was a velocity dispersion chosen randomly from a Gaussian velocity distribution. The rotation in the spheroid, which is responsible for the flattening of the spheroid was neglected in our calculations. Each tracer particle in the spheroid was subjected to the same negative energy condition as before.

(c) The Halo Density Tracers

The initial positions and velocities of the particles to trace the density distribution of the halo in our spiral galaxy model were chosen as follows :

The density and the mass distributions chosen in the halo were

$$\rho_H(r) = \frac{\rho_h}{1 + (r/r_h)^2} \qquad (4.57)$$

and

$$M_H(r) = 4\pi r_h^3 \rho_h \left[(r/r_h) - \tan^{-1}(r/r_h) \right] \qquad (4.58)$$

The mass of the halo is given by

$$(\text{total})\ M_H = N_H m_i \qquad i = 1, \text{---} N_H \qquad (4.59)$$

where N_H = 1000, is the total number of tracers in the halo and m_i is the mass of the halo tracer particle, assumed to be the same for all the tracers in the halo and is given by

$$m = \frac{M_H}{N_H}$$

In the equation (4.58) we put

$$K = 4\pi r_h^3 \left[\left(\frac{r}{r_h}\right) - \tan^{-1}\left(\frac{r}{r_h}\right) \right] \qquad (4.60)$$

Then we get

$$M_H(r) = K \cdot \rho_h \qquad (4.61)$$

As before, we distribute the halo tracers in shells of thickness

$$\Delta r = \frac{R_H}{n_H} \qquad (4.62)$$

where R_H is the radial extent of the halo (= 28 Kpc) and n_H is the number of shells chosen (= 100).

The mass fraction in each shell is given by

$$\Delta M_H(r, r+\Delta r) = 4\pi \rho_H(r) r^2 \Delta r$$

$$= \frac{4\pi \rho_h r^2 \Delta r}{1+(r/r_h)^2} \qquad (4.63)$$

The number of particles in each shell is then given by

$$\Delta N_H = \frac{\Delta M}{m_h}$$

which is

$$\Delta N_H = \frac{4\pi \rho_h r^2 \Delta r}{1+(r/r_h)^2 m_h} \qquad (4.64)$$

From the equations (4.59) and (4.61) we find that

$$\Delta N_H = \frac{4\pi N_H r^2 \Delta r}{K\left[1+(r/r_h)^2\right]} \qquad (4.65)$$

where K is given by equation (4.61).

The positions for the particles in each shell are then chosen randomly as before.

The halo tracer particles were assumed to be in local

virial equilibrium, giving

$$u_j^2 = \frac{1}{2}|U_j| \quad ; \quad j = 1, \cdots N_H \qquad (4.66)$$

where

$$U_j = -\frac{\Sigma m_i}{r_{ij}} \qquad (4.67)$$

is the potential at the position of particle j and the factor 1/2 comes from the fact that the total energies satisfy approximately the virial theorem for the system given by

$$-2T = -\sum_j m_j u_j^2 = -\frac{1}{2}\sum_{\substack{i=1 \\ i\neq j}}^{N_H} \frac{m_i m_j}{r_{ij}} = W \qquad (4.68)$$

Each particle is then given a circular velocity in random direction, giving an isothermal model and a velocity dispersion chosen from a Gaussian velocity distribution, with the variance σ chosen in such a way that it satisfies the virial theorem. That is

$$\sigma = \frac{2T}{|W|} \qquad (4.69)$$

The particles in the halo are then subjected to the negative-energy condition as before.

IV.4 Initial Conditions: Elliptical Galaxies

To our models of elliptical galaxies, we had chosen only one

component, a spheroid, to represent the entire configuration. The tracer particles in the type galaxy are required to trace the density distribution in this spheroid. We modelled the spheroid to have a density distribution given by

$$\rho(r) = \frac{\rho_e}{\left[1+(r/r_c)^2\right]^{3/2}} \qquad (4.70)$$

where r_c is the core radius and R_{gal} is the radial extent of the galaxy (See Table IX).

The mass distribution for these models is given by

$$M_{Gal}(r) = 4\pi\rho_e r_c^3 \left[\frac{-(r/r_c)}{\sqrt{1+(r/r_c)^2}} + \log\left(r/r_c + \sqrt{1+(r/r_c)^2}\right)\right] \qquad (4.71)$$

where M_{gal} is the total mass of the galaxy. The masses of the tracer particles were taken to be all equal, given by

$$m = \frac{M_{gal}}{N} \qquad (4.72)$$

The total number of tracer particles N here was taken to be 5000, which is the same as the total number of particles chosen to represent the density of the spiral galaxy.

The initial positions and the velocities for the tracer particles in the elliptical galaxy are chosen in the same way as that for the tracers in the spheroidal component of the spiral galaxy. The parameters used were given in table IX .

IV.5 The Globular Cluster Model

The last sub-system modelled for the RNB code was the globular cluster. In most of our runs, this was chosen to be a point mass. In few cases however, we modelled the cluster to be a spherical Plummer sphere with a volume density given by

$$\rho_{gc} = \frac{3 M_{gc}}{4\pi r^3} \qquad (4.73)$$

where M_{gc} is the mass of the globular cluster.

The masses chosen for the globular clusters were in the range $5 * 10^5 - 5 * 10^7$. The orbital parameters chosen for the clusters will be discussed in the section containing preliminary results in the next chapter.

CHAPTER FIVE

NUMERICAL WORK: SPIRAL GALAXIES

The initial conditions and the galaxy models were discussed in the last chapter. In this chapter, the computational details of the problem will be presented for the case of the spiral galaxies. Elliptical galaxies will be discussed in the next chapter.

In section V.1 of this chapter, some details regarding the RNB code will be presented. In section V.2, the equations of motion will be given. The meaning of the corresponding energy integral will be investigated in section V.3. Units are defined in V.4. The initial phase mixing and relaxation stages will be discussed in V.5. The force calculations and the numerical integration will be presented in sections V.6 and V.7 respectively. In the final section, V.8, some preliminary results and discussion will be given regarding the orbital evolution of globular clusters in spiral galaxies.

V.1 The RNB Code

As discussed before, our numerical code was broken into three sub-systems : The galaxy potential, which is kept fixed in space and time, the globular cluster and the tracer particles that trace the density distribution of the galaxy. These tracer particles respond to the forces imposed by the earlier two sub-systems but

do not interact with one another. That is, we are neglecting the self-gravity of our galaxy. White (1983) has shown that by suppressing the self-gravity of the system, the orbital decay rates were reduced by a factor of more than two in his simulations. Quinn and Goodman (1986) had come to the same conclusion in their numerical work. It is therefore necessary to run a full N-body simulation where the inter-tracer particle forces are not neglected. Since this means an enormous increase in the computational time, we had planned to do this at a later stage. For the present, the RNB code was used for the simulations.

In a typical N-body code, full or the RNB type, a galaxy of mass $M_{GAL} = 10^{11} M_{\odot}$ is represented by N number of particles, with N limited to 10^{3}- 10^{4} by the present day computers. The masses of the particles generally considered equal are given by

$$m = \frac{M_{Gal}}{N} \qquad (5.1)$$

$$\sim 10^{8} \quad \text{for } N = 1000$$

This mass of each particle is of the order of a dwarf galaxy. That is, we assume that our galaxy is made up of 1000 such dwarf galaxies. Now, in order to study the action of dynamical friction on a globular cluster, having a mass of the order of $M_{GC} = 10^{6} M_{\odot}$, orbiting in a galaxy comprised of N such particles, each representing, say a star in the galaxy, we at once run into a difficulties as each particle (star) is having more mass than the globular cluster. One way to resolve this problem is to increase N but the problems connected by increasing N have already been discussed in chapter three. The problem connected with the

masses for the particles can be resolved in another way by writing the equations of motion for the system in such a way that we compute the drag force on the globular cluster irrelevant of the masses of the particles that are responsible for this drag. These particles do not represent real stars in the galaxy but just trace the density distribution of the galaxy. The distribution of these tracers has already been discussed in chapter four. In our code then, each individual particle could have any mass as long as the sum of the total masses of the tracer particles is equal to the total mass of the galaxy. These equations of motion will be given in the next section.

V.2 The Equations of Motion

The orbits of the tracer particles are computed under the assumption that the disk, spheroid and halo's self-gravity are not important in determining the response of these components to the presence of the globular cluster. The tracer particles are therefore made to feel an acceleration due to the mean field formed by the three components they are part of, and the globular cluster. The globular cluster feels an acceleration due to the three components, but this acceleration is computed from the distribution of the tracer particles. The potential wells of the three components are held fixed in space and time since the masses of the globular clusters considered are very small compared to the total mass of the system. The equations of motion for the globular cluster and the tracer particles are then :

$$\ddot{\underline{r}}_s = -G \sum_{i=1}^{N} \frac{m_i \left[\underline{r}_s - \underline{r}_i \right]}{\left[|\underline{r}_s - \underline{r}_i|^2 + \varepsilon^2 \right]^{3/2}} \qquad (5.2)$$

$$\ddot{\underline{r}}_i = -\frac{\partial \phi_{disk}}{\partial \underline{r}} - \frac{\partial \phi_{spheroid}}{\partial \underline{r}} - \frac{\partial \phi_{halo}}{\partial \underline{r}} - \frac{G m_s (\underline{r}_i - \underline{r}_s)}{\left[|\underline{r}_i - \underline{r}_s|^2 + \varepsilon^2 \right]^{3/2}}$$

$$i = 1, \cdots N$$

where G is the Gravitational constant

$\underline{r}_s$ and m_s are the position vector and mass of the cluster

$\underline{r}_i$ and m_i are the position vector and mass of the i^{th} particle respectively

ε = is the softening parameter

ϕ_{disk}, $\phi_{spheroid}$ and ϕ_{halo} are the potentials due to the disk, spheroid and halo components of the spiral galaxy. The calculations of these potentials was discussed in the last chapter. The dots in the above equations represent time derivatives.

From the above equations of motion we see that by making the tracer particles move in the fixed potentials of the galaxy, we have ignored the drag forces on the tracer particles. The changes in the tracer particles due to the traversing globular cluster are reflected back on the globular cluster (equation) as the drag force. We see that the masses of the particles become irrelevant in this way.

V.3 The Energy Conservation

The equations of motion (5.2) do not describe a fully

self-consistent system. The energy integral of this system is given by

$$E = \frac{1}{2} m_s \dot{\underline{r}}_s^2 + \frac{1}{2} \sum_{i=1}^{N} m_i \dot{\underline{r}}_i^2 - \sum_{i=1}^{N} m_i \phi_{gal} - m_s \sum_{i=1}^{N} m_i \phi_{is} \qquad (5.3)$$

This equation is derived in Appendix D. This energy E was used to check the accuracy of the code. The deviations from a constant value of E however should not be confused with the physical deviations from total energy conservations, since the equations of motion used by us are not fully self-consistent. In the Appendix D, we had called the energy integral as an approximate integral since it does not represent the real energy integral of an N-body system.

V.4 The Units

A dimensional system of units were chosen in the code, in which the gravitational constant, the total disk mass M_D and the disk's exponential scale-length α were all set to unity. The table below summarizes the choice of the units.

TABLE ✖

Dimensional quantity	Symbol in the text	Units	Physical values
Mass of the Disk	M_D	1.0	$0.78 * 10^{11} M_\odot$
Disk's Exponential scale length	α	1.0	3.5 Kpc
Gravitational constant	G	1.0	$6.67 * 10^{-8}$

In these units, the total mass of the galaxy (disk+spheroid+halo) becomes $M_{Total} = 5.0024$, corresponding to a mass $3.93 * 10^{11} M_\odot$ and a cut-off radius R = 8, corresponding to 28 Kpc. The time unit in the code is measured in terms of the crossing time of the system given as

$$Tcr = \left[\frac{R^3}{G M_{total}}\right]^{1/2} = 10 \text{ time units} \qquad (5.4)$$

The velocity units are defined as

$$\text{velocity} = \left[\frac{G M_{total}}{R}\right]^{1/2} = 0.7923 \qquad (5.5)$$

The following equations demonstrate the translation from dimensionless to physical units for a galaxy model with $M_{Total} = 3.93 * 10^{11} M_\odot$ and R = 28 Kpc.

10 time units = $\sim 2 * 10^8$ years (5.6)

0.793 velocity units = ~ 244 Kms^{-1} (5.7)

The softening parameter, ε, used in the code was 1.0,

corresponding to 3.5 Kpc. Length scales over which one wants reliable information should be larger than this ε. This softening parameter was close to the mean tracer particle separation in the galaxy.

V.5 Phase Mixing

In order to minimize any systematic effects of the initialization procedure, the initial model of the galaxy was run through a mixing phase during which the mass of the globular cluster was taken to be zero. For a specified length of time, usually about 50 time units (5 crossing times), the N tracer particles were allowed to move exclusively in the gravitational field of the galaxy ($\phi_{gal} = \phi_{disk} + \phi_{spheroid} + \phi_{halo}$). A check on the particle distribution after the phase mixing stage shows that the tracers retained their initial density profile within the cut-off radius R = 28 Kpc. The globular cluster mass was turned on after this initial phase mixing period was over.

V.6 The Force Calculations

In the right hand side of the equations of motion (5.2) , the derivatives of the potentials, the forces ($\frac{\partial \phi_{disk}}{\partial r}$, $\frac{\partial \phi_{spheroid}}{\partial r}$, $\frac{\partial \phi_{Halo}}{\partial r}$) at each time step are required. Analytical expressions for , could be easily obtained for the spheroid and the halo as

$$\frac{\partial \Phi_{spheroid}}{\partial r} = \frac{4\pi \rho_s r_s^3}{r^2}\left[\frac{(r/r_s)}{\sqrt{1+(r/r_s)^2}} - \log(r/r_s) + \sqrt{1+(r/r_s)^2}\right] \qquad (5.8)$$

and

$$\frac{\partial \Phi_{Halo}}{\partial r} = \frac{4\pi \rho_H r_h^2}{r}\left[\frac{(r/r_h)}{1+(r/r_h)^2} + \frac{1}{1+(r/r_h)^2} - \frac{\tan^{-1}(r/r_h)}{(r/r_h)}\right]$$

The force on each particle from the disk component is however not available so straightforwardly. The axisymmetric disk potentials computed numerically in cylindrical co-ordinates, discussed in the last chapter, were stored on a grid of size 132 * 132, at each grid- cell point. The radial and the vertical force on each particle are then found by using linear interpolation as

$$F_r(P) = (1-T_r)\left[(1-T_z)F_{i,j} + T_z F_{i,j+1}\right] + T_r\left[(1-T_z)F_{i+1,j} + T_z F_{i+1,j+1}\right] \qquad (5.9)$$

and

$$F_z(P) = (1-T_z)\left[(1-T_r)F_{i,j} + T_r F_{i,j+1}\right] + T_z\left[(1-T_r)F_{i+1,j} + T_r F_{i+1,j+1}\right] \qquad (5.10)$$

These expressions are derived in Appendix E. Since the code uses cartesian co-ordinates, the following transformations were made :

$$\begin{aligned} F_x(P) &= F_r(P)\cos\theta \\ F_y(P) &= F_r(P)\sin\theta \\ F_z(P) &= F_z(P) \end{aligned} \qquad (5.11)$$

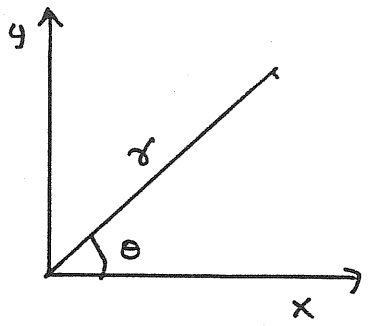

From the figure, we see that,

$$\cos\theta = \frac{x}{r}$$

$$\sin\theta = y/r$$

and therefore

$$F_x(p) = F_r(p) \cdot \frac{x}{r} \qquad (5.12)$$

$$F_y(p) = F_r(p) \cdot y/r$$

which were the expressions used in the code.

The first step before computing equations (5.11) and (5.12) is however to find where and in which grid each tracer particle is, in order to compute the disk force (equations (5.9) and (5.10)) on it, at a given time. That is, we need a search algorithm to find the positions of 5000 particles in a given grid cell. This search algorithm has to be efficient and fast since it will be used at every time steps. In our code, we performed the following trick which proved to be an useful and effective search algorithm. Since the positions of the tracer particles $\underline{r}_i$ (i = 1, N) and the grid positions are known, it was possible to find the smaller radius of the grid position by simply taking the integer part of the particle position. Once the smaller radius is known, we know in which grid cell the particle happens to be, because the particle position $\underline{r}$ would always be greater than this smaller radius of the grid cell. This procedure is shown below.

We first compute a 2-dimensional grid on the disk on which we store the potentials by

$$r_{grid} = r_0 + (i-1) * h_r$$

$$z_{grid} = z_0 + (j-1) * h_z \qquad (5.13)$$

where r_0 and z_0 are the lower limits of our disk configuration. We had chosen r_0 =0.0 and z_0 = -10.0 , referring to the lower co-ordinates in which we placed the tracer particles. The upper limits of the configuration are r_f = 10.0 and z_f = 10.0. The mesh-sizes h_r and h_z are given by

$$h_r = \frac{r_f - r_0}{n_r}$$

$$h_z = \frac{z_f - z_0}{n_z} \qquad (5.14)$$

where nr = 131 and nz = 131, are the number of grid points in r and z respectively. The computed potentials are stored at each grid point.

We have chosen a grid that is two cell sizes more than our actual disk configuration (recall that R_D = 8 in units of table X) for the following reason. In our linear interpolation formula (equations 5.9 and 5.10), the forces need not be calculated on the boundary of the configuration, since these boundary points do not contribute to the interpolation.

Now suppose (r_p, z_p) refer to the tracer particle position in cylindrical co-ordinates. Then with respect to the grid we have

$$r_p = r_0 + (II - 1) * h_r \qquad (5.15)$$

$$z_p = z_0 + (JJ - 1) * h_z \qquad (5.16)$$

where r_0 and z_0 are the same lower limits of the grid as before. Here, II and JJ are integers, both going from 1 to 132. These integers can be obtained from the equations (5.15) and (5.16) as

$$II = \frac{r_p - r_0}{h_r} + 1.0 \qquad (5.17)$$

$$JJ = \frac{z_p - z_0}{h_z} + 1.0$$

Thus by computing the integers II and JJ for each particle, we can obtain the smaller radius of the grid cell in which the particle lies. Therefore, at a given time we know in which grid cell each tracer particle is and since the potentials at the points of this cell are known we can compute the force on the tracer particle which lies within this cell. The forces are given by the equations (5.9) and (5.10).

Once the right hand sides of the equations of motion are calculated, only numerical integration is left to solve these equations. This will be discussed in the next section.

V.7 The Numerical Integration

The algorithms to solve the equations of motion have already been discussed in chapter three. We have used the following second-order predictor-corrector method in the code.

$$v_{k+1/2} = v_k + \Delta t * f_k$$

$$r_{k+1} = r_k + \Delta t * [v_{k+1/2}] \qquad (5.18)$$

$$v_{k+1} = v_k + \frac{\Delta t}{2} * [f_k + f_{k+1}]$$

where f, v and r refer to acceleration, velocity and the position of the particle and Δt refers to the integration time step.

This time step was chosen to be a variable in the code and was determined by the maximum velocity or acceleration at each step.

An average simulation lasted for 1000 time units ($\sim 10^2$ crossing times, corresponding to a Hubble time of $\sim 10^{10}$ years), and took $\sim$ 3 hours of Cpu time on the Gould 32/97 computer.

A measure of the accuracy of the integration method was the fractional energy change $\Delta E/E$ in each run, where E is computed as shown before (equation 5.3). In all our runs we have found $\Delta E/E$ to be less than 2 % .

V.8 Preliminary Results and Discussion

The parameters describing our models can be divided into two parts: those of the parent galaxy and the globular cluster. We have kept the outer radius R_{Gal} and the mass of the galaxy M_{Gal} fixed in our runs. These were R_{Gal}= 8 and M_{Gal} = 5.0 in the units of table X . The number of tracer particles in it was also kept fixed at N = 5000 in the simulations reported here. We explored a

range of masses, orbital radii and eccentricities for the globular clusters in these runs. We discuss each case separately below. All the values for the parameters chosen in the runs are defined in the units given in table X . In all the runs, the meaning of time is as follows:

10 time units = 1 Tcr $\approx 2 \times 10^8$ years

Case 1:

Figure 22 shows the time evolution of the 5000-tracer particle galaxy and the globular cluster, marked in the figure as a star. The mass chosen for the globular cluster was $M_{GC} = 1.24 * 10^{-4}$ and was placed initially at radius r = 4.0, in the plane of the disk. The view in the time evolution pictures is from above the disk plane in this and all subsequent figures unless otherwise stated. The orbital evolution of the this globular cluster is shown in figure 23 .

The simulation went upto 2043 time units, corresponding to about 205 crossing times ($2 * 10^{10}$ years). The orbital period of the cluster is 22.4 time units and completed 91 orbits in this run. The cluster which started off at an initial radius of 4.0 decayed to r = 1.7 during this run.

The most striking feature in the figure 23 is that the orbit of the globular cluster decayed to r = 2.9 initially in 9 orbits and then seemed to have gained energy and angular momentum and moved outward to r = 3.7. After this peculiar feature the orbit of

FIGURE 22

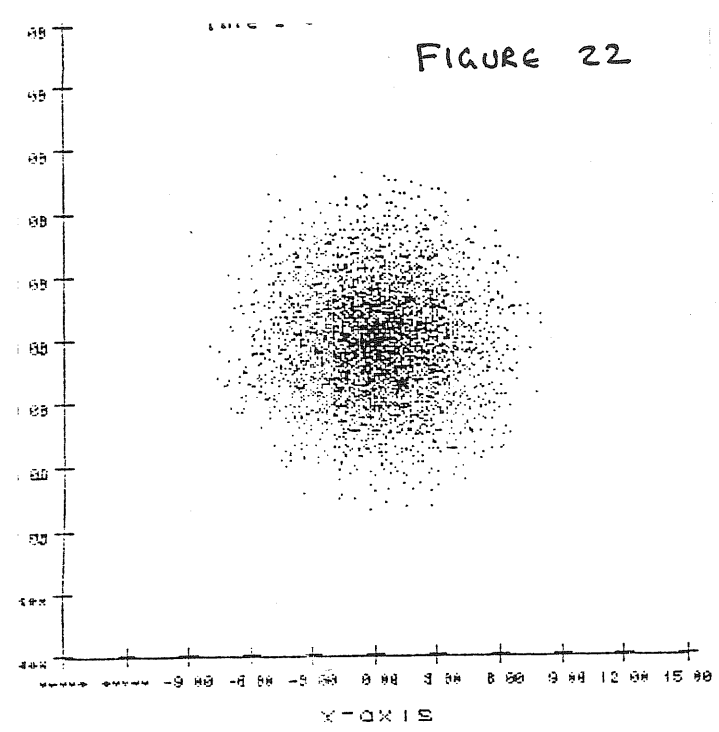

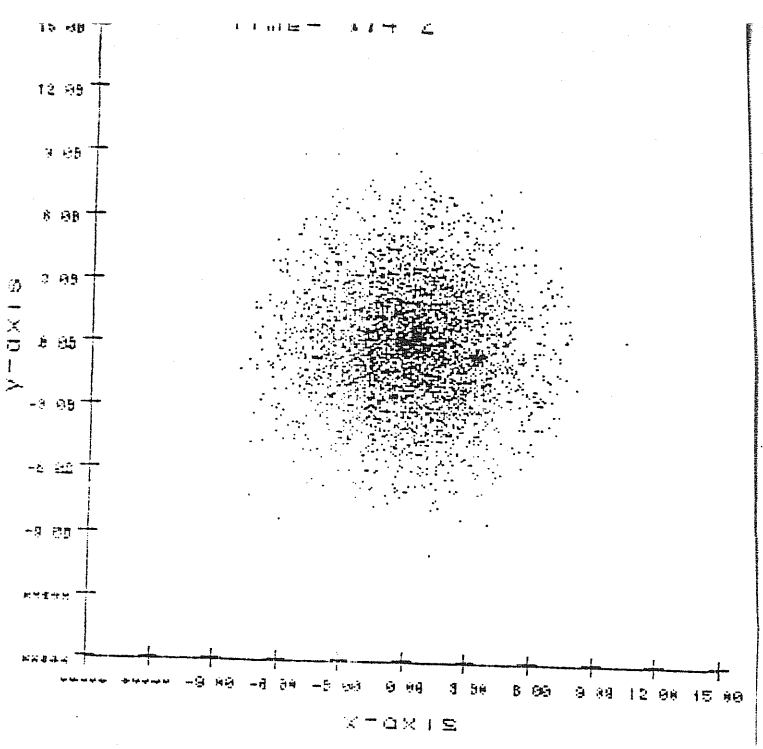

Time= 199 7

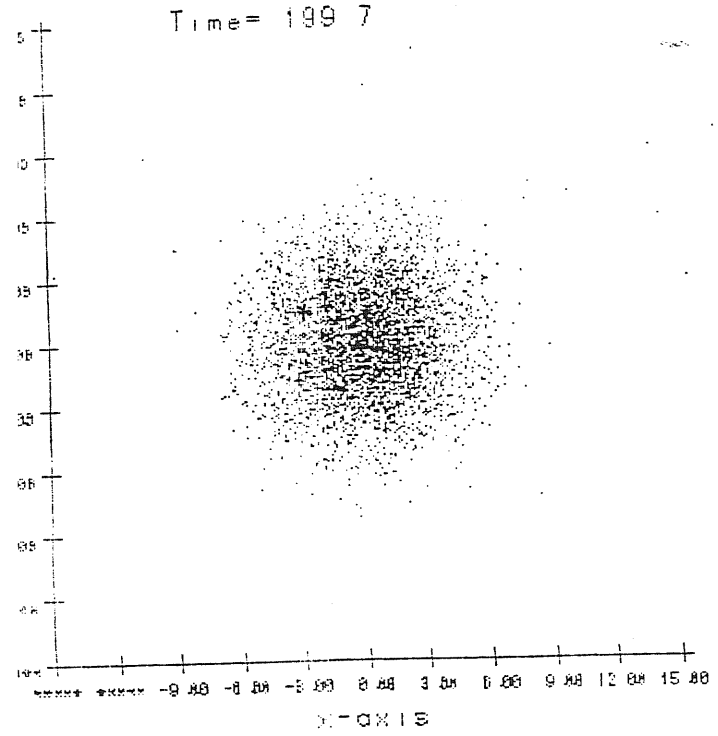

Time= 300 4

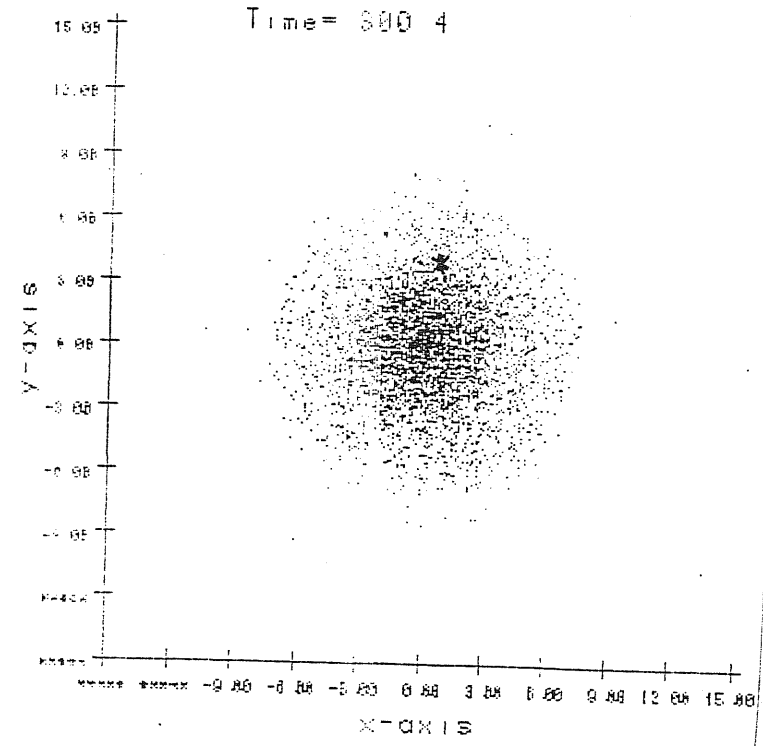

Time= 416 2

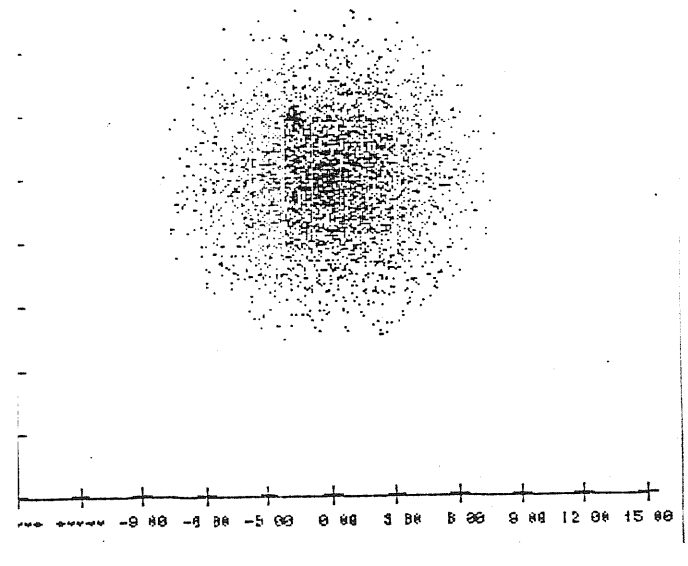

Time= 501 9

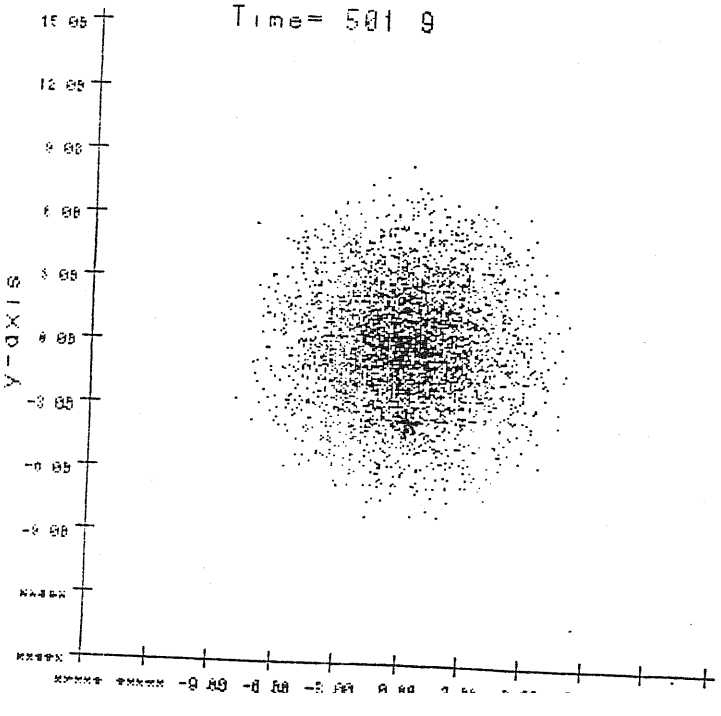

FIGURE 22

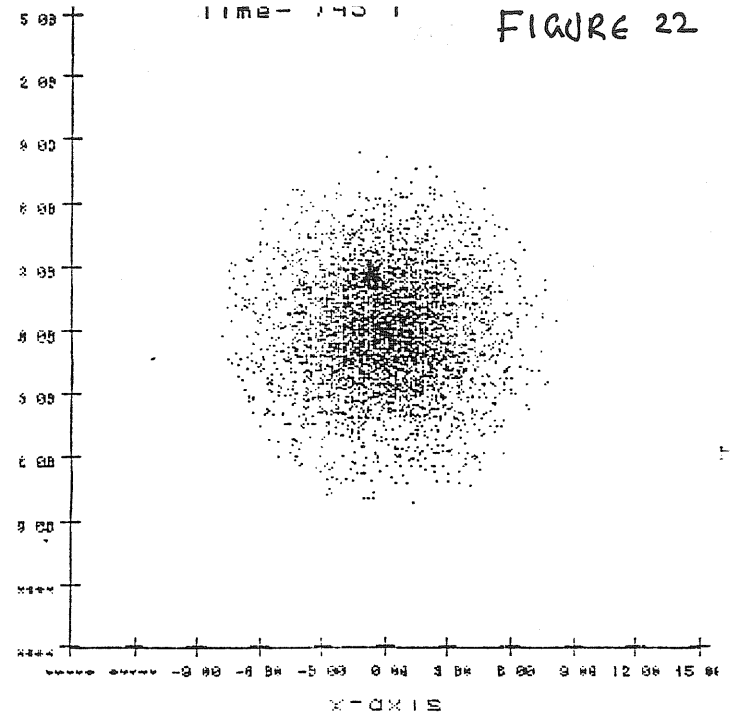
Time= 745 1
x-axis

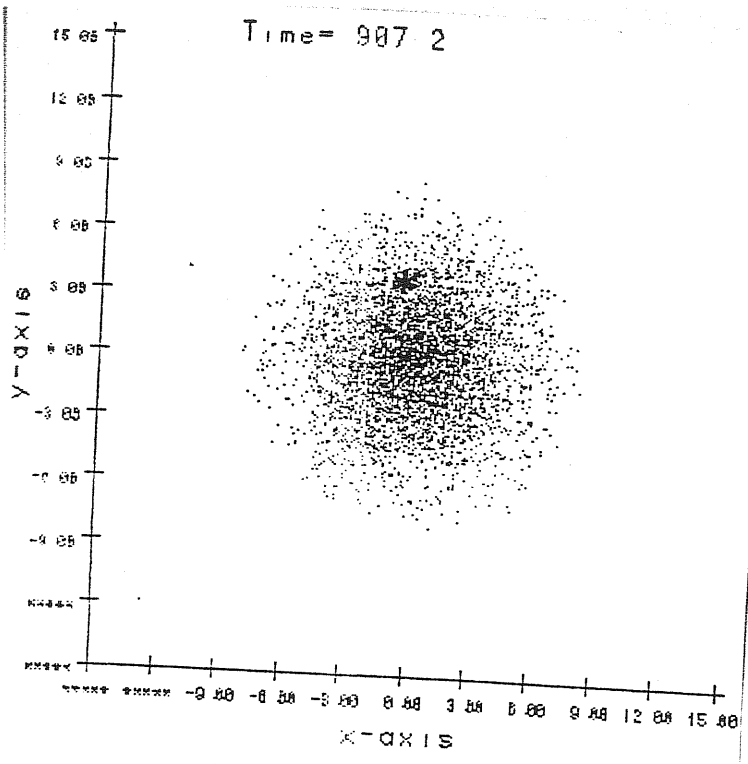
Time= 907 2
y-axis
x-axis

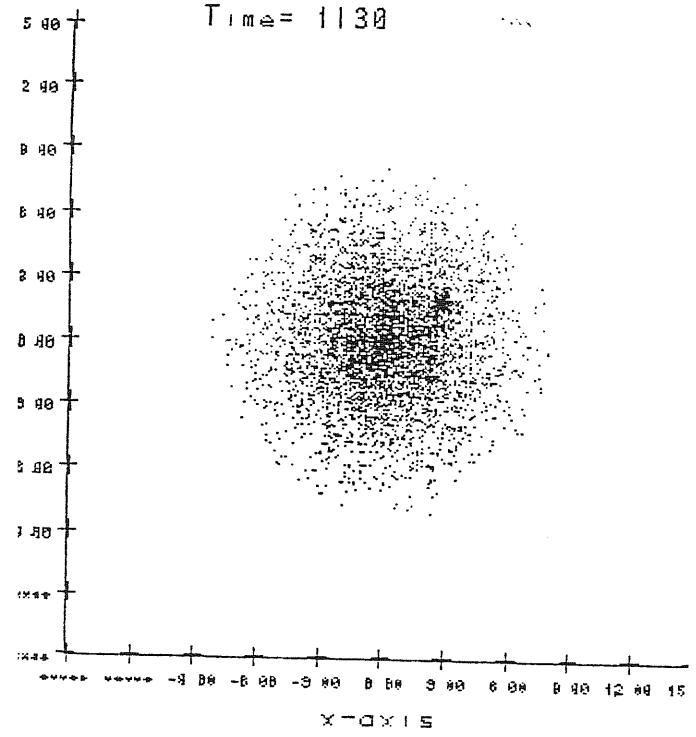
Time= 1130
x-axis

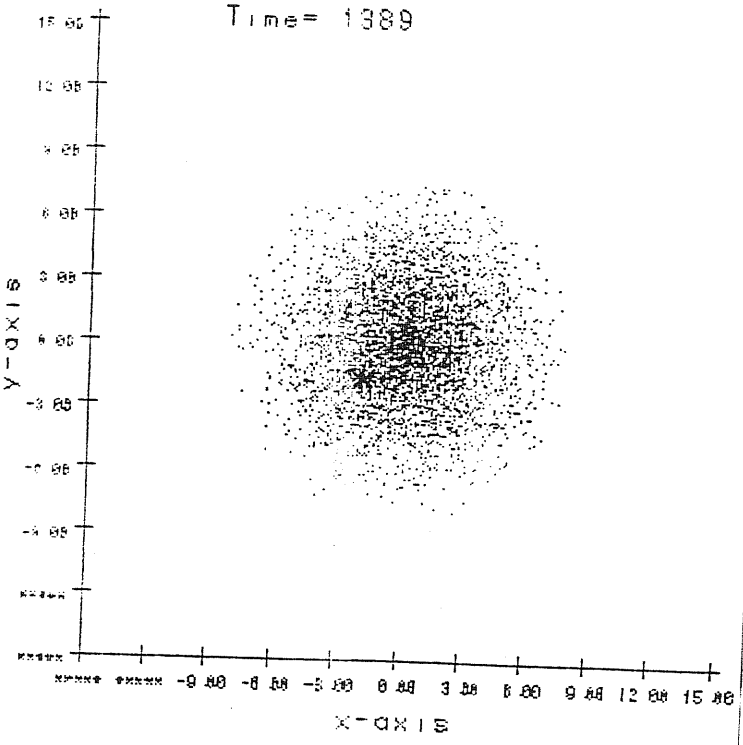
Time= 1389
y-axis
x-axis

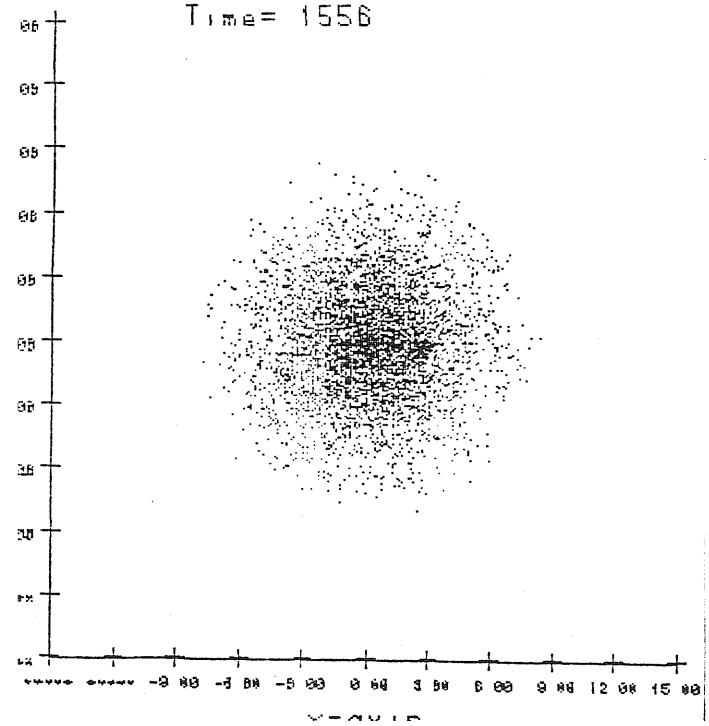
Time= 1556

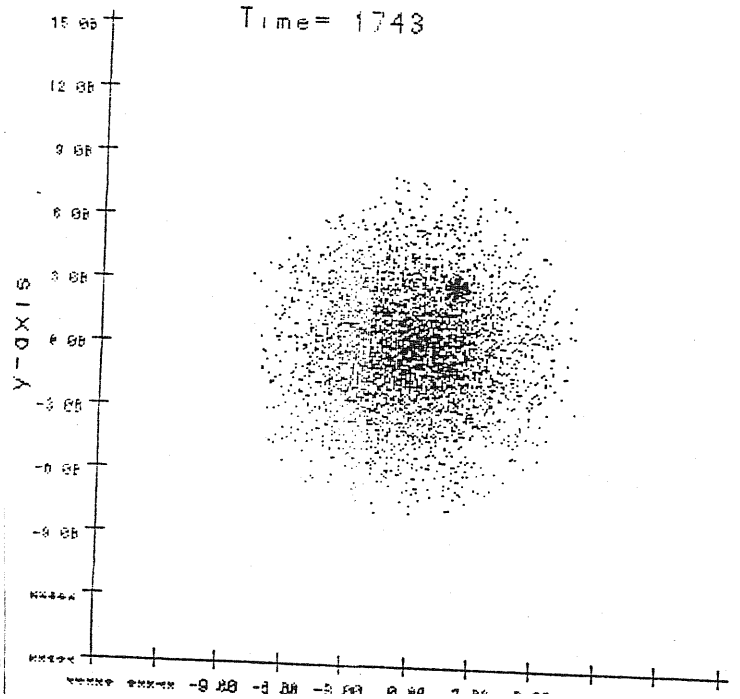
Time= 1743
y-axis

FIGURE 23

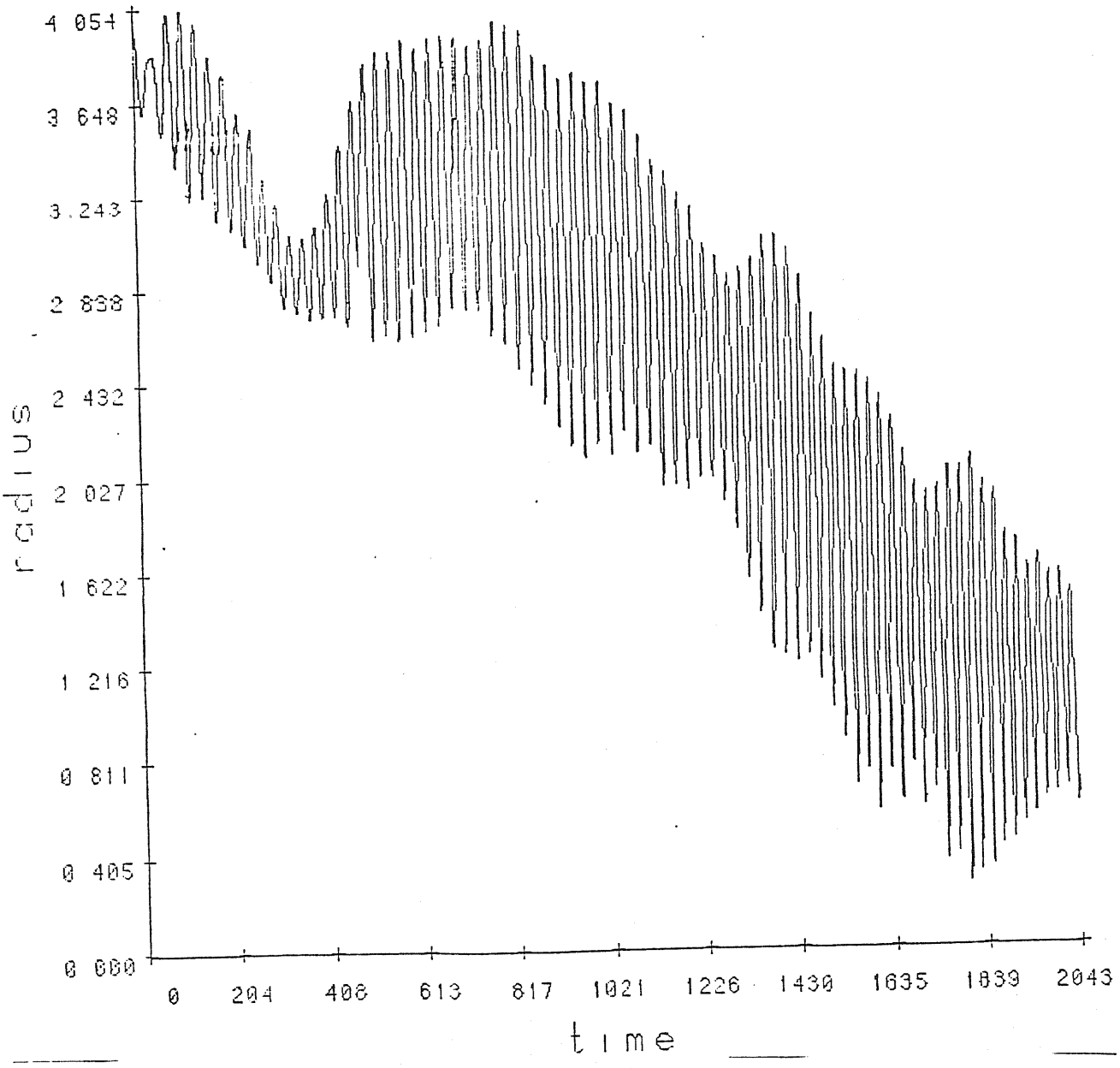
4 054
3 648
3.243
2 838
2 432
2 027
1 622
1 216
0 811
0 405
0 000
radius
0
204
408
613
817
1021
1226
1430
1635
1839
2043
time

the cluster seems to decay once again.

In chapter two, we have shown that the secular effects on an object in the linear approximation are caused solely by interactions at resonances: that is radii $r_{l,m}$ such that

$$l\,K(r_{l,m}) + m\,\Omega(r_{l,m}) = \Omega_p$$

where Ω_p is the orbital angular velocity of the object, $K(r_{l,m})$ is the epicyclic frequency at the resonance and l,m are integers. The sign convention is that $m > 0$ and $l > 0$ or $l < 0$ according as $r_{l,m} > 0$ or $r_{l,m} < r$. Co-rotation corresponds to $l = 0$. The important resonances in our case are the co-rotation $l = 0$ and Lindblad resonances, $l = 1$.

For our case, we see that for $m = 2$, there are two inner Lindblad resonances, at $r = 2.9$ and $r = 0.7$. At exactly $r = 2.9$, we see that the globular cluster moves outwards because of the linear interactions of the particles at this resonance. We could not check this at the other inner resonance $r = 0.7$.

Case 2

Figure 24 shows the orbital evolution of a globular cluster of a globular cluster of mass $M_{GC} = 6.4 * 10^{-5}$ ($5 * 10^{6}\ M_{\odot}$) which started off at an initial radius of $r = 4.5$. The simulation lasted only for 58 crossing times ($7 * 10^{9}$ years) and the cluster had completed only 18 orbits. There was no orbital decay observed for this cluster and also no striking features were seen in the

FIGURE 24

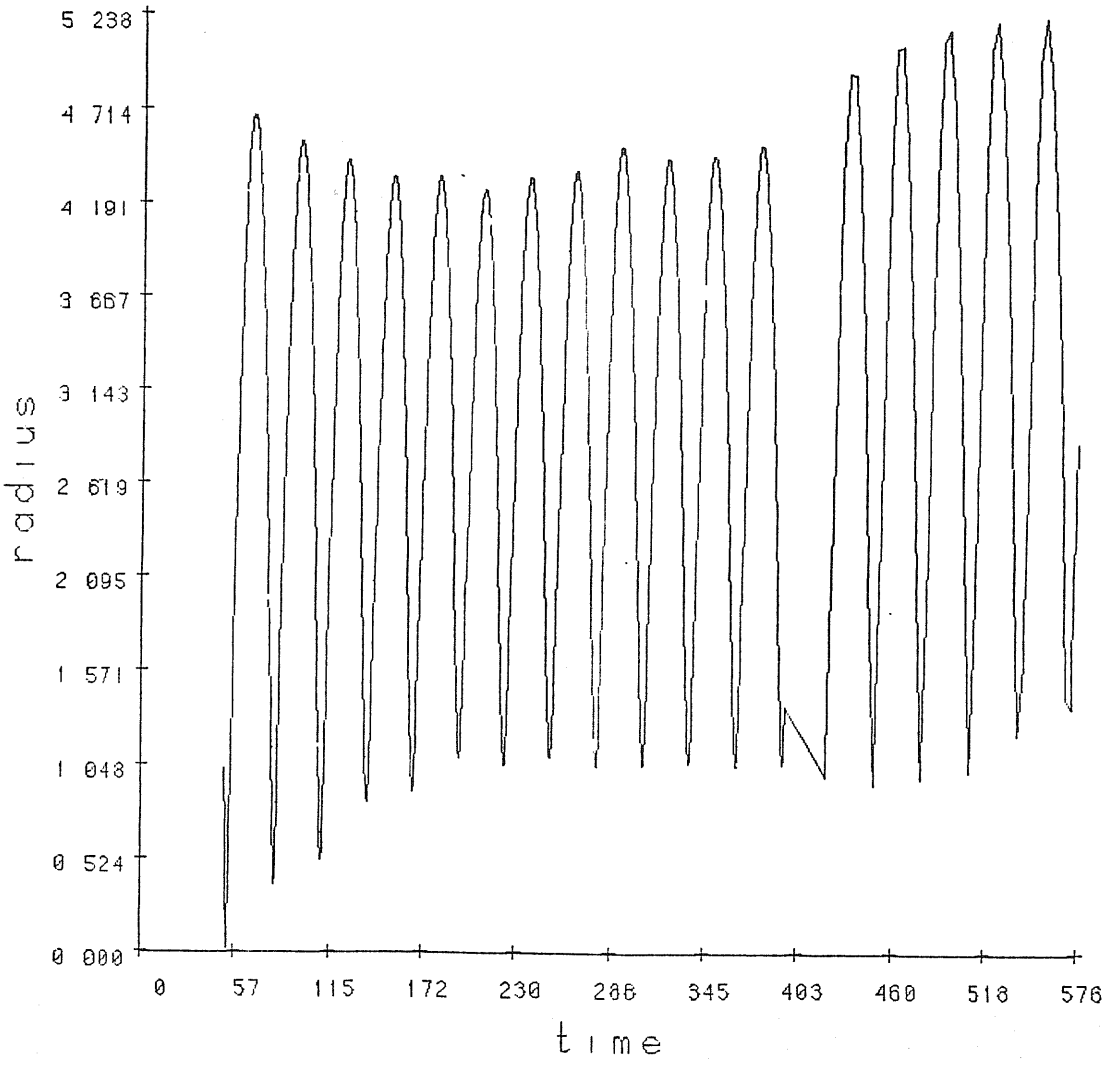
radius
5 238
4 714
4 191
3 667
3 143
2 619
2 095
1 571
1 048
0 524
0 000
0
57
115
172
230
288
345
403
460
518
576
time

orbital evolution as in the previous case. The time evolution of the galaxy-cluster system is shown in figure. 25

Case 3

Figure 26 shows the evolution of a globular cluster of mass same as in the previous case (case 2) but started off on an non-circular orbit at r = 2 (7 Kpc.). This simulation completed about 82 crossing times, (about 10^{10} years) and the cluster completed 40 orbits in this run. In this simulation, the globular cluster started moving outwards after 8 orbits, sank slowly again and at r = 2.19, it started moving outwards again and continued to move outwards till the run was stopped ($\sim$ 10^{10} years). The time evolution of the system is shown in figure 27.

Case 4

Figure 28 shows the evolution of a cluster whose mass was $M_{GC} = 7 * 10^{-9}$ ($5 * 10^{8} M_{\odot}$) started off at an initial radius of r = 4. This cluster's mass is almost the order of a dwarf galaxy. The orbital decay here is quite rapid as expected for massive objects.

These few preliminary runs have shown that :

(i) Interactions between the globular cluster and the particles is determined mainly at resonances. More numerical simulations and detailed analytical work needs to be done for understanding the processes that occur at resonances.

(ii) The decay rates obtained for the few cases we had run were not rapid enough to destroy the globular clusters over a Hubble time.

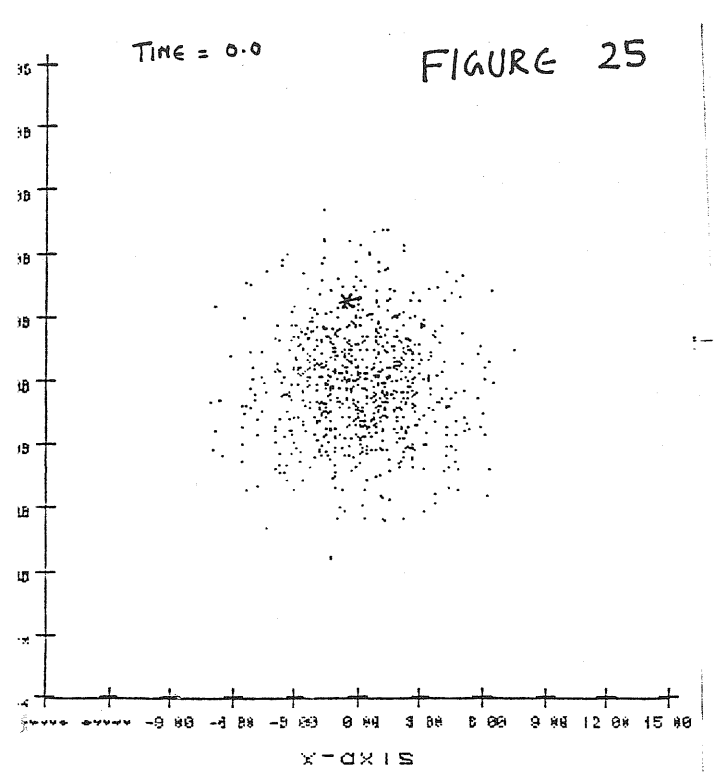
TIME = 0.0
x-axis

FIGURE 25

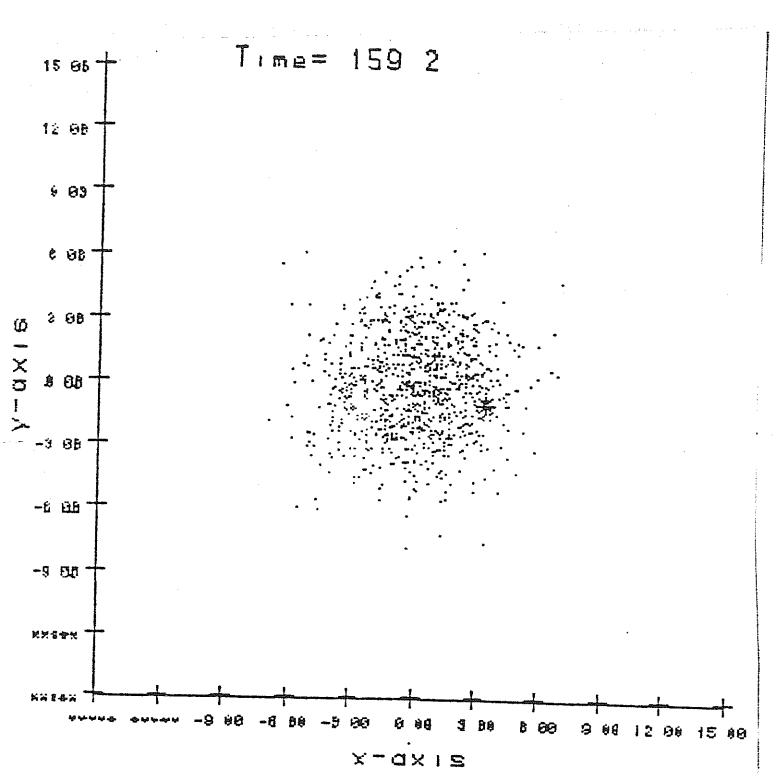
Time= 159 2
y-axis
x-axis

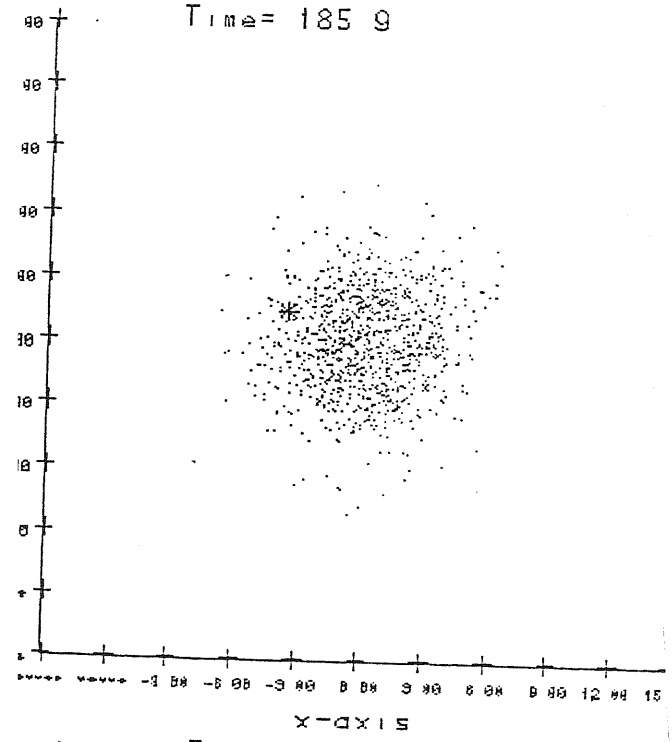
Time= 185 9
x-axis

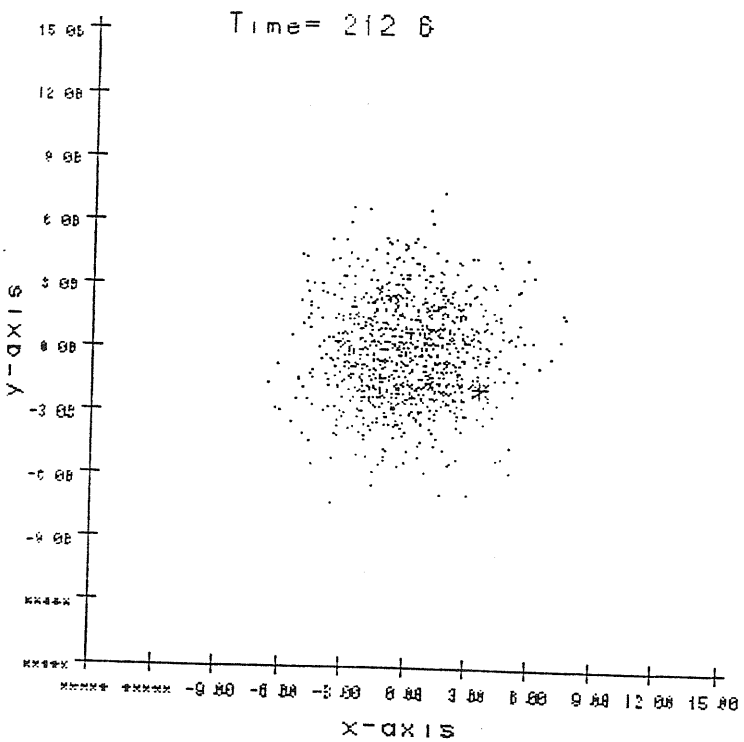
Time= 212 6
y-axis
x-axis

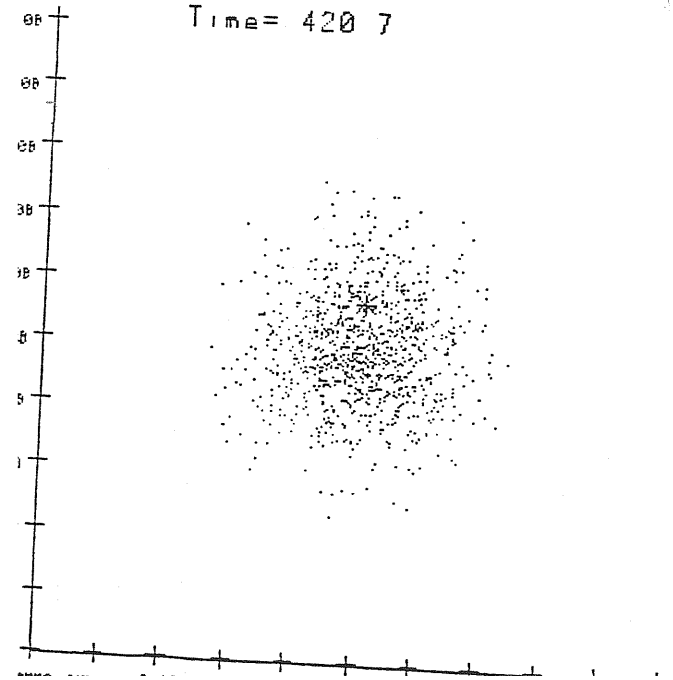
Time= 420 7

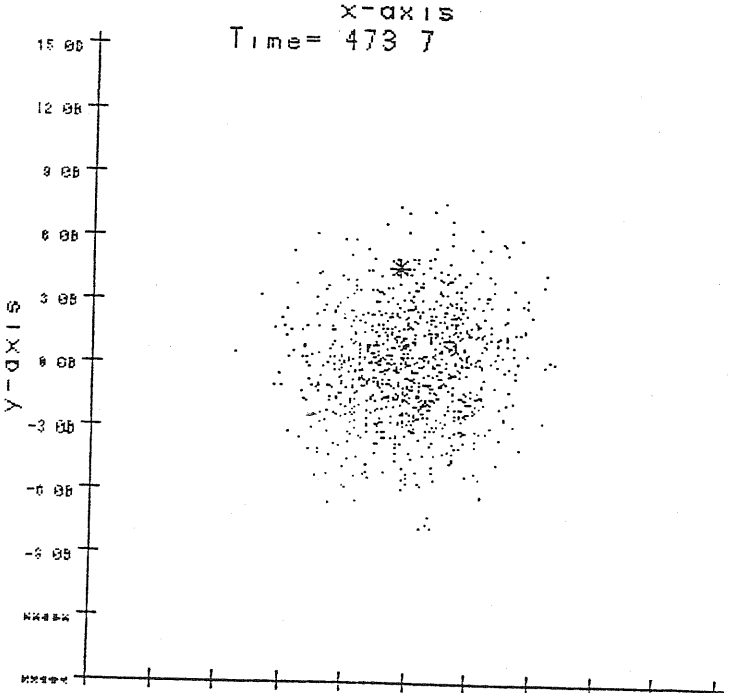
Time= 473 7
y-axis

FIGURE 26

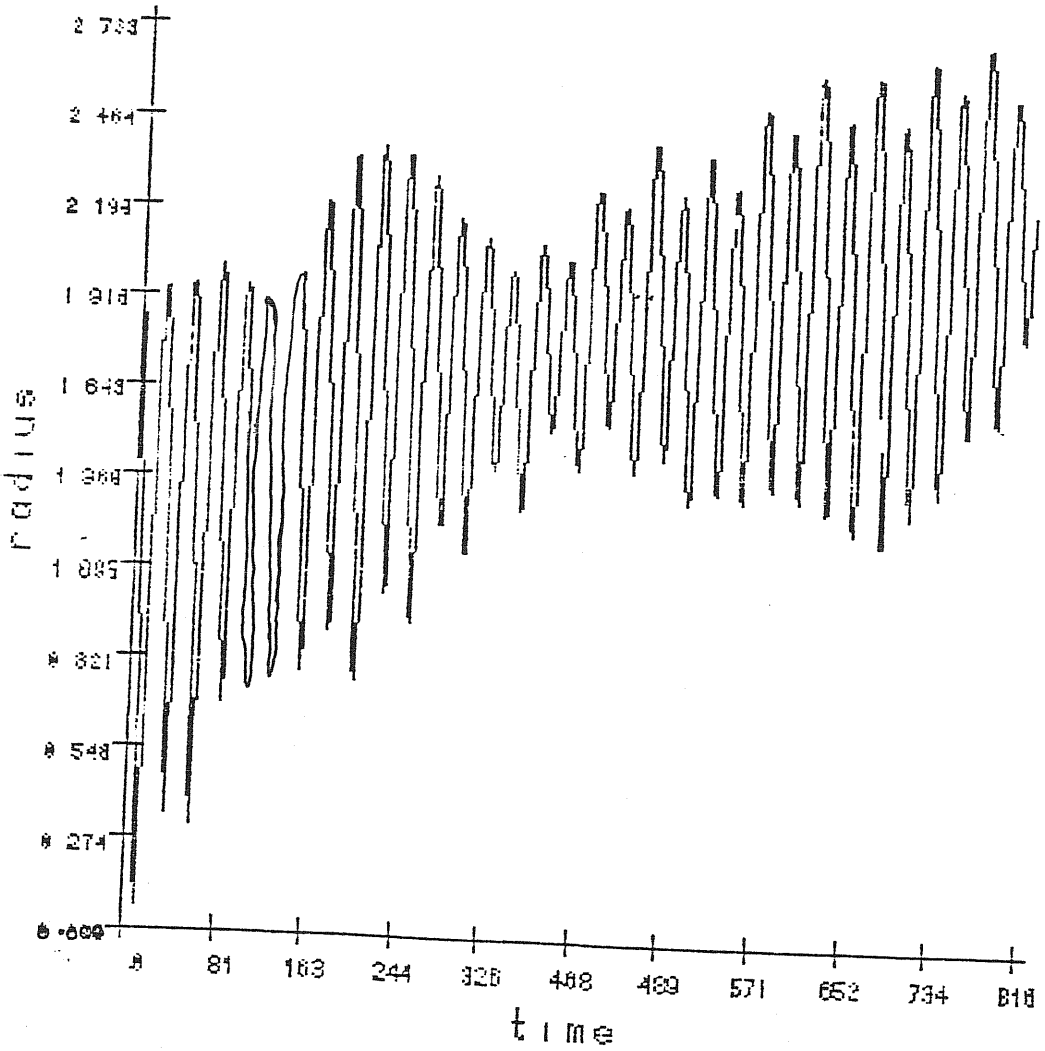

FIGURE 27

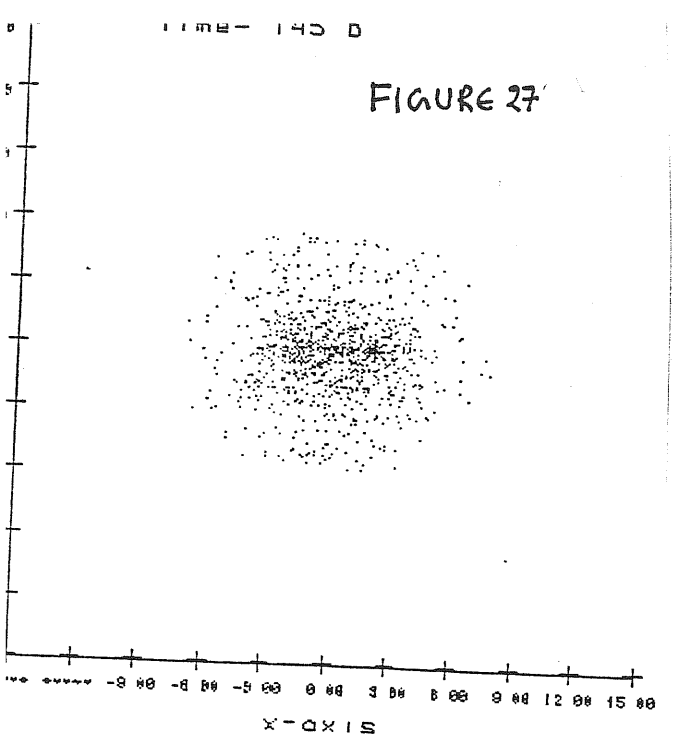
Time= 145 0
x-axis

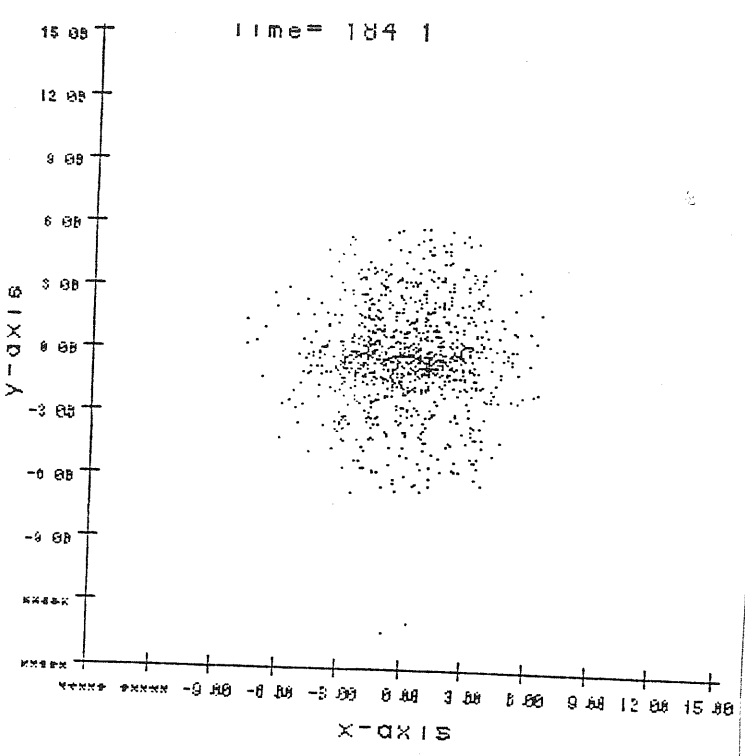
Time= 184 1
y-axis
x-axis

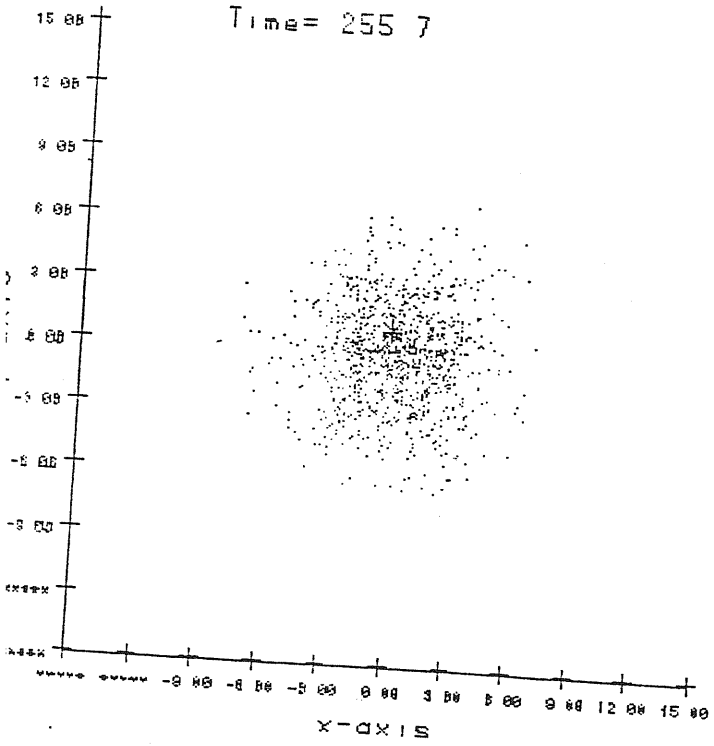
Time= 255 7
x-axis

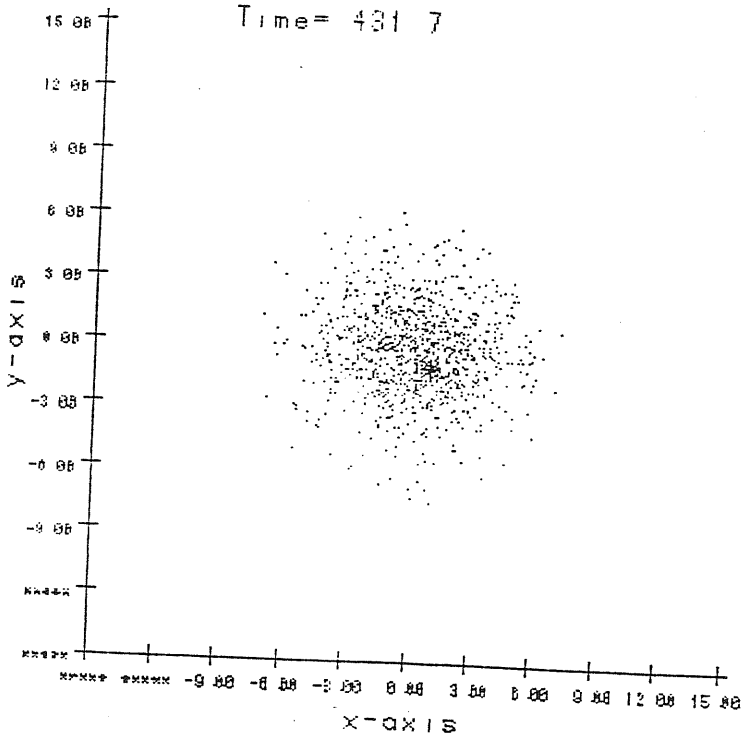
Time= 431 7
y-axis
x-axis

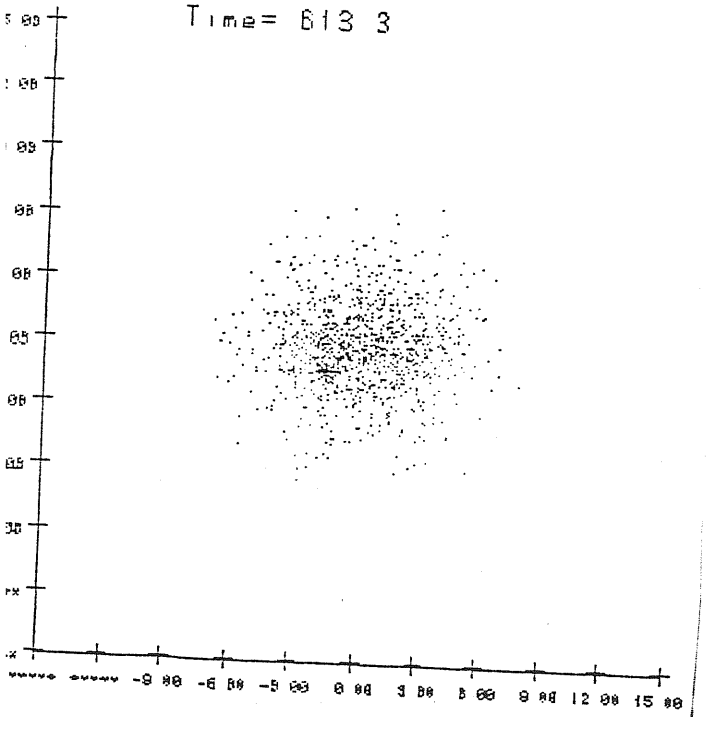
Time= 613 3

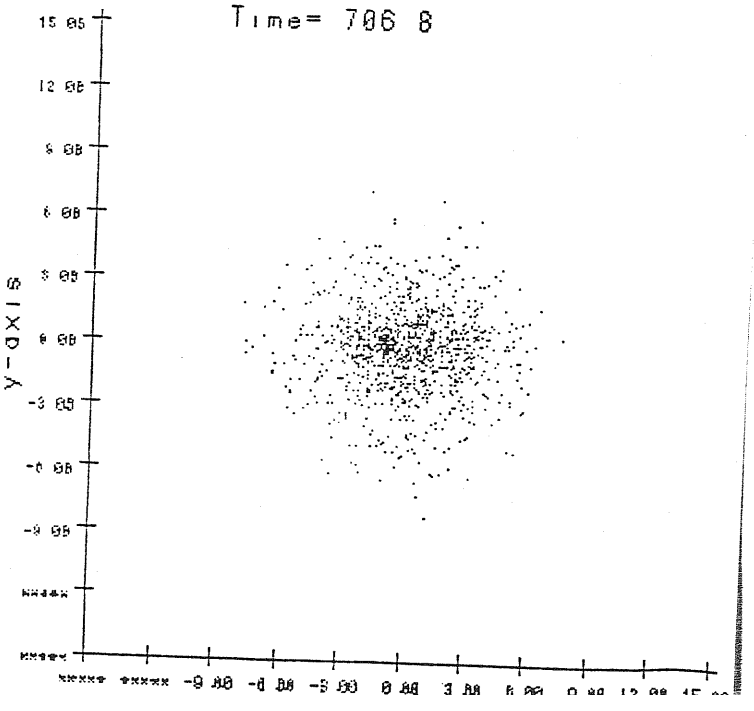
Time= 706 8
y-axis

FIGURE 28

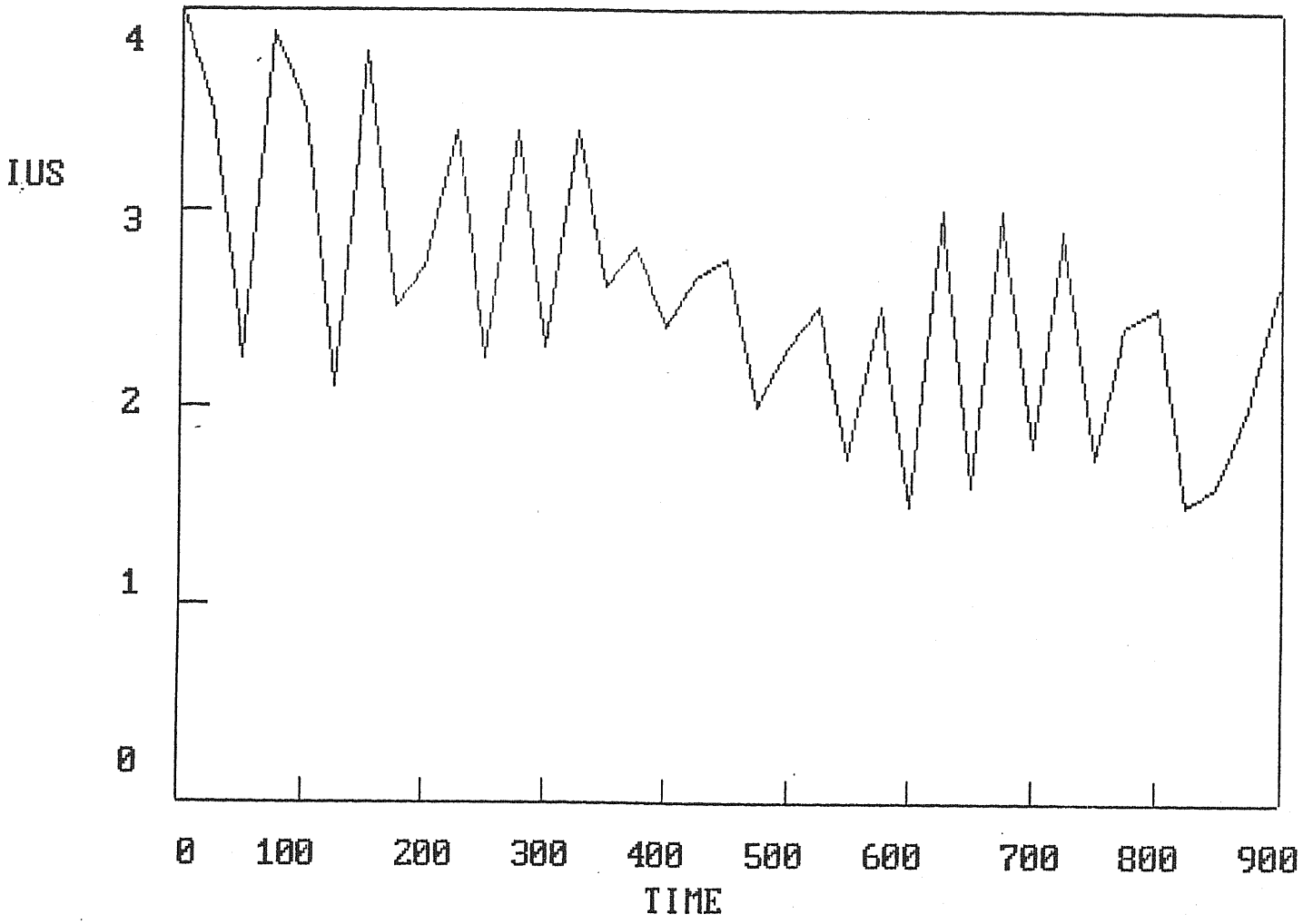

CHAPTER SIX

NUMERICAL WORK: ELLIPTICAL GALAXIES

The same RNB code discussed before was used to study the evolution of orbits of the globular clusters in elliptical galaxies. The elliptical galaxy models and the initial conditions for the particles used to trace the density distributions in these galaxies were already discussed in chapter four. The calculations in the case of elliptical galaxies were relatively easy as we had chosen a single, simple spheroidal model to mimic our galaxy.

In this chapter, section V1.1 discusses the code and section V1.2 gives the equations of motion. V1.3 discusses the energy integral and the units are defined in V1.4. Force calculations and phase mixing are discussed in section V1.5. The numerical integration is presented in V1.6 and some preliminary results of our simulations are discussed in section V1.7.

V1.1 The Numerical code

In the case of the elliptical galaxies, the three sub-systems in the code are :

(i) The potential of the spheroid which is kept fixed in space and time. The analytical form of this potential is

$$\Phi_{Gal} = -\frac{4\pi \rho_e r_c^3}{r}\left[\log\left(r/r_c\right) + \sqrt{1+(r/r_c)^2}\right] \qquad (6.1)$$

(ii) The tracer particles that follow the density distribution of

the elliptical galaxy and which have equal masses given by

$$m = \frac{M_{Gal}}{N} \qquad (6.2)$$

The total number of the tracer particles in the system was taken to be N_{total}= 5000, which was the same as the total number of tracers chosen in spiral galaxy runs. The same assumption, that is the forces between the particles being neglected was also used here.

(iii) The globular cluster was the final sub-system. The masses of the clusters were taken identical to the ones chosen in spiral galaxies runs, so that a direct comparison of the action of dynamical friction on these clusters could be made in both the types of galaxies.

As before, the tracer particles were made responsive to the forces imposed by the galaxy and the globular cluster.

VI.2 The Equations of Motion

The equations of motion for the globular cluster and the tracer particles in the case of the elliptical galaxy simulations are

$$\ddot{\underline{r}}_s = -G \sum_{i=1}^{N} \frac{m_i \left(\underline{r}_s - \underline{r}_i \right)}{\left\{ |\underline{r}_s - \underline{r}_i|^2 + \epsilon^2 \right\}^{3/2}} \qquad (6.3)$$

$$\ddot{\underline{r}}_i = \frac{-\partial \phi_{Gal}}{\partial \underline{r}} - \frac{G m_s \left(\underline{r}_i - \underline{r}_s \right)}{\left\{ |\underline{r}_i - \underline{r}_s|^2 + \epsilon^2 \right\}^{3/2}}$$

where $\underline{r}_s$ and m_s are the position and mass of the globular cluster

$\underline{r}_i$ and m_i are the position and mass of the i^{th} particle

ϕ_{gal} is the fixed galaxy potential

and the dots represent the time derivatives.

V1.3 The Energy Conservation

The energy integral, derived in a similar way as discussed in Appendix D, is

$$E = \frac{1}{2} m_s \dot{\underline{r}}_s^2 + \frac{1}{2} \sum_{i=1}^{N} m_i \dot{\underline{r}}_i^2 - \sum_i m_i \phi_{gal} - m_s \sum_{i=1}^{N} m_i \phi_{is} \qquad (6.4)$$

This energy E was used to check the accuracy of the code. As warned before, this energy integral is only an approximate one, since the equations of motion do not describe a fully self-consistent system.

V1.4 The Units

A dimensionless system of units were chosen where the Gravitational constant, G, the total mass of the galaxy M_{gal} and the total extent of the galaxy R_{gal} were all taken to be unity. The time and velocity units are

$$\text{Crossing time, } Tcr = \left[\frac{R_{gal}^3}{G M_{gal}}\right]^{1/2} = 1 \text{ time unit} \qquad (6.5)$$

and

$$\text{velocity} = \left[\frac{G M_{gal}}{R_{gal}}\right]^{1/2} = 1.0 \qquad (6.6)$$

Table X1 summarizes the units used in the code for the case of elliptical galaxy runs.

TABLE X1

Dimensional quantity	Symbol used in the text	Units	Physical values
Galaxy mass	M_{gal}	1.0	$4.0 * 10^{11} M_{\odot}$
Galaxy Radius	R_{gal}	1.0	28 Kpc.
Gravitational Constant	G	1.0	$6.68 * 10^{8}$

The translation from dimensionless units to physical units for the case when $M_{gal} = 4 * 10^{11} M_{\odot}$ and $R_{gal} = 28$ Kpc is as follows:

$$1 \text{ time unit} = 1.12 \times 10^{8} \text{ years} \qquad (6.7)$$

and

$$1 \text{ velocity unit} = 246 \text{ kms}^{-1} \qquad (6.8)$$

V1.4 Force Calculation and Phase Mixing

The derivative of the potential $\frac{\partial \phi_{gal}}{\partial r}$ used in equation (6.3) is given by

$$\frac{\partial \Phi_{gal}}{\partial r} = \frac{4\pi \rho_e r_c^3}{r^2}\left[\frac{(r/r_c)}{\sqrt{1+(r/r_c)^2}} - \log(r/r_c) + \sqrt{1+(r/r_c)^2}\right] \quad (6.9)$$

The initial model of the galaxy, comprised of the tracer particles is run through a mixing phase during which the globular cluster mass is kept zero. This is done to minimize any systematic effects of the initialization procedure. The phase mixing lasts for time units = 5 which corresponds to 5 crossing times. After this, the mass of the globular cluster is introduced into the runs.

V1.6 The Numerical Integration

The same second-order predictor-corrector method was used here for solving the equations of motion (6.3). The step-size chosen was again a variable one and was determined by the maximum velocity or acceleration

The Cpu time taken for a typical elliptical galaxy simulation was about 2 hours on the Gould 32/97.

The accuracy of the integrator was tested by the fractional change in $\Delta E/E$, where E is given by equation (6.4). The energy changes were less than 0.01 % in these runs. The accuracy observed in elliptical galaxy simulations was much higher than in spiral runs. We feel that the linear interpolation scheme used to compute the disk forces might be the cause for this poor accuracy in the case of the spiral galaxy simulations. A better interpolation scheme, such as the cubic spline might give good

accuracies in the case of spiral runs too.

V1.7 Preliminary results and discussion

The parameters determining our models of elliptical galaxies, the mass and radius were chosen to be, $M_{Gal} = 4 * 10^{11}$ $M_{\odot}$ and R_{Gal} = 28 Kpc. respectively. A total of N = 5000 tracer particles were chosen to trace the density distribution of the elliptical galaxy. The globular cluster parameters, mass, orbital radius and eccentricities were chosen to be the same as those for the spiral galaxy cases, converted to the units defined in table XI . The the values of the parameters reported in this section use the system of units given in that table. The results of each simulation are discussed independently below.

Case 1

Figure 29 shows the time evolution of a 5000-particle elliptical galaxy and a globular cluster simulation. The globular cluster can be seen as a star in these pictures. The mass of the globular cluster taken in this run was $M_{Gc} = 1.25 * 10^{-5}$, placed initially at a radius of r = 0.466. The orbital evolution of the cluster is shown in figure 30 . From the figure we see that the orbit remains almost unchanged in $2 * 10^{10}$ years.

Case 2

Figure 31 shows the orbital evolution of a cluster of mass M_{GC} = $1.25 * 10^{-4}$ placed initially on an orbit of radius r = 0.903,

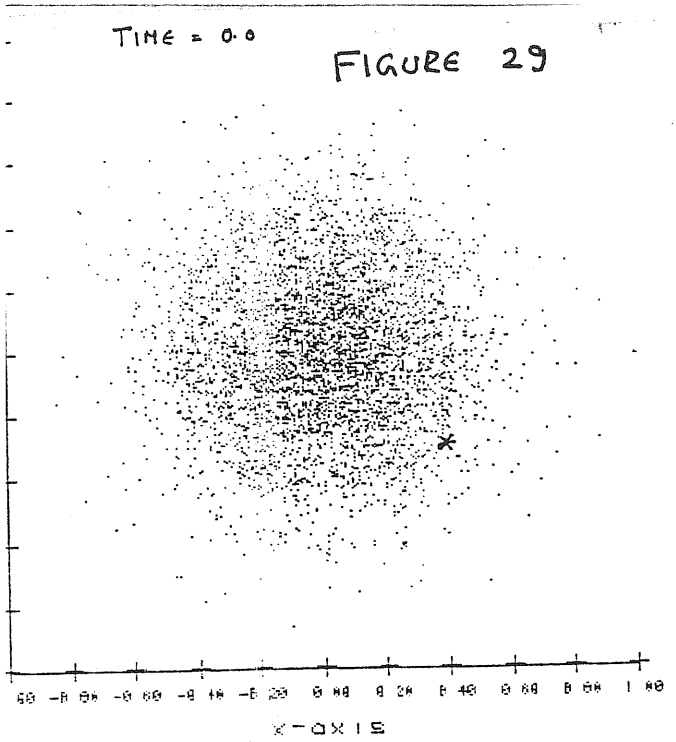
TIME = 0.0
x-axis

FIGURE 29

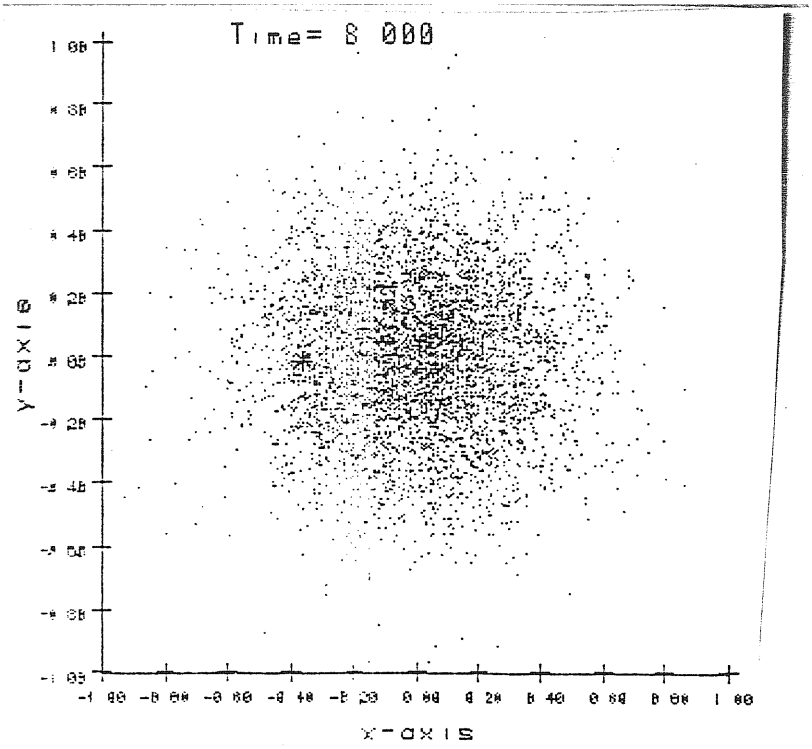
Time= 8.000
y-axis
x-axis

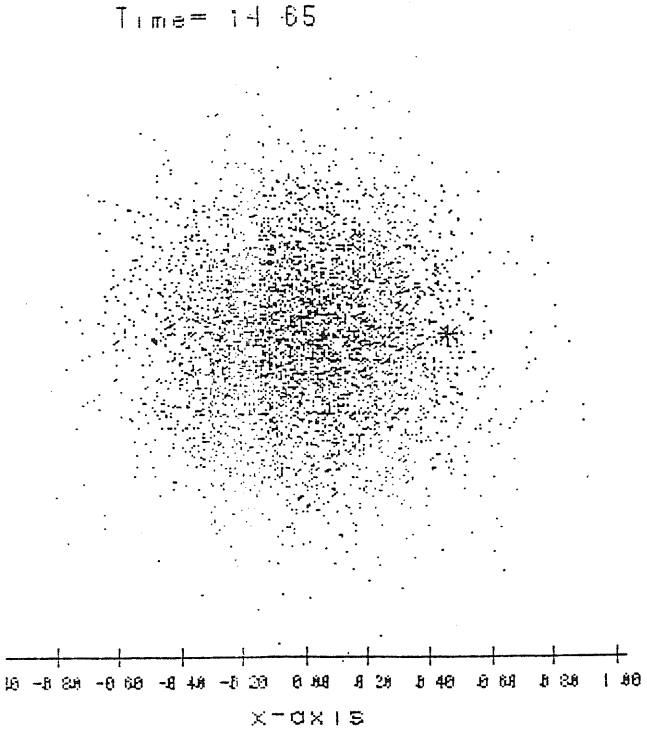
Time= 14.65
x-axis

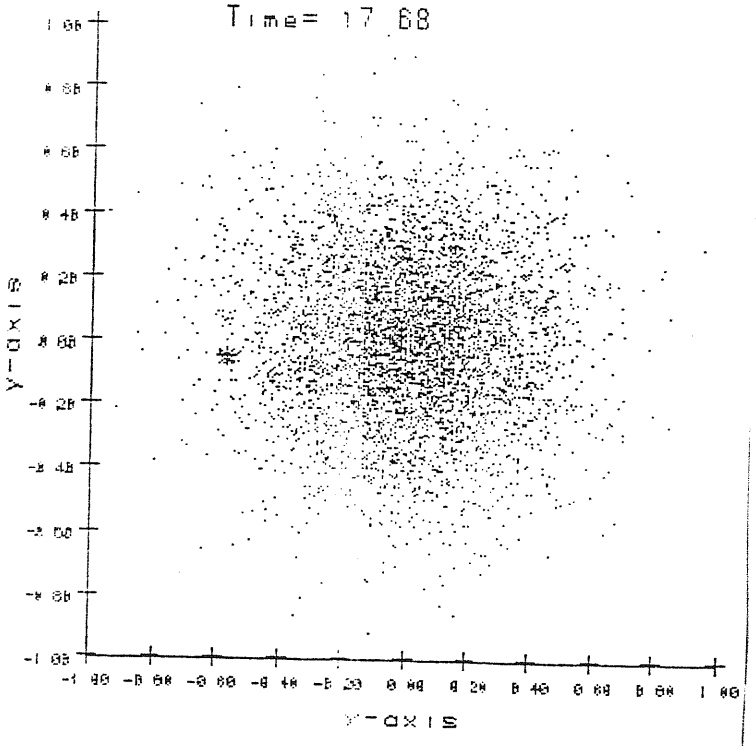
Time= 17.68
y-axis
x-axis

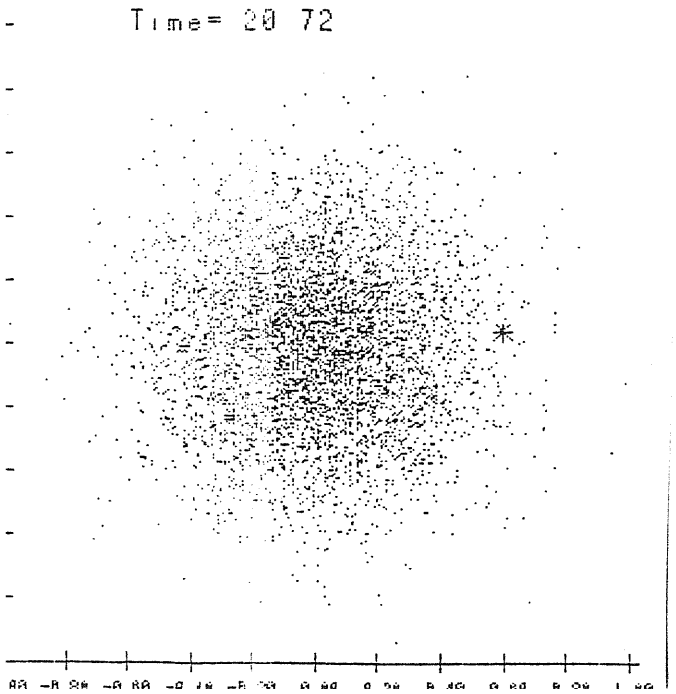
Time= 20.72

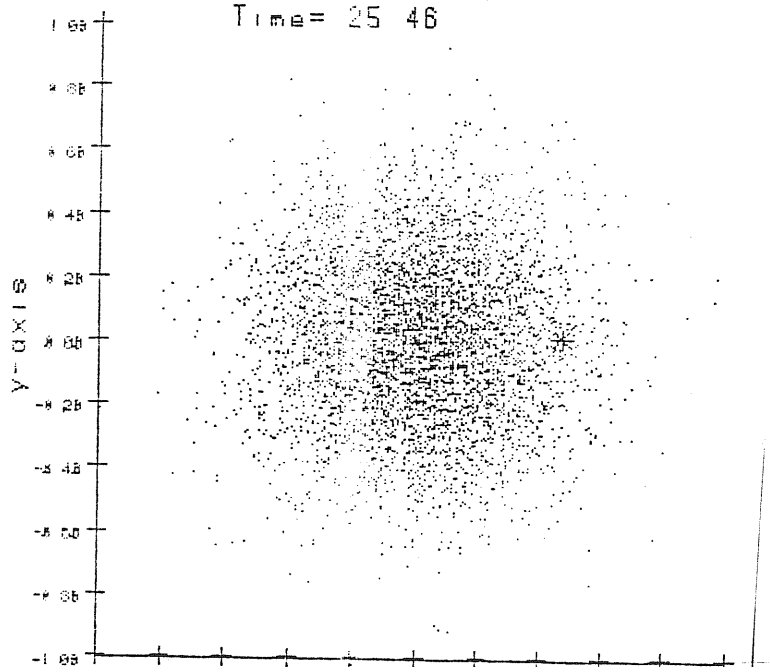
Time= 25.46
y-axis

FIGURE 30

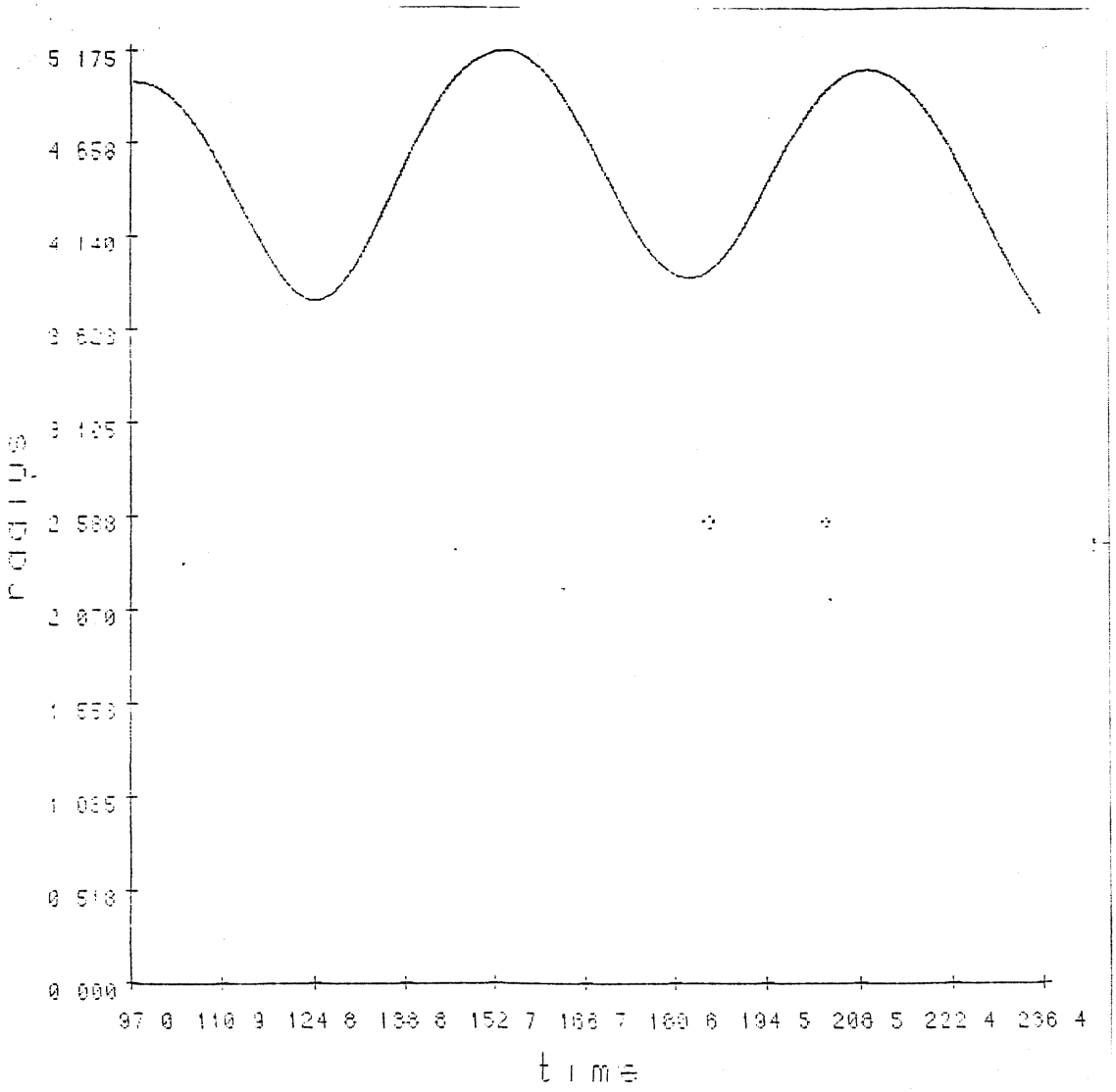
5 175
4 658
4 140
3 623
3 105
2 588
2 070
1 553
1 035
0 518
0 000
97 0
110 9
124 8
138 8
152 7
166 7
180 6
194 5
208 5
222 4
236 4
time

FIGURE 31

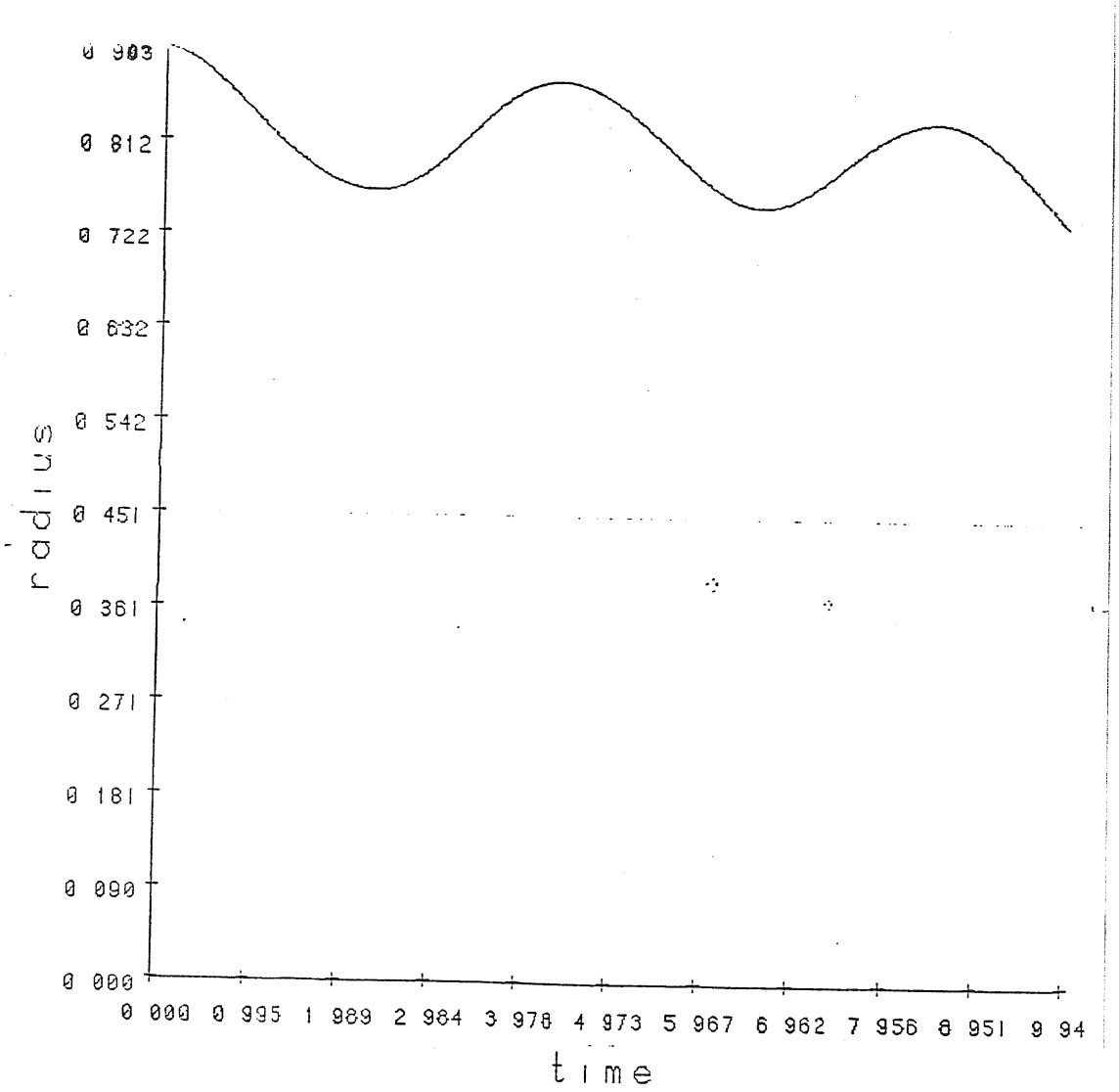
0 903
0 812
0 722
0 632
0 542
0 451
0 361
0 271
0 181
0 090
0 000
radius
0 000 0 995 1 989 2 984 3 978 4 973 5 967 6 962 7 956 8 951 9 94
time

corresponding to 25 Kpc., which is almost at the edge of our galaxy. (R_{Gal} = 28 Kpc.). From the figure, we see that there is a slow orbital decay for this cluster. In $\sim 10^9$ years, its orbit has changed from r = 0.903 to r = 0.83. The decay rate matches the value predicted by Chandrasekhar's dynamical friction formula.

Case 3

Figure 32 shows the orbital evolution of a globular cluster of mass $M_{Gc} = 1.25 * 10^{-5} M_{\odot}$, placed initially at a radius r = 0.25. From the figure, we see that there is no decay in the orbit of this cluster in 10^{10} years.

Case 4

Figure 33 shows the orbital evolution of a globular cluster of mass $M_{GC} = 1.25 * 10^{-4}$, placed initially at a radius r = 0.5. We notice that there is a slow decay in the orbit to r = 0.45 in 10^9 years. The sinking rate appears to be comparable to the rate observed for a cluster of the same mass but placed almost at the edge of the galaxy (case 2) than at half-way as in this case.

These simulations to study the orbital decay of globular clusters in elliptical galaxies show that

(i) The decay rates for globular clusters in these galaxies are negligible suggesting that dynamical friction on globular clusters in ellipticals is small. Observations of globular clusters in M87 agrees with this result. (Grillmair , Pritchet and van den Bergh

1986).

(ii) The larger decay rates obtained for globular clusters in spirals having the same masses as those considered here, must be due to the extra disk component present in those galaxies.

FIGURE 32

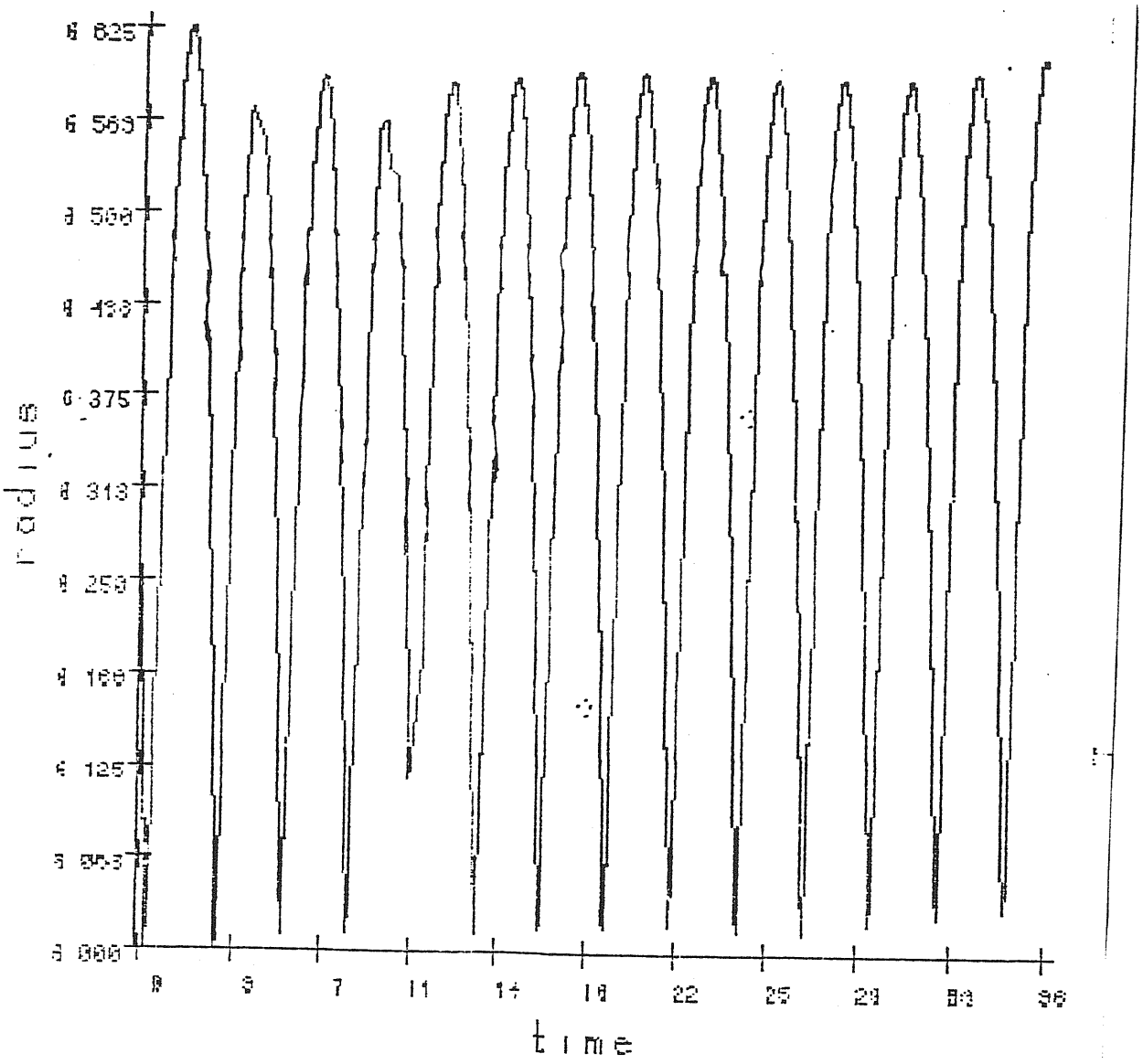
0.625
0.563
0.500
0.438
0.375
0.313
0.250
0.188
0.125
0.063
0.000
radius
0
3
7
11
14
18
22
25
29
33
36
time

FIGURE 33

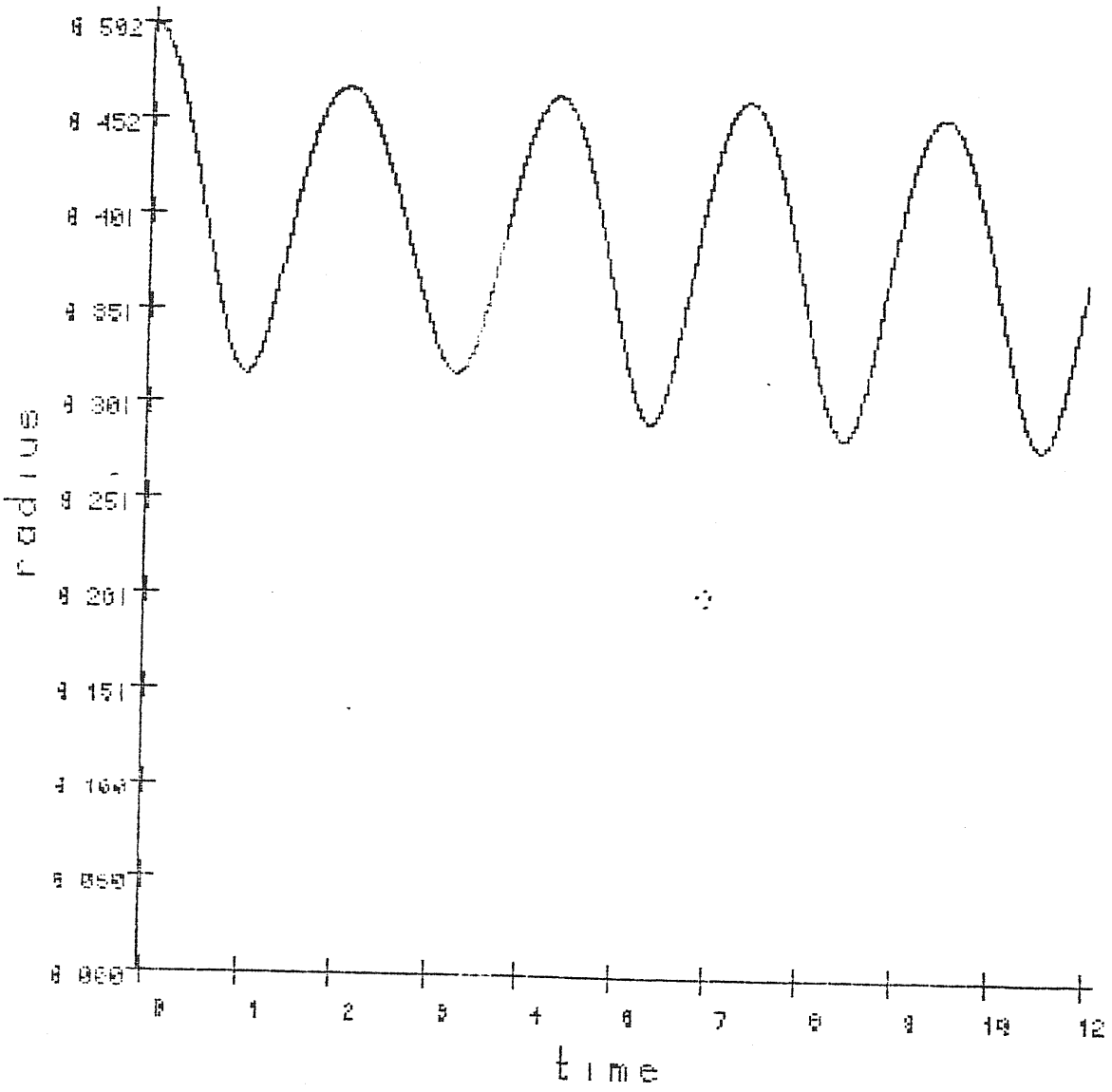
0.502
0.452
0.401
0.351
0.301
0.251
0.201
0.151
0.100
0.050
0.000
radius
0
1
2
3
4
5
6
7
8
9
10
11
12
time

CHAPTER SEVEN

Comments and Conclusions

A semi-restricted N-body (RNB) code was developed to study the action of dynamical friction on globular clusters in galaxies, especially to study and compare orbital decay rates of these clusters in elliptical and spiral galaxies. The question about the existence of an universal luminosity function for globular clusters , based on which extragalactic distances were determined was the motivation behind embarking on such a problem. These evaluated distances were used to obtain the Hubble constant, H_o, and the values of H_o obtained were in the range normally quoted i.e. 50 - 100 kms^{-1} Mpc^{-1}.The determination of these values did not take into account the uncertainty resulting from the assumption that the luminosity functions for globular clusters has the same form everywhere. Globular clusters in spirals are subjective to disruptive events like disk passages and moreover, these disks of spiral galaxies may enhance the action of dynamical friction leading to a rapid orbital decay for globular clusters in spirals than for the globular clusters in elliptical galaxies.

The RNB we developed proved to be very useful in studying the orbits of these clusters in both these kinds of galaxies. The main drawback of such a code was that we had neglected the self-gravity of our systems. The gain in computer time however is very large for such a code and this makes it possible to run many simulations. The results of our simulations can be summarized as

(i) The orbits of the globular clusters in spiral galaxies did not decay rapidly, indicating that dynamical friction is not very effective in removing massive globular clusters over a Hubble time and therefore account for the difference seen in the luminosity functions for the clusters in spirals and ellipticals.

(ii) The orbital evolution of globular clusters in the spiral galaxies proved to be complex, with the interactions between the particles and the globular cluster occurring mainly at resonance points. In a galaxy, the resonance structure is complicated and we know that near-resonant particles exert torques on satellites (in our case the globular cluster) and whether these torques are analogs of the Chandrasekhar's drag force or give opposite results, where the satellite gains energy and angular momentum has to be studied carefully. In one of our runs, we had found that the globular cluster gains energy and angular momentum at the inner Lindblad resonance point and begins to move outwards. Many runs are required to make any conclusive reports and understand the processes at resonances.

(iii) Elliptical galaxy simulations have shown that there is no decay in the globular cluster orbits compared to the decay rates seen for globular clusters in spirals. Observations of the M87 globular cluster systems (Grillmair, Pritchet and van den Bergh 1986) have also shown that dynamical friction on globular clusters is not an effective process in this giant elliptical galaxy.

(iv) Increasing the mass of the globular cluster by two orders of magnitude than what we considered for the above cases, we had obtained decay rates that were comparable to the ones predicted by

Chandrasekhar's formula. This indicates that Chandrasekhar's formula for dynamical friction does gives a rough estimate of the rate of orbital decay, in circumstances such as those that interest us here.

(v) From the few simulations we could carry out so far, it is possible to say that the disks in spirals play an important role on the orbits of the globular clusters and it would be very interesting and fruitful to do detail simulations on the interactions between the disks and satellites of spiral galaxies. For example, it would be interesting to check if disks slows or halts the satellites by adding angular momentum to the orbits of the satellites as fast as the halo component removes it. Detailed studies of resonances would answer many of these points. The RNB code becomes useful here, as it is possible to run many simulations with limited computing budgets.

Fully consistent N-body calculations are needed at this stage to study the consequences of neglecting self-gravity in our systems. This we plan to do immediately and see if there are any changes in the results.

The results obtained so far have indicated that dynamical friction alone cannot reproduce the luminosity function for globular clusters in spirals which is different from the function seen for elliptical globular clusters. However, we intend to run many more simulations before we are conclusive about this result. Including self-gravity in the system may enhance decay rates but we feel that it still might not be enough to remove the massive globular clusters in spirals and explain why we see this difference in luminosity functions. There is also the possibility

that the luminosity functions were never the same and we conclude on the note that Space Telescope observations on globular clusters in distant galaxies might be the answer to check for the universality of globular cluster luminosity functions and give definite answers to some of the questions raised here.

APPENDIX A

Multi-Grid techniques for solving the Poisson's equation in cylindrical co-ordinates

The basic idea of the multi-level adaptive techniques is to work not with a single grid but with a sequence of grids (" levels ") of increasing fineness, each of which may be introduced, changed in the process and constantly made to interact with one another. The method can be understood from the following simple example :

Consider a differential problem of the form

$$LU = F \qquad \text{in the domain } \Omega \qquad (A\cdot1)$$

With the boundary condition

$$\Lambda U = B \qquad (A\cdot2)$$

where L and Λ are linear operaters.

Suppose there are a set of grids G^0, G^1, ...G^M, all approximating the same domain Ω, with corresponding mesh-sizes $h_0 > h_1 \ldots\ldots > h_M$. Let the mesh-size ratio in this simple case with uniform square grids be $h_{K+1} : h_K = 1 : 2$. The equations ( ) and ( ) can be approximated by difference equations on each grid G^K as

$$L^K U^K = F^K \qquad (A\cdot3)$$

and the boundary condition as

$$\Lambda^K U^K = B^K \qquad (A\cdot 4)$$

After few iterations of any procedure, suppose we get an approximate solution u^M and we let

$$L^M u^M = F^M - f^M \qquad (A\cdot 5)$$

and

$$\Lambda^M u^M = B^M - b^M \qquad (A\cdot 6)$$

Here, the discrepancies, f^M and ϕ^M are called residuals. Now The exact solution of the problem we considered, U^M, can be written as

$$U^M = u^M + V^M \qquad (A\cdot 7)$$

where V^M is the correction that satisfies the equations

$$L^M V^M = f^M \qquad (A\cdot 8)$$

and

$$\Lambda^M V^M = b^M \qquad (A\cdot 9)$$

Equations (A·8) and (A·9) are called residual equations. To solve these equations to a good first approximation, just interpolation from the solutions on the coarser grids is not enough because not every G^M problem has a meaningful approximation on a coarser grid G^K. For instance, if the right hand side, f^M fluctuates rapidly on G^M with wavelengths less than $4h_M$, these

fluctuations are not visible on the coarser grids and therefore a good approximate solution is not possible. However, there is an effective way to damp these rapid fluctuations. This by using suitable relaxation procedures. Relaxation reduces high frequency components and the only modes left after few relaxation sweeps are the smooth ones. The result being , we are left with smooth function V^M, which can be approximated by a coarser grid function V^K, that satisfies

$$L^K v^K = I^K_M f^K \qquad (A\cdot 10)$$

Here I^K_M is a fine to coarse grid transfer operator. Since the coarse grid has less points than the fine grid, it is much faster to solve equation (A·10) than to solve equation (A·9). Having obtained an approximate solution v^k of equation (A·10), we can use it to accelerate the convergence of the fine grid .

$$u^M \leftarrow u^M + I^M_K v^K \qquad (A\cdot 11)$$

where I^M_K is a coarse to fine grid interpolation operator.

The multi-grid method can be seen in two complementary ways:

(i) The coarser grids can be seen viewed as correction grids, accelerating convergence of a relaxation scheme on the finest grid by efficiently liquidating smooth error components.

(ii) The finer grids can be regarded as the correction grids, improving accuracy on coarser grids by correcting their forcing terms. This makes it possible to manipulate accurate solutions on coarser grids, with only few visits to pieces of finer levels.

The multi-grid method is very efficient. A discrete system of n equations (n points in the finest grid) is solved to the

desired accuracy in O(n) computer operations.

The example discussed above outlines the basic principles involved in multi-grid methods. Suitable relaxation, residual transfers and interpolation schemes are to be designed according to the problem that has to be solved.

We have used the algorithm provided by Brandt (1977) to solve our Poisson's equation, to obtain the potential of an axisymmetric disk in the models of our spiral galaxies.

The Poisson's equation in cylindrical co-ordinates of our disk is

$$\frac{1}{r}\frac{\partial}{\partial r}\left(r\frac{\partial \phi}{\partial r}\right) + \frac{\partial^2 \phi}{\partial z^2} = -4\pi f_0 e^{-\alpha r} e^{-\beta|z|} \qquad (A.12)$$

And the boundary conditions are

$$r = 0, \quad \frac{\partial \phi}{\partial r} = 0 \quad ; \quad r \to \infty, \quad \phi = 0 \qquad (A.13)$$

$$z = 0, \quad \frac{\partial \phi}{\partial z} = 0 \quad ; \quad |z| \to \infty, \quad \phi = 0 \qquad (A.14)$$

The discretized form of the equation (A.12) can be written as

$$r\left[\frac{\phi_{i+1,j} - 2\phi_{i,j} + \phi_{i-1,j}}{h_r^2}\right] + \left[\frac{\phi_{i+1,j} - \phi_{i-1,j}}{2h_r}\right] + r\left[\frac{\phi_{i,j+1} - 2\phi_{i,j} + \phi_{i,j-1}}{h_z^2}\right] = f(r, z) \qquad (A.15)$$

where

$$f(r,z) = -4\pi f_0 r e^{-\alpha r} e^{-\beta|z|}$$

and h_r and h_z are the mesh-sizes in r and z respectively. For our disk, we have $h_r >> h_z$.

After few simple manipulations, equation (A·14) can be written as

$$2r\left[\frac{h_r}{h_z}+\frac{h_z}{h_r}\right]\phi_{i,j} = h_r h_z f(r,z) - \left[\frac{h_z}{h_r} r\left(\phi_{i+1,j}+\phi_{i-1,j}\right) + \frac{h_z}{2}\left(\phi_{i+1,j}-\phi_{i-1,j}\right) + \frac{h_r}{h_z} r\left[\phi_{i,j+1}+\phi_{i,j-1}\right]\right] \quad (A.16)$$

This is the expression that will be solved in the multi-grid code.

The algorithm provided by Brandt written in cartesian co-ordinates needed considerable modifications to solve this equation. The changes involved were the following:

(1) Relaxation

The Gauss-Seidel relaxation scheme which involves point relaxation was found not to be effective in reducing errors on the boundary because of the coupling of the errors. (Recall h_r h_z). A line relaxation scheme had to be used where one updates the solution simultaneously along a grid line at a time. This means we had to solve a tridiagonal system. Brandt's code was for Direchlet boundary conditions. Neumann type boundary conditions (equations ( ) needs to be treated separately from interior equations, otherwise the smoothness of the errors will be destroyed (Brandt 1977). We have treated the boundary conditions as follows:

(a) For $\frac{\partial\phi}{\partial r} = 0$

Let

$$\frac{\partial \phi}{\partial r} = g \qquad (A\cdot 17)$$

$$\frac{\partial^2}{\partial z^2}\left(\frac{\partial \phi}{\partial r}\right) = \frac{\partial^2}{\partial z^2} g \qquad (A\cdot 18)$$

We write

$$\frac{\partial \phi}{\partial r} = \frac{\phi_{i,2} - \phi_{i,-1}}{2h_r} \qquad (A\cdot 19)$$

Using an extrapolation of the form (see figure)

$$x_{-1} = 3x_1 - 3x_2 + x_3$$

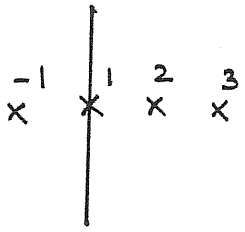

equation (A·19) becomes

$$\frac{\partial \phi}{\partial r} = \frac{\phi_{i,2} - 3\phi_{i,1} + 3\phi_{i,2} - \phi_{i,3}}{2h_r} = g \qquad (A\cdot 20)$$

Now we can write equation (A·18) as

$$\frac{\partial^2}{\partial z^2}\left[\frac{\phi_{i,2} - 3\phi_{i,1} + 3\phi_{i,2} - \phi_{i,3}}{2h_r}\right] = \frac{\partial^2}{\partial z^2} g \qquad (A\cdot 21)$$

$$\frac{\partial^2}{\partial z^2}\left[\frac{-1\cdot 5\,\phi_{i,1} + 2\phi_{i,2} - 0\cdot 5\,\phi_{i,3}}{h_r}\right] = \frac{\partial^2}{\partial z^2} g \qquad (A\cdot 22)$$

$$\frac{-1.5}{h_r}\left[\frac{\phi_{i+1,1}-2\phi_{i,1}+\phi_{i-1,1}}{h_z^2}\right]+\frac{2}{h_r}\left[\frac{\phi_{i+1,2}-2\phi_{i,2}+\phi_{i-1,2}}{h_z^2}\right]$$

(A.23)

$$-\frac{0.5}{h_r}\left[\frac{\phi_{i+1,3}-2\phi_{i,3}+\phi_{i-1,3}}{h_z^2}\right]=\frac{g_{i+1}-2g_{i,1}+g_{i-1,1}}{h_z^2}$$

which becomes

$$\frac{1.5}{h_r}\left[\phi_{i+1,1}-2\phi_{i,1}+\phi_{i-1,1}\right]=g_{i+1,1}-2g_{i,1}+g_{i-1,1}-$$

$$\frac{2}{h_r}\left[\phi_{i+1,2}-2\phi_{i,2}+\phi_{i-1,2}\right]+\frac{0.5}{h_r}\left[\phi_{i+1,3}-2\phi_{i,3}+\phi_{i-1,3}\right]$$

(A.24)

The final equation after simple algebra is

$$\frac{.5}{h_r}(2\phi_{i,1})=g_{i+1,1}+\frac{1.5}{h_r}\phi_{i+1,1}-\frac{2}{h_r}\phi_{i+1,2}+\frac{0.5}{h_r}\phi_{i+1,3}+$$

$$g_{i-1,1}+\frac{1.5}{h_r}\phi_{i-1,1}-\frac{2}{h_r}\phi_{i-1,2}+\frac{0.5}{h_r}\phi_{i-1,3}-2g_{i,1}$$

$$+\frac{2}{h_r}*2\phi_{i,2}-\frac{0.5}{h_r}*2\phi_{i,3}$$

(A.25)

The same procedure is done for the other boundary condition

The residuals were obtained as following.

$$r_{i,1} = g_{i,1} - \frac{\left(-1.5\phi_{i,1} + 2\phi_{i,2} - 0.5\phi_{i,3}\right)}{h_r}$$

$$r_{i+1,1} = g_{i+1,1} - \frac{\left(-1.5\phi_{i+1,1} + 2\phi_{i+1,2} - 0.5\phi_{i+1,3}\right)}{h_r} \qquad (A \cdot 26)$$

$$r_{i-1,1} = g_{i-1,1} - \frac{\left(1.5\phi_{i-1,1} + 2\phi_{i-1,2} - 0.5\phi_{i-1,3}\right)}{h_r}$$

Substituting these in the equation (A·25), we get

$$\frac{1.5}{h_r}\left(\phi_{i,1}\right) = r_{i+1,1} + r_{i-1,1} - 2\left(g_{i,1} + \frac{2}{h_r}\phi_{i,2} - \frac{0.5}{h_r}\phi_{i,3}\right) \qquad (A \cdot 27)$$

$$\frac{1.5}{h_r}\left(\phi_{i,1}\right) = -\left(g_{i,1} - \frac{2}{h_r}\phi_{i,2} + \frac{0.5}{h_r}\phi_{i,3}\right) + \frac{1}{2}\left(r_{i+1,1} + r_{i-1,1}\right)$$

If

$$\delta\phi_{i,1} = \phi_{i,1}^{New} - \phi_{i,1}^{old}$$

$$\phi_{i,1}^{New} = \phi_{i,1}^{old} + \delta\phi_{i,1} \qquad (A \cdot 28)$$

Where $\delta\phi_{i,1}$ is a small change by which the current approximate solution $\phi_{i,1}$, is updated during the iteration.

Now the equation (A·27) can be written as

$$\frac{1.5}{h_r}\left(\phi^{old}_{i,1} + \delta\phi_{i,1}\right) = -\left(g_{i,1} - \frac{2}{h_r}\phi_{i,2} + \frac{0.5}{h_r}\phi_{i,3}\right) + \frac{1}{2}\left(r_{i+1,1} + r_{i-1,1}\right.$$

$$\frac{1.5}{h_r}\left[\delta\phi_{i,1}\right] = -\left(g_{i,1} + \frac{1.5}{h_r}\phi^{old}_{i,1} - \frac{2}{h_r}\phi_{i,2} + \frac{0.5}{h_r}\phi_{i,3}\right) + \frac{1}{2}\left[r_{i+1,1} + r_{i-1,1}\right]$$

$$\frac{1.5}{h_r}\left[\delta\phi_{i,1}\right] = \frac{1}{2}\left[r_{i+1,1} + r_{i-1,1}\right] - r_{i,1} \qquad (A\cdot29)$$

Then the change $\delta\phi_{i,1}$ is

$$\delta\phi_{i,1} = \left\{\frac{1}{2}\left[r_{i+1,1} + r_{i-1,1}\right] - r_{i,1}\right\} * \frac{h_r}{1.5} \qquad (A\cdot30)$$

(2) Residual Transfers

In the case of cylindrical co-ordinates the Poisson's equation has non constant coefficients. Therefore a straight injection of the residual transfer is not enough. A full weighting of the residuals is necessary. A nine-point formula of the kind

$$\frac{1}{16}\begin{pmatrix} 1 & 2 & 1 \\ 2 & 4 & 2 \\ 1 & 2 & 1 \end{pmatrix} \qquad (A\cdot31)$$

was used. The residual transfer of the boundary conditions were treated separately in our code too.

From the expression for the density of the disk we see that the potential does not fall to zero as fast as we would like it to. This means to use $\phi = 0$ is not a satisfactory solution on the boundary of our finite grid. What is really needed are higher-order terms of the potential and since this means solving an integral at every grid point on the boundary line, we chose to use the solution of the problem obtained by an alternate method (direct integration) as the values of the potential on the boundary.

The multi-grid method took 43 seconds to solve for the potentials on a grid of size 132 * 132 on the Gould 32/97 computer.

APPENDIX B

Evaluation of the Disk potential using Fourier transforms

The Poisson's equation for the axisymmetric disk in cylindrical co-ordinates is

$$\frac{\partial^2\phi}{\partial r^2} + \frac{1}{r}\frac{\partial\phi}{\partial r} + \frac{\partial^2\phi}{\partial z^2} = -4\pi G \rho_0 e^{-\alpha r} e^{-\beta|z|} \qquad (B.1)$$

$$r^2\frac{\partial^2\phi}{\partial r^2} + r\frac{\partial\phi}{\partial r} + r^2\frac{\partial^2\phi}{\partial z^2} = -r^2 4\pi G \rho_0 e^{-\alpha r} e^{-\beta|z|} \qquad (B.2)$$

Following Toomre (1963), we have written down the exponential density in the radial direction r as

$$e^{-\alpha r} = \int_0^\infty J_0(kr)\, S(k)\, dk \qquad (B.3)$$

where

$$S(k) = \int_0^\infty J_0(kr)\, r\, e^{-\alpha r}\, dr \qquad (B.4)$$

$$= \frac{\alpha}{[\alpha + k^2]^{3/2}}$$

Equation (B.2) can be now be written as

$$r^2\frac{\partial^2\phi}{\partial r^2} + r\frac{\partial\phi}{\partial r} + r^2\frac{\partial^2\phi}{\partial z^2} = -r^2 4\pi G \rho_0 e^{-\beta|z|}\int_0^\infty J_0(k_0 r)\, S(k)\, dk \qquad (B.5)$$

We have

$$\frac{\partial^2 \underline{G}}{\partial r^2} + \frac{1}{r}\frac{\partial \underline{G}}{\partial r} + \frac{\partial^2 \underline{G}}{\partial z^2} = 0$$

$$\underline{G} = \int_0^\infty dk\, J_0(kr)\, e^{ikz} \qquad (B.6)$$

where $\underline{G}$ is the Green's function.

The disk's potential can now be written as

$$\phi(r,z) = -4\pi G\rho_0 \int_0^\infty dk \int_0^\infty dk' \int_0^\infty dz' \int_0^\infty dr' \left[J_0\left[k(r-r')\right] J_0\left[k'\alpha r'\right]\right] * k' s(k')\, e^{ik(z-z') - \beta z'} \qquad (B.7)$$

$$\phi(r,z) = -4\pi G\rho_0 \int_0^\infty dk' \int_0^\infty dk \int_0^\infty dr' \int_0^\infty J_0\left[k(r'-r)\right] J_0\left[k'\alpha r'\right] * \frac{\alpha k'}{\left[\alpha^2+k'^2\right]^{3/2}} e^{ik(z-z') - \beta|z|} \qquad (B.8)$$

$$\phi(r,z) = -4\pi G\rho_0 \int_0^\infty dk' \int_0^\infty dk \int_0^\infty dr'\, J_0\left[k(r-r')\right] J_0\left[k'\alpha r'\right] * \frac{\alpha k'}{\left[\alpha^2+k'^2\right]^{3/2}} e^{ikz} \int_0^\infty dz'\, e^{-z'(ik+\beta)} \qquad (B.9)$$

The next step is to find these integrals by just tedious algebra. The main steps are outlined here. The final equation in this appendix was the one used to compute the potentials numerically by a Gauss-Quadrature integrator routine.

$$\phi(r,z) = \int_0^\infty dk' \int_0^\infty dk \int_0^\infty dr'\, J_0\left[k(r-r')\right] J_0\left[k'\alpha r'\right] \frac{\alpha k'}{\left[\alpha^2+k'^2\right]^{3/2}} e^{ikz} \frac{1}{ik+\beta}$$

$$:r,z) = \int_0^\infty dk' \frac{\alpha k'}{(\alpha^2+k'^2)^{3/2}} \int_0^\infty dk \frac{1}{(ik+\beta)} e^{ikz} \int_0^\infty dr' J_0\left[k(r-r')\right] J_0\left[k'\alpha r'\right]$$

$$:r,z) = \int_0^\infty dk' \frac{\alpha k'}{(\alpha^2+k'^2)^{3/2}} \int_0^\infty dr' J_0\left[k'\alpha r'\right] \int_0^\infty dk \frac{e^{ikz}}{(ik+\beta)} J_0\left[k(r-r')\right]$$

$$r,z) = \int_0^\infty dk' \frac{\alpha k'}{(\alpha^2+k'^2)^{3/2}} \int_0^\infty dr' J_0\left[k'\alpha r'\right] i\left\{\sinh(\beta z) K_0\left[\beta(r-r')\right]\right.$$

$$\left. + \cosh(\beta z) K_0\left[\beta(r-r')\right] - \pi e^{-\beta z} I_0\left[\beta(r-r')\right]\right.$$

$$:r,z) = \int_0^\infty dk' \frac{\alpha k'}{(\alpha^2+k'^2)^{3/2}} \int_0^\infty dr' J_0\left[k'\alpha r'\right] iK_0\left[\beta(r-r')\right]\left[\sinh(\beta z) + \right.$$

$$\left. \cosh(\beta z)\right] - \pi e^{-\beta z} I_0\left[\beta(r-r')\right]$$

$$r,z) = \int_0^\infty dk' \frac{\alpha k'}{(\alpha^2+k'^2)^{3/2}} \int_0^\infty dr' J_0\left[k'\alpha r'\right] iK_0\left[\beta(r-r')\right] *$$

$$\left[\frac{1}{2}\left(e^{\beta|z|} - e^{-\beta|z|}\right) + \frac{1}{2}\left(e^{\beta|z|} + e^{-\beta|z|}\right)\right] - \pi e^{-\beta|z|} I_0\left[\beta(r-r')\right]$$

$$r,z) = \int_0^\infty dk' \frac{\alpha k'}{\left[\alpha^2+k'^2\right]^{3/2}} \int_0^\infty dr' J_0\left[k'\alpha r'\right]\left\{ iK_0\left[\beta(r-r')\right] e^{\beta z}\right.$$

$$\left. - \pi e^{-\beta|z|} I_0\left[\beta(r-r')\right]\right\}$$

$$\phi(r,z) = -\int_0^\infty dk' \frac{\alpha k'}{\left[\alpha^2 + k'^2\right]^{3/2}} \frac{\beta^2}{(\beta^2 - k^2)} \left[\frac{e^{-k|z|}}{k} - \frac{e^{-\beta|z|}}{\beta}\right]$$

Which is the expression used (equation (4.9)) in chapter four to derive the potential of the disk numerically.

APPENDIX C

Analytical derivations for the Potentials and the Forces for the Spheroid and Halo components of a Spiral Galaxy

(i) The Spheroid

The expression for the density distribution of the spheroid is

$$\rho_{sp}(r) = \frac{\rho_s}{\left[1 + (r/r_s)^2\right]^{3/2}} \qquad (C.1)$$

The mass distribution is given by

$$M_{sp}(r) = 4\pi \int_0^{R_{sp}} \rho_s(r)\, r^2\, dr \qquad (C.2)$$

Where R_{sp} is the radial extent of the spheroid.

Putting equation (C.1) in this, we have

$$M_{sp}(r) = 4\pi \rho_s \int_0^{R_{sp}} \frac{r^2}{\left[1 + (r/r_s)^2\right]^{3/2}}\, dr \qquad (C.3)$$

Solving the integral we obtain

$$M_{sp}(r) = 4\pi \rho_s r_s^3 \left[\frac{-(r/r_s)}{\sqrt{1+(r/r_s)^2}} + \log\left\{ (r/r_s) + \sqrt{1+(r/r_s)^2} \right\} \right] \quad (C.4)$$

The potential can be obtained by solving the Poisson's equation

$$\nabla^2 \phi_{sp}(r) = -4\pi G \rho_{sp}(r) \quad (C.5)$$

A particular solution of equation (C.5) which falls to zero, as $r \to \infty$ and also excludes a point at the origin is

$$\phi_{sp}(r) = \frac{4\pi}{r} \int_0^\infty \rho_{sp}(r)\, r^2\, dr + 4\pi \int_r^\infty \rho(r)\, r\, dr \quad (C.6)$$

$$\phi_{sp}(r) = \frac{4\pi}{r} \int_0^\infty \frac{\rho_s r^2}{\left[1+(r/r_s)^2\right]^{3/2}} dr + 4\pi \int_r^\infty \frac{\rho_s r}{\left[1+(r/r_s)^2\right]^{3/2}} dr \quad (C.7)$$

$$\phi_{sp}(r) = \frac{4\pi \rho_s r^2}{r} \int_0^\infty \frac{(r/r_s)^2}{\left[1+(r/r_s)^2\right]^{3/2}} dr + 4\pi \rho_s r_s \int_r^\infty \frac{(r/r_s)}{\left[1+(r/r_s)^2\right]^{3/2}} \quad (C.8)$$

Solving the integrals, we obtain

$$\phi_{sp}(r) = \frac{4\pi \rho_s r_s^3}{r} \left[\frac{-(r/r_s)}{\sqrt{1+(r/r_s)^2}} + \log\left(\frac{r}{r_s} + \sqrt{1+(r/r_s)^2} \right) + \frac{(r/r_s)}{\sqrt{1+(r/r_s)^2}} \right]$$

which gives

$$\phi_{sp}(r) = -\frac{4\pi \rho_s r_s^3}{r}\left[\log\left\{(r/r_s) + \sqrt{1+(r/r_s)^2}\right\}\right] \qquad (C.10)$$

The force is then given by

$$\frac{\partial \phi_{sp}(r)}{\partial r} = \frac{4\pi \rho_s r_s^3}{r}\left[\frac{(r/r_s)}{\sqrt{1+(r/r_s)^2}} - \log\left(r/r_s + \sqrt{1+(r/r_s)^2}\right)\right] \qquad (C.11$$

These are the equations used in chapter four.

(ii) <u>The Halo</u>

The density distribution for the spherically symmetric halo is

$$\rho_H(r) = \frac{\rho_h}{1+(r/r_h)^2} \qquad (C.12)$$

The mass distribution is given by

$$M_H(r) = \int_0^{R_H} \rho_H(r)\, r^2\, dr, \quad \text{where } R_H \text{ is the cut-off radius.} \qquad (C.13)$$

Putting equation (C.12) in this expression we have

$$M_H(r) = 4\pi \rho_h r_h^2 \int_0^{R_H} \frac{(r/r_h)^2}{1+(r/r_h)^2}\, dr \qquad (C.14)$$

Solving the integral we obtain

$$M_H(r) = 4\pi \rho_h r_h^3 \left[(r/r_h) - \tan^{-1}(r/r_h) \right] \qquad (C.15)$$

The potential is obtained by solving the Poisson's equation

$$\nabla^2 \bar{\Phi}_H(r) = -4\pi G \rho_H(r) \qquad (C.16)$$

The solution of equation (C.16) that tends to zero when $\rho_H = 0$ at $r >> R_H$ is

$$\bar{\Phi}_H(r) = \frac{4\pi}{} \int_0^{R_H} \rho(r) r^2 dr + 4\pi \int_{R_H}^{\infty} \rho(r) r \, dr \qquad (C.17)$$

Substituting equation (C.12) and solving the integrals we get

$$\bar{\Phi}_H(r) = -4\pi \rho_h r_h^2 \left[1 - \frac{\tan^{-1}(r/r_h)}{(r/r_h)} - \frac{1}{2} \log \left\{ 1 + (r/r_h)^2 \right\} \right] \qquad (C.18)$$

The force then is

$$\frac{\partial \bar{\Phi}_H(r)}{\partial r} = -\frac{4\pi \rho_h r_h^2}{r^2} \left[\frac{(r/r_h)^2}{1+(r/r_h)^2} + \frac{1}{1+(r/r_h)^2} - \frac{\tan^{-1}(r/r_h)}{(r/r_h)} \right] \qquad (C.19)$$

Equations (C.18) and (C.19) are the desired expressions.

APPENDIX D

The Approximate Energy Integral

The equations of motion in the RNB code are

$$m_s \ddot{\underline{r}}_s = -m_s \sum_{i=1}^{N} \frac{m_i (\underline{r}_i - \underline{r}_i)}{\left\{ (\underline{r}_s - \underline{r}_i)^2 + \epsilon^2 \right\}^{3/2}} \qquad (D.1)$$

$$m_i \ddot{\underline{r}}_i = -\frac{m_i \partial \Phi_{Gal}}{\partial r_i} - \frac{m_i m_s (\underline{r}_i - \underline{r}_s)}{\left\{ |\underline{r}_i - \underline{r}_s|^2 + \epsilon^2 \right\}^{3/2}} \qquad (D.2)$$

where $\underline{r}_s$ and m_s are the position vector and mass of the globular cluster,

$\underline{r}_i$, m_i are the position and mass of the i^{th} particle,

$\Phi_{Gal} = \Phi_{disk} + \Phi_{spheroid} + \Phi_{Halo}$ in the case of the spiral galaxy and

$\Phi_{Gal} = \Phi_{Spheroid}$ in the case of the elliptical galaxy.

Multiplying scalarly, equation (D.1) by $\dot{\underline{r}}_s$ and equation (D.2) by $\dot{\underline{r}}_i$, where $\dot{\underline{r}}_s$ and $\dot{\underline{r}}_i$ denote the velocities of the satellite and the i^{th} particle respectively, and taking a sum over i in equation (D.2), we get

$$m_s \ddot{\underline{r}}_s \dot{\underline{r}}_s = -m_s \sum_{i=1}^{N} \frac{m_i (\underline{r}_s - \underline{r}_i)}{\left\{ |\underline{r}_s - \underline{r}_i|^2 + \epsilon^2 \right\}^{3/2}} \cdot \dot{\underline{r}}_s \qquad (D.3)$$

$$\sum_i m_i \ddot{\underline{r}}_i \dot{\underline{r}}_i = - \sum_i m_i \frac{\partial \Phi_{cal}}{\partial \underline{r}_i} \cdot \dot{\underline{r}}_i - m_s \sum_i m_i \frac{(\underline{r}_i - \underline{r}_s)}{\left\{ |\underline{r}_i - \underline{r}_s|^2 + \epsilon^2 \right\}^{3/2}} \cdot \dot{\underline{r}}_i \qquad (D.4)$$

Adding equations (D.3) and (D.4) we get

$$m_s \ddot{\underline{r}}_s \cdot \dot{\underline{r}}_s + \sum_i m_i \ddot{\underline{r}}_i \cdot \dot{\underline{r}}_i = - \sum m_i \frac{\partial \Phi_{cal}}{\partial \underline{r}_i} \cdot \dot{\underline{r}}_i - m_s \sum_{i=1}^{N} \frac{m_i (\underline{r}_s - \underline{r}_i)}{\left\{ (\underline{r}_s - \underline{r}_i)^2 + \epsilon^2 \right\}^{3/2}} \cdot \dot{\underline{r}}_s$$

$$- m_s \sum_i m_i \frac{(\underline{r}_i - \underline{r}_s)}{\left\{ |\underline{r}_i - \underline{r}_s|^2 + \epsilon^2 \right\}^{3/2}} \cdot \dot{\underline{r}}_i \qquad (D.5)$$

It is important to note that Φ is a function only of the position co-ordinates and not a function of the velocity components and that the independent variable time t, is not explicitly present in the expression for Φ. As a consequence of these properties, the following relation will hold:

$$\frac{d\Phi}{dt} = \frac{\partial \phi}{\partial \underline{r}} \dot{\underline{r}}_i \qquad (D.7)$$

Therefore equation (D.6) can be written as

$$\frac{d}{dt}\left(\frac{1}{2} m_s \dot{\underline{r}}_s^2 + \frac{1}{2} \sum_i m_i \dot{\underline{r}}_i^2 \right) = \sum m_i \frac{d\phi_{cal}}{dt} + m_s \sum m_i \frac{d\phi_{is}}{dt} \qquad (D.8)$$

where $$\phi_{is} = \frac{-(\underline{r}_i - \underline{r}_s)}{\left[|\underline{r}_i - \underline{r}_s|^2 + \varepsilon^2\right]^{1/2}} \qquad (D.9)$$

Equation (D.8) becomes

$$\frac{d}{dt}\left(\frac{1}{2} m_s \dot{\underline{r}}_s^2 + \frac{1}{2} \sum_i m_i \dot{\underline{r}}_i^2 - \sum m_i \phi_{cal} - m_s \sum m_i \phi_{is}\right) = 0 \qquad (D.10)$$

Integrating equation (D.10), we obtain

$$\frac{1}{2} m_s \dot{\underline{r}}_s^2 + \frac{1}{2} \sum_i m_i \dot{\underline{r}}_i^2 - \sum m_i \phi_{cal} - m_s \sum m_i \phi_{is} = E \qquad (D.11)$$

which is the energy integral of the system.

APPENDIX E

The Disk Force Calculations

The potentials of the disk computed numerically, either by the multi-grid method or the Gauss-Quadrature method, were stored on a grid at the grid-positions (i,j), with i,j = 1 to 132. The resultant acceleration on each particle was then determined by a simple linear interpolation scheme.

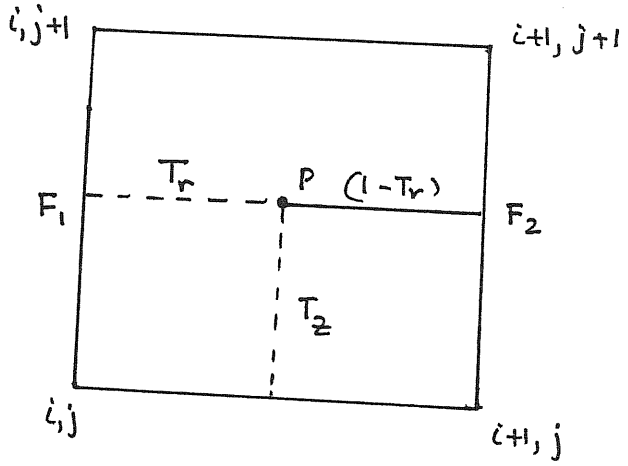

In the figure, let P be the position of the particle on which the force has to be computed from the known potentials at the grid points (i,j), (i+1,j), (i,j+1) and (i+1,j+1).

Let F_r (P) be the radial force on the particle and it is written down as

$$F_r(P) = (1 - T_r) F_1 + T_r F_2 \qquad (E\cdot1)$$

using simple linear interpolation. In the above equation, F_1 and F_2 are given by (see the above figure)

$$F_1 = (1 - T_2) F_{i,j} + T_2 F_{i,j+1} \qquad (E\cdot2)$$

$$F_2 = (1 - T_2) F_{i+1,j} + T_2 F_{i+1,j+1} \qquad (E\cdot3)$$

where $F_{i,j}$, $F_{i,j+1}$, $F_{i+1,j}$ and $F_{i+1,j+1}$ are forces at the

grid-points (i,j),(i,j+1),(i+1,j) and (i+1,j+1) respectively. These are evaluated using a central difference formula from the potentials as

$$F_{i,j} = \frac{\phi_{i,j+1} - \phi_{i,j-1}}{2h_r}$$

$$F_{i,j+1} = \frac{\phi_{i,j+2} - \phi_{i,j}}{2h_r} \qquad (\epsilon\cdot 4)$$

$$F_{i+1,j} = \frac{\phi_{i+1,j+1} - \phi_{i+1,j-1}}{2h_r}$$

$$F_{i+1,j+1} = \frac{\phi_{i+1,j+2} - \phi_{i+1,j}}{2h_r}$$

where h_r is the mesh-size in the radial direction.

Substituting equations ($\epsilon\cdot 2$), ($\epsilon\cdot 3$) and ($\epsilon\cdot 4$) into ($\epsilon\cdot 1$), the radial force equation becomes

$$F_r(p) = (1-T_r)\left[(1-T_z)F_{i,j} + T_z F_{i,j+1}\right] + T_r\left[(1-T_z)F_{i+1,j} + T_z F_{i+1,j+1}\right] \qquad (\epsilon\cdot 5)$$

which is the expression used in the code.

The vertical force F_z on the particle is obtained in a

similar way and is given by

$$F_z(p) = (1-T_z)\left[(1-T_r)F_{i,j} + T_r F_{i,j+1}\right] + T_z\left[(1-T_r)F_{i+1,j} + T_r F_{i+1,j+1}\right] \qquad (E\cdot 6)$$

Here the force components are given by

$$F_{i,j} = \frac{\phi_{i,j+1} - \phi_{i,j-1}}{2h_z}$$

$$F_{i,j+1} = \frac{\phi_{i,j+2} - \phi_{i,j}}{2h_z} \qquad (E\cdot 7)$$

$$F_{i+1,j} = \frac{\phi_{i+1,j+1} - \phi_{i+1,j-1}}{2h_z}$$

$$F_{i+1,j+1} = \frac{\phi_{i+1,j+2} - \phi_{i+1,j}}{2h_z}$$

which is the desired expression for the vertical force used in the code.

REFERENCES

Aaronson, M. , & Mould, J. (1983) Ap. j. 265, 1

Aaronson, M. (1983) Ap. J.(Letters). 266, L11

Aarseth, S.J., & Binney, J.J. (1978) 185 227

Aarseth, S.J. (1972) In Gravitational N-body Problem ,Ed. Lecar, Dordrecht-Holland. P.373

Ables, H.D., Newell, E.B., & O'Neill, E.J. (1974) Pub. Astron. Soc. Pac. 86, 311

Ahmed, A. & Cohen, L,. (1973) J.Comp.Phys. 12 389

Antony Ralston & Philip Rabinowitz In A First Curse in Numerical analysis. McGraw-Hill International book company .

Bahcall, J.N. &. Casertano, S., (1980) Ap. J.(Letters). 284 L35

Bahcall, J.N. & Soneira, R.M. (1980) Ap.J. Supp. 44 73

Bertola, F. & Cappaccioli, M. (1975) Ap.J. 200 459

Bettis, D.G. & Szebehely, V. (1972) In Gravitational N-body Problem, Ed. Lecar, Dordrecht-Holland. P. 388

Binney, J. J (1978) M.N.R.A.S. 183 501

Binney, J. J. &.Silk, J. (1979) M.N.R.A.S. 188 273

Binney, J.J. (1982) Ann. Rev. Aston. Ap. 20 399

Borne, K. D (1982) Ap. J. 287 503

Bosma, A. (1983) In IAU Symposium 100 Internal kinematics and Kinematics of Galaxies, ed. E. Anthanssoula P.253

Brandt, A. (1977) Mathematics of computations 31 333

Burkhead, M.S. (1979) In Photometry, Kinematics and Dynamics of Galaxies, Ed. D.S.Evans, P.143

Caldwell, J.A.R. & Ostriker, J. P. (1981) Ap.J. 251 61

Caputo, F & Castellani, V. (1984) M.N.R.A.S. 207 185

Chandrasekhar, S. (1942) In Principles of Stellar Dynamics Dover

Chandrasekhar, S. (1943) Ap. J. 97 255

Crampton, D., Schade,D.,Chayer. P, & Cowley, A.P. (1985) Ap.J 288

Davis, M., Geller, M.J., & Huchra, J. (1978) Ap. J. 221 1

Dawe, J.A., & Dickens, R. J.(1976) Nature 263 395

Dekel, A, Lecar, M. & Shaham, J (1980) Ap.J 241 946

de Vaucouleurs, G. (1948) Ann. d' Ap. 11 247

de Vaucouleurs, G. (1970) Ap.J. 159 435

de Vaucouleurs, G. &. Freeman, K.C. (1972) In Vistas in Astronomy Ed. A. Beer; P.163
de Vaucouleurs, G. (1977) Nature 266 126
de Vaucouleurs, G. & Neito, J.L. (1978) Ap. J. 220 449
de Vaucouleurs, G. (1978a) Ap. J. 223 331
de Vaucouleurs, G. (1978b) Ap. J. 224 14
de Vaucouleurs, G. (1979) Ap.J. 227 729
de Vaucouleurs, G. (1979) Ap. J 233 433
Efstathiou, G. & Jones, B.J.T. (1979) M.N.R.A.S. 186 133
Faber, S.M., & Jackson, R.E. (1976) 204 668
Faber, S.M., & Gallagher, J.S. (1979) Ann.Rev.Aston.Ap. 17 135
Faber, S.M., & Lin, D.N.C. (1983) Ap. J (Letters) 266 L21
Fall, S.M. & Rees, M.J. (1977) M.N.R.A.S. 181 37
Forte,J.C.,Strom,S.E., & Strom,K.M. (1981) Ap.J.(Letters) 245 L9
Freeman, K.C. (1970) Ap. J. 160 811
Goldreich, P &. Tremaine, S. (1979) Ap.J. 233 857
Grillmair,C.,Pritchet,C. & van den Bergh,S. (1986) Aston.J 91 1328
Hanes, D.A. (1977a) M.N.R.A.S 180 309
Hanes, D.A. (1977b) Mem.R. Astron. Soc. 84 45
Hanes, D.A. (1977d) M.N.R.A.S 179 331
Hanes, D.A. (1978) In Globular Clusters NATO Symposium. P.213
Hanes, D.A. (1979) M.N.R.A.S 188 901
Hanes,D.A. & Harris, W.E. (1986) Ap.J. 304 599
Harris, W.E. (1976) Astron .J. 81 1095
Harris, W.E & Racine,R. (1979) Ann.Rev.Aston.Ap. 17 241
Harris, W.E. (1981) Ap.J. 251 497
Harris, W.E & van den Bergh, S (1981) Astron.J 86 1627
Harris, W.E, Harris, H.C., & Harris,G.L.H (1984) Astron.J 89 216
Harris,G.L.H.,Hesser,J.E.,Harris,H.C.,Curry,P (1984) Ap.J 287 175
Harris, W.E (1985) Preprint
Hodge, P. W. (1981) Ann.Rev.Astron.Ap. 19 373
Hubble, E.P (1926) Ap. J 63 236
Hubble, E.P (1936) Ap. J. 84 158
Huchra,J.P., Davis, R.J. & Latham, D.W. (1984) In Clusters and Groups of Galaxies, Reidel, Dordrecht. P. 79
Humason,M.L.,Mayall,N.U.,Sandage,A.R (1956) Ap. J 61 97

Illingworth,G. (1977) Ap.J. (Letters) 218 L43
Innanen, K.A (1973) Astron. Space Sci 22 393
Innanen, K.A, Harris,W.E. & Webbink,R.F.(1983) Astron.J. 88 338
Kalnajs, A.J. (1972) In Gravitational N-body Problem Ed. Lecar, Dordrecht-Holland. P. 13
Keenan, D.W (1979) Aston. Ap. 71 245
King, I.R. (1962) Astron.J 67 471
King, I.R. (1966) Astron.J 71 64
Kormendy, J (1977) Ap.J 218 333
Kormendy, J and Illingworth, G. (1982) Ap. J 265 166
Lin, D.N.C & Lynden-Bell, D. (1982) M.N.R.A.S 198 707
Lin, D.N.C & Tremaine, S. (1983) Ap J. 264 364
Lynden-Bell, D & Kalnajs, A.J. (1972) M.N.R.A.S 157 1
Mc Millan (1958) In The Theory of the Potential, Dover, New York
Mihalas,D & Binney, J (1981) In Galactic Astronomy Second Edition
Miller, R.H. (1978) Ap. J. 223 122
Oemler, G (1976) Ap. J. 209 693
Oort, J. (1965) In Stars and Stellar Systems, Vol.5 P.483
Ostirker, J.P.,Spitzer,L,Chevalier,R.A. (1972) Ap.J(Letts) 176 L51
Ostriker, J.P & Tremaine, S.d. (1975) Ap. J (Letters) 202 L113
Ostriker, J.P.,Peebles,P.J.E. & Yahil,A (1974) Ap.J(Letts) 193 L1
Ostriker, J.P. & Tremaine, S.D. (1975) Ap. J (Letts) 202 L113
Ostriker, J.P & Turner, E.L. (1979) Ap. J 234 785
Palmer, P.L. & Papaloizou, J. (1982) M.N.R.A.S. 199 869
Palmer, P.L (1983) M.N.R.A.S. 204 507
Palmer,P.L. & Papaloizou, J. (1985) M.N.R.A.S. 215 691
Peebles, P.J.E. & Dicke, R.H. (1968) Ap. J 176 91
Peebles, P.J.E (1980) In The Large Structure Of the Universe Princeton Univ. Press Princeton.
Peebles, P.J.E (1984) Ap. J. 277 470
Peterson, S.D (1979) Ap J. 232 20
Pritchet,C.J., & van den Bergh, S. (1985) Aston. J. 90 2027
Quinn, P.J & Goodman, J. (1986) Preprint
Racine, R. (1968) J.R. Astr.Soc.Can 62 367
Racine, R. (1973) Aston. J. 78 180
Racine, R. & Shara, M. (1979) Astron. J. 84 1694
Richstone, D. & Sargent, W.L.W. (1972) Ap. J. 176 91

Rubin,V.C, Ford,W.K. Thonrard,N Burstein,D (1982) Ap. J. 261 439
Sandage,A.R. (1958) Ap.J 127 513
Sandage, A.R (1968) Ap. J (Letters) 152 L149
Sandage, A.R. & Tammann,G.A. (1971) Ap. J. 167 399
Sandage, A.R. & Tammann, G.A. (1974) Ap. J 190 525
Sandage, A.R. & Tammann, G.A. (1976) Ap. J. 210 7
Sandage, A.R. & Tammann, G.A (1976b) Ap. J.(Letters) 207 L1
Schechter, P.L. & Gumm, J.E (1979) Ap. J. 229 472
Schechter, P.L. (1980) Astron J 85 801
Spinrad,H.,Ostriker,J.P Stone,R.P.S. et. al (1978) Ap.J 225 56
Spitzer, L & Hart, M.H (1971) Ap. J 164 399
Spitzer, L.& Chevalier, R.A (1973) Ap. J 183 565
Spitzer, L (1975) In Dynamics of Stellar Systems IAU Sym. 69 P. 3
Strom,S.E. et. al (1981) Ap. J 245 416
Tammann, G.A. (1973) In Confrontation of Cosmological Theories with Observational Data IAU Sym 63 P 47
Tammann, G.A & Sandage, A.R (1984) Preprint
Thuan, T.X & Gott, J.R (1977) Ap. J 216 194
Toomre, A. (1963) Ap. J 138 385
Toomre, A. (1964) Ap. J 139 1217
Toomre, A & Toomre, J. (1972) Ap. J 178 623
Tremaine, S.D Ostriker, J.P & Spitzer,L (1975) Ap.J 196 407
Tremaine, S.D (1976a) Ap. J 203 72
Tremaine, S.D (1976) Ap. J. 203 345
Tremaine, S.D (1980) In The Structure and Evolution of Normal Galaxies Cambridge Press Cambridge P 67
Tremaine, S.D & Weinbergh, M.D (1984) M.N.R.A.S 209 729
Tully, R.B & Fisher, J.R (1977) Aston. & Ap. 54 661
Turner, E.L (1976) Ap. J 208 20
van Albada, T.S & van Gorkom, J.H (1977) Astron.& Ap. 54 121
van den Bergh, S (1960) Publ.David Dunlop Obs 2 159
van den Bergh, S (1967) Astron J. 72 70
van den Bergh, S. (1969) Ap.J Supp. 19 145
van den Bergh, S (1972) Astron & Ap. 20 469
van den Bergh, S (1975) Astron & Ap. 44 231
van den Bergh, S (1977) Astron. J 82 796
van den Bergh, S (1981) Science 213 825

van den Bergh,S. & Harris, W.E. (1982) Astron J. 87 494
van den Bergh,S (1984) Publ.Astron.Soc.Pac. 96 329
van den Bergh, S (1984) Q.J.R.Astron.Soc 25 137
van den Bergh, S (1985) Ap. J 297 361
van den Bergh,S.,Pritchet,C.,Grillmair,C. (1985) Astron J. 90 595
Webbink, R.F. (1985) Preprint
Weinberg, M.D. (1985) M.N.R.A.S. 213 451
Weinberg, M.D. (1986) Ap.J 300 93
White, S.D.M (1976a) M.N.R.A.S. 174 19
White, S.D.M (1976b) M.N.R.A.S. 174 467
White, S.D.M (1978) M.N.R.A.S. 184 185
White, S.D.M. (1979) M.N.R.A.S. 189 831
White, S.D.M & Valdes, F. (1980) M.N.R.A.S. 190 55
White, S.D.M (1983) Ap. J 274 53
Wilson, L.P. (1975) Astron.J 80 175